



ISSN 1343-2230

CNS-REP-90  
March, 2013

# Annual Report 2011

Center for Nuclear Study,  
Graduate School of Science, the University of Tokyo

Editors  
Shinsuke Ota

## **Center for Nuclear Study**

CNS Reports are available from:  
Wako-Branch at RIKEN  
Center for Nuclear Study,  
Graduate School of Science, the University of Tokyo  
2-1 Hirosawa, Wako  
351-0198, Japan  
Tel: +81-48-464-4191  
Fax: +81-48-464-4554

# Annual Report 2011

Center for Nuclear Study,  
Graduate School of Science, the University of Tokyo



# Preface

This is the annual report of the Center for Nuclear Study (CNS), Graduate School of Science, the University of Tokyo, for the fiscal year 2011 (April 2011 through March 2012). In the CNS, during this period, a large number of scientific activities in various fields of nuclear physics have been carried out and a wide variety of fruitful results have been obtained. This report presents a report of such activities. Some highlights of the report are mentioned here.

The NUSPEQ (NUclear SPectroscopy for Extreme Quantum system) group studies exotic structure in high-isospin and/or high-spin states in nuclei. The CNS GRAPE (Gamma-Ray detector Array with Position and Energy sensitivity) is a major apparatus for high-resolution in-beam gamma-ray spectroscopy. Missing mass spectroscopy using the SHARAQ is going to start as another approach on exotic nuclei. In 2011, the following progress has been made.

Analysis of  $\alpha$  inelastic scattering data from nuclei in the island of inversion, which was taken by using GRAPE, has progressed. Experiments for searching new isomers by using  $^{238}\text{U}$  and  $^{124}\text{Xe}$  primary beams from SRC were performed and the analysis of the obtained data is in progress. A plunger system for recoil distance method was developed for the approved experiments of the lifetime measurements of neutron-rich fp-shell nuclei. The readout system of 12 detectors of the CNS GRAPE was upgraded, where digital pulse data taken by sampling ADCs are analyzed by FPGAs on boards. Experimental setup of studying tetra neutron system using the double-charge exchange reaction  $^4\text{He}(^8\text{He}, ^8\text{Be})4n$  at 200 A MeV was developed for the measurement at the SHARAQ in April 2012.

The nuclear astrophysics group is studying astrophysical reactions particularly at high temperature phenomena, such as supernovae and X-ray bursts, using the low-energy beam separator, CRIB. In 2011, the operation of CRIB was shut down for half a year, due to the earthquake. "Review Meeting on CRIB Activities", which summarizes the activities at CRIB for 10 years, was held in June. After the operation was restarted, we performed several experiments under international collaborations. An active target (GEM-MSTPC) had been developed and used for  $(\alpha, p)$  reaction measurements in the previous years, and a direct measurement of  $^{22}\text{Mg}(\alpha, p)$ , proposed by Vietnamese group, was performed with the active target.  $^{16}\text{N}$  beam production was first tested at CRIB with Italian group (INFN-LNS), and the beam will be used for indirect measurement of  $^{12}\text{C}(\alpha, \gamma)$  reaction rate. A proton resonant scattering experiment of  $^{22}\text{Na}+p$  was also performed, with Chinese collaborators in CIAE and IMP. OMEG11, the 11th symposium on nuclear astrophysics, was held in November, hosted by CNS with other institutions. Prof. Kubono, who has been working for CRIB for more than a decade, retired at the end of the fiscal year.

One of the Major tasks of the accelerator group is the AVF upgrade project that includes development of ion sources, upgrading the AVF cyclotron of RIKEN and the beam line to CRIB. Development of ECR heavy ion sources is to provide a new HI beams, higher and stable beams of metallic ions, and to improve the control system. Two CNS ECR sources provide all the beams for the AVF cyclotron and support not only CRIB experiments but also a large number of RIBF experiments. Injection beam monitoring and control are being studied. New ion-source beam diagnosis and monitoring system (ISDM) was designed. This new beam monitor becomes a powerful tool for all the RIBF facility.

The SHARAQ group performed a physics experiment to investigate the spin-isospin excitations of magicity-melted  $^{12}\text{Be}$  nucleus by the  $(p,n)$  reaction in the inverse kinematics. A neutron-detector array, called WINDS, was newly constructed to measure the slow neutrons produced by the  $(p,n)$  reaction. WINDS was installed so that it surrounds the reaction target and operated successfully throughout the experiment. Thus we have acquired a new method to explore the spin-isospin properties of unstable nuclei.

Main goal of the quark physics group is to understand the properties of hot and dense nuclear matter created by colliding heavy nuclei at relativistic energies. The group has been involved in the PHENIX experiment at Relativistic Heavy Ion Collider (RHIC) at Brookhaven National

Laboratory, and in the ALICE experiment at Large Hadron Collider (LHC) at CERN. In PHENIX, the group has been concentrating on the physics analysis involving leptons and photons, the main topics of which are direct photon production using the virtual-gamma method, and  $J/\psi$  production in ultra-peripheral Au+Au collisions. The Si VTX detector, whose construction and commissioning the CNS group has been involved in, has been successfully used in the Au+Au runs performed in the spring of 2012. In ALICE, the group has been involved in the installation/commissioning of the Transition Radiation Detector (TRD), and calibration and performance study of Time Projection Chamber (TPC). The group has significant contribution to the data analysis in ALICE. The main topics of the analysis are collective flow of the medium, parton energy loss in the medium, and dilepton production in Pb-Pb collisions. The group has also been working for the development of FoCal (forward calorimeter) for future ALICE upgrade. Significant progress of the prototype R&D has been made in 2011.

R&D of gas electron multiplier (GEM) and related techniques has been continuing. Development of resistive GEM with resistive anodes and Glass-GEM has been progressing in collaboration

In a project of active target development launched as an intergroup collaboration in 2009, two types of active target have been developed. The GEM-MSTPC for the astrophysics interest is used in the measurement of  $(\alpha, p)$  reactions as mentioned above. The other type of active target called CAT was tested in the test experiment using  $^{56}\text{Fe}$  of 250 MeV/u and the data analysis is in progress.

The nuclear theory group has been promoting the RIKEN-CNS collaboration project on large-scale nuclear structure calculations since 2001 and maintaining its parallel computing clusters. Based on this experience, we participated in activities of HPCI Strategic Programs for Innovative Research (SPIRE) Field 5 "The origin of matter and the universe" since 2011. The SPIRE project aims at the comprehensive understanding of the origin and structure of matter and the Universe utilizing the K computer. In 2011, we developed the program of the Monte Carlo shell model to perform large-scale shell model calculations in massively parallel computers and described nuclear structure of some exotic nuclei such as neutron-rich Ni isotopes and Ba isotopes microscopically.

The 10th CNS International Summer School (CNSSS11) has been organized in September 2011 with many invited lecturers including three foreign distinguished physicists. There were 82 participants from 5 countries mainly from Asia.

For the accidents at the Fukushima Daiichi Nuclear Power Plant in March 2011, members of the CNS participated to the radiation screening of evacuated people in Fukushima just after the accidents. Radiation maps in wide area around the power plant were made by a collaboration of scientists from various universities and institutes. CNS acted as a hub of the collaboration, where tasks such as receiving and checking about 6000 samples from Fukushima; sending them to 22 analysis groups depending on their capacities; and collecting, checking, and summarizing the results were performed.

Finally, I thank Ms. M. Hirano and other administrative and technical staff members for their heartfelt contributions throughout the year.

Takaharu Otsuka  
Director of CNS



# Table of Contents

## 1a. Experimental Nuclear Physics: Low and Intermediate Energies

Progress in the analysis of the direct measurement of the $^{11}\text{C}(\alpha, p)^{14}\text{N}$ reaction .....	3
<i>S. Hayakawa, S. Kubono, D. Kahl, H. Yamaguchi, D. N. Binh, T. Hashimoto, Y. Wakabayashi, J. J. He, N. Iwasa, S. Kato, T. Komatsubara, Y. K. Kwon, T. Teranishi, and S. Wanajo</i>	
Experimental study of key astrophysical $^{18}\text{Ne}(\alpha, p)^{21}\text{Na}$ reaction .....	5
<i>L.Y. Zhang, J.J. He, S.W. Xu, H. Yamaguchi, S. Kubono, Y. Wakabayashi, S.Z. Chen, J. Hu, P. Ma, Y. Togano, T. Hashimoto, D. Kahl, T. Teranishi, R.F. Chen, H.W. Wang, W.D. Tian, B. Guo, S. Hayakawa, N. Iwasa, T. Yamada, and T. Komatsubara</i>	
RI Beam Production in the $^{22}\text{Mg} + \alpha$ Experiment at CRIB .....	7
<i>N. N. Duy, L. H. Khiem, S. Kubono, H. Yamaguchi, D. M. Kahl, T. Hashimoto, S. Ota, Y. Wakabayashi, T. Komatsubara, T. Teranishi, S. Kato, N. Iwasa, T. Yamada, Y. K. Kwon, A. Kim, Y.H. Kim, J.S. Song, J. Hu, and J. Ito.</i>	
Role of the $^{22}\text{Mg}(\alpha, p)^{25}\text{Al}$ Reaction and Its First Direct Measurement .....	9
<i>N. N. Duy, L. H. Khiem, S. Kubono, H. Yamaguchi, D. M. Kahl, T. Hashimoto, S. Ota, Y. Wakabayashi, T. Komatsubara, T. Teranishi, S. Kato, N. Iwasa, T. Yamada, Y. K. Kwon, A. Kim, Y.H. Kim, J.S. Song, J. Hu, and J. Ito.</i>	
Study of the $^{22}\text{Na}+p$ Resonance Scattering at CRIB .....	11
<i>S. J. Jin, Y. B. Wang, J. Su, S. Q. Yan, Y. J. Li, Z. H. Li, B. Guo, W. P. Liu, S. Kubono, H. Yamaguchi, D. Kahl, J. Hu, H. S. Jung, J. Y. Moon, T. Teranishi, H. W. Wang, H. Ishiyama, H. Iwasa, H. Komatsubara</i>	
Study of resonant states in $^{26}\text{Si}$ and $^{27}\text{P}$ with radioactive ion beams .....	13
<i>H.S. Jung, C.S. Lee, Y.K. Kwon, J.Y. Moon, J.H. Lee, C.C. Yun, S. Kubono, H. Yamaguchi, T. Hashimoto, D. Kahl, S. Hayakawa Seonho Choi, M.J. Kim, Y.H. Kim, Y.K. Kim, J.S. Park, E.J. Kim, C.-B. Moon, T. Teranishi, Y. Wakabayashi, N. Iwasa, T. Yamada, Y. Togano, S. Kato, S. Cherubini and G.G. Rapisarda</i>	
Heavy-ion double charge exchange reaction on $^9\text{Be}$ .....	16
<i>H. Matsubara, M. Takaki, T. Uesaka, S. Shimoura, N. Aoi, M. Dozono, T. Fujii, K. Hatanaka, T. Hashimoto, T. Kawabata, S. Kawase, K. Kisamori, Y. Kikuchi, Y. Kubota, C.S. Lee, H.C. Lee, Y. Maeda, S. Michimasa, K. Miki, H. Miya, S. Noji, S. Ota, S. Sakaguchi, Y. Sasamoto, T. Suzuki, L.T. Tang, K. Takahisa, H. Tokieda, A. Tamii, K. Yako, Y. Yasuda, N. Yokota, R. Yokoyama, and J. Zenihiro</i>	
Study of low-lying states of $^{12}\text{Be}$ via the heavy-ion double-charge exchange $^{12}\text{C}(^{18}\text{O}, ^{18}\text{Ne})$ reaction .....	18
<i>M. Takaki, H. Matsubara, T. Uesaka, S. Shimoura, N. Aoi, M. Dozono, T. Fujii, T. Hashimoto, K. Hatanaka, T. Kawabata, S. Kawase, K. Kisamori, C.S. Lee, H.C. Lee, Y. Maeda, S. Michimasa, K. Miki, H. Miya, S. Noji, S. Ota, S. Sakaguchi, M. Sasano, T. Suzuki, K. Takahisa, T.L. Tang, A. Tamii, H. Tokieda, K. Yako, N. Yokota, R. Yokoyama and J. Zenihiro</i>	
The parity-transfer reaction ( $^{16}\text{O}, ^{16}\text{F}$ ) for studies of pionic $0^-$ mode .....	20
<i>M. Dozono, T. Uesaka, M. Sasano, H. Matsubara, S. Shimoura, K. Yako, S. Michimasa, S. Ota, Y. Sasamoto, S. Noji, H. Tokieda, S. Kawase, R. Tang, Y. Kikuchi, K. Kisamori, M. Takaki, Y. Kubota, C. S. Lee, T. Fujii, R. Yokoyama, H. Sakai, T. Kubo, K. Yoshida, Y. Yanagisawa, N. Fukuda, H. Takeda, D. Kameda, N. Inabe, T. Wakasa, K. Fujita, S. Sakaguchi, H. Sagawa, M. Yamagami, and M. Ichimura,</i>	
Identification of isovector non-spin-flip excitation by the super-allowed Fermi type charge reaction .....	22

<i>Y. Sasamoto, T. Uesaka, S. Shimoura, S. Michimasa, S. Ota, K. Miki, S. Noji, K. Yako, H. Tokieda, H. Miya, S. Kawase, Y. Kikuchi, K. Kisamori, M. Takaki, M. Dozono, H. Mathubara, H. Sakai, T. Kubo, Y. Yanagisawa, H. Takeda, K. Yoshida, T. Ohnishi, N. Fukuda, D. Kameda, N. Inabe, N. Aoi, S. Takeuchi, T. Ichihara, H. Baba, S. Sakaguchi, P. Doornenbal, H. Wang, R. Chen, Y. Shimizu, T. Kawahara, T. Kawabata, N. Yokota, Y. Maeda, H. Miyasako, G. P. A. Berg</i>	
A new spectroscopic tool by the radioactive-isotope-beam induced exothermic charge-exchange reaction	24
<i>S. Noji, H. Sakai, N. Aoi, H. Baba, G. P. A. Berg, P. Doornenbal, M. Dozono, N. Fukuda, N. Inabe, D. Kameda, T. Kawabata, S. Kawase, Y. Kikuchi, K. Kisamori, T. Kubo, Y. Maeda, H. Matsubara, S. Michimasa, K. Miki, H. Miya, H. Miyasako, S. Sakaguchi, Y. Sasamoto, S. Shimoura, M. Takaki, H. Takeda, S. Takeuchi, H. Tokieda, T. Ohnishi, S. Ota, T. Uesaka, H. Wang, K. Yako, Y. Yanagisawa, N. Yokota, K. Yoshida</i>	
Measurement of $^{12}\text{Be}(p, n)^{12}\text{B}$ reaction at 200A MeV in inverse kinematics	26
<i>K. Yako, H. Sakai, H. Baba, M. Dozono, T. Fujii, N. Inabe, S. Kawase, T. Kawabata, Y. Kikuchi, K. Kisamori, T. Kubo, Y. Kubota, H. Matsubara, S. Michimasa, K. Miki, H. Miya, M. Kurata-Nishimura, S. Noji, C.S. Lee, T. Ohnishi, S. Ota, Y. Sasamoto, M. Sasano, Y. Shimizu, S. Shimoura, M. Takaki, H. Takeda, T.L. Tang, H. Tokieda, T. Uesaka, Z.Y. Xu, R. Yokoyama and R.G.T. Zegers</i>	
Experimental design for $^A\text{O}(\vec{p}, pN)$ reaction measurement in inverse kinematics	27
<i>S. Kawase, T. Uesaka, S. Shimoura, K. Yako, S. Ota, S. Michimasa, H. Tokieda, H. Miya, T. L. Tang, K. Kisamori, M. Takaki, Y. Kubota, C. S. Lee, R. Yokoyama, T. Fujii, M. Kobayashi, M. Sasano, J. Zenihiro, H. Matsubara, M. Dozono, T. Kawahara, T. Waku, S. Sakaguchi</i>	
Proton Inelastic Scattering Study on Neutron-rich $^{32,34,36}\text{Mg}$ Isotopes	29
<i>S. Michimasa, Y. Yanagisawa, K. Inafuku, N. Aoi, Z. Elekes, Zs. Fülöp, Y. Ichikawa, N. Iwasa, K. Kurita, M. Kurokawa, T. Machida, T. Motobayashi, T. Nakamura, T. Nakabayashi, M. Notani, H. J. Ong, T. K. Onishi, H. Otsu, H. Sakurai, M. Shinohara, T. Sumikama, S. Takeuchi, K. Tanaka, Y. Togano, K. Yamada, M. Yamaguchi, and K. Yoneda</i>	
$\alpha$ inelastic scattering on neutron-rich nuclei around $^{32}\text{Mg}$	31
<i>T. Fujii, S. Ota, S. Shimoura, N. Aoi, E. Takeshita, S. Takeuchi, H. Suzuki, H. Baba, T. Fukuchi, T. Fukui, Y. Hashimoto, E. Ideguchi, K. Ieki, N. Iwasa, H. Iwasaki, S. Kanno, Y. Kondo, T. Kubo, K. Kurita, T. Minemura, S. Michimasa, T. Motobayashi, T. Murakami, T. Nakabayashi, T. Nakamura, J. Niikura, T. Okumura, T. Onishi, H. Sakurai, M. Shinohara, D. Suzuki, M. Suzuki, M. Tamaki, K. Tanaka, Y. Togano, and Y. Wakabayashi</i>	
Search for new isomers near the N=Z line by using projectile-fragmentation of $^{124}\text{Xe}$	33
<i>S. Go, D. Kameda, T. Kubo, N. Inabe, N. Fukuda, H. Takeda, H. Suzuki, K. Yoshida, K. Kusaka, K. Tanaka, Y. Yanagisawa, M. Ohtake, H. Sato, Y. Shimizu, H. Baba, M. Kurokawa, D. Nishimura, N. Iwasa, A. Chiba, Y. Okoda, E. Ideguchi, R. Yokoyama, T. Fujii, K. Ieki, D. Murai, H. Nishibata, S. Momota, M. Lewitowics, G. Defrance, I. Celikovic, K. Steiger, D. J. Morrissey, and D. P. Bazin</i>	
Search for short-lived isomers in neutron-rich $Z \sim 60$ nuclei produced by in-flight fission of $^{238}\text{U}$	35
<i>R. Yokoyama, D. Kameda, T. Kubo, N. Inabe, N. Fukuda, H. Takeda, H. Suzuki, K. Yoshida, K. Kusaka, K. Tanaka, Y. Yanagisawa, M. Ohtake, H. Sato, Y. Shimizu, H. Baba, M. Kurokawa, D. Nishimura<sup>1</sup>, T. Ohnishi, N. Iwasa, A. Chiba, T. Yamada, E. Ideguchi<sup>2</sup>, S. Go, T. Fujii, H. Nishibata, K. Ieki, D. Murai, S. Momota, Y. Sato, J. Hwang, S. Kim, O. B. Tarasov, D. J. Morrissey, B. M. Sherrill, and G. Simpson</i>	
<b>1b. Experimental Nuclear Physics: PHENIX Experiment at BNL-RHIC and ALICE Experiment at CERN-LHC</b>	
Identified particle flow measurement in Pb-Pb collisions at $\sqrt{s_{NN}}=2.76$ TeV measured by the ALICE experiment at the LHC	39

<i>Y. Hori, T. Gunji, H. Hamagaki for the ALICE collaboration</i>	
Measurements of $\pi^0$ with respect to reaction plane in $\sqrt{s_{NN}} = 2.76$ TeV Pb+Pb collisions at LHC-ALICE	41
<i>T. Tsuji, H. Hamagaki, T. Gunji, H. Torii, for the ALICE collaboration</i>	
Measurement of $J/\psi$ photoproduction in ultra-peripheral Au+Au collisions at $\sqrt{s_{NN}}=200$ GeV using the PHENIX detector	43
<i>A. Takahara, H. Hamagaki, T. Gunji, Z. Conesa del Valle, Y. Akiba, M. Chiu, J. Nystrand, S. White, K. Skjerdal, E. T. Atomssa</i>	
Neutral pion and $\eta$ meson production in proton-proton collisions at $\sqrt{s} = 0.9$ TeV and $\sqrt{s} = 7$ TeV	45
<i>H. Torii for the ALICE Collaboration</i>	
Measurement of Di-electrons in Pb-Pb Collisions at LHC-ALICE	47
<i>T. Gunji for the ALICE Collaboration</i>	
Direct virtual photon measurement in $\sqrt{s} = 200$ GeV $p+p$ collisions at RHIC-PHENIX	49
<i>Y.L. Yamaguchi, H. Hamagaki, Y. Akiba, and T. Gunji, for the PHENIX collaboration</i>	

## 2. Accelerator and Instrumentation

Development of the wide-dynamic range Front-end ASIC for the W+Si sampling Calorimeter .....	53
<i>S. Hayashi, H. Hamagaki, T. Gunji, M. Tanaka, and H. Ikeda,</i>	
Development of W+Si Electromagnetic Calorimeter for the LHC-ALICE Upgrade .....	55
<i>T. Gunji, H. Hamagaki, Y. Hori, S. Hayashi, Y. Sekiguchi, for the ALICE-FOCAL Collaboration</i>	
Track Reconstruction with Silicon Vertex Tracker for the RHIC-PHENIX Experiment .....	57
<i>R. Akimoto, Y. Akiba<sup>a,b</sup>, H. Asano<sup>c</sup>, T. Gunji, T. Hachiya<sup>a</sup>, H. Hamagaki, M. Kurosawa<sup>b</sup>, M. Shimomura<sup>d</sup> (for the PHENIX Collaboration)</i>	
Development of GEM with Glass Insulator .....	59
<i>Y. Sekiguchi, H. Hamagaki, T. Gunji, and T. Tamagawa</i>	
SHARAQ Project — Progress in FY2011 — .....	61
<i>S. Michimasa, S. Ota, S. Shimoura, T. Uesaka, Y. Sasamoto, K. Miki, S. Noji, H. Matsubara, M. Dozono, H. Miya, H. Tokieda, S. Kasase, S. Sasano, K. Kisamori, M. Takaki, R. Yokoyama, T. Fujii, Y. Kubota, C.S. Lee, H. Kurei, T. Kawabata, K. Yako, N. Yamazaki, A. Yoshino, H. Sakai, T. Kubo, N. Inabe, Y. Yanagisawa, D. Kameda, H. Suzuki, H. Takeda, T. Ichihara, H. Baba, G.P. Berg, P. Roussel-Chomaz, D. Bazin, for the SHARAQ collaboration.</i>	
$\mu$ Hodoscope using 1-mm square plastic scintillators for the experiments with high-intensity beam .....	63
<i>Y. Kikuchi, S. Ota, H. Matsubara, Y. Kubota, C.S. Lee, S. Kawase, and T. Uesaka</i>	
Development of LP-MWDCs for high resolution spectroscopies with high intensity RI beam .....	65
<i>H. Miya, S. Ota, H. Matsubara, S. Kawase, Y. Kikuchi, C. S. Lee, T. Fujii, Y. Kubota, and S. Shimoura</i>	
Development of WINDS: wide-angle inverse-kinematics neutron detectors for SHARAQ .....	67
<i>K. Yako, H. Sakai, M. Dozono, T. Fujii, S. Kawase, Y. Kikuchi, K. Kisamori, Y. Kubota, H. Matsubara, S. Michimasa, K. Miki, H. Miya, S. Noji, C.S. Lee, T. Ohnishi, S. Ota, Y. Sasamoto, M. Sasano, S. Shimoura, M. Takaki, H. Tokieda, T. Uesaka, Z.Y. Xu and R. Yokoyama</i>	
Development of the detection system for tetra-neutron experiment via ${}^4\text{He}({}^8\text{He}, {}^8\text{Be})4n$ reaction .....	68
<i>K. Kisamori, S. Shimoura, S. Michimasa, S. Ota, S. Noji, A. Tokieda, R. Yokoyama and H. Baba</i>	
Modification of Active Target for the forward angle scattering and measurement of deuteron induced reaction on ${}^{56}\text{Fe}$ .....	70
<i>S. Ota, H. Tokieda, C.S. Lee, M. Dozono, H. Matsubara, S. Kawase, Y. Kubota, S. Michimasa, H. Yamaguchi, M. Sako, T. Gunji, Y. Kikuchi, T. Hashimoto, H. Hamagaki, T. Uesaka, S. Kubono, H. Otsu, Y. Maeda, E. Takada</i>	
The Performance Evaluation of NaI Detectors for CNS Active Target .....	72
<i>C. S. Lee, S. Ota, H. Tokieda, M. Dozono, H. Matsubara, S. Kawase, Y. Kubota, S. Michimasa, H. Yamaguchi, H. Hamagaki, M. Sako, Y. Maeda, T. Uesaka, H. Otsu and S. Kubono</i>	
Development of neutron detector for the study of neutron single particle state .....	74
<i>Y. Kubota, T. Uesaka, S. Ota, M. Dozono, and Y. Kikuchi</i>	
Simulation Study of the Ionization Cooling .....	76
<i>C. S. Lee, T. Uesaka, M. Sasano and S. Ota</i>	
Dynamic nuclear polarization on para-terphenyl at room temperature .....	78

*T.L. Tang, A. Shiibusawa, T. Kawahara, T. Wakui, T. Uesaka*

Laser pulse structure dependency on proton polarization of para-terphenyl at room temperature ..... 80  
*T.L. Tang, T. Uesaka*

Beam Scanner of The HyperECR ..... 82  
*S. Watanabe, Y. Ohshiro, S. Yamaka, S. Kubono, H. Yamaguchi, S. Shimoura, Y. Kotaka, M. Kase, K. Hatanaka, A. Goto, W. Yokota, T. Mitsumoto*

Test operation of new extraction system ..... 84  
*Y. Ohshiro, S. Yamaka, S. Watanabe, H. Muto, H. Yamaguchi, and S. Shimoura*

### 3. Theoretical Nuclear Physics

$\beta$ -Decays of Waiting-point Nuclei at N=126 and R-Process Nucleosynthesis ..... 89  
*T. Suzuki, T. Yoshida, T. Kajino and T. Otsuka*

Systematic study of low-lying  $E1$  modes  
using a time-dependent mean field theory ..... 91  
*S. Ebata, T. Nakatsukasa and T. Inakura*

Cluster structure in  $^{12}\text{C}$  and  $^{16}\text{O}$  using algebraic approach ..... 93  
*T. Yoshida, N. Itagaki and K. Katō*

Development of the Monte Carlo Shell Model for K computer ..... 95  
*N. Shimizu, Y. Utsuno, T. Abe, Y. Tsunoda and T. Otsuka*

Benchmarks of the no-core MCSM method in light nuclei ..... 97  
*T. Abe, P. Maris, T. Otsuka, N. Shimizu, Y. Utsuno and J. P. Vary*

Exploring Three-Nucleon Forces on the Lattice ..... 99  
*T. Doi (for HAL QCD Collaboration)*

### 4. Other Activities

Analysis of Gamma-ray Activities in Soils Sampled from Surrounding Area of Fukushima Daiichi Nuclear Power Plant ..... 103  
*Susumu Shimoura, Eiji Ideguchi, Shinsuke Ota, Daisuke Nakajima, Masahiko Tanaka, Ryo Yoshino, Shintaro Go, Rin Yokoyama, and Takaharu Otsuka*

The 10th CNS International Summer School (CNSSS11) ..... 104  
*S. Michimasa, T. Gunji, H. Hamagaki, S. Kubono, T. Nakatsukasa, T. Otsuka, H. Sakai, S. Shimoura, T. Suzuki and T. Uesaka*

Laboratory Exercise for Undergraduate Students ..... 105  
*S. Ota, K. Yako, R. Yokoyama, C.S. Lee, H. Sakurai and S. Shimoura*

## Appendices

Symposium, Workshop, Seminar, PAC and External Review .....	109
CNS Reports .....	111
Publication List .....	112
Talks and Presentations .....	117
Personnel .....	124

# Experimental Nuclear Physics: Low and Intermediate Energies



# Progress in the analysis of the direct measurement of the $^{11}\text{C}(\alpha, p)^{14}\text{N}$ reaction

S. Hayakawa<sup>a,1</sup>, S. Kubono<sup>b</sup>, D. Kahl<sup>a</sup>, H. Yamaguchi<sup>a</sup>, D. N. Binh<sup>c</sup>, T. Hashimoto<sup>d</sup>,  
Y. Wakabayashi<sup>b</sup>, J. J. He<sup>e</sup>, N. Iwasa<sup>f</sup>, S. Kato<sup>g</sup>, T. Komatsubara<sup>h</sup>, Y. K. Kwon<sup>i</sup>,  
T. Teranishi<sup>j</sup>, and S. Wanajo<sup>k</sup>

<sup>a</sup>Center for Nuclear Study, Graduate School of Science, University of Tokyo

<sup>b</sup>RIKEN (The Institute of Physical and Chemical Research)

<sup>c</sup>Institute of Physics

<sup>d</sup>Research Center for Nuclear Physics, Osaka University

<sup>e</sup>Institute of Modern Physics

<sup>f</sup>Tohoku University

<sup>g</sup>Yamagata University

<sup>h</sup>University of Tsukuba

<sup>i</sup>Chung Ang University

<sup>j</sup>Department of Physics, Kyushu University

<sup>k</sup>National Astronomical Observatory of Japan

We have studied the  $^{11}\text{C}(\alpha, p)^{14}\text{N}$  stellar reaction which bridges the  $pp$ -chain elements to the CNO-cycle elements [1] in high-temperature hydrogen-burning processes, and is important for the nucleosynthesis to the heavier nuclei. We aimed at determination of the total reaction rate including both the ground-state transition ( $\alpha, p_0$ ) and the excited-state transitions ( $\alpha, p_1$ ) and ( $\alpha, p_2$ ) relevant to the stellar temperature  $T_9 = 1.5\text{--}3$  ( $T_9 \equiv 1$  GK). For a more detailed introduction, see the reference [2]. Here we report a progress in the analysis.

We performed a direct measurement of this reaction as one of the first few successful experiments for the  $\alpha p$ -process reactions [3]. We observed the  $^{11}\text{C}(\alpha, p)^{14}\text{N}$  reaction events in a center-of-mass energy range  $E_{\text{cm}} = 1.2\text{--}4.5$  MeV by means of the thick target method [4] in inverse kinematics with  $^{11}\text{C}$  radioactive beams. The  $^{11}\text{C}$  beams were produced by the in-flight technique with CRIB (Center for Nuclear Study Radioactive Ion Beam separator [5]). A  $^{11}\text{B}^{3+}$  primary beam at 4.6 MeV/u and with a maximum intensity of  $1\ \mu\text{A}$  was bombarded to a cryogenic  $^1\text{H}_2$  gaseous target with a thickness of  $1.2\text{--}1.7$  mg/cm<sup>2</sup>. The secondary ions were purified by the double achromatic system and the Wien filter of CRIB. We created  $^{11}\text{C}$  beams at two different on-target energies  $10.1 \pm 0.9$  MeV and  $16.9 \pm 0.7$  MeV in order to cover a wide energy range. The experimental setup consisted of two beam-line monitors (PPAC: Parallel Plate Avalanche Counter [6] or MCP: MicroChannel Plate detector [7]), a  $^4\text{He}$  gaseous target, and  $\Delta E$ - $E$  position-sensitive silicon detector telescopes at three different angles. We carefully designed the target length (140 mm), the pressure (400 Torr) and the incident beam energies in order to differentiate each transition in time of flight (TOF) between the first PPAC and the silicon telescopes, corresponding to different reaction positions in the target gas for a certain detected energy of ejected protons.

Although the separations in time between different

transitions were not very clear, we successfully extracted the mixing ratios of the numbers of events of each transition by Gaussian fittings to the time spectra at every center-of-mass energy bin through the following improved procedure: 1) modifying the TOF by shifting at every energy so that the ( $\alpha, p_0$ ) line to be settled at  $t = 0$ , 2) converting laboratory energy to center-of-mass energy for each transition, 3) projecting the spectrum to the time axis at each center-of-mass energy bin, 4) determining the mixing ratios of the transitions at each energy by fitting with Gaussian functions. To obtain better results from low-statistics data, we reduced the degrees of freedom by fixing the peak positions of the Gaussian functions based on the calculated value, and fixing the widths of the Gaussian functions based on those of the ( $\alpha, p_0$ )-only events. An example of the procedure of this analysis is demonstrated in Fig. 1, where the left figure represents the population of several transitions on the modified TOF-energy histogram with calculation lines for ( $\alpha, p_0$ ), ( $\alpha, p_5$ ), and the right one demonstrates a projection to the time axis for a single energy bin with the fitted Gaussian functions for each transition. We assumed isotropic angular distributions although we had limited angular range of measurement, since the angular distributions did not show strong dependence on angle. In Fig. 2, the obtained astrophysical  $S$ -factors for

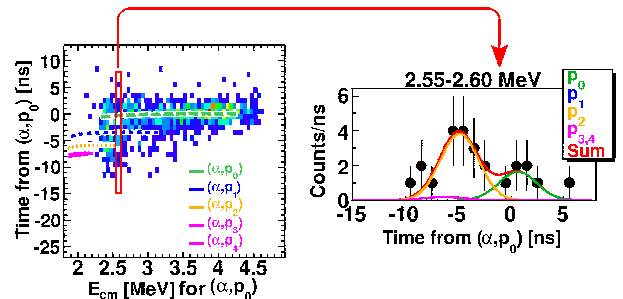


Figure 1. Example of the procedure to determine the numbers of events of each transition.

<sup>1</sup>Present address: Istituto Nazionale di Fisica Nucleare, Laboratori Nazionali del Sud

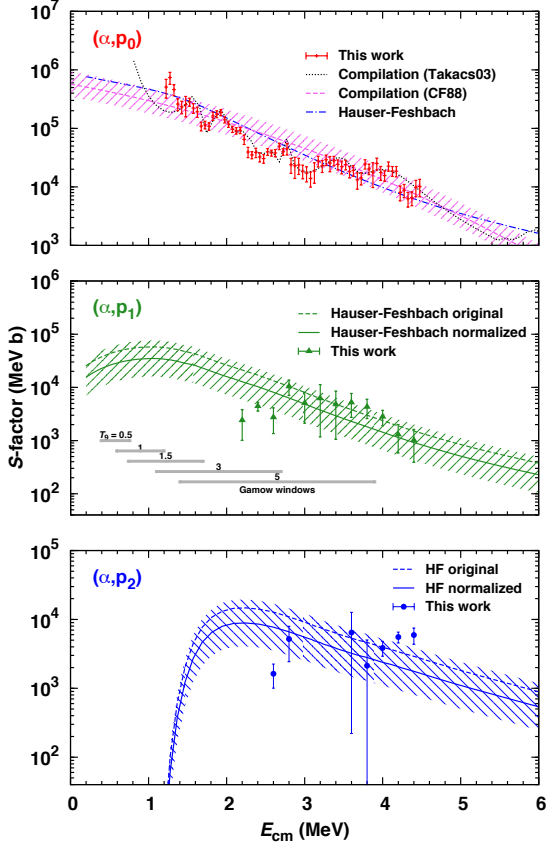


Figure 2.  $S$ -factors for  $^{11}\text{C}(\alpha, p_0)^{14}\text{N}$  (top),  $^{11}\text{C}(\alpha, p_1)^{14}\text{N}$  (middle) and  $^{11}\text{C}(\alpha, p_2)^{14}\text{N}$  (bottom). The present  $(\alpha, p_0)$   $S$ -factors are shown as dots with error bars. For  $(\alpha, p_0)$ , the fitted quadratic function with its error (“CF88”, dashed line and hatch [8, 9]), of the Padé approximation (“Takacs03”, dotted line) and the Hauser-Feshbach statistical model calculation (dashed-dotted line) are shown. For  $(\alpha, p_1)$  and  $(\alpha, p_2)$ , the original Hauser-Feshbach calculations (dashed lines) and the normalized ones with their errors (solid lines and hatches) are shown together.

$(\alpha, p_0)$  (top),  $(\alpha, p_1)$  (middle) and  $(\alpha, p_2)$  (bottom) are shown. In the top figure, the previous  $(\alpha, p_0)$   $S$ -factors, obtained from the time-reversal reaction data, of the fit with a quadratic function with its error (“CF88” [8, 9]), and of the Padé approximation (“Takacs03” [10]), and the Hauser-Feshbach statistical model calculation by the code NON-SMOKER<sup>WEB</sup> [11] are shown together. In the middle and the bottom figures, the original Hauser-Feshbach calculations and the normalized ones by the logarithmic least-squares method with their errors are shown. The errors of the CF88  $S$ -factor for  $(\alpha, p_0)$  and the Hauser-Feshbach  $S$ -factors for  $(\alpha, p_1)$  and  $(\alpha, p_2)$  are defined as the logarithmic standard deviations from the present experimental data. We confirmed that the present  $(\alpha, p_0)$  excited function is eventually consistent with Takacs03. For the whole-energy  $S$ -factor of  $(\alpha, p_0)$ , we adopted and those of CF88, and Takacs03 below and above the experimental energy range, respectively. For the whole-energy  $(\alpha, p_1)$  and the  $(\alpha, p_2)$   $S$ -factors, we tentatively used the normalized Hauser-Feshbach ones as extrapolations.

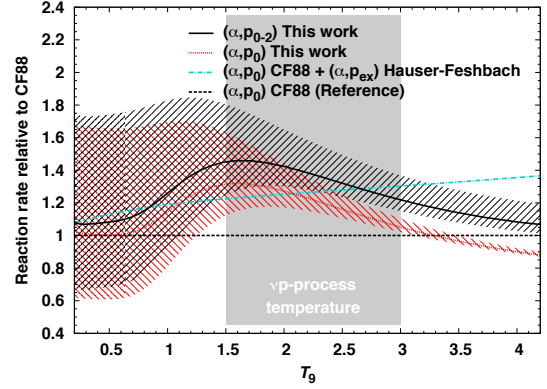


Figure 3. The present  $(\alpha, p_0)$  (dotted line) and total (solid line) reaction rates and the previous recommended rate (dashed-dotted line) relative to the CF88 rate (dashed line). The errors of the present rates are drawn in hatches. The temperature range of the  $\nu p$ -process [12] is indicated in gray.

Figure 3 shows the present  $(\alpha, p_0)$  and total reaction rates and the previous recommended rate relative to the CF88 rate. The errors of the present rates are drawn in hatches. In the  $\nu p$ -process temperature range [12], shown in the gray area, the present  $(\alpha, p_0)$  reaction rate is enhanced from the CF88 rate by 30% at most, mainly due to the resonance at 1.25 MeV which was not taken into account previously. The contribution from the  $(\alpha, p_1)$  and  $(\alpha, p_2)$  reaction rate to the total reaction rate is about 15% of the  $(\alpha, p_0)$  at most. The error of the total reaction rate is about 25% at  $T_9 = 1.5$  and 10% at  $T_9 = 3$ . We confirmed that the previous total reaction rate is eventually consistent with the present one within its error, and the difference is less than 20%, which could result in no significant change on the stellar models.

## References

- [1] M. Wiescher *et al.*, *Astrophys. J.* **343** (1989) 352.
- [2] S. Hayakawa *et al.*, *CNS Ann. Rep.* 2009 **86** (2011) 7.
- [3] S. E. Woosley, *AIP Conf. Proc.* **115** (1984) 709.
- [4] K. P. Artemov *et al.*, *Sov. J. Nucl. Phys.* **52** (1990) 408.
- [5] Y. Yanagisawa *et al.*, *NIM A* **539** (2005) 74.
- [6] H. Kumagai *et al.*, *NIM A* **470** (2001) 562.
- [7] S. Hayakawa, Master’s Thesis, Univ. of Tokyo, 2008.
- [8] P. D. Ingalls *et al.*, *Phys. Rev. C* **13** (1976) 524.
- [9] G. R. Caughlan and W. A. Fowler, *Atomic Data and Nuclear Data Tables* **40** (1988) 283.
- [10] S. Takács *et al.*, *NIM B* **211** (2003) 169.
- [11] T. Rauscher, private communication.
- [12] S. Wanajo, H. T. Janka and S. Kubono, *Astrophys. J.* **729** (2011) 46.

# Experimental study of key astrophysical $^{18}\text{Ne}(\alpha, p)^{21}\text{Na}$ reaction

L.Y. Zhang<sup>1,2,3</sup>, J.J. He<sup>1</sup>, S.W. Xu<sup>1</sup>, H. Yamaguchi<sup>4</sup>, S. Kubono<sup>4</sup>, Y. Wakabayashi<sup>5</sup>,  
S.Z. Chen<sup>1,2</sup>, J. Hu<sup>1</sup>, P. Ma<sup>1</sup>, Y. Togano<sup>6</sup>, T. Hashimoto<sup>4</sup>, D. Kahl<sup>4</sup>, T. Teranishi<sup>7</sup>,  
R.F. Chen<sup>1</sup>, H.W. Wang<sup>8</sup>, W.D. Tian<sup>8</sup>, B. Guo<sup>9</sup>, S. Hayakawa<sup>4</sup>, N. Iwasa<sup>10</sup>, T. Yamada<sup>10</sup>,  
and T. Komatsubara<sup>11</sup>

<sup>1</sup>*Institute of Modern Physics, CAS, Lanzhou, China*

<sup>2</sup>*Graduate University of CAS, Beijing, China*

<sup>3</sup>*Lanzhou University, Lanzhou, China*

<sup>4</sup>*Center for Nuclear Study (CNS), University of Tokyo, Japan*

<sup>5</sup>*Advanced Science Research Center, JAEA, Japan*

<sup>6</sup>*RIKEN, 2-1 Hirosawa, Wako, Saitama 351-0198, Japan*

<sup>7</sup>*Department of Physics, University of Kyushu, Japan*

<sup>8</sup>*Shanghai Institute of Applied Physics, CAS, China*

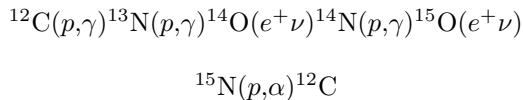
<sup>9</sup>*China Institute of Atomic Energy (CIAE), Beijing, China*

<sup>10</sup>*Department of Physics, University of Tohoku, Japan*

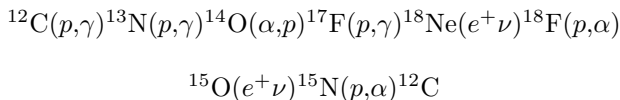
<sup>11</sup>*Department of Physics, University of Tsukuba, Japan*

A nuclear astrophysics experiment was performed at CRIB (CNS low-energy Radioactive-Ion Beam separator) on Mar. 2011. The goal of this experiment was to study the rate of the  $^{18}\text{Ne}(\alpha, p)^{21}\text{Na}$  reaction, which is considered to be a key breakout reaction from the hot CNO cycle to the explosive hydrogen burning, the rp-process [2]. Yet, the reaction rate is not well understood.

Explosive hydrogen burning is thought to be the main source of energy generation and a source of nucleosynthesis in X-ray burst and nova [3, 4]. In X-ray burst, for example, at the typical temperature of 0.4–2 GK, the hydrogen burning occurs in the hot CNO cycle:



where the  $^{13}\text{N}(e^+ \nu)^{13}\text{C}$  reaction in the CNO cycle is bypassed by the  $^{13}\text{N}(p, \gamma)^{14}\text{O}$  reaction. With the progress of compressing and exothermic nuclear reactions, the temperature of the accretion disk increases. When the temperature reaches about 0.4 GK, the second hot CNO cycle becomes dominant:



It is predicted [3, 4] that the  $^{18}\text{Ne}$  waiting point in the second hot CNO cycle can be bypassed by the  $^{18}\text{Ne}(\alpha, p)^{21}\text{Na}$  reaction at  $T \sim 0.6$  GK, and subsequently, the reaction chain breaks out to the rp-process. Hence it is very important to study this reaction rate. An 89 MeV  $^{21}\text{Na}$  radioactive beam produced

by CRIB bombarded a 93  $\mu\text{m}$  thick polyethylene target, and the cross section data for  $^{18}\text{Ne}(\alpha, p)^{21}\text{Na}$  could be obtained indirectly by measuring those for the time-reversal reaction of  $^{21}\text{Na}(p, \alpha)^{18}\text{Ne}$ . The  $^{21}\text{Na}$  beam intensity was about  $2 \times 10^5$  pps, with a purity of about 70% on the target. In this study, we mainly focused on the 8.51 and 8.61 MeV resonance states in the compound  $^{22}\text{Mg}$  nucleus. In a previous experiment [1], we tentatively made new spin-parity assignments for these states. In this experiment, it is aimed to confirm the assignments with much higher statistics. The properties of the resonances (such as  $J^\pi, \Gamma_\alpha$ , and  $\Gamma_p$ ) of the compound  $^{22}\text{Mg}$  nucleus were studied by measuring the  $^{21}\text{Na}+p$  resonant elastic/inelastic scattering cross sections. As shown in Fig. 1, we used two PPACs for determining the timing and the direction of the incident beam particles and three sets of  $\Delta E$ -E silicon telescopes for measuring the energies and scattering angles of the recoiled particles. A NaI array was placed for detecting the  $\gamma$ -rays. Several runs with a carbon target were performed for C background subtraction

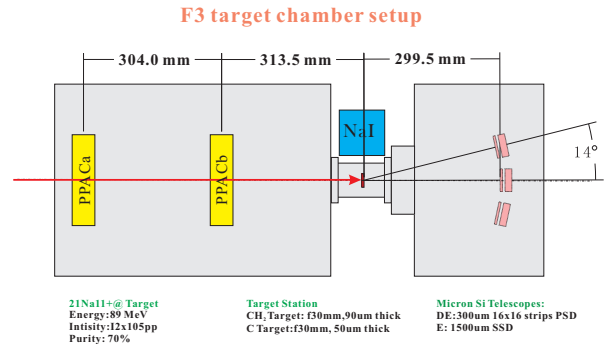


Figure 1. Schematic view of the detector setup.

We could measure successfully the cross section of the time-reversal reaction  $^{21}\text{Na}(p, \alpha)^{18}\text{Ne}$ . Thus, the forward  $^{18}\text{Ne}(\alpha, p)^{21}\text{Na}$  cross section could be calculated by using the detailed balance theorem.

Fig. 2 shows a typical particle identification plot.

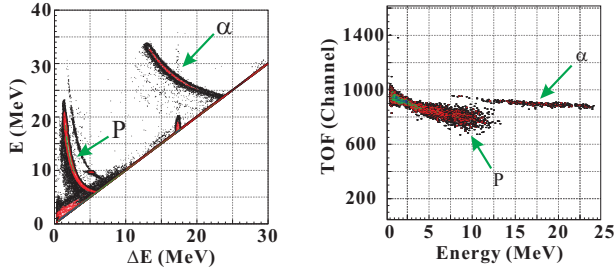


Figure 2. PID of E-E and E-TOF. The start TOF signal is given by PPACa, and the stop signal is given by PSD

$\Delta E$  and E signals are measured by the silicon telescopes; TOF is the time of flight between PPACb and  $\Delta E$ . The E-TOF method mainly identifies the low-energy particles stopped in the  $\Delta E$  detector.

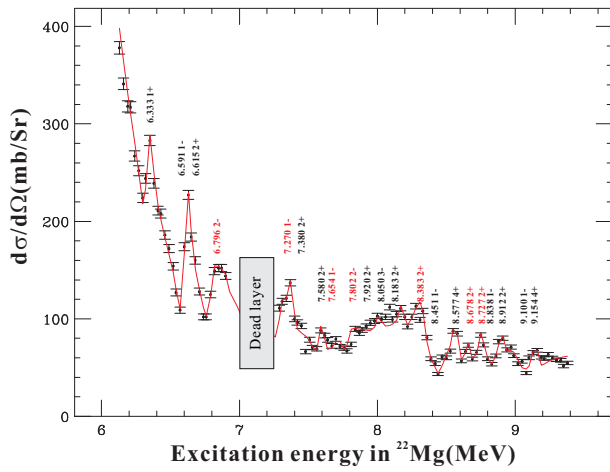


Figure 3. Proton spectrum and R-matrix fitting result

Fig. 3 shows the  $R$ -matrix fitting of the c.m. differential cross section for the resonant elastic scattering of  $^{21}\text{Na}+p$  measured at  $\theta_{c.m.} \approx 175^\circ$ . The red levels in Fig3 refer to the levels which have a new spin-parity assignment based on present analysis. Further data analysis is on-going.

## References

- [1] J. J. He, *et al.*, Phys. Rev. C **80** (2009) 015801.
- [2] W. Bradfield-Smith *et al.*, Phys. Rev. C **59** (1999) 3402
- [3] A. E. Champagne and M. Wiescher, Annu. Rev. Nucl. Part. Sci. **42** (1992) 39.
- [4] M. Wiescher, *et al.*, J. Phys. G: Nucl. Part. Phys. **25** (1999) R133.

# RI Beam Production in the $^{22}\text{Mg} + \alpha$ Experiment at CRIB

N. N. Duy<sup>a,b</sup>, L. H. Khiem<sup>a</sup>, S. Kubono<sup>b</sup>, H. Yamaguchi<sup>b</sup>, D. M. Kahl<sup>b</sup>, T. Hashimoto<sup>b</sup>,  
 S. Ota<sup>b</sup>, Y. Wakabayashi<sup>c</sup>, T. Komatsubara<sup>d</sup>, T. Teranishi<sup>e</sup>, S. Kato<sup>f</sup>, N. Iwasa<sup>g</sup>, T.  
 Yamada<sup>g</sup>,  
 Y. K. Kwon<sup>h</sup>, A. Kim<sup>i</sup>, Y.H. Kim<sup>i</sup>, J.S. Song<sup>i</sup>, J. Hu<sup>j</sup>, and J. Ito<sup>k</sup>.

<sup>a</sup>*Institute of Physics, Vietnam Academy of Science and Technology*

<sup>b</sup>*Center for Nuclear Study, Graduate School of Science, The University of Tokyo.*

<sup>c</sup>*Japan Atomic Energy Agency*

<sup>d</sup>*Department of Physics, Tsukuba University*

<sup>e</sup>*Department of Physics, Kyushu University*

<sup>f</sup>*Department of Physics, Yamagata University*

<sup>g</sup>*Department of Physics, Tohoku University*

<sup>h</sup>*Department of Physics, Chung-Ang University, Korea*

<sup>i</sup>*Department of Physics, Seoul University, Korea*

<sup>j</sup>*Institute of Modern Physics, Chinese Academy of Science*

<sup>k</sup>*Low Energy Experimental Nuclear Physics Gr., Tsukuba University*

## 1. Introduction

The stellar reaction  $^{22}\text{Mg}(\alpha, p)^{25}\text{Al}$  and proton capture  $^{22}\text{Mg}(p, \gamma)^{23}\text{Al}$  play important roles in explosive Hydrogen burning stage under high temperature and high density condition such as X-ray bursts and type II supernovae. The nucleosynthesis involves up to  $^{22}\text{Mg}$  and leading to break-out from HCNO cycles. It is believed that the  $^{22}\text{Mg}$  is a waiting point in  $\alpha p$ -process [1]. At high temperatures, the  $^{22}\text{Mg}(\alpha, p)^{25}\text{Al}$  reaction is expected to be the dominant but there is no experimental data up to date. In nuclear structure, resonance states of  $^{26}\text{Si}$  above the alpha threshold 9.17 MeV is still limited comparing to the mirror nucleus  $^{26}\text{Mg}$  [2]. Therefore, we have a plan to measure directly the  $^{22}\text{Mg} + \alpha$  system in invert-kinematics using the  $^{22}\text{Mg}$  beam so that we can investigate the stellar reaction  $^{22}\text{Mg}(\alpha, p)^{25}\text{Al}$  and proton-rich nucleus  $^{26}\text{Si}$  above the alpha threshold. For its feasibility, we performed a measurement of the production rates of a low energy  $^{22}\text{Mg}$  beam by using CRIB (Center for Nuclear Study (CNS) low-energy RI Beam separator of the University of Tokyo) [3].

## 2. Experiment

The  $^{22}\text{Mg}$  of 3.73 MeV/u beam was produced by using CRIB spectrometer located at RIKEN in October, 2011. The radioactive ions are produced via  $^3\text{He}(^{20}\text{Ne}, ^{22}\text{Mg})n$  reaction by bombarding a Havar-windowed cryogenic gas target [4] of  $^3\text{He}$  at 90 K with the primary beam  $^{20}\text{Ne}$  of 6.2 MeV/u from AVF cyclotron [5]. We optimized the intensity together with purity of  $^{22}\text{Mg}$  beam based on pressure of production target and intensity of the primary beam of  $^{20}\text{Ne}$ . We tested different thicknesses of production target and adjusted slightly the primary beam intensity to find out the maximum yield of  $^{22}\text{Mg}$  at the interested energy. The RI beam including contaminants is more preferentially populated at achromatic focal plane F2 using dipole magnets and identified by beam monitors PPACs [6]. The contaminants are further separated in velocity by using the Wien Filter before com-

$^{20}\text{Ne}^{10+}$ beam	Purity of $^{22}\text{Mg}^{12+}$	Intensity of $^{22}\text{Mg}^{12+}$
0.450 eμA	29 %	$0.74 \times 10^3$ pps
0.700 eμA	30 %	$1.20 \times 10^3$ pps
1.000 eμA	21 %	$0.86 \times 10^3$ pps
1.300 eμA	17 %	$0.44 \times 10^3$ pps
1.800 eμA	11 %	$0.22 \times 10^3$ pps

Table 1. Purity and intensity of  $^{22}\text{Mg}^{12+}$  produced at F3 focal plane.

ing through active-target, and therefore, a high purity of  $^{22}\text{Mg}$  can be obtained on the experimental plane F3. Particle identification of different species from production reaction is carried out by radiofrequency time of flight (ToF) and energy of particles measured by PPACs at F2 and F3.

## 3. Results and discussion

The intensity of  $^{22}\text{Mg}^{12+}$  at 3.73 MeV/u reaches to maximum value with the production target  $^3\text{He}$  at 170 torr of pressure and 700 enA of primary beam current. In such condition, the  $^{22}\text{Mg}^{12+}$  beam is 30% of purity and  $1.2 \times 10^3$  pps of intensity on the active target at F3. As can be seen in Table 1, the intensity of the  $^{22}\text{Mg}^{12+}$  is not always proportional to the intensity of the  $^{20}\text{Ne}$  beam. The phenomena is considered to be caused by heating effect on the beam axis.

Although the  $^{22}\text{Mg}^{12+}$  has poor purity of 5% at F2, it is easily distinguished from the contaminants by ToF of RF signal and energy measured at F2. The beams after the Wien Filter, almost all the contaminants are separated, and the remains are only the leaky beams of  $^{20}\text{Ne}^{10+}$  and  $^{21}\text{Na}^{11+}$ , as shown in Fig. 1. By using the Wien Filter, the purity of the beam is improved at F3 with 30%. The transmission of Wien Filter investigated is 40% with a high voltage supply of  $\pm 65$  kV. It is expected that the yield of the interest beam will be increased if the Wien Filter works with higher voltage.

In general, the  $^{22}\text{Mg}$  beam of 3.73 MeV/u is produced successfully for direct measurement of the  $^{22}\text{Mg}$

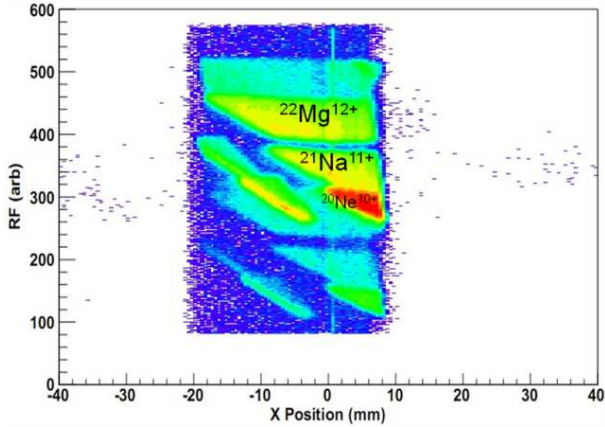


Figure 1. The histogram indicates X-position of the particles on the PPACa at F3 plane. Here, the main contaminants are only primary beam  $^{20}\text{Ne}^{10+}$  and  $^{21}\text{Na}^{11+}$ . We can distinguish the interested beam by RF signal and energy at F3.

+  $\alpha$  system at CRIB. In order to get the experimental data with higher statistical accuracy, it is necessary to continue developing the beam production. The heating power in the gas along the beam axis affecting on the yield of the beam should be treated. It is necessary to investigate this problem for beam production using  $^3\text{He}$  gas. In addition, the thickness of production target and energy of primary beam should be optimized in appreciation case. And improvement of purity of the beam and transmission of the Wien Filter gives an opportunity for a high yield of RI beam production in future.

## References

- [1] J. L. Fisker, F. K. Thieleman and M. Wiescher, the *Astrophys. J.*, **608** (2004) L61L64.
- [2] P. M. Endt et al., *Nuclear Physics A* **521** (1990), 166-197.
- [3] S. Kubono et al., *Nucl. Instr. and Meth. A* **539** (2005) 7483.
- [4] H. Yamaguchi et al, *Nucl. Instr. and Meth. A* **589** (2008) 150.
- [5] A. S. Vorozhtsov et al., *CNS Report* 82 (2009).
- [6] H. Kumagai, A. Ozawa, et al. *Nucl. Instru. Meth. A* **470** (2001) 562-570.

# Role of the $^{22}\text{Mg}(\alpha, p)^{25}\text{Al}$ Reaction and Its First Direct Measurement

N. N. Duy<sup>a,b</sup>, L. H. Khiem<sup>a</sup>, S. Kubono<sup>b</sup>, H. Yamaguchi<sup>b</sup>, D. M. Kahl<sup>b</sup>, T. Hashimoto<sup>b</sup>,  
S. Ota<sup>b</sup>, Y. Wakabayashi<sup>c</sup>, T. Komatsubara<sup>d</sup>, T. Teranishi<sup>e</sup>, S. Kato<sup>f</sup>, N. Iwasa<sup>g</sup>, T.  
Yamada<sup>g</sup>,  
Y. K. Kwon<sup>h</sup>, A. Kim<sup>i</sup>, Y.H. Kim<sup>i</sup>, J.S. Song<sup>i</sup>, J. Hu<sup>j</sup>, and J. Ito<sup>k</sup>.

<sup>a</sup>*Institute of Physics, Vietnam Academy of Science and Technology*

<sup>b</sup>*Center for Nuclear Study, Graduate School of Science, The University of Tokyo.*

<sup>c</sup>*Japan Atomic Energy Agency*

<sup>d</sup>*Department of Physics, Tsukuba University*

<sup>e</sup>*Department of Physics, Kyushu University*

<sup>f</sup>*Department of Physics, Yamagata University*

<sup>g</sup>*Department of Physics, Tohoku University*

<sup>h</sup>*Department of Physics, Chung-Ang University, Korea*

<sup>i</sup>*Department of Physics, Seoul University, Korea*

<sup>j</sup>*Institute of Modern Physics, Chinese Academy of Science*

<sup>k</sup>*Low Energy Experimental Nuclear Physics Gr., Tsukuba University*

The  $rp$ -process following a path away from stable isotopes through beta-unstable nuclei is competed by  $\alpha p$ -process under high temperature and high density in X-ray bursts [1]. Under such burning conditions, the nucleosynthesis including a series of  $(\alpha, p)$  reactions up to  $Z \sim 20$  involves mainly through the chain of  $^{14}\text{O}(\alpha, p)^{17}\text{F}(p, \gamma)^{18}\text{Ne}(\alpha, p)^{21}\text{Na}(p, \gamma)^{22}\text{Mg}(\alpha, p)^{25}\text{Al}(p, \gamma)^{26}\text{Si}(\alpha, p)^{29}\text{P}(p, \gamma)^{30}\text{S}(\alpha, p)^{33}\text{Cl}(p, \gamma)^{34}\text{Ar}(\alpha, p)^{37}\text{K}(p, \gamma)^{38}\text{Ca}$ . The stellar reaction  $^{22}\text{Mg}(\alpha, p)^{25}\text{Al}$  is one of significant links in the sequence. It would affect considerably the observation of 1.275 MeV gamma-ray, abundance of  $^{22}\text{Na}$  as well as the isotopic anomalies of ratio  $^{20}\text{Ne}/^{22}\text{Ne}$  in meteorites called Ne-E problem [2, 3]. The reaction also plays an important role in explanation for suspicion of the waiting point  $^{22}\text{Mg}$  in the  $rp$ -process. Indeed, the evolution of nucleosynthesis can pass through three ways, proton capture  $^{22}\text{Mg}(p, \gamma)^{23}\text{Al}$ ,  $\beta^+$  decay  $^{22}\text{Mg}(\beta^+)^{22}\text{Na}$  and the  $^{22}\text{Mg}(\alpha, p)^{25}\text{Al}$  reaction. And the  $(\alpha, p)$  reaction is thought to dominate even if it has been underestimated by a factor 100 [4]. Because of the small Q-value (0.125 MeV) for  $^{22}\text{Mg}(p, \gamma)^{23}\text{Al}$ , the photodisintegration of  $^{23}\text{Al}$  prevents a significant flow through the  $^{23}\text{Al}(p, \gamma)^{24}\text{Si}$  reaction.

The  $^{22}\text{Mg}(\alpha, p)^{25}\text{Al}$  reaction is related also to the nuclear structure of  $^{26}\text{Si}$  just above the alpha-threshold ( $E = 9.17$  MeV). Though only limited numbers of level are known for  $^{26}\text{Si}$ , a lot more levels should exist above the threshold, since many levels are identified in the mirror nucleus  $^{26}\text{Mg}$ . A special interest is possible  $\alpha$ -structure in some of the levels expected by the threshold rule for finding  $\alpha$ -cluster states. The non-statistical contribution from resonances with large  $\alpha$ -widths would enhance the cross section as compared to the statistical model calculation by, for example, the NON-SMOKER code [5] based on the Hauser-Feshbach model.

There was an effort of extracting the reaction rate [6] but its accuracy is still limited due to lack of precise experimental data, which have not been measured yet. In order to obtain experimental data of the stellar re-

Target	Purity	$^{22}\text{Mg}$ at F3
0.726 mg/cm <sup>2</sup>	30 %	$1.2 \times 10^3$ cps

Table 1.  $^{22}\text{Mg}^{12+}$  of 3.73 MeV/u was produced with the primary beam of 700 enA.

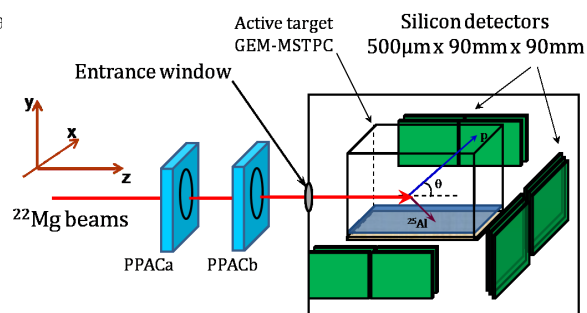


Figure 1. Experimental setup of the  $^{22}\text{Mg}(\alpha, p)^{25}\text{Al}$  experiment.

action  $^{22}\text{Mg}(\alpha, p)^{25}\text{Al}$ , we performed a direct measurement in inverse kinematics in the center-of-mass energy range from 1 to 4.2 MeV, corresponding to Gamow windows at temperatures from 1 to 3 Giga Kelvin of astrophysical interest.

We carried out the experiment by means of thick-target method using the active-target detector MSTPC [7] with a radioactive beam of  $^{22}\text{Mg}$  produced by CRIB (CNS Radioactive Ion Beam separator) [8] at the Center for Nuclear Study (CNS), the University of Tokyo in October 2011. The  $^{22}\text{Mg}$  beam was produced via the  $^3\text{He}(^{20}\text{Ne}, ^{22}\text{Mg})n$  reaction. Primary beams of  $^{20}\text{Ne}$  of 6.2 MeV/u energy extracted from CNS HyperECR ion source and accelerated by the AVF cyclotron bombarded a cryogenic gas target [9] of  $^3\text{He}$  cooled to 90K with 2.5 袖 m Harvar-windows. See Table 1 for details.

The target and detection system were set at the experimental plane F3 of CRIB as shown in Fig. 1. The target was gas mixture of  $^4\text{He}+\text{CO}_2$  (10%) at 140 torr

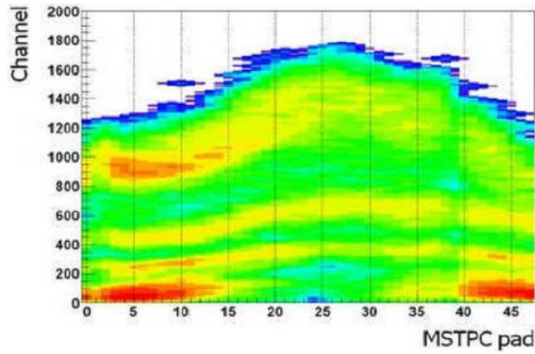


Figure 2. Energy loss spectra of  $^{22}\text{Mg}$ ,  $^{21}\text{Na}$  and  $^{20}\text{Ne}$  in the gas target were measured by the MSTPC. A Bragg curve can be deduced from the spectra to obtain the interested events.

at the room temperature filled in a chamber in which electrode structures of MSTPC and arrays of telescopes of silicon detectors were installed.

The trajectory and timing information of incoming  $^{22}\text{Mg}$  were measured by the beam monitors for particle identification. The monitors also provided event-trigger signals. In the experiment, the events due to the elastic scattering  $^{22}\text{Mg}(\alpha, \alpha)^{22}\text{Mg}$  or the  $^{22}\text{Mg}(\alpha, p)^{25}\text{Al}$  reaction were discriminated from the ones due to production of beam contaminants, based on the Bragg curves of the outgoing  $^{22}\text{Mg}$  and  $^{25}\text{Al}$ , which is determined from energy loss measured by MSTPC as shown in Fig. 2. On the other hand, protons and alphas were detected by the silicon detectors installed around MSTPC.

The elastic scattering and the interest reaction data were measured during 7 days. The data analysis is in process. Extraction of the experimental cross section and R-matrix analysis [10] to obtain the reaction rate will be made in future.

## References

- [1] H. Schatz, K.E.Rehm, Nuclear Physics A **777** (2006) 601622.
- [2] M. Arnould and H. Norgaard, Astron. Astrophys. **64** (1978) 195-213.
- [3] W. Hillebrandt and F. K. Thielemann, the Astrophysical. Journal **255** (1982) 617-623.
- [4] J.L. Fisker et al., The Astrophys. J, **L63** (2004).
- [5] [http://nucastro.orgreaclib.html#ns\\_web](http://nucastro.orgreaclib.html#ns_web).
- [6] A. Matic et al., Phys. Rev. C **84** (2011) 025801.
- [7] T. Hashimoto et al., CNS Annual Rep., (2008) 17.
- [8] S. Kubono et al., Eur. Phys. J, A **13** (2002) 217.
- [9] H.Yamaguchi et al: Nucl.Instrum.Meth. A **589** (2008) 150.
- [10] A. M. Lane et al., Rev. Mod. Phys. **30** (1958) 257.



Fig. 2 shows a typical particle identification of the  $^{22}\text{Na}$  secondary beam at F3 focal plane.

The experimental setup at F3 chamber is shown in Fig. 3. Before the 300 mm gas target, two PPACs were used to record the position and timing of the secondary beam particles. After penetrating through the PPACs and the front window of the gas target ( $2.5\ \mu\text{m}$  Havar), the energy of  $^{22}\text{Na}$  entering the hydrogen gas is 37.1 MeV, which is given by a calibrated SSD (Single Silicon Detector) before experimental measurement. To identify the reaction products, we used three sets of detector telescope, which are composed by thin PSDs (Position Sensitive Detector) and SSDs. During the  $^{22}\text{Na}+p$  measurement runs, the hydrogen gas pressure in the 300 mm target was maintained within  $310\pm 2$  Torr by a flow-gas system, which can fully stop the  $^{22}\text{Na}$  particles.

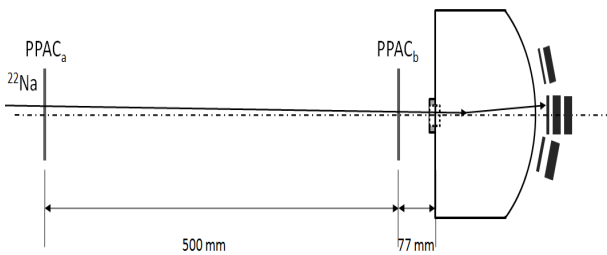


Figure 3. Experimental setup at F3 chamber.

A typical particle identification of the lighter reaction products is shown in Fig. 4. A large amount of data were accumulated for  $^{22}\text{Na}+p$ , and  $^{22}\text{Na}+\alpha$  as well, data analysis is in progress to obtain the experimental excitation function and extract the resonance parameters.

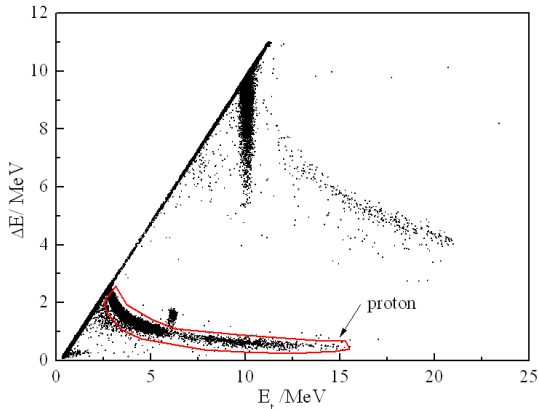


Figure 4. A calibrated scatter plot for the energy loss in PSD ( $\Delta E$ ) and total energy ( $E_t$ ) measured with the detector telescope.

This work was performed at the RI Beam Factory operated by RIKEN Nishina Center and CNS, University of Tokyo. The authors are grateful to the CNS and RIKEN accelerator staff for the smooth operation of the machine. This work is supported by the National Natural Science Foundation of China under Grant Nos 11175261 and 11021504.

## References

- [1] J. José, A. Coc, M. Hernanz, *Astrophys. J.* **520** (1999) 347.
- [2] W. R. Hix *et al.*, *Nucl. Phys. A* **718** (2003) 620c.
- [3] A. L. Sallaska *et al.*, *Phys. Rev. Lett.* **105** (2010) 152501.
- [4] Y. Yanagisawa, S. Kubono *et al.*, *Nucl. Instr. Meth. A* **539** (2005) 74.

# Study of resonant states in $^{26}\text{Si}$ and $^{27}\text{P}$ with radioactive ion beams

H.S. Jung, C.S. Lee, Y.K. Kwon<sup>a</sup>, J.Y. Moon, J.H. Lee<sup>a</sup>, C.C. Yun<sup>a</sup>, S. Kubono<sup>c</sup>,  
H. Yamaguchi<sup>b</sup>, T. Hashimoto<sup>j</sup>, D. Kahl<sup>b</sup>, S. Hayakawa<sup>k</sup> Seonho Choi<sup>d</sup>, M.J. Kim<sup>d</sup>,  
Y.H. Kim<sup>d</sup>, Y.K. Kim<sup>a</sup>, J.S. Park<sup>e</sup>, E.J. Kim<sup>f</sup>, C.-B. Moon<sup>g</sup>, T. Teranishi<sup>h</sup>,  
Y. Wakabayashi<sup>c</sup>, N. Iwasa<sup>i</sup>, T. Yamada<sup>i</sup>, Y. Togano<sup>c</sup>, S. Kato<sup>j</sup>, S. Cherubini<sup>l</sup> and  
G.G. Rapisarda<sup>l</sup>

*Department of Physics, Chung-Ang university*

<sup>a</sup>*Institute for Basic Science*

<sup>b</sup>*Center for Nuclear Study, University of Tokyo*

<sup>c</sup>*RIKEN (The Institute of Physical and Chemical Research)*

<sup>d</sup>*Department of Physics and Astronomy, Seoul National University*

<sup>e</sup>*Department of Nuclear Engineering, Hanyang University*

<sup>f</sup>*Division of Science Education, Chonbuk National University*

<sup>g</sup>*Faculty of Sciences, Hoseo University*

<sup>h</sup>*Department of Physics, Kyushu University*

<sup>i</sup>*Department of Physics, Tohoku University*

<sup>j</sup>*Department of Physics, Yamagata University*

<sup>k</sup>*RCNP, Osaka University*

<sup>l</sup>*Laboratori Nazionali del Sud-INFN*

The rapid proton capture process (rp process) is a dominant reaction sequence in explosive hydrogen burning, which synthesizes heavier elements, especially proton-rich unstable nuclides. In explosive stellar environments, processing occurs mostly via the rp process, a sequence of  $(p, \gamma)$  reactions,  $(\alpha, p)$  reactions and  $\beta$  decays. Therefore, accurate reaction rates for nuclear reactions on the rp process are essential for an understanding of the nucleosynthesis processes and energy production.

We studied proton resonant states in  $^{26}\text{Si}$  and  $^{27}\text{P}$  via elastic scattering to investigate the  $^{25}\text{Al}(p, \gamma)^{26}\text{Si}$  and  $^{26}\text{Si}(p, \gamma)^{27}\text{P}$  reactions, which are important ones in the rp-process path for the understanding of the nucleosynthesis in explosive hydrogen burning [1, 2, 3]. These reactions are also relevant to the production of  $^{26}\text{Al}$ . The  $^{25}\text{Al}(p, \gamma)^{26}\text{Si}$  reaction becomes significantly faster than  $\beta$  decay of  $^{25}\text{Al}$  [4] at the higher temperatures. Moreover, the  $^{26}\text{Si}(p, \gamma)^{27}\text{P}$  reaction competes with  $\beta$  decay of  $^{26}\text{Si}$  to  $^{26m}\text{Al}$ , which can produce  $^{26gs}\text{Al}$  via thermal excitation, therefore the destruction of  $^{26}\text{Si}$  by proton capture is important and the rate of this reaction should be determined accurately.

The states in  $^{26}\text{Si}$  have been studied with different reactions of the  $(p, t)$ ,  $(^3\text{He}, ^6\text{He})$ ,  $(^3\text{He}, n)$ ,  $(^4\text{He}, ^6\text{He})$ , and proton elastic scattering. Although many states have been discovered, their parameters relevant for the higher temperatures are not determined yet. Moreover, a comparison with its mirror nucleus  $^{26}\text{Mg}$  reveals that missing states still remain. The structure of  $^{27}\text{P}$  has been studied with measurements of the  $(^3\text{He}, ^8\text{Li})$ ,  $(^7\text{Li}, ^8\text{He})$ , and Coulomb dissociation. However, the knowledge of the structure of this nucleus is still insufficient because of uncertain resonance parameters, such as resonance energies and spin-parity assignments.

The measurement of the  $^{25}\text{Al}+p$  and  $^{26}\text{Si}+p$  elastic scattering were performed at the low-energy RI beam facility CRIB (CNS Radioactive Ion Beam separator)

Table 1. Beam specification

Beam	$^{25}\text{Al}$	$^{26}\text{Si}$
Energy (MeV)	$71.58 \pm 0.54$	$79.01 \pm 0.60$
Intensity (pps)	$3.3 \times 10^4$	$1.2 \times 10^4$
Purity (%)	62	23

of the Center for Nuclear Study (CNS), the University of Tokyo [5, 6], by bombarding a  $^{26}\text{Si}$  radioactive ion beam onto a  $\text{H}_2$  gas target in inverse kinematics [7] and detecting scattered protons using silicon detectors for a  $\Delta E$ -E telescope. We applied the thick-target method [8, 9] to scan the entire energy region of interest simultaneously. The excitation function was obtained from the scattered proton energy spectrum by a kinematics conversion process. The experimental setup is shown in Fig. 1. A  $^{24}\text{Mg}$  primary beam with an energy of 7.5 MeV/A and an intensity of 1.6  $\mu\text{A}$  extracted from the AVF cyclotron bombarded a  $^3\text{He}$  gas target which was at 550 Torr and 90 K. Then secondary beams of  $^{25}\text{Al}$  and  $^{26}\text{Si}$  were produced by the  $^3\text{He}(^{24}\text{Mg}, ^{25}\text{Al})d$  and  $^3\text{He}(^{24}\text{Mg}, ^{26}\text{Si})n$  reactions, respectively and were separated by CRIB using the in-flight method. Beam properties in front of the secondary target are summarized in Table 1. Protons elastically scattered to forward angles in the laboratory frame were detected by a  $\Delta E$ -E telescope, which consisted of a 75- $\mu\text{m}$ -thick double-sided 16-channel-by-16-channel strip Position-sensitive Silicon Detector (PSD) and two 1.5-mm single channel Silicon Strip Detectors (SSDs), both with an area of  $5 \times 5 \text{ cm}^2$ .

By calculating the kinematics, including energy loss in the target, the measured proton energy of each event was converted to a center-of-mass energy. Then the experimental differential cross sections of the proton scattering events were calculated from the number of selected proton events and incident beam ions, the target thickness, and the different solid angles depending on

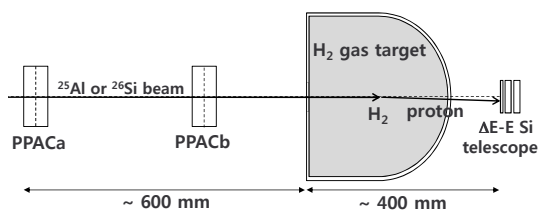


Figure 1. Experimental setup of the measurement of the  $^{25}\text{Al}+p$  and  $^{26}\text{Si}+p$  elastic scattering in inverse kinematics at the final focal plane.

the interaction position in the thick target. The excitation functions of  $^{25}\text{Al}+p$  and  $^{26}\text{Si}+p$  elastic scattering cross sections obtained in this work are shown in Fig. 2 and 3, respectively. Structures with several peaks were clearly observed. We performed an analysis using the R-matrix calculation code (SAMMY-8.0.0) [10, 11] to deduce resonance parameters such as excitation energy  $E_x$ , spin  $J$ , parity  $\pi$ , and proton partial width  $\Gamma_p$  of resonance states. Figure 2 and 3 show best-fit results for the excitation function.

For resonant states in  $^{26}\text{Si}$  spin-parity assignment for the fourth resonance at 2.14 MeV and fifth resonance around 2.46 MeV could not be determined because fitting results of both  $J^\pi = 2^+$  and  $3^+$  were consistent with experimental data. These results are different from previous ones [12], which also performed proton resonant elastic scattering with solid  $\text{CH}_2$  target at CRIB facility. Our gas target is free from background contributions over the scanned energy region of interest owing to the pure hydrogen gas in comparison with a solid polyethylene ( $\text{CH}_2$ ) target, which can contribute to the background by carbon atoms.

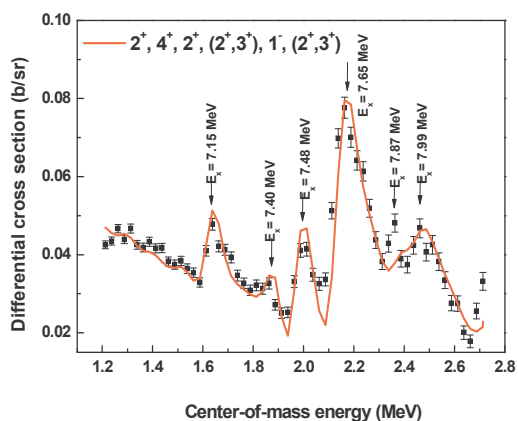


Figure 2. Final results for the excitation function of  $^{25}\text{Al}+p$  as the best fits for  $J^\pi = 2^+, 4^+, 2^+, (2^+, 3^+), 1^-$ , and  $(2^+, 3^+)$  are shown but without firm spin-parity assignment for the fourth at 2.14 MeV and fifth at 2.46 MeV prominent resonant peaks.

Six new resonant states in  $^{27}\text{P}$  have been suggested, and we mostly determined their resonance parameters such as resonance energy, width, and spin-parity with the R-matrix calculation. These parameters of resonant states in  $^{27}\text{P}$  are expected to contribute to the nu-

clear data as input for nuclear reaction network calculation of the rp-process nucleosynthesis. Moreover, previous estimate of the total reaction rate of  $^{26}\text{Si}(p,\gamma)^{27}\text{P}$ , which was evaluated by Iliadis *et al.* [13], should be re-analyzed with the nuclear physics input newly obtained in present work.

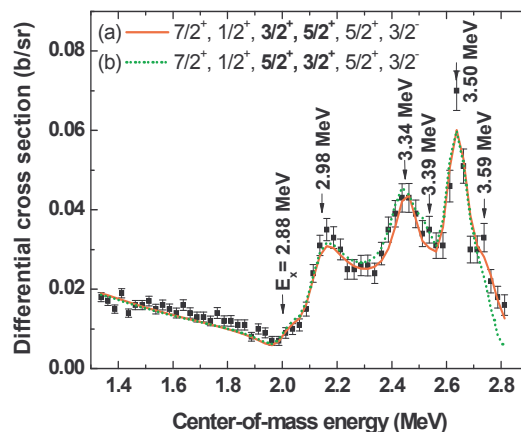


Figure 3. Final results for the excitation function of  $^{26}\text{Si}+p$  as the best fits for  $J^\pi = 7/2^+, 1/2^+, (3/2^+, 5/2^+), 5/2^+$ , and  $3/2^-$  are shown but without firm spin-parity assignment for the doublet around 2.5 MeV.

## References

- [1] H. Herndl, J. Görres, M. Wiescher, B.A. Brown, and L. VanWormer, *Phys. Rev. C* **52**, 1078 (1995).
- [2] J. L. Fisker, H. Schatz, and F.-K. Thielemann, *Astrophys. J.* bf 174, 261 (2008).
- [3] A. Parikh *et al.*, *Astrophys. J. Suppl. Ser.* bf 178, 110 (2008).
- [4] A. Matic *et al.*, *Phys. Rev. C* **82**, 025807 (2010).
- [5] S. Kubono *et al.*, *Eur. Phys. J. A* bf 13, 217 (2002).
- [6] Y. Yanagisawa *et al.*, *Nuc. Instrum. Methods Phys. Res. Sect. A* **539**, 74 (2005).
- [7] K.P. Artemov *et al.*, *Nuc. Phys.* **52**, 408 (1990).
- [8] W. Galster *et al.*, *Phys. Rev. C* **44**, 2776 (1991).
- [9] S. Kubono, *Nuc. Phys. A* **693**, 221 (2001).
- [10] A.M. Lane and R.G. Thomas, *Rev. Mod. Phys.* **30**, 257 (1958).
- [11] N.M. Larson, A code system for multilevel R-Matrix fits to neutron data using Bayes' equations, ORNL/TM-9179/R5 (2000, unpublished).
- [12] J. Chen *et al.*, *Phys. Rev. C* **85**, 015805 (2012).
- [13] C. Iliadis *et al.*, *Nuc. Phys. A* **841**, 31 (2010).

# Heavy-ion double charge exchange reaction on ${}^9\text{Be}$

H. Matsubara<sup>a</sup>, M. Takaki<sup>a,b</sup>, T. Uesaka<sup>a</sup>, S. Shimoura<sup>b</sup>, N. Aoi<sup>c</sup>, M. Dozono<sup>a</sup>, T. Fujii<sup>b</sup>, K. Hatanaka<sup>c</sup>, T. Hashimoto<sup>c</sup>, T. Kawabata<sup>d</sup>, S. Kawase<sup>b</sup>, K. Kisamori<sup>a,b</sup>, Y. Kikuchi<sup>b</sup>, Y. Kubota<sup>b</sup>, C.S. Lee<sup>a</sup>, H.C. Lee<sup>b</sup>, Y. Maeda<sup>e</sup>, S. Michimasa<sup>b</sup>, K. Miki<sup>a,c</sup>, H. Miya<sup>b</sup>, S. Noji<sup>b</sup>, S. Ota<sup>b</sup>, S. Sakaguchi<sup>f</sup>, Y. Sasamoto<sup>b</sup>, T. Suzuki<sup>c</sup>, L.T. Tang<sup>b</sup>, K. Takahisa<sup>c</sup>, H. Tokieda<sup>b</sup>, A. Tamii<sup>c</sup>, K. Yako<sup>b</sup>, Y. Yasuda<sup>c</sup>, N. Yokota<sup>d</sup>, R. Yokoyama<sup>b</sup>, and J. Zenihiro<sup>a</sup>

<sup>a</sup>*RIKEN (The Institute of Physical and Chemical Research)*

<sup>b</sup>*Center for Nuclear Study, Graduate School of Science, University of Tokyo*

<sup>c</sup>*Research Center for Nuclear Physics (RCNP), Osaka University*

<sup>d</sup>*Department of Physics, Kyoto University*

<sup>e</sup>*Department of Applied Physics, Miyazaki University*

<sup>f</sup>*Department of Physics, Kyusyu University*

## 1. Introduction

The  ${}^9\text{He}$  nucleus has a large  $A/Z$  ratio of 4.5. Although it is unbound, the first excited state of  ${}^9\text{He}$  is reported to have a remarkably narrow width at a level of 100 keV [1]. Because the  ${}^{10}\text{He}$  ground state is also unbound, neutron pickup reactions, such as  $(p, d)$  and  $(d, t)$  reactions, can not be applied to investigate the level structure of  ${}^9\text{He}$ . Thus, small number of works have been devoted to study the energy levels, widths and spin-parities in  ${}^9\text{He}$ . Most of the spin-parities and widths, however, are still uncertain or scarcely known, as summarized in Table 1.

We have developed a new powerful probe to study neutron rich nuclei, which is heavy-ion double charge exchange (HIDCX) ( ${}^{18}\text{O}$ ,  ${}^{18}\text{Ne}$ ) reaction by making use of the high resolution spectrometer Grand Raiden (GR) at the Research Center for Nuclear Physics (RCNP), Osaka University. This probe has noticeable advantages, *i.e.* (a) unstable nuclei can be investigated even by using stable nuclei for the target and for the beam, (b) missing mass measurement enables us to observe an excitation function both below and above the particle threshold, (c) out-going particles of  ${}^{18}\text{Ne}$  can be clearly identified through the spectrometer because the  ${}^9\text{B}$  nucleus is unbound and thus the  $A/Q=9/5$  is unique for  ${}^{18}\text{Ne}$ , and (d) the HIDCX transition rate between  ${}^{18}\text{O}_{\text{g.s.}}$  and  ${}^{18}\text{Ne}_{\text{g.s.}}$  is expected to be relatively large because of the overlapping of their wavefunctions in  $r$ -space, which arises from the fact that they are in the super-multiplet members. It should be noted that the advantage (d) is essential for the HIDCX measurement since a double charge exchange transition is considered to be a two-step reaction and its rate is usually small. Therefore, the ( ${}^{18}\text{O}$ ,  ${}^{18}\text{Ne}$ ) reaction that has a large transition rate would provide us some information to investigate the unbound nucleus  ${}^9\text{He}$  from the stable nucleus  ${}^9\text{Be}$ .

## 2. Experimental setup

The experiment was performed at the WS course of the RCNP. A primary beam of  ${}^{18}\text{O}$  was accelerated up to 1432 MeV (79.6 MeV/nucleon), which is the maximum at the RCNP, by the coupled cyclotrons. A typical beam intensity was 20 pA. A beam energy spread was 1 MeV (FWHM) including a width owing to detector system at the focal plane of the GR spectrom-

Table 1. Energy levels, spin-parities, and widths in  ${}^9\text{He}$ .

$E_x$ (MeV)	$J^\pi$	$\Gamma$ (MeV)
0.0	$1/2^+$	
1.10	$1/2^-$	0.1
2.26		0.7
4.2		
5.0		
8.0		

eter. The  ${}^{18}\text{O}$  beam bombarded a self-supporting foil target of  ${}^9\text{Be}$  with an areal density of 5.0(1) mg/cm<sup>2</sup>, where the isotopic abundance of  ${}^9\text{Be}$  is naturally 100%. The scattered particles were momentum-analyzed by the GR spectrometer. Then, they were detected by the focal plane detector system, which consists of two vertical drift chambers (VDC's) and two plastic scintillation counters. Thicknesses of the two scintillators were 1 and 3 mm from the upstream. Coincident signals from the scintillation counters were used to trigger the data acquisition (DAQ) system. The detail of the experiment can be found in Ref. [2].

## 3. Result and discussion

The particle identification to select  ${}^{18}\text{Ne}$  was realized by using the information of Time-of-Flight between RF from the accelerator and the triggering signals and by making use of its unique  $A/Q$  value. Detailed descriptions for the analysis may be found in Ref. [3]. An excitation energy spectrum of the  ${}^9\text{Be}({}^{18}\text{O}, {}^{18}\text{Ne}){}^9\text{He}$  reaction at 0-0.6° is compared with that of  ${}^{12}\text{Be}({}^{18}\text{O}, {}^{18}\text{Ne}){}^{12}\text{Be}$  reaction as shown in Fig. 1. Although the same beam, the same detector system, and the same analysis procedure were applied for both  ${}^9\text{Be}$  and  ${}^{12}\text{C}$ , only continuous increment caused by quasi-free scattering are seen in the spectrum of  ${}^9\text{He}$ . There are no prominent structures. Figure 2 shows coupled-channel calculations by the code ECIS [4] with assuming two-phonon states to reproduce the HIDCX transition. The microscopic form factors were obtained [5] by folding the projectile and the target transition densities with the USD [6] and SFO [7] effective interactions, respectively. The simplest transition path assumed for the

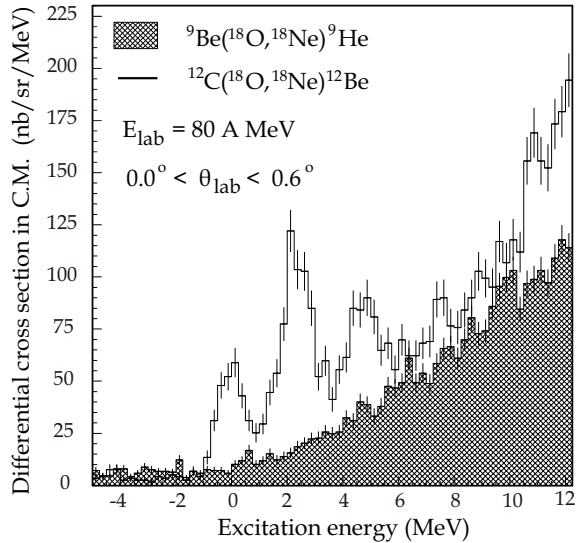


Figure 1. Excitation energy spectra for the  ${}^9\text{Be}({}^{18}\text{O}, {}^{18}\text{Ne}){}^9\text{He}$  and the  ${}^{12}\text{C}({}^{18}\text{O}, {}^{18}\text{Ne}){}^{12}\text{Be}$  reactions at  $\theta_{\text{lab}} = 0\text{-}0.6^\circ$ .

calculation is double Gamow-Teller transitions from the  ${}^9\text{Be}(3/2^-_{g.s.})$  to the  ${}^9\text{He}(1/2^-_{g.s.})$  via the  ${}^9\text{Li}(3/2^-_{g.s.})$ . The calculation indicates that the differential cross section is less than 1 nb/sr owing to a tiny B(GT) value from the  ${}^9\text{Be}(3/2^-_{g.s.})$  to the  ${}^9\text{Li}(3/2^-_{g.s.})$ . Because 10 nb/sr was the lower detection limit in the previous experimental condition, the cross section of the  ${}^9\text{Be}({}^{18}\text{O}, {}^{18}\text{Ne})$  reaction producing  ${}^9\text{He}$  was too small to be observed. Spatial deformation of  ${}^9\text{Be}$  [8] is supposed to cause small overlapping of wavefunctions between  ${}^9\text{Be}$  and  ${}^9\text{Li}$ , resulting in a small cross section of the  ${}^9\text{Be}({}^{18}\text{O}, {}^{18}\text{Ne}){}^9\text{He}$  reaction.

As a next step for the establishment of the HIDCX ( ${}^{18}\text{O}, {}^{18}\text{Ne}$ ) reaction as a spectroscopic tool, we are planning to measure  ${}^{13}\text{C}({}^{18}\text{O}, {}^{18}\text{Ne}){}^{13}\text{Be}$  reaction since the  ${}^{13}\text{Be}$  nucleus is unbound. A calculation predicts the differential cross section of 20-40 nb/sr at  $0^\circ$  for the transition reaction to  ${}^{13}\text{Be}_{g.s.}$ . Because the cross section predicted is one thirds of  ${}^{12}\text{C}({}^{18}\text{O}, {}^{18}\text{Ne}){}^{12}\text{Be}_{g.s.}$ , the HIDCX ( ${}^{18}\text{O}, {}^{18}\text{Ne}$ ) reaction on  ${}^{13}\text{C}$  would be the first successful application for spectroscopy of unbound nucleus.

## References

- [1] H.G. Bohlen *et al.*, Prog. Part. Nucl. Phys. **42** (1999) 17-26.
- [2] H. Matsubara *et al.*, CNS Annual Report (2010).
- [3] M. Takaki *et al.*, CNS Annual Report (2010).
- [4] J. Raynal, program code ECIS-97.
- [5] J. Cook and J.A. Carr, computer program FOLD, Florida State University (unpublished); based on F. Petrovich and D. Stanley, Nucl. Phys. A275, (1977) 487; modified as described in J. Cook, K.W. Kemper, P.V. Drumm, L.K. Fifield, M.A.C. Hotchkis, T.R. Ophel, and C.L. Woods, Phys. Rev. C 30, (1984) 1538; R.G.T. Zegers *et al.*, Phys. Rev. C **74**, (2006) 024309.
- [6] B.H. Wildenthal, Prog. Part. Nucl. Phys **11**, (1984) 5.

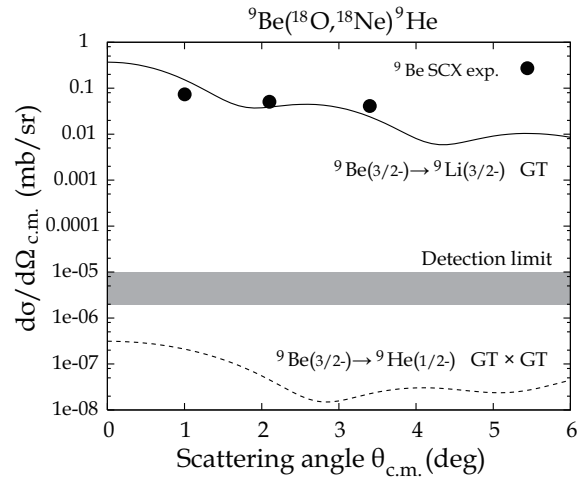


Figure 2. Angular distributions for the  ${}^9\text{Be}({}^{18}\text{O}, {}^{18}\text{Ne}){}^9\text{He}$  reaction without normalization factor. The cross section of the DCX transition is predicted as less than 1 nb/sr which is much smaller than the detection limit.

- [7] T. Suzuki, R. Fujimoto, T. Otsuka., Phys. Rev. C **67**, (2003) 044302.
- [8] C. Scholl *et al.*, Phys. Rev. C **84** (2011) 014308.

# Study of low-lying states of $^{12}\text{Be}$ via the heavy-ion double-charge exchange $^{12}\text{C}(^{18}\text{O}, ^{18}\text{Ne})$ reaction

M. Takaki, H. Matsubara<sup>a</sup>, T. Uesaka<sup>a</sup>, S. Shimoura, N. Aoi<sup>b</sup>, M. Dozono<sup>a</sup>, T. Fujii, T. Hashimoto<sup>b</sup>, K. Hatanaka<sup>b</sup>, T. Kawabata<sup>c</sup>, S. Kawase, K. Kisamori, C.S. Lee, H.C. Lee<sup>a</sup>, Y. Maeda<sup>d</sup>, S. Michimasa, K. Miki<sup>b</sup>, H. Miya, S. Noji<sup>e</sup>, S. Ota, S. Sakaguchi<sup>f</sup>, M. Sasano<sup>a</sup>, T. Suzuki<sup>b</sup>, K. Takahisa<sup>b</sup>, T.L. Tang, A. Tamii<sup>b</sup>, H. Tokieda, K. Yako, N. Yokota<sup>c</sup>, R. Yokoyama and J. Zenihiro<sup>b</sup>

*Center for Nuclear Study, Graduate School of Science, University of Tokyo*

<sup>a</sup>*RIKEN (The Institute of Physical and Chemical Research)*

<sup>b</sup>*Research Center for Nuclear Physics, Osaka University*

<sup>c</sup>*Department of Physics, Kyoto University*

<sup>d</sup>*Department of Applied Physics, Miyazaki University*

<sup>e</sup>*National Superconducting Cyclotron Laboratory, Michigan State University*

<sup>f</sup>*Department of Physics, Kyushu University*

Neutron-rich nuclei have attracted much attention due to their exotic phenomena such as halo-structures, disappearance of conventional magic numbers and low-lying intruder states.

The neutron-rich nucleus  $^{12}\text{Be}$  provides the crucial evidence for the disappearance of the neutron magic number  $N = 8$  [1,2]. Configurations of the ground ( $0_1^+$ ) and  $0_2^+$  states in  $^{12}\text{Be}$  are of much current interest. Earlier experimental and theoretical studies highlighted that the normal  $(0s)^4(0p)^8$  “ $0\hbar\omega$ ” configuration mainly contributes to the  $0_2^+$  state, while the  $(0s)^4(0p)^6(0sd)^2$  “ $2\hbar\omega$ ” configuration mainly contributes to the  $0_1^+$  state. However, the levels of the mixing of the  $0\hbar\omega$  and  $2\hbar\omega$  configurations to the  $0^+$  states remain as a subject of intense debate [3, 4, 5, 6, 7].

We have developed a spectroscopic tool, which is the  $\beta^+$ -type heavy-ion double-charge exchange (HIDCX) ( $^{18}\text{O}, ^{18}\text{Ne}$ ) reaction at an intermediate energy with a missing mass method. The spectroscopic tool can be an efficient probe to investigate light neutron-rich nuclei because those near or over the neutron drip line can be studied even by using stable nuclei as a target and observing its excitation energy spectrum below and above the particle threshold on the same footing. Another obvious advantage of the ( $^{18}\text{O}, ^{18}\text{Ne}$ ) reaction is that the transition probability between the ground states  $^{18}\text{O}$  and  $^{18}\text{Ne}$  is expected to be large because the ground states of  $^{18}\text{O}$  and  $^{18}\text{Ne}$  are members of the same super-multiplet. In addition, the  $^{18}\text{Ne}$  having a unique  $A/Q$  value of 1.8 which makes particle identification of  $^{18}\text{Ne}$  easier in this experiment since  $^9\text{B}$  is unbound.

The HIDCX  $^{12}\text{C}(^{18}\text{O}, ^{18}\text{Ne})^{12}\text{Be}$  reaction experiment was performed to study the low-lying states of  $^{12}\text{Be}$  by using the high resolution Grand Raiden (GR) spectrometer at the WS course of Research Center for Nuclear Study (RCNP), Osaka University. The GR spectrometer was set at 0 degree. The  $^{18}\text{O}$  beam with an energy of 79.6 MeV bombarded a natural carbon target with an areal density of 2.2(1) mg/cm<sup>2</sup>. The typical  $^{18}\text{O}$  beam intensity was 25 pA. Scattering particles were momentum-analyzed by the GR spectrometer, and then detected by the focal plane detectors

which are two vertical drift chambers (VDCs) and two plastic scintillators. Particle identification was done with the energy loss in the plastic scintillators and the  $A/Q$  value derived from the time-of-flight and the  $B\rho$  information. The detail of the particle identification is found in Ref. [8]. We obtained the excitation energy spectrum of  $^{12}\text{Be}$  with the total energy resolution of 1.1 MeV mainly limited by the incident beam energy spread of  $\sim 1$  MeV. We also obtained angular distributions of the cross section for the low-lying states of  $^{12}\text{Be}$  within the GR spectrometer acceptance of  $0.0^\circ$ – $2.5^\circ$ .

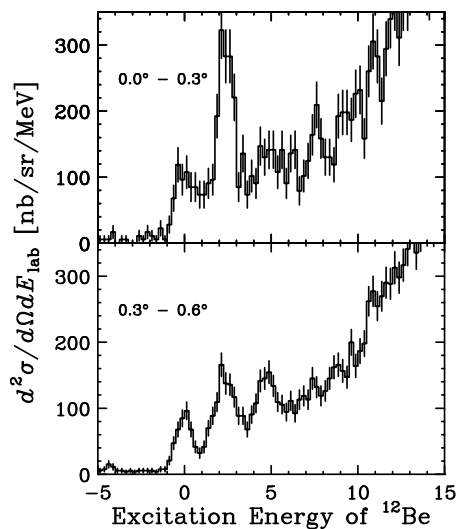


Figure 1. Excitation energy spectrum of  $^{12}\text{Be}$  within the scattering angle range of  $0.0^\circ$ – $0.3^\circ$  (upper panel) and  $0.3^\circ$ – $0.6^\circ$  (lower panel).

Figure 1 shows the excitation energy spectrum of  $^{12}\text{Be}$ . One can find three clear peaks with the excitation energy of 0.0, 2.2 and 4.5 MeV, respectively.  $^{12}\text{Be}$  has the three states that can contribute to the 2.2 MeV peak:  $2_1^+$  (2.11 MeV),  $0_2^+$  (2.24 MeV) and  $1_1^-$  (2.68 MeV). The peak with the excitation energy of 7.5 MeV that appears at the scattering angle range of  $0.0^\circ$ – $0.3^\circ$  (upper panel of Fig. 1) might be the  $0_3^+$

state which has not been observed so far [3,5]. Figure 2 shows angular distributions of differential cross sections for the  $^{12}\text{C}(^{18}\text{O}, ^{18}\text{Ne})^{12}\text{Be}$  reaction. The ground state has a forward peaking shape. The  $0_2^+$  state is the main component of the 2.2 MeV peak because its angular distribution is also forward peaking, as well as the angular distribution for the ground state. In contrast, the 4.5 MeV state has a flat shape. The 4.56 MeV state has been suggested its spin-parity is  $2^+$  [9]. Therefore the angular distribution of the 4.5 MeV peak might be a  $\Delta L = 2$  distribution. The present result indicates that the HIDCX reaction at an intermediate energy has the sensitivity to multiplicities.

- [6] S.D. Pain *et al.*, Phys. Rev. Lett **96** (2006) 032502.
- [7] R. Meharchant *et al.*, Phys. Rev. Lett **108** (2012) 122501.
- [8] M. Takaki *et al.*, CNS annual report (2010).
- [9] H. Fortune *et al.*, Phys. Rev. C **50** (1994) 1355.

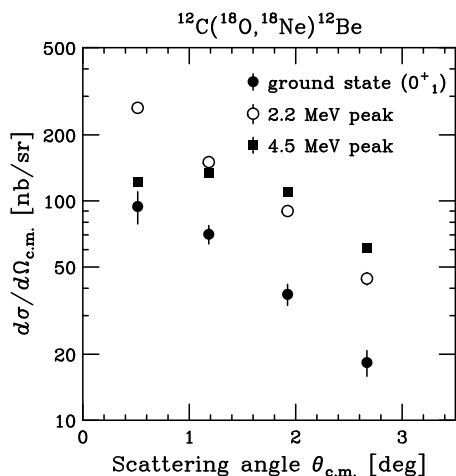


Figure 2. Angular distributions of differential cross sections for the observed three peaks: the ground state (closed circle), the 2.2 MeV peak (open circle) and the 4.5 MeV peak (closed square).

In summary, we succeeded in the observation of three isolated peaks, corresponding to the ground and low-lying excited states of  $^{12}\text{Be}$ , by employing the HIDCX  $^{12}\text{C}(^{18}\text{O}, ^{18}\text{Ne})^{12}\text{Be}$  reaction. It is noted that this experiment is the first case which clearly observed the clear peaks and obtained its angular distribution with the HIDCX reaction at an intermediate energy. Now, we develop a reaction calculation method for the HIDCX. After we establish the calculation method, we will perform a multipole decomposition analysis to extract the  $0\hbar\omega$  components of  $0_1^+$  and  $0_2^+$  states. Then, we can deduce the levels of the  $0\hbar\omega$  contribution for the  $0^+$  states.

## References

- [1] A. Navin *et al.*, Phys. Rev. Lett. **85** (2000) 266.
- [2] H. Iwasaki *et al.*, Physics Letters B **481** (2000) 7; *ibid* **491** (2000) 8.
- [3] F.C. Barker, J. Phys. G **2**, L45 (1976).
- [4] S. Shimoura *et al.*, Physics Letters B **560** (2003) 31; *ibid* **654**, (2007) 87.
- [5] H. Fortune and R. Sherr, Phys. Rev. C **74** (2006) 024301.

# The parity-transfer reaction ( $^{16}\text{O}$ , $^{16}\text{F}$ ) for studies of pionic $0^-$ mode

M. Dozono<sup>a</sup>, T. Uesaka<sup>a</sup>, M. Sasano<sup>a</sup>, H. Matsubara<sup>a</sup>, S. Shimoura<sup>b</sup>, K. Yako<sup>b</sup>,  
 S. Michimasa<sup>b</sup>, S. Ota<sup>b</sup>, Y. Sasamoto<sup>b</sup>, S. Noji<sup>b</sup>, H. Tokieda<sup>b</sup>, S. Kawase<sup>b</sup>, R. Tang<sup>b</sup>,  
 Y. Kikuchi<sup>b</sup>, K. Kisamori<sup>b</sup>, M. Takaki<sup>b</sup>, Y. Kubota<sup>b</sup>, C. S. Lee<sup>b</sup>, T. Fujii<sup>b</sup>, R. Yokoyama<sup>b</sup>,  
 H. Sakai<sup>a</sup>, T. Kubo<sup>a</sup>, K. Yoshida<sup>a</sup>, Y. Yanagisawa<sup>a</sup>, N. Fukuda<sup>a</sup>, H. Takeda<sup>a</sup>, D. Kameda<sup>a</sup>,  
 N. Inabe<sup>a</sup>, T. Wakasa<sup>c</sup>, K. Fujita<sup>c</sup>, S. Sakaguchi<sup>c</sup>, H. Sagawa<sup>d</sup>, M. Yamagami<sup>d</sup>, and  
 M. Ichimura<sup>a</sup>,

<sup>a</sup>RIKEN (The Institute of Physical and Chemical Research)

<sup>b</sup>Center for Nuclear Study, Graduate School of Science, University of Tokyo

<sup>c</sup>Department of Physics, Kyushu University

<sup>d</sup>Center for Mathematics and Physics, University of Aizu

The pion is the most important particle for understanding nuclear forces. The pseudo-scalar nature of the pion leads to a strong tensor correlation, which plays a characteristic role in nuclear structure. The investigation of tensor correlation in nuclei is thus indispensable in understanding the fundamental nature of a nuclear many-body system.

The spin-isospin excitations provide a unique opportunity to study the tensor correlation effects in nuclei. The spin-dipole (SD)  $0^-$  excitations are of particular interest as they carry the same quantum number as a pion. Recently, the effects of tensor correlations on the  $0^-$  excitations have been investigated by using self-consistent HF+RPA calculations [1, 2]. According to the calculations, it was found that the tensor correlations produce a strong hardening (shifting toward a higher excitation energy) effect on the collective  $0^-$  resonance, and the effect is very sensitive to the magnitude of the tensor strength. Therefore, from the study of  $0^-$  states, we are able to identify the tensor correlation effects. However, in spite of this importance, experimental information on  $0^-$  states is very limited. The lack of experimental tools suited for  $0^-$  studies is responsible for this situation.

In this report, we propose a new probe, a parity-transfer reaction for the  $0^-$  study. The parity-transfer reaction is a direct nuclear reaction where the probe particle changes from the initial  $0^+$  state to the final  $0^-$  state ( $0^+ \rightarrow 0^-$ ). This reaction has advantages over other reactions used so far. Table 1 shows the  $J^\pi$  states that are excited by using the parity-transfer reaction and traditional reactions such as  $(p, n)[1/2^+ \rightarrow 1/2^+]$  and  $(d, ^2\text{He})[1^+ \rightarrow 0^+]$ . With all the traditional reaction probes, it is very difficult to separate  $0^-$  states from the  $1^-$  and  $2^-$  states as these SD states are excited with the same  $\Delta L = 1$ . On the other hand, the new probe, the parity-transfer reaction, excites only one  $J^\pi$  component with each  $\Delta L$ . Thus, the  $J^\pi$  components can be assigned uniquely from the angular distribution. In addition, due to its unique feature as an exclusive probe of unnatural-parity states, the contribution from the natural-parity  $1^-$  excitation is negligible. Thus, the parity-transfer reaction can be a powerful tool for reliable determination of the  $0^-$  strength distribution.

This technique is based on the transition from the  $0^+$  g.s. of  $^{16}\text{O}$  to the  $0^-$  g.s. of  $^{16}\text{F}$  (See Fig. 1). All

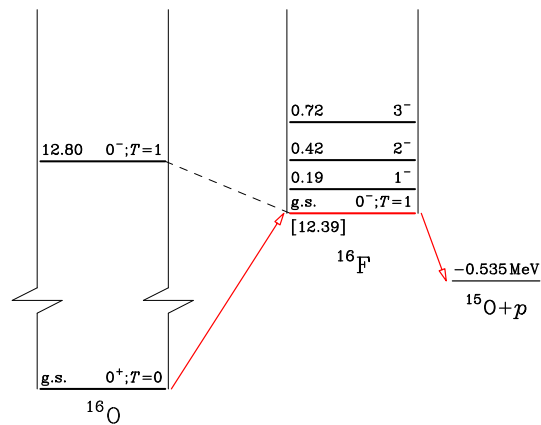


Figure 1. Energy level diagram for  $^{16}\text{F}$

the states in  $^{16}\text{F}$  are unbound to  $^{15}\text{O} + p$ . We perform the coincidence measurements of the decayed  $^{15}\text{O} + p$  pairs, and the  $0^-$  g.s. of  $^{16}\text{F}$  is identified by using the invariant-mass method. In this method, the transitions to the other spin-dipole states,  $1^-$  state at  $E_x = 0.19$  MeV and  $2^-$  state at  $E_x = 0.42$  MeV, can also be observed simultaneously. Using these transitions, we can also study the  $1^-$  and  $2^-$  strength distributions in nuclei. For example, the ( $^{16}\text{O}, ^{16}\text{F}^*(1^-, 0.19 \text{ MeV})$ ) reaction selectively excites  $1^-$  states with  $\Delta L = 0$ , enabling us to observe the  $1^-$  strength distribution at  $0^\circ$ .

The RIBF accelerators at RIKEN in combination with the SHARAQ spectrometer [3] provide the opportunity for studies of the parity-transfer ( $^{16}\text{O}, ^{16}\text{F}$ ) reaction at an energy of 200–300 MeV/A. In this energy region, the single-step process is dominant [4], and thus, we can extract the nuclear structure information reliably. In order to confirm the validity of the method of the parity-transfer reaction, we plan to perform a  $^{12}\text{C}(^{16}\text{O}, ^{16}\text{F})^{12}\text{B}$  experiment at 250 MeV/A. The  $^{12}\text{C}$  target has been often investigated by using charge-exchange reactions [5, 6, 7], and there is the known  $0^-$  state at  $E_x = 9.3$  MeV in  $^{12}\text{B}$ . Therefore, this state serves as a benchmark to verify the effectiveness of the parity-transfer reaction. Figure 2 shows a schematic layout of the experimental setup. A primary  $^{16}\text{O}$  beam

Table 1. The spin-parity states excited via the parity-transfer reaction and traditional reactions.

	$\Delta L = 0$	$\Delta L = 1$	$\Delta L = 2$	$\dots$
Parity-trans. ( $0^+ \rightarrow 0^-$ )	$0^-$	$1^+$	$2^-$	$\dots$
( $p, n$ ), ( $d, {}^2\text{He}$ ) etc.	$0^+, 1^+$	$0^-, 1^-, 2^-$	$1^+, 2^+, 3^+$	$\dots$

of 250 MeV/A is transported onto a  ${}^{12}\text{C}$  target. The outgoing  ${}^{16}\text{F} \rightarrow p + {}^{15}\text{O}$  are momentum analyzed in the SHARQA spectrometer. The analyzed  ${}^{15}\text{O}$  are detected with the focal plane detector of SHARQA, while the protons are detected with the detector at the low-momentum side of the first dipole magnet. Once this new method is established, it will open new opportunities for the study of the  $0^-$  strengths in nuclei and for exclusive excitation feeding to the unnatural-parity states in general.

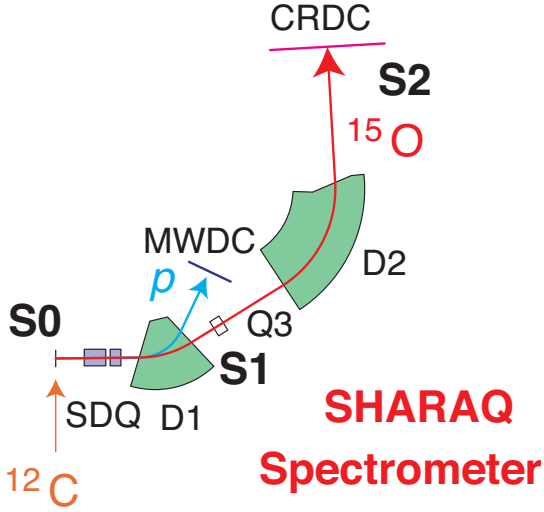


Figure 2. Experimental setup of the  ${}^{12}\text{C}({}^{16}\text{O}, {}^{16}\text{F}){}^{12}\text{B}$  experiment.

## References

- [1] C. L. Bai, H. Q. Zhang, H. Sagawa, X. Z. Zhang, G. Colo and F. R. Xu, Phys. Rev. Lett. **105**, 072501 (2010).
- [2] C. L. Bai, H. Q. Zhang, H. Sagawa, X. Z. Zhang, G. Colo and F. R. Xu, Phys. Rev. C **83**, 054316 (2011).
- [3] T. Uesaka *et al.*, Nucl. Instrum. Meth. B **266**, 4218 (2008).
- [4] M. Ichimura, H. Sakai, and T. Wakasa, Prog. Part. Nucl. Phys. **56**, 446 (2006).
- [5] H. Okamura *et al.*, Phys. Rev. C **66**, 054602 (2002).
- [6] M. A. de Huu *et al.*, Phys. Lett. **B649**, 25 (2007).
- [7] M. Dozono *et al.*, J. Phys. Soc. Jpn. **77**, 014201 (2008).

# Identification of isovector non-spin-flip excitation by the super-allowed Fermi type charge reaction

Y. Sasamoto, T. Uesaka, S. Shimoura, S. Michimasa, S. Ota, K. Miki<sup>a,b</sup>, S. Noji<sup>b</sup>, K. Yako<sup>b</sup>, H. Tokieda, H. Miya, S. Kawase, Y. Kikuchi, K. Kisamori, M. Takaki, M. Dozono, H. Mathubara, H. Sakai<sup>a</sup>, T. Kubo<sup>a</sup>, Y. Yanagisawa<sup>a</sup>, H. Takeda<sup>a</sup>, K. Yoshida<sup>a</sup>, T. Ohnishi<sup>a</sup>, N. Fukuda<sup>a</sup>, D. Kameda<sup>a</sup>, N. Inabe<sup>a</sup>, N. Aoi<sup>a</sup>, S. Takeuchi<sup>a</sup>, T. Ichihara<sup>a</sup>, H. Baba<sup>a</sup>, S. Sakaguchi<sup>a</sup>, P. Doornenbal<sup>a</sup>, H. Wang<sup>a</sup>, R. Chen<sup>a</sup>, Y. Shimizu<sup>a</sup>, T. Kawahara<sup>c</sup>, T. Kawabata<sup>d</sup>, N. Yokota<sup>d</sup>, Y. Maeda<sup>e</sup>, H. Miyasako<sup>e</sup>, G. P. A. Berg<sup>f</sup>

*Center for Nuclear Study, Graduate School of Science, University of Tokyo*

<sup>a</sup>*RIKEN Nishina center*

<sup>b</sup>*Department of Physics, University of Tokyo*

<sup>c</sup>*Department of Physics, Toho University*

<sup>d</sup>*Department of Physics, Kyoto University*

<sup>e</sup>*Department of Physics, Miyazaki University*

<sup>f</sup>*Department of Physics and Joint Institute for Nuclear Astrophysics, University of Notre Dame*

## 1. Introduction

Isvector non-spin-flip monopole resonance (IVMR) is of particular interest, because it is an oscillation mode of isovector density  $\rho_{IV} = \rho_n - \rho_p$  and its energy and width should be closely related to properties of asymmetric nuclear matter [1] and to isospin mixture in nuclei [2].

In spite of its importance, however, experimental data on IVMR are scarce so far. Pion charge exchange reactions ( $\pi^\pm, \pi^0$ ) [3] and heavy-ion charge exchange (HICE) such as, ( $^{13}\text{C}, ^{13}\text{N}$ ) [4,5] and ( $^7\text{Li}, ^7\text{Be}$ ) [6], have been used to study IVMR. These reactions provided inconsistent results of excitation energy, width, and/or multipolarity of the state [4].

To understand nature of IVMR, a HICE probe selective to the non-spin-flip ( $\Delta T = 1, \Delta S = 0$ ) modes is essentially important. We propose the the super-allowed Fermi type charge exchange ( $^{10}\text{C}, ^{10}\text{B}(\text{IAS})$ ) reaction. This selectivity is achieved only with the RI beam induced reaction [7]. Our idea to probe the isovector non-spin-flip states is based on the use of a super-allowed Fermi transition between isobaric analog states in the projectile. The analog state of the  $^{10}\text{C}$  ground state locates at  $E_x=1.74$  MeV in  $^{10}\text{B}$  as shown in Fig. 1. The transition from the  $^{10}\text{C}$  ground state to the 1.74-MeV state in  $^{10}\text{B}$  can be experimentally identified by observing the emitted  $\gamma$  ray of 1022 keV. Thus, coincident detection of  $^{10}\text{B}$  and 1022-keV  $\gamma$  rays in the final state will be a clear signature of  $0^+ \rightarrow 0^+$  transition in the projectile, and consequently, of the non-spin-flip excitation in the target.

We have applied the ( $^{10}\text{C}, ^{10}\text{B}(\text{IAS})$ ) reaction at  $^{10}\text{C}$  beam energy of 200 MeV/nucleon to  $^7\text{Li}$ . In this report, we report the experimental result to identify the isovector non-spin-flip excitation by the ( $^{10}\text{C}, ^{10}\text{B}(\text{IAS})$ ) reaction.

## 2. Experiment and result

The experiment was performed at the RIBF facility in RIKEN using the SHARAQ spectrometer [8]. The secondary  $^{10}\text{C}$  beam was produced as fragments of 250 MeV/u  $^{14}\text{N}$  using a  $^9\text{Be}$  target with a thickness of 20 mm. A purity of approximately 95% was achieved

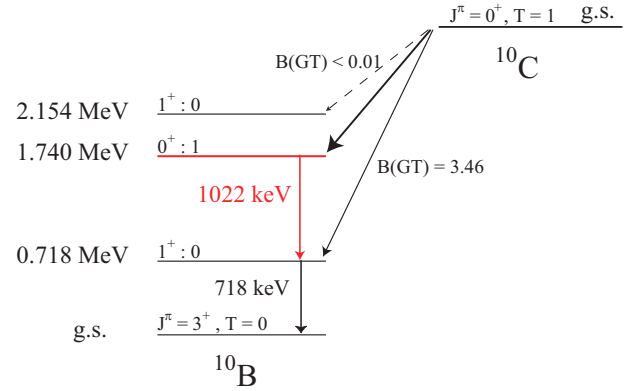


Figure 1. Levels in  $^{10}\text{B}$ . The analog state of the  $^{10}\text{C}$  ground state is found at  $E_x=1.74$  MeV in  $^{10}\text{B}$ .

for  $^{10}\text{C}$  by using an Al wedge-type energy degrader with thickness of 810 mg/cm<sup>2</sup>. The intensity of the  $^{10}\text{C}$  beam was approximately  $2 \times 10^6$  pps at the secondary target. The beam trajectories were measured by the multiwire drift chambers [9] upstream of the secondary target to determine the position and incident angle of the beam. High-resolution beamline was set to the dispersion-matched mode so as to cancel the effect of energy spread of the beam itself [10]. A secondary  $^{90}\text{Zr}$  target with a thickness of 150 mg/cm<sup>2</sup> was used. The emitted 1022-keV  $\gamma$ -rays to define the non-spin-flip transition were detected by the NaI detector array (DALI2 [11]) located near the secondary target. Scattered  $^{10}\text{B}$  particles were momentum analyzed by the SHARAQ spectrometer.

We successfully obtained the  $\gamma$ -ray spectra characteristic of the spin-flip/non-spin-flip transitions in the  $^7\text{Li}$  target with a reasonably small background as shown in Fig. 2. For the heavier target, the  $\gamma$ -ray spectra suffered from background contributions. The background contributions are caused by the secondary bremsstrahlung and the emission of  $\gamma$  rays from the target nuclei.

The results from the  $^7\text{Li}(^{10}\text{C}, ^{10}\text{B}\gamma)$  reaction allowed

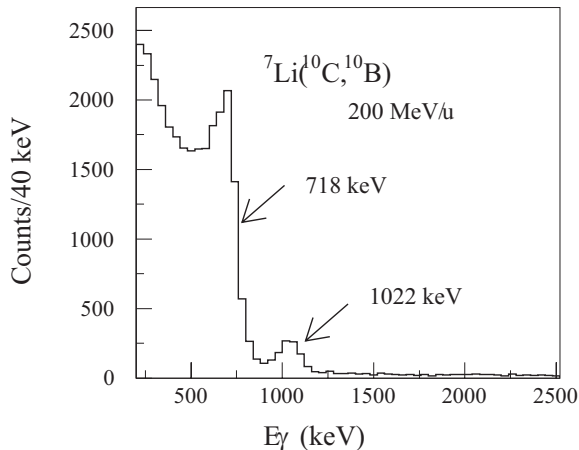


Figure 2. Doppler-corrected  $\gamma$ -ray spectrum of  ${}^7\text{Li}({}^{10}\text{C}, {}^{10}\text{B})$  obtained by DALI2.

us to evaluate the effectiveness of this reaction. We confirmed that the isovector non-spin-flip transition is extracted by using the 1022-keV  $\gamma$  ray based on the results as follows. It is found that the feedings from highly excited GT states are negligibly small because prominent  $\gamma$ -ray peaks, expected when the highly GT states are populated, were not observed in the obtained  $\gamma$ -ray spectrum. We concluded that the feedings for the non-spin-flip transition are less than 10% on the assumption that there is the feeding from the three excited states at  $E_x=2154$ , 3587 and 5164 keV in  ${}^{10}\text{B}$ , and the contribution from 2868- and 3009-keV  $\gamma$  rays and background distribution in the  $\gamma$ -ray spectrum.

We confirmed a non-spin-flip selectivity as can be seen in coincident  $\gamma$ -ray spectra. Left panel of Fig. 3 shows a two-dimensional plot of coincident  $\gamma$  rays. The horizontal and vertical axes show the highest  $\gamma$ -ray energy with Doppler-shift correction and the other energies of coincident  $\gamma$  rays without Doppler-shift correction for each secondary-beam event. To confirm the  $\gamma$ -ray coincidences, we produced spectra by gating on Doppler-corrected  $\gamma$ -ray energies. Right panel of Fig. 3 show spectra with  $\gamma$ -ray energy gating in the range of 590–750 keV (spin-flip) with dashed line and 950–1250 keV (non-spin-flip) with solid line, respectively. The coincident events are observed between 718-keV  $\gamma$  rays with Doppler-shift corrections and 430-keV  $\gamma$  rays without Doppler-shift corrections as shown with the dashed line. On the contrary, 1022-keV  $\gamma$  rays with Doppler-shift corrections are not coincident with 430-keV  $\gamma$  rays without Doppler-shift corrections as seen in the solid line. This indicates that a non-spin-flip transition is identified by using  $\gamma$ -ray energies because 430-keV  $\gamma$  rays without Doppler-shift corrections are emitted through the spin-flip transition of the target.

### 3. Summary

Our idea to excite isovector non-spin-flip states selectively is based on a super-allowed Fermi transition between isobaric analog states in the projectile. We have applied this reaction to the  ${}^7\text{Li}$  target and successfully observed the 1022-keV  $\gamma$  rays emitted from  ${}^{10}\text{B}(\text{IAS})$  which is a signature of the non-spin-flip transition. We concluded that the the feedings for the non-spin-flip

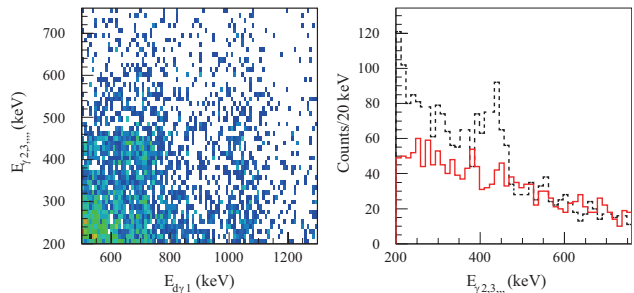


Figure 3. Coincident  $\gamma$ -ray spectra. Left panel shows the two-dimensional plot where the horizontal and vertical axes show the highest  $\gamma$ -ray energy with Doppler-shift corrections and the other energies of coincident  $\gamma$  rays without Doppler-shift corrections for each secondary beam event. Right panel show spectra with  $\gamma$ -ray energy gating in the range of 590–750 keV (spin-flip) with dashed line and 950–1250 keV (non-spin-flip) with solid line, respectively.

transition are less than 10% using the obtained  $\gamma$ -ray spectrum. We also confirmed a non-spin-flip selectivity using the obtained coincident  $\gamma$ -ray spectra with 430-keV  $\gamma$  rays without Doppler-shift corrections which are emitted through the spin-flip transition of the target.

### References

- [1] G. Colo and N. Van Giai, Phys. Rev. C **53**, 2201 (1996).
- [2] A. Bohr and B. Mottelson, "Nuclear Structure".
- [3] A. Erell et al., Phys. Rev. C **34**, 1822 (1986).
- [4] I. Lhenry, Nucl. Phys. A **599**, 245c (1996).
- [5] T. Ichihara et al., Phys. Rev. Lett. **89**, 142501 (2002).
- [6] S. Nakayama et al., Phys. Rev. Lett. **83**, 690 (1999).
- [7] Y. Sasamoto et. al., CNS Ann. Rep. 2009, 27 (2010).
- [8] T. Uesaka et al.: Nucl. Instrum. Meth. in Phys. Res. B **266**, 4218 (2008).
- [9] H. Miya et al.: In this report.
- [10] T. Kawabata et al.: Nucl. Instrum. and Meth. in Phys. Res. B **266**, 4201 (2008).
- [11] S. Takeuchi et. al.: RIKEN Accel. Prog. Rep. **36**, 148 (2003).

# A new spectroscopic tool by the radioactive-isotope-beam induced exothermic charge-exchange reaction

S. Noji<sup>1</sup>, H. Sakai<sup>a</sup>, N. Aoi<sup>b</sup>, H. Baba<sup>a</sup>, G. P. A. Berg<sup>c</sup>, P. Doornenbal<sup>a</sup>, M. Dozono<sup>a</sup>,  
N. Fukuda<sup>a</sup>, N. Inabe<sup>a</sup>, D. Kameda<sup>a</sup>, T. Kawabata<sup>d</sup>, S. Kawase, Y. Kikuchi, K. Kisamori,  
T. Kubo<sup>a</sup>, Y. Maeda<sup>e</sup>, H. Matsubara, S. Michimasa, K. Miki<sup>b</sup>, H. Miya, H. Miyasako<sup>e</sup>,  
S. Sakaguchi<sup>f</sup>, Y. Sasamoto, S. Shimoura, M. Takaki, H. Takeda<sup>a</sup>, S. Takeuchi<sup>a</sup>, H. Tokieda,  
T. Ohnishi<sup>a</sup>, S. Ota, T. Uesaka<sup>a</sup>, H. Wang<sup>a</sup>, K. Yako<sup>g</sup>, Y. Yanagisawa<sup>a</sup>, N. Yokota<sup>d</sup>,  
K. Yoshida<sup>a</sup>

*Center for Nuclear Study, Graduate School of Science, University of Tokyo*

<sup>a</sup>*RIKEN (The Institute of Physical and Chemical Research)*

<sup>b</sup>*Research Center for Nuclear Physics, Osaka University,*

<sup>c</sup>*Department of Physics, University of Notre Dame, and Joint Institute for Nuclear Physics*

<sup>d</sup>*Department of Physics, Kyoto University*

<sup>e</sup>*Department of Applied Physics, University of Miyazaki*

<sup>f</sup>*Department of Physics, Kyushu University*

<sup>g</sup>*Department of Physics, University of Tokyo*

Nuclear reactions using accelerated beams have been successfully employed in the study of nuclear structure through the response of the nucleus. The spin-isospin responses in particular have been extensively studied by charge-exchange reactions [1] induced by nucleon beams, light-ion beams, and heavy-ion beams at intermediate energies. Since radioactive-isotope beams have become available recently, measurements of nuclear reactions induced by radioactive-isotope beams are now possible [2]. Such reactions introduce kinematical conditions and selectivities in transferred quantum numbers, which cannot be realized by stable-beam-induced reactions.

In this work, we studied the  $^{90}\text{Zr}(^{12}\text{N}, ^{12}\text{C})^{90}\text{Nb}$  reaction at 175 MeV/ $u$ . This is the first exothermic charge-exchange reaction study at intermediate energy ever performed. This reaction realizes small momentum transfer for high excitation energy, owing to the large positive mass difference of the projectile and the ejectile,  $\Delta m = +16.83$  MeV (See Fig. 1). By selecting the final state of  $^{12}\text{C}$  by detecting the de-excitation  $\gamma$  rays, the transferred spin and isospin can be exclusively specified to be  $(\Delta S, \Delta T) = (1, 1)$  and  $(1, 0)$ . The effectiveness of the reaction can therefore be demonstrated through the observation of the Gamow-Teller giant resonance (GTGR) and the isobaric analog state (IAS). In addition to the above-mentioned advantages, this reaction is absorptive because this is a heavy-ion reaction. This means that this reaction is particularly sensitive to the IVSMR. The usefulness of the reaction can be reinforced by the observation of the IVSMR. Therefore, we chose  $^{90}\text{Zr}$  as the target nucleus for the present study, since the GTGR and IAS of this nucleus have been well-studied and signatures of the IVSMR in the  $\beta^-$  direction have been reported in the previous experiments [3, 4]. However, this reaction is associated with a background process due to the in-flight  $\beta$  decay of the  $^{12}\text{N}$  projectile, whose half-life is 11.0 ms [5].

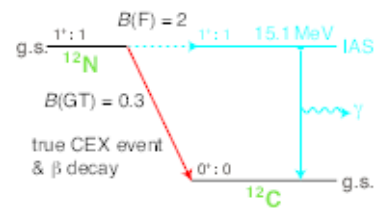


Figure 1. Energy relationship between  $^{12}\text{N}$  and  $^{12}\text{C}$ .

This process produces  $^{12}\text{C}$  nuclei, the amount of which is about  $10^2$  times larger than that of the true charge-exchange reaction products. This requires additional detectors to remove this background contribution since these  $^{12}\text{C}$  nuclei are not separable with the response of the focal plane detectors.

The experiment was performed at the RI Beam Factory (RIBF) of RIKEN Nishina Center. The primary  $^{14}\text{N}$  beam at 250 MeV/ $u$  was converted to the secondary  $^{12}\text{N}$  beam at 175 MeV/ $u$  via the projectile fragmentation reaction. The maximal intensities of the primary and secondary beams were 400 pA and 1.8 Mcps, respectively. The secondary  $^{12}\text{N}$  beam was separated by the BigRIPS fragment separator [6, 7] and transported by using the dispersion matching technique [8] to the reaction target. The target was  $^{90}\text{Zr}$  with a thickness of 154 mg/ $\text{cm}^2$  and with an isotopic enrichment of 99.4%. The  $^{12}\text{C}$  reaction product was momentum analyzed by the SHARAQ spectrometer [9]. The trajectories of the incoming beam particles were measured with the LP-MWDCs [10] and those of the reaction products were measured with the CRDCs [11]. The de-excitation  $\gamma$  rays were detected with the NaI(Tl) scintillator array DALI2 [12] surrounding the target. In addition, for the rejection of the aforementioned background events due to the  $\beta$  decay of  $^{12}\text{N}$ , a pair of plastic scintillators was installed immediately upstream and downstream of the  $^{90}\text{Zr}$  tar-

<sup>1</sup>Present address: National Superconducting Cyclotron Laboratory, Michigan State University.

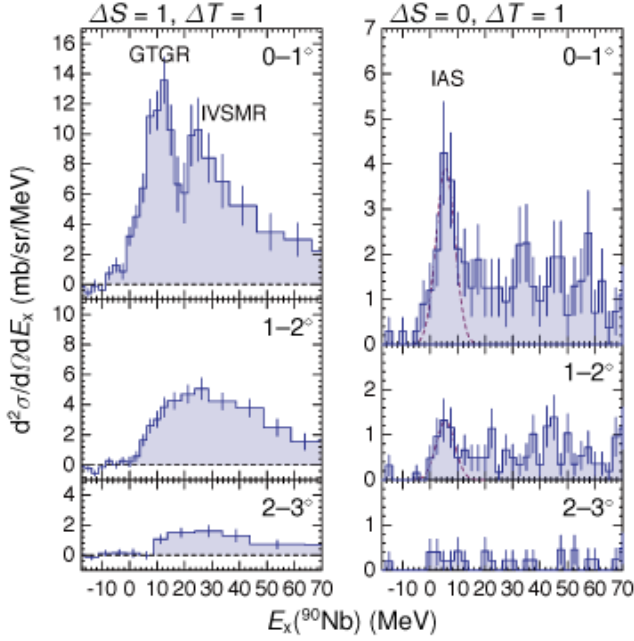


Figure 2. The double differential cross section data for the  $^{90}\text{Zr}(^{12}\text{N}, ^{12}\text{C})^{90}\text{Nb}$  reaction for the  $(\Delta S, \Delta T) = (1, 1)$  and  $(0, 1)$  modes.

get. These plastic scintillators worked well to remove the background contribution of that large amount.

The double differential cross section data for the  $^{90}\text{Zr}(^{12}\text{N}, ^{12}\text{C})^{90}\text{Nb}$  reaction at the angular range of  $0-3^\circ$  and the excitation energy range of  $0-70$  MeV were successfully obtained for both of the  $(\Delta S, \Delta T) = (1, 1)$  and  $(0, 1)$  modes. Figure 2 shows the double differential cross section spectra. The energy resolution was  $\Delta E = 8$  MeV (FWHM), which includes the intrinsic energy spread of the beam of  $4.6$  MeV and the difference of the energy loss of  $6$  MeV of the  $^{12}\text{N}$  projectile and the  $^{12}\text{C}$  ejectile. The angular resolution was  $\Delta\theta = 0.6^\circ$  (FWHM).

In the  $(\Delta S, \Delta T) = (1, 1)$  mode, the GTGR peak at  $E_x \approx 10$  MeV was observed. Another peak at  $30$  MeV was observed, which we concluded to correspond to the IVSMR. In the  $(\Delta S, \Delta T) = (1, 0)$  mode, the IAS peak at  $E_x \approx 5$  MeV was observed. The angular distributions of the cross sections were compared with the DWBA calculation, and they showed a good agreement. These results demonstrated that this probe was useful to study the  $(\Delta S, \Delta T) = (1, 1)$  and  $(0, 1)$  modes separately. Therefore, this probe is a powerful spectroscopic tool with these selectivities. They also showed that it has a sensitivity to the excitation of the IVSMR.

In addition, the ratio of the cross section of the GTGR per Gamow-Teller transition strengths of the target-residual and projectile-ejectile systems,  $\hat{\sigma}_{\text{GT}}^*$ , to that of the IAS per Fermi transition strengths,  $\hat{\sigma}_{\text{F}}^*$ , was found to be  $\hat{\sigma}_{\text{GT}}^*/\hat{\sigma}_{\text{F}}^* \sim 18$ , which is large compared with the  $(p, n)$  cross sections [1]. This enhancement is attributed to the absorptive nature of this probe, which can emphasize the longer-range spin-isospin-flip force  $V_{\sigma\tau}$  compared to the shorter-range isospin-flip force  $V_\tau$  [13].

## References

- [1] Recent review on spin-isospin responses by the nucleon induced charge-exchange reaction for example: M. Ichimura, H. Sakai and T. Wakasa, Prog. Part. Nucl. Phys. **56**, 446 (2006).
- [2] T. Uesaka et al., Prog. Theor. Phys. Supplement **196**, 150 (2012).
- [3] D. L. Prout et al., Phys. Rev. C **63**, 014603 (2000).
- [4] A. Brockstedt et al., Nucl. Phys. **A530**, 571 (1991).
- [5] F. Ajzenberg-Selove, Nucl. Phys. **A506**, 1 (1990).
- [6] T. Kubo et al., IEEE Trans. Appl. Supercon. **17**, 1069 (2007).
- [7] T. Ohnishi et al., J. Phys. Soc. Jpn. **77**, 083201 (2008).
- [8] T. Kawabata et al., Nucl. Instrum. Methods Phys. Res. **B266**, 4201 (2008).
- [9] T. Uesaka et al., Nucl. Instrum. Methods Phys. Res. **B266**, 4218 (2008).
- [10] H. Miya et al., CNS Ann. Rep. 2011 (2012), and references therein.
- [11] H. Tokieda et al., CNS Ann. Rep. 2009 (2010), and references therein.
- [12] S. Takeuchi et al., RIKEN Accel. Prog. Rep. **36**, 148 (2003).
- [13] M. Steiner et al., Phys. Rev. Lett. **76**, 26 (1996), Phys. Rev. Lett. **76**, 3042 (1996).

# Measurement of $^{12}\text{Be}(p, n)^{12}\text{B}$ reaction at 200A MeV in inverse kinematics

K. Yako, H. Sakai<sup>a</sup>, H. Baba<sup>a</sup>, M. Dozono<sup>a</sup>, T. Fujii, N. Inabe<sup>a</sup>, S. Kawase, T. Kawabata<sup>b</sup>, Y. Kikuchi, K. Kisamori, T. Kubo<sup>a</sup>, Y. Kubota, H. Matsubara<sup>a</sup>, S. Michimasa, K. Miki<sup>c</sup>, H. Miya, M. Kurata-Nishimura<sup>a</sup>, S. Noji<sup>d</sup>, C.S. Lee, T. Ohnishi, S. Ota, Y. Sasamoto, M. Sasano<sup>a</sup>, Y. Shimizu<sup>a</sup>, S. Shimoura, M. Takaki, H. Takeda<sup>a</sup>, T.L. Tang, H. Tokieda, T. Uesaka<sup>a</sup>, Z.Y. Xu<sup>e</sup>, R. Yokoyama and R.G.T. Zegers<sup>d</sup>

*Center for Nuclear Study, Graduate School of Science, University of Tokyo*

<sup>a</sup>*RIKEN Nishina Center*

<sup>b</sup>*Department of Physics, Kyoto University*

<sup>c</sup>*RCNP, Osaka University*

<sup>d</sup>*NSCL, Michigan State University*

<sup>e</sup>*Department of Physics, University of Tokyo*

Charge-exchange reactions at intermediate energies are excellent probes of spin-isospin excitations in nuclei, which are characterized by changes in the spin and the isospin ( $\Delta S = \Delta T = 1$ ). The  $(p, n)$  and  $(n, p)$  reactions are among the most successful probes in the spin-isospin studies of stable nuclei owing to the simple reaction mechanism. Therefore, we constructed a facility at SHARAQ where  $(p, n)$  reactions on unstable nuclei can be studied in inverse kinematics.

In June 2011, we performed the measurement of the  $^{12}\text{Be}(p, n)$  reaction as the first  $(p, n)$  measurement in inverse kinematics at RIBF. The  $^{12}\text{Be}$  nucleus is a neutron-rich nucleus with a large isospin asymmetry factor  $\epsilon \equiv (N - Z)/A = 0.33$ . Although the neutron number  $N = 8$  indicates a simple structure, it is known to possess exotic properties, e.g., breaking of  $N = 8$   $p$ -shell closure [1] and cluster/molecular structure like  $2\alpha + 4n$  configuration [2]. It is interesting to see how these properties change the aspects of Gamow-Teller (GT,  $\Delta S = \Delta T = 1, \Delta L = 0$ ) and spin-dipole (SD,  $\Delta S = \Delta T = \Delta L = 1$ ) excitations.

A primary beam of  $^{18}\text{O}$  was accelerated up to 250A MeV, and it was focused on the production target of 20-mm-thick Be at BigRIPS-F0, yielding a secondary  $^{12}\text{Be}$  beam of 200A MeV by projectile fragmentation.  $^{12}\text{Be}$  with a purity of 95% was selected at F3 and then transported in the achromatic mode to a liquid hydrogen target with a thickness of 14 mm at the pivot position of SHARAQ (S0). The size of the beam spot was  $\sigma = 7$  mm (5 mm) in the horizontal (vertical) direction on the target. The typical beam intensity was  $5 \times 10^5$  counts/s with a 100 pA primary beam.

The missing mass spectra of the  $^{12}\text{Be}(p, n)$  reaction were derived from the scattering angle of the neutron ( $\theta_{\text{lab}}$ ) and its kinetic energy ( $T_n$ ). These were measured by the time-of-flight (TOF) method using a set of newly developed neutron counters (WINDS) [3]. The timing information of the TOF start was obtained from the plastic counter ( $1 \text{ mm}^2$ ) at F-H10 located 2 m upstream of the SHARAQ target position. To obtain clean TOF spectra for relatively slow neutrons with  $T_n \sim 2$  MeV, a beam buncher at RILAC was operated with a frequency that was 1/4 of base frequency of the cyclotrons, so that the interval of beam bunches was 122 ns. SHARAQ and the detectors at its focal plane (S2) were used to tag the residual nucleus ( $^{12}\text{B}$ ) or its

decay products ( $^{11}\text{B}$  or  $^{10}\text{B}$ ).

Figure 1 shows the spectrum of the  $^{12}\text{Be}(p, n)^{12}\text{B}$  reaction with tagging of  $^{12}\text{B}$  at S2, covering the excitation energy region of 0 to 3.4 MeV. Here, the angular distributions of GT and SD components are expected to have peaks at  $\theta_{\text{cm}} = 0^\circ$  ( $T_n \sim 0$  MeV) and  $8-12^\circ$  ( $T_n = 4.5-8.0$  MeV), respectively. The observed locus is due to the GT transition to the ground state of  $^{12}\text{B}$ , for which the  $B(\text{GT})$  value is known to be 3.8. Data analysis for the GT and SD strengths is in progress.

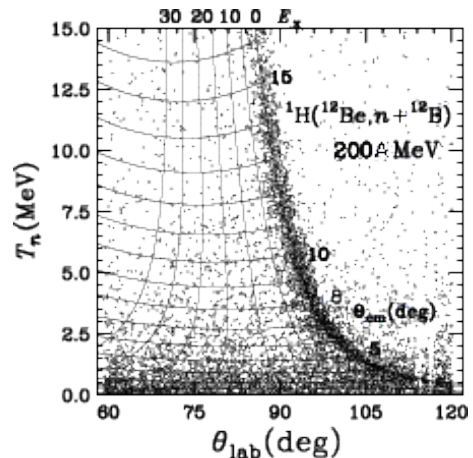


Figure 1. Preliminary spectrum of the  $^{12}\text{Be}(p, n)^{12}\text{B}$  reaction with tagging of  $^{12}\text{B}$  at S2.

## References

- [1] T. Suzuki and T. Otsuka, Phys. Rev. C **56** (1997) 847.
- [2] Y. Kanada-En'yo *et al.*, Phys. Rev. C **68** (2003) 014319.
- [3] K. Yako *et al.*, "Development of WINDS: wide-angle inverse-kinematics neutron detectors for SHARAQ", elsewhere in this Report.

# Experimental design for ${}^A\text{O}(\vec{p}, pN)$ reaction measurement in inverse kinematics

S. Kawase, T. Uesaka<sup>a</sup>, S. Shimoura, K. Yako, S. Ota, S. Michimasa, H. Tokieda, H. Miya, T. L. Tang, K. Kisamori, M. Takaki, Y. Kubota, C. S. Lee, R. Yokoyama, T. Fujii, M. Kobayashi, M. Sasano<sup>a</sup>, J. Zenihiro<sup>a</sup>, H. Matsubara<sup>a</sup>, M. Dozono<sup>a</sup>, T. Kawahara<sup>b</sup>, T. Wakui<sup>c</sup>, S. Sakaguchi<sup>d</sup>

*Center for Nuclear Study, Graduate School of Science, University of Tokyo*

<sup>a</sup>*RIKEN Nishina Center*

<sup>b</sup>*Department of Physics, Toho University*

<sup>c</sup>*Cyclotron and Radioisotope Center (CYRIC), Tohoku University*

<sup>d</sup>*Department of Physics, Kyushu University*

Strong spin-orbit coupling, which was introduced independently by Mayer and Jensen to explain magic numbers in nuclear system, is essential in nuclear structure. It is so strong that it can shuffle the level sequences with different principal quantum numbers, or in different major shells. The spin-orbit splitting is a direct measure of the strength of the spin-orbit coupling. We are interested in how the spin-orbit splitting changes as a function of nucleon number in isotopes. There are three reasons to study oxygen isotopes: (i) they have “proton magicity” and the shell model picture is thought to work well; (ii) they have moderate number of nucleons, therefore ab-initio calculation will be realized in near future; (iii) isotopes from proton drip-line to neutron drip-line are available at the RIKEN RI Beam Factory (RIBF).

The  $(\vec{p}, pN)$  reaction at the higher energy can be considered as a direct knockout of a nucleon in nucleus by injected proton. Therefore it is a suitable probe for the investigation of single hole states in nuclei. The separation energy ( $S_p$ ) is calculated using the scattering angles and momenta of two scattered nucleons. Each peak in separation energy spectrum corresponds to the hole states in residual nuclei. The orbital angular momentum of the states can be directly determined by analyzing missing momentum dependence of the cross section. Due to the polarization of proton, we can also determine total angular momentum ( $J$ ) by analyzing momentum dependence of the vector analyzing power [1].

We performed a pilot experiment at RCNP, Osaka University in June 2010 for the verification of  $J$  determination capability by measuring  $(\vec{p}, 2p)$  reaction on oxygen stable isotopes [2]. Spin-parities for several states were determined successfully. The result indicates the 1p spin-orbit splitting of  ${}^{18}\text{O}$  is reduced by several hundred keV from that of  ${}^{16}\text{O}$ . Even in stable isotopes the change of spin-orbit splitting are not negligible. Therefore the study in unstable isotopes is necessary to understand the nuclear structure.

The experiment will be performed at RIKEN RIBF and the experimental setup has been considered as follows. Beams of  ${}^{14}\text{O}$ ,  ${}^{22-24}\text{O}$  at energy of around 250 MeV is generated from  ${}^{48}\text{Ca}$  via projectile-fragmentation reaction. They are transported into the high-resolution beamline, separated from contaminants by using BigRIPS, and bombard the polarized proton target [3] mounted at SHARAQ S0 focal plane.

The beam particles are tracked by two low pressure multiwire drift chambers (LP-MWDC) [4] located at upstream of the target. Recoil particles are detected by a pair of detector systems located at the both side of beamline. Each detector system consists of a multiwire drift chamber (MWDC) [5], a trigger plastic scintillator of the size of  $13 \times 1500 \times 500 \text{ mm}^3$  and a neutron hodoscope. The neutron hodoscope consists of 40 plastic scintillators with a dimension of  $65 \times 65 \times 2200 \text{ mm}^3$ . The MWDC and the trigger scintillator are used to measure scattering angle and time of flight (TOF), respectively. The neutron hodoscope is used to measure the scattering angle and TOF for neutrons. The covered range of scattering angle is  $25^\circ < \theta < 65^\circ$ . Momentum of residual particles are analyzed by an LP-MWDC and an MWDC located upstream and downstream of quadrupole (Q) and dipole (D) magnets. Schematic drawing of the setup is shown in Fig.1.

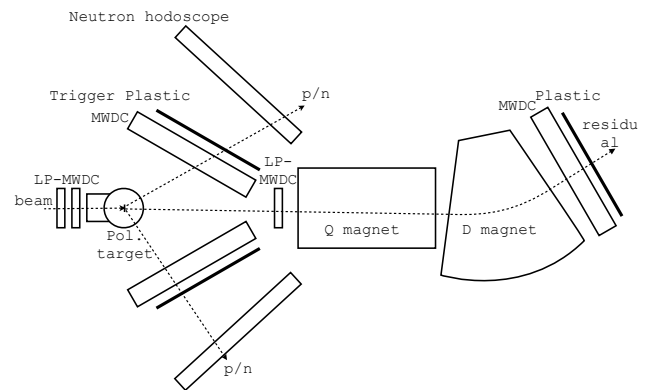


Figure 1. Schematic drawing of the setup for  $(\vec{p}, pN)$  reaction measurement

We also developed a new chamber for the polarized proton target. This chamber is dually structured such as a vacuum flask and consists of (outer) vacuum chamber and (inner) cooling chamber. Inside of the inner chamber is cooled with liquid nitrogen to keep the polarized target at low temperature as 100 K. The window of the chamber through which beam and recoil particle go out is designed to achieve sufficiently large acceptance (horizontal opening:  $\pm 72^\circ$ , vertical opening:  $\pm 16.5^\circ$ ) for the knockout reaction. This design also allows the future enlargement of the target crys-

tal.



Figure 2. New inner chamber for the polarized target

This experiment is scheduled in May 2012. The preparation of the target and the detectors are in progress.

### References

- [1] G. Jacob, Th. A. J. Maris, C. Schneider, and M. R. Teodoro, *Physics Letters B* **45**, 181 (1973).
- [2] S. Kawase *et al.*, *CNS Ann. Rep.* 2010 (2011).
- [3] T. Wakui *et al.*, *Nuclear Instruments and Methods in Physics Research A* **550**, 521 (2005).
- [4] A. Saito *et al.*, *CNS Ann. Rep.* 2006 (2007).
- [5] H. Okamura *et al.*, *Nuclear Instruments and Methods in Physics Research A* **406**, 78 (1998).

# Proton Inelastic Scattering Study on Neutron-rich $^{32,34,36}\text{Mg}$ Isotopes

S. Michimasa, Y. Yanagisawa<sup>a</sup>, K. Inafuku<sup>b</sup>, N. Aoi<sup>a</sup>, Z. Elekes<sup>c</sup>, Zs. Fülöp<sup>c</sup>, Y. Ichikawa<sup>d</sup>, N. Iwasa<sup>b</sup>, K. Kurita<sup>e</sup>, M. Kurokawa<sup>a</sup>, T. Machida<sup>e</sup>, T. Motobayashi<sup>a</sup>, T. Nakamura<sup>f</sup>, T. Nakabayashi<sup>f</sup>, M. Notani<sup>g</sup>, H. J. Ong<sup>a</sup>, T. K. Onishi<sup>d</sup>, H. Otsu<sup>a</sup>, H. Sakurai<sup>a</sup>, M. Shinohara<sup>f</sup>, T. Sumikama<sup>h</sup>, S. Takeuchi<sup>a</sup>, K. Tanaka<sup>a</sup>, Y. Togano<sup>e</sup>, K. Yamada<sup>a</sup>, M. Yamaguchi<sup>i</sup>, and K. Yoneda<sup>a</sup>

*Center for Nuclear Study, Graduate School of Science, University of Tokyo*

<sup>a</sup>*RIKEN (The Institute of Physical and Chemical Research)*

<sup>b</sup>*Department of Physics, Tohoku University*

<sup>c</sup>*ATOMKI, Hungary*

<sup>d</sup>*Department of Physics, University of Tokyo*

<sup>e</sup>*Department of Physics, Rikkyo University*

<sup>f</sup>*Department of Physics, Tokyo Institute of Technology*

<sup>g</sup>*Argonne National Laboratory, USA*

<sup>h</sup>*Department of Physics, Faculty of Science and Technology, Tokyo University of Science*

<sup>i</sup>*National Institute of Advanced Industrial Science and Technology*

We report here on the in-beam  $\gamma$ -ray spectroscopy using the very neutron-rich  $^{32,34,36}\text{Mg}$  beam and a hydrogen target. The  $^{36}\text{Mg}$  nucleus is located in the middle of the shell closures of  $N = 20$  and 28 and is closer to the neutron drip line than nuclei belonging to the so-called ‘island of inversion’. In previous experimental studies on neutron-rich magnesium isotopes,  $^{32}\text{Mg}$  was reported to be a well-deformed nucleus [1], and the disappearance of the magicity at  $N = 20$  was indicated. The deformation of  $^{34}\text{Mg}$  was reported to be larger than that of  $^{32}\text{Mg}$  [2]. The excitation energy of the  $2_1^+$  state in  $^{36}\text{Mg}$  was reported to be 660 keV [3] and this may indicate that  $^{36}\text{Mg}$  is deformed as large as that of  $^{34}\text{Mg}$ . The present study is aiming to investigate evolution of nuclear deformations up to  $^{36}\text{Mg}$  as a function of the neutron number.

The experiment was performed at the unstable nuclear beam line RIPS [4] in RIKEN. Ions of  $^{48}\text{Ca}$  were accelerated up to 63 MeV/nucleon using the acceleration scheme of RFQ-RILAC-CSM-RRC and impinged on a 150- $\mu\text{m}$   $^{181}\text{Ta}$  plate. A radioactive  $^{36}\text{Mg}$  beam was isotopically separated. Particle identification of the secondary beam was performed by a standard method based on the energy loss, time of flight and magnetic rigidity. The secondary beam bombarded a liquid hydrogen target [5] of 95 mg/cm<sup>2</sup>.

To obtain a sufficient mass resolution for the reaction products, the TOF spectrometer [6] was placed downstream of the secondary target. The scattered particles were detected using a telescope placed at the end of the spectrometer. The telescope consisted of a silicon detector of 500- $\mu\text{m}$  thick and two NaI(Tl) calorimeters. Most of the scattered particles passed through the silicon detector and stopped in the NaI(Tl) crystals. Scattered particles were identified based on TOF through the spectrometer, energy loss in the silicon detector and total energy measured using the calorimeter. Evaluated detection efficiency of the telescope for scattered particles was more than 90%.

De-excitation  $\gamma$  rays from the inelastically scattered particle were detected using 160 NaI(Tl) scintillators (DALI2) [7] surrounding the secondary target. Further details on the experiment setup and condition of the secondary beam were described in Ref. [8].

To estimate the angular-integrated cross section to populate the  $2_1^+$  state, We calculated the yield of the  $2_1^+ \rightarrow 0_1^+$  transition with  $\gamma$ -ray multiplicity ( $M_\gamma$ ) equal to one. The  $\gamma$ -ray multiplicity was defined to be the number of detected  $\gamma$  rays in an event of inelastic scattering. The limitation of  $M_\gamma$  worked to eliminate the cascade events, where produced nuclei emit two or more photons. The  $M_\gamma$  limitation for determining the cross section of the  $2_1^+$  state was performed as in Ref. [9] and worked well.

The spectra on  $^{32,34,36}\text{Mg}$  gated by  $M_\gamma = 1$  are shown in Figs. 1. In the figures, the plots with error bars show the experimental data. The thin histograms show the background and simulated  $\gamma$  spectrum of  $2_1^+ \rightarrow 0_1^+$  transition, and the thick line is the sum of the thin lines.

In  $^{32}\text{Mg}$ , the cross section to populate the  $2_1^+$  state was determined to be  $40_{-8}^{+9}$  mb from the data shown in Fig. 1(a). The present value is consistent with 47.6(5.3), which was the result of the precise proton inelastic scattering study on  $^{32}\text{Mg}$  by Takeuchi *et al.* [10].

The  $\gamma$ -ray spectrum of inelastic scattering on  $^{34}\text{Mg}$  gated by  $M_\gamma = 1$  is shown in Fig. 1(b). A clear peak was found at 658(4) keV, and was consistent with the reported excitation energy of the first  $2^+$  state [11, 12, 13]. The cross section to populate the  $2^+$  state was determined to be 63(5) mb and that of  $2_1^+ \rightarrow 0_1^+$  transition to be 78(6) mb. The total cross section of the transition is consistent with the previous measurement [13]. The  $2^+$  population is estimated to dominate as much as 80% of the 658-keV transition.

An excited state in  $^{36}\text{Mg}$  was reported at 660(6) keV in Ref. [3] and the present result is consistent with this result as shown in Fig. 1(c). The  $\gamma$ -ray energy

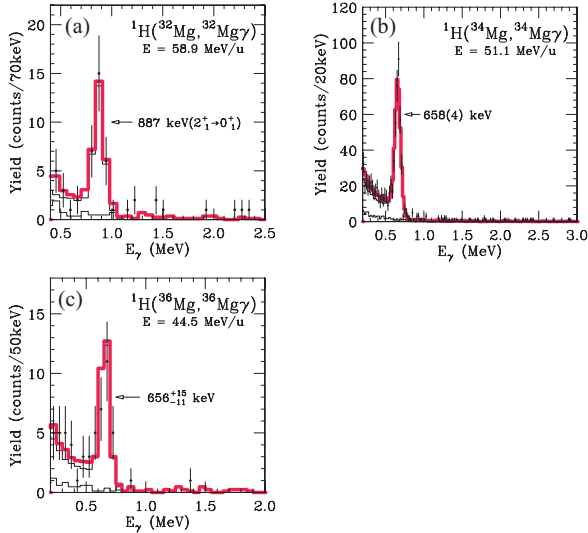


Figure 1. Gamma-ray spectra from the (a)  ${}^1\text{H}({}^{32}\text{Mg}, {}^{32}\text{Mg}\gamma)$ , (b)  ${}^1\text{H}({}^{34}\text{Mg}, {}^{34}\text{Mg}\gamma)$ , and (c)  ${}^1\text{H}({}^{36}\text{Mg}, {}^{36}\text{Mg}\gamma)$  reactions with  $\gamma$ -ray multiplicity equal to one. The solid circles with error bars show the experimental data. The thin histograms show the background and simulated  $\gamma$  spectrum of  $2_1^+ \rightarrow 0_1^+$  transition, and the thick solid histogram is the sum of the thin lines.

determined in present experiment is  $656_{-11}^{+15}$  keV. The cross sections to populate  $2^+$  state and of the 656-keV transition were determined to be 50(8) mb and 48(8) mb. The rate of  $2^+$ -state populating to the total 656-keV transition was estimated to be almost unity, and  $\gamma$  rays from higher states were not identified in the present experiment.

To study a systematic trend of quadrupole deformations in the interested region, angular-integrated cross sections obtained by  $M_\gamma = 1$  event selection were analyzed by the coupled-channel calculation using the ECIS97 code. For the initial and exit channels, the global potential WP09 [14] was employed. The WP09 potential was suggested recently to provide the isospin dependent optical potential for analyzing proton/neutron scattering by nuclei far from stability. It was determined based on the data not only of global stable isotopes but also of light unstable nuclei. This potential is fully suitable for the present experiment in the beam energies, masses and isospins of interested nuclei.

Obtained deformation lengths  $\delta_{(p,p')}$  are summarized in Table 1, and illustrated in Fig. 2. In the figure, the closed circles show deformation lengths determined from the present experiment. The open circle indicates the deformation length estimated from the  $2_1^+$  cross section reported by Takeuchi *et al.* [10]. The deformation lengths of  ${}^{32}\text{Mg}$  well agree between the present and previous works.

In  ${}^{32,34}\text{Mg}$ , the deformation lengths obtained from the proton inelastic scattering and Coulomb excitation experiments are equivalent within the errors. According to Ref. [15], their collectivities are considered to attribute to both protons and neutrons in the nuclei.

In the magnesium isotopes with  $N = 20$ –24, the deformation length increases from  $N = 20$  to 22 as shown

Table 1. Deduced deformation lengths ( $\delta_{(p,p')}$ ) and deformation parameters ( $\beta_{(p,p')}$ ) of  ${}^{32,34,36}\text{Mg}$ .

Nucleus	$\sigma(2_1^+)$ (mb)	$\delta_{(p,p')}$ (fm)	$\beta_{(p,p')}$
${}^{32}\text{Mg}$	$40_{-8}^{+9}$	$1.85 \pm 0.20$	$0.51_{-0.05}^{+0.06}$
	47.6(53)	$1.83_{-0.11}^{+0.10}$ *	$0.50 \pm 0.03$ *
${}^{34}\text{Mg}$	63(5)	$2.30_{-0.10}^{+0.09}$	$0.62 \pm 0.03$
${}^{36}\text{Mg}$	48(8)	$1.92_{-0.17}^{+0.16}$	$0.51 \pm 0.04$

\*The  $\beta_{(p,p')}$  and  $\delta_{(p,p')}$  were estimated by using the WP09 optical potential from the reported cross section for the  $2_1^+$  state [10].

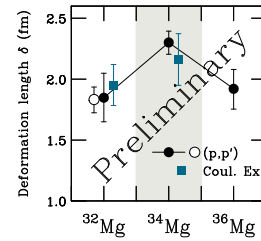


Figure 2. Deduced deformation lengths in  ${}^{32,34,36}\text{Mg}$ .

The closed circles show the present results. The open circle shows the value estimated from the  $2_1^+$  cross section by Takeuchi *et al.* [10]. The squares indicate the deformation lengths deduced from the Coulomb excitation works [1, 11, 12].

in Fig. 2. The deformation length of  ${}^{36}\text{Mg}$  is smaller than that of  ${}^{34}\text{Mg}$  and is a similar value with  ${}^{32}\text{Mg}$ , although the excitation energies of the  $2_1^+$  states in  ${}^{34,36}\text{Mg}$  are quite similar. Therefore, the collectivity in  ${}^{36}\text{Mg}$  is considered to decrease from  ${}^{34}\text{Mg}$ , and  ${}^{34}\text{Mg}$  is expected to have a peak of the quadrupole deformation along neutron-rich even-even magnesium isotopes. We need further discussions on the mismatching between the systematics of the  $2^+$  energies and of the collectivities in  ${}^{34,36}\text{Mg}$ .

## References

- [1] T. Motobayashi *et al.*, Phys. Lett. B **346** (1995) 9.
- [2] H. Iwasaki *et al.*, Phys. Lett. B **522** (2001) 227.
- [3] A. Gade *et al.*, Phys. Rev. Lett. **99** (2007) 072502.
- [4] T. Kubo *et al.*, Nucl. Instrum. Methods Phys. Res. B **70** (1992) 309.
- [5] H. Ryuto *et al.*, Nucl. Instrum. Methods Phys. Res. A **555** (2005) 1.
- [6] N. Aoi *et al.*, RIKEN Accel. Prog. Rep. **38** (2005) 176.
- [7] S. Takeuchi *et al.*, RIKEN Accel. Prog. Rep. **36** (2003) 148.
- [8] S. Michimasa *et al.*, CNS-REP-76 (2007) 15.
- [9] N. Aoi *et al.*, Phys. Rev. Lett. **102** (2009) 012502.
- [10] S. Takeuchi *et al.*, Phys. Rev. C **79** (2009) 054319.
- [11] H. Iwasaki *et al.*, Phys. Lett. B **522** (2001) 227.
- [12] J.A. Church *et al.*, Phys. Rev. C **72** (2005) 054320.
- [13] Z. Elekes *et al.*, Phys. Rev. C **73** (2006) 044314.
- [14] S.P. Weppner *et al.*, Phys. Rev. C **80** (2009) 034608.
- [15] A.M. Bernstein *et al.*, Rhys. Lett. B **103** (1981) 255.

# $\alpha$ inelastic scattering on neutron-rich nuclei around $^{32}\text{Mg}$

T. Fujii, S. Ota, S. Shimoura, N. Aoi<sup>a</sup>, E. Takeshita<sup>a</sup>, S. Takeuchi<sup>a</sup>, H. Suzuki<sup>b</sup>, H. Baba<sup>a</sup>,  
T. Fukuchi<sup>c</sup>, T. Fukui<sup>d</sup>, Y. Hashimoto<sup>e</sup>, E. Ideguchi, K. Ieki<sup>f</sup>, N. Iwasa<sup>g</sup>, H. Iwasaki<sup>h</sup>,  
S. Kanno<sup>a</sup>, Y. Kondo<sup>b</sup>, T. Kubo<sup>a</sup>, K. Kurita<sup>f</sup>, T. Minemura<sup>a</sup>, S. Michimasa,  
T. Motobayashi<sup>a</sup>, T. Murakami<sup>d</sup>, T. Nakabayashi<sup>e</sup>, T. Nakamura<sup>e</sup>, J. Niikura, T. Okumura<sup>e</sup>,  
T. Onishi<sup>b</sup>, H. Sakurai<sup>a</sup>, M. Shinohara<sup>e</sup>, D. Suzuki<sup>b</sup>, M. Suzuki<sup>b</sup>, M. Tamaki, K. Tanaka<sup>a</sup>,  
Y. Togano<sup>f</sup>, and Y. Wakabayashi<sup>i</sup>

*Center for Nuclear Study, Graduate School of Science, University of Tokyo*

<sup>a</sup>*RIKEN (The Institute of Physical and Chemical Research)*

<sup>b</sup>*Department of Physics, University of Tokyo*

<sup>c</sup>*Department of Physics, Osaka University*

<sup>d</sup>*Department of Physics, Kyoto University*

<sup>e</sup>*Department of Physics, Tokyo Institute Technology*

<sup>f</sup>*Department of Physics, Rikkyo University*

<sup>g</sup>*Department of Physics, Tohoku University*

<sup>h</sup>*Institut de Physique Nucléaire, IN2P3-CNRS, 91406 Orsay, France*

<sup>i</sup>*Department of Physics, Kyusyu University*

The  $^{32}\text{Mg}$  nucleus has attracted much interest because its nature is disagree with the  $N=20$  magic number. Until now, several studies have been conducted to reveal the nature of this nucleus. For example, the  $B(E2; 0_{g.s.}^+ \rightarrow 2_1^+)$  value was measured by the coulomb excitation [1], and the value of  $B(E2) = 454(78)e^2$  showed that  $^{32}\text{Mg}$  has large deformed ground state.  $\beta$  decay study [2] made the level structure. They found the states are completely dominated by intruder states comparing with the Monte Carlo shell model calculation. In the present work, we discuss the deformation parameter of nuclei around  $^{32}\text{Mg}$  with  $\alpha$ -inelastic scattering.  $\alpha$ -inelastic scattering is considered as a best tool for investigating the isoscalar multipole excitation since the  $\alpha$  particle is a  $T=0, S=0$  probe. Using this probe and cocktail beam, we can study the deformation of nuclear matter systematically around  $N=20$  region. The purpose of this study is to investigate how the breaking of magic number shows up in this systematics.

The experiment was performed at RIKEN [3]. A 63 MeV/nucleon  $^{40}\text{Ar}$  beam from the ring cyclotron was fragmented in a 1 mm-thick carbon target. And fragmentation products was separated by RIKEN projectile fragmentation separator, RIPS [4]. A particle identification was accomplished by measuring the energy loss in a silicon detector and time-of-flight(TOF). The TOF was obtained from the timing information of RF-signal and a plastic detector at the third focal plane(F3). Then, the secondary  $^{32}\text{Mg}$  beam bombarded a liquid helium target. The Gamma-Ray detector Array with Energy and Position sensitivity(GRAPE [5]) was positioned around the reaction target to tag individual excited states populated in the reaction. Each segment of GRAPE has position sensitivity by about 3 mm FWHM, so the doppler shift of  $\gamma$  ray from outgoing particle moving at  $\beta \sim 0.26$  can be corrected. For outgoing particles' identification, TOF-Spectrometer [6] was used. The TOF was obtained from the timing information of two plastic scintillators. The flight length between them is 386 cm, which is long enough

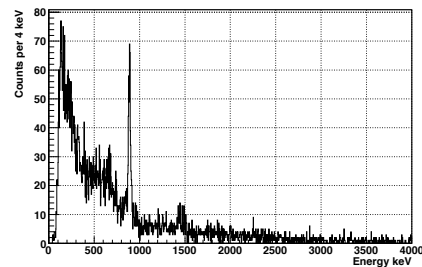


Figure 1. Doppler corrected  $\gamma$  ray spectrum for the  $^{32}\text{Mg}(\alpha, \alpha')^{32}\text{Mg}$  reaction. One clear peak positions at 887 keV. There is a small peak around 1436 keV. This peak corresponds to  $4_1^+ \rightarrow 2_1^+$ .

to separate each nucleus. Super-conducting Triplet Quadrupole magnets (STQ) [6] was used in order to focus the outgoing particles which spread while a long-distance flight. The energy loss was measured by silicon detectors. For the purpose of mass identification, NaI Wall [7] was positioned at the end of the beam line, and it enabled us to measure the total energy of outgoing particles. The incoming beam and scattered particles were measured with PPAC's. Three of them were placed upstream of the target, and two was placed downstream. By these PPAC's we could obtain the reaction position in the target and the scattering angle.

The  $\gamma$  ray spectrum after doppler correction is shown in Fig. 1. To obtain this spectrum, we selected the event which the beam particle and scattered particle were both considered to be  $^{32}\text{Mg}$ . We can see a clear peak at 887 keV which corresponds to de-excitation from the first excited  $2^+$  state at 885 keV to the ground state of  $^{32}\text{Mg}$ . An energy resolution after doppler correction is 27 keV for 887 keV peak. We can also see smaller peak at 1437 keV from 2321 keV state to the first  $2^+$  state. Selecting the events correspond to individual excitations by this spectrum and using the information of scattering angle measured by PPAC's,

the differential cross section is going to be obtained. In comparing the obtained cross section data with the calculated one using ECIS [8] code, the deformation parameter of  $^{32}\text{Mg}$  finally will be deduced. Fig.2 shows the result of particle identification of the secondary beam. We can see the  $^{32}\text{Mg}$  as the most abundant nucleus. And there is a  $^{36}\text{Si}$ , which is also even-even nucleus. We plan to study these nuclei. Data analysis

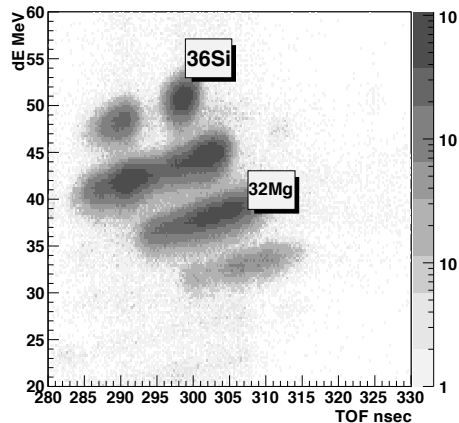


Figure 2.  $\Delta E$  versus TOF plot for the secondary beam. RF signal and plastic scintillator at F3 were used for TOF. Energy deposits were measured by a silicon detector at F2.

is in progress, and We will report the results later.

## References

- [1] T. Motobayashi *et al.*, Physics Letters B **346**, 9 (1995).
- [2] V. Tripathi *et al.*, Phys. Rev. C **77**, 034310 (2008).
- [3] S. Ota *et al.*, CNS Annual Report 2004 , 24 (2005).
- [4] T. Kubo *et al.*, Nucl. Instr. Meth. B **70**, 309 (1992).
- [5] S. Shimoura, Nuclear Instruments and Methods in Physics Research Section A **525**, 188 (2004).
- [6] N. Aoi *et al.*, RIKEN Accel. Prog. Rep. **38**, 176 (2005).
- [7] T. Tamaki *et al.*, CNS-REP **59**, 76 (2003).
- [8] J. Raynal, coupled-channel code ECIS97 (unpublished) .

# Search for new isomers near the $N=Z$ line by using projectile-fragmentation of $^{124}\text{Xe}$

S. Go, D. Kameda<sup>a</sup>, T. Kubo<sup>a</sup>, N. Inabe<sup>a</sup>, N. Fukuda<sup>a</sup>, H. Takeda<sup>a</sup>, H. Suzuki<sup>a</sup>, K. Yoshida<sup>a</sup>, K. Kusaka<sup>a</sup>, K. Tanaka<sup>a</sup>, Y. Yanagisawa<sup>a</sup>, M. Ohtake<sup>a</sup>, H. Sato<sup>a</sup>, Y. Shimizu<sup>a</sup>, H. Baba<sup>a</sup>, M. Kurokawa<sup>a</sup>, D. Nishimura<sup>a</sup>, N. Iwasa<sup>b</sup>, A. Chiba<sup>b</sup>, Y. Okoda<sup>b</sup>, E. Ideguchi, R. Yokoyama, T. Fujii, K. Ieki<sup>c</sup>, D. Murai<sup>c</sup>, H. Nishibata<sup>d</sup>, S. Momota<sup>e</sup>, M. Lewitowicz<sup>f</sup>, G. DeFrance<sup>f</sup>, I. Celikovic<sup>f</sup>, K. Steiger<sup>g</sup>, D. J. Morrissey<sup>g</sup>, and D. P. Bazin<sup>g</sup>

*Center for Nuclear Study, Graduate School of Science, University of Tokyo*

<sup>a</sup>*RIKEN (The Institute of Physical and Chemical Research)*

<sup>b</sup>*Department of Physics, Tohoku University*

<sup>c</sup>*Department of Physics, Rikkyo University*

<sup>d</sup>*Department of Physics, Osaka University*

<sup>e</sup>*School of Environmental Science and Engineering, Kochi University of Technology*

<sup>f</sup>*Grand Accelérateur National d'Ions Lourds, France*

<sup>g</sup>*National Superconducting Cyclotron Laboratory, Michigan State University USA*

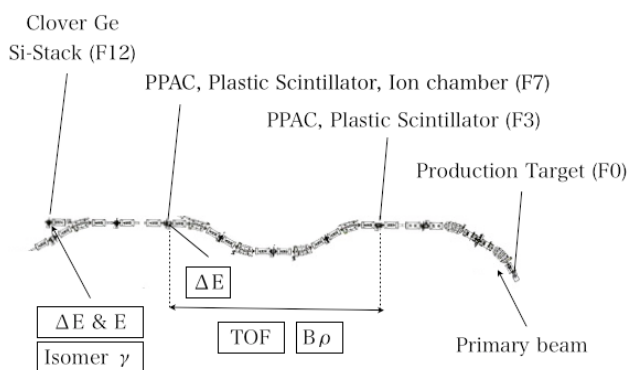


Figure 1. Beam line from F0 target to final focal plane F12. The information of time of flight (TOF) and  $B\rho$  is used to deduce mass to charge ratio  $A/Q$ .  $\Delta E$  was measured by ion chamber at F7 and Si detectors at F12.

Nuclei around doubly-magic  $^{100}\text{Sn}$  exhibit a rich variety of phenomena. Recently spin aligned neutron-proton pairs were reported in  $^{92}\text{Pd}$  [1]. The isoscalar component of the neutron and proton interaction is essential to explain the spin-gap isomer of  $^{96}\text{Cd}$  [2]. In  $^{94}\text{Ag}$ , an inversion of in the spin ordering of the  $19^+$  and  $21^+$  occurs owing to an additional correlation energy of protons, and the evidence of the two proton decay was reported [3]. In addition, nuclei in this region is of astrophysical importance as the rapid proton capture process lies around  $^{100}\text{Sn}$  [4]. The largest Gamow-Teller strength so far was measured in  $^{100}\text{Sn}$  [5]. To determine the structure of the nuclei in this region has an important meaning for understanding these phenomena.

To find new isomeric states in this region, isomer spectroscopy was performed at RIBF. Isomeric nuclei were produced by the fragmentation reaction of the  $^{124}\text{Xe}$  beam at an energy of 345 MeV/u on a  $^9\text{Be}$  target of 4 g/cm<sup>2</sup> thickness. The intensity of the primary beam was about 8 pnA. The secondary beam was identified by using the BigRIPS separator [6], and transported to the final focal plane F12 (See Fig. 1).

The particle identification (PID) was based on the  $\Delta E$ -TOF- $B\rho$  method, in which the energy loss ( $\Delta E$ ) of the particle, time of flight (TOF), and magnetic rigidity ( $B\rho$ ) were measured to deduce the atomic number  $Z$  and the mass-to-charge ratio  $A/Q$  of particle. The TOF was measured by using plastic scintillators between the focal plane F3 and F7, and the  $\Delta E$  was measured by using an ion chamber placed at F7. The average total counting trigger rate at F7 was about 1.5 kcps. A stack of Si detectors, placed on the final focal plane F12, served as the active stopper of the isotopes. The  $\Delta E$  and the total kinetic energy ( $E$ ) were measured. The  $\gamma$ -rays emitted from the excited state of nuclei were detected by 4 clover-type Ge detectors placed around the stack of Si detectors. These detectors were placed perpendicular to the beam axis. The dynamic range of  $\gamma$ -ray energy was set up to 4 MeV. The time window of TDC was up to 20  $\mu\text{s}$  from the timing of trigger signal. By analyzing the delayed component,  $\gamma$ -rays associated with many transitions were identified. Observed known  $\gamma$ -ray transitions in this experiment are summarized in Table 1. For example, the known transition in  $^{98}\text{Cd}$  observed at 147, 198, 688, 1395 keV were successfully identified [12], and 103 keV in  $^{106}\text{Sb}$  was observed [14]. These information served as confirmation of the particle identification.

Figure 2 shows the gamma-ray spectrum of  $^{96}\text{Pd}$  summed up for all the Ge detectors. Here the timing gate of  $t > 500$  ns after the prompt  $\gamma$ -ray emission was adopted to avoid the background due to the beam irradiation. Strong peaks were observed at 106, 352, 684, and 1415 keV. These transitions agree with the reported values [11]. The decay curve obtained by gating on the isomeric  $\gamma$ -ray at 106.2 keV is presented in Fig. 3. The half life is preliminarily deduced to be  $1.9 \pm 0.4 \mu\text{s}$ . This value agrees with the value reported half life, 2.2  $\mu\text{s}$  within errors.

In summary, we have performed isomer spectroscopy around  $^{100}\text{Sn}$  at RIBF. Nuclei were produced by the fragmentation reaction of the  $^{124}\text{Xe}$  beam, and the  $\gamma$ -rays from the excited states of these nuclei were measured. As a result, many known isomers were observed. There is the possibility of finding new isomeric transi-

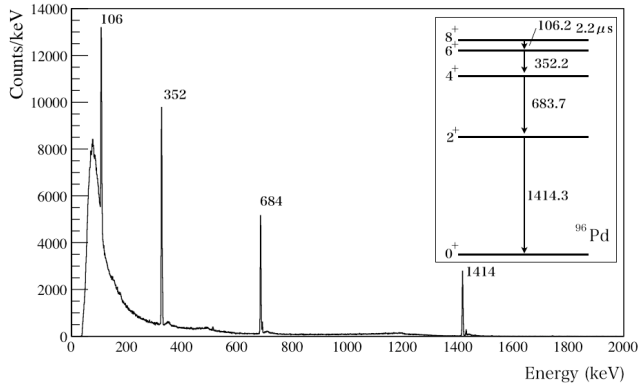


Figure 2.  $\gamma$ -ray energy spectrum of  $^{96}\text{Pd}$  in this experiment. Inset shows a partial level scheme of  $^{96}\text{Pd}$  [11]. The observed energies agree with the reported values.

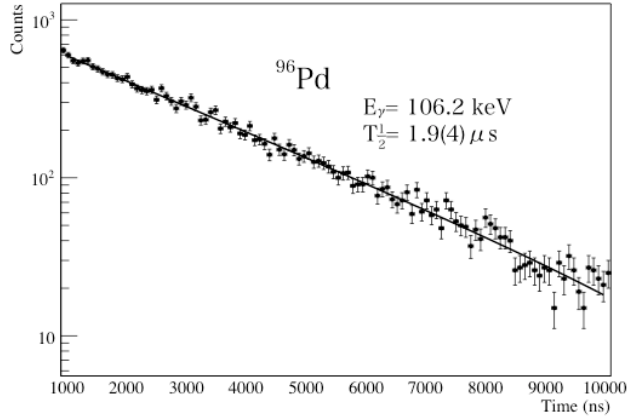


Figure 3. Decay curve spectrum of  $^{96}\text{Pd}$  gated by the known transition at the energy of 106.2 keV. The deduced half life agrees with errors the reported value 2.2  $\mu\text{s}$  [11].

tion in this region, and the analysis is now in progress.

## References

- [1] B. Cederwall et al., Nature **469** (2011) 68.
- [2] B. S. Nara Singh, et al., Phys. Rev. Lett. **107** (2011) 172502.
- [3] I. Mukha et al., Nature **439** (2006) 439.
- [4] C. Mazzocchi et al., Phys. Rev. Lett. **98** (2007) 212501.
- [5] C. B. Hinke et al., Nature **486** (2012) 341.
- [6] T. Kubo, Nucl. Instr. and Meth. B **204** (2003) 97.
- [7] S. Ho  $\ddot{u}$ mann et al., Z. Phys. A Atom. Nucl. **325** (1986) 37.
- [8] C. Y. Wu et al., Phys. Rev. C **39** (1989) 250.
- [9] L.S. Caceres et al, Acta Physica Polonica B **38** (2007) 1271.
- [10] A. B. Garnsworthy et al. Phys. Lett. B **660** (2008) 326.
- [11] L. Batist et al., Nucl. Phys. A **624** (1997) 185.
- [12] A. Blazhev et al., Phys. Rev. C **69** (2004) 064304.

Nucleus	$E_{\text{level}}$ (keV)	$T_{1/2}$ ( $\mu\text{s}$ )	Transition	Energy (keV)
$^{76}\text{Rb}$ [7]	317	3.20	$(4^+) 3^-$	71
	246		$3^{(-)} 2^{(-)}$	145
	246		$3^{(-)} 1^{(-)}$	246
	101		$2^{(-)} 1^{(-)}$	101
$^{81}\text{Sr}$ [8]	79	0.40	$5/2^- 1/2^-$	79
$^{82}\text{Nb}$ [9]	1180	0.09	$5^+ 4^+$	124
	1056		$4^+ 2^+$	638
	418		$2^+ 0^+$	418
$^{86}\text{Tc}$ [10]	1524	1.59	$(6^+) (4^+)$	81
	1443		$(4^+) (3, 4^+)$	269
	1443		$(4^+) (2^+)$	850
	593		$(2^+) (0^+)$	593
$^{96}\text{Pd}$ [11]	2531	2.2	$8^+ 6^+$	106
	2424		$6^+ 4^+$	325
	2099		$4^+ 2^+$	684
	1415		$2^+ 0^+$	1415
$^{98}\text{Cd}$ [12]	2423	0.17	$8^+ 6^+$	147
	2280		$6^+ 4^+$	198
	2082		$4^+ 2^+$	688
	1395		$2^+ 0^+$	1395
$^{102}\text{Sn}$ [13]	1472	0.62	$2^+ 0^+$	1472
$^{106}\text{Sb}$ [14]	103	0.23	$(4^+) (2^+)$	103

Table 1. Observed known  $\gamma$ -ray transitions in this experiment (partial). Half lives on the order of microsecond or sub-microsecond were successfully observed in many isotopes. These information served as the confirmation of the particle identification.

[13] M. Lipoglavsek et al., Phys. Lett. B **440** (1998) 246.

[14] D. Sohler et al., Nucl. Phys. A **753** (2005) 251.

# Search for short-lived isomers in neutron-rich $Z \sim 60$ nuclei produced by in-flight fission of 345 MeV/nucleon $^{238}\text{U}$

R. Yokoyama, D. Kameda<sup>A</sup>, T. Kubo<sup>A</sup>, N. Inabe<sup>A</sup>, N. Fukuda<sup>A</sup>, H. Takeda<sup>A</sup>, H. Suzuki<sup>A</sup>, K. Yoshida<sup>A</sup>, K. Kusaka<sup>A</sup>, K. Tanaka<sup>A</sup>, Y. Yanagisawa<sup>A</sup>, M. Ohtake<sup>A</sup>, H. Sato<sup>A</sup>, Y. Shimizu<sup>A</sup>, H. Baba<sup>A</sup>, M. Kurokawa<sup>A</sup>, D. Nishimura<sup>A1</sup>, T. Ohnishi<sup>A</sup>, N. Iwasa<sup>B</sup>, A. Chiba<sup>B</sup>, T. Yamada<sup>B</sup>, E. Ideguchi<sup>2</sup>, S. Go, T. Fujii, H. Nishibata<sup>C</sup>, K. Ieki<sup>D</sup>, D. Murai<sup>D</sup>, S. Momota<sup>E</sup>, Y. Sato<sup>F</sup>, J. Hwang<sup>F</sup>, S. Kim<sup>F</sup>, O. B. Tarasov<sup>G</sup>, D. J. Morrissey<sup>G</sup>, B. M. Sherrill<sup>G</sup>, and G. Simpson<sup>H</sup>

*Center for Nuclear Study, Graduate School of Science, University of Tokyo*

<sup>A</sup>*RIKEN, Nishina Center*

<sup>B</sup>*Department of Physics Tohoku University*

<sup>C</sup>*Department of Physics, Osaka University*

<sup>D</sup>*Department of Physics, Rikkyo University*

<sup>E</sup>*School of Environmental Science and Engineering, Kochi University of Technology*

<sup>F</sup>*Department of Physics and Astronomy, Seoul National University*

<sup>G</sup>*National Superconducting Cyclotron Laboratory Michigan State University*

<sup>H</sup>*LPSC-IN2P3*

In-flight fission of the  $^{238}\text{U}$  beam at RIBF, RIKEN enables the production of the beams of highly neutron-rich radioisotopes (RIs) with a wide range of atomic masses. Before RIBF, little has been known about the excited states of neutron-rich medium-heavy-to-heavy nuclides. It is expected that some isomeric states are excited in the production of the RI beams. If the life of an isomer is sufficiently long, it can be measured by  $\gamma$ -ray spectroscopy at the end of the separator beam line.

Previously, neutron-rich isotopes from  $Z \sim 20$  to  $Z \sim 50$  region had been investigated by the in-flight fission of a  $^{238}\text{U}$  beam at the RIBF in 2008 [1]. In 2011, the research was expanded to  $Z \sim 60$  region. The schematic view of the RIBF beamline is shown in Fig.1. The primary  $^{238}\text{U}$  beam was bombarded to the production target (made of Be with 4.93mm thick for higher  $Z$  setting, and 3.96mm thick for lower  $Z$  setting) placed at the F0 focal plane. The energy and the intensity of the primary beam were 345 MeV/nucleon and 0.31pnA respectively. The produced RI beams were identified event-by-event by their proton number ( $Z$ ) and mass-to-charge ratio ( $A/Q$ ). These quantities were obtained by the measurement of the magnetic rigidity ( $B\rho$ ), time of flight (TOF), and energy loss ( $\Delta E$ ) in the BigRIPS separator. The TOF was obtained by the time difference between plastic scintillation counters at F3 and F7. More detailed explanation of the particle identification at the BigRIPS is shown in Ref [1]. In addition, a total kinetic energy (TKE) detector was installed in the F12 focal plane at the end of the BigRIPS beamline. This is to identify ions with different atomic charge states, which becomes important for  $Z > 60$  elements. The TKE detector consists of 14 layers of Si detectors and is designed to stop all ions of interest. A set of PPACs was also installed just before the TKE

detector, as a tracker of the ions implanted to the TKE detector.

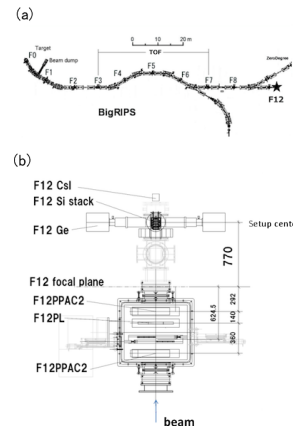


Figure 1. (a) Schematic view of the RIBF beamline. (b) the detector setup at F12.

The  $\gamma$  rays from the ions stopped at F12 were detected by four clover-type HPGe detectors placed around the TKE detector. The energies and timings of delayed  $\gamma$  rays were detected within a time window of 20  $\mu\text{s}$  following the implantation of the beam. Isomers with lives shorter than the time of flight between the production target and the F12 decay during the transportation. Therefore, this measurement is adequate for the detection of the  $\gamma$  rays from isomeric states with half-lives on the order of microseconds or sub-microseconds. The clover-type Ge detector consists of four crystals which are to improve the signal-to-noise ratio by adding back Compton-scattered events in the neighboring crystals.

To search for new isomers, energies and half-lives of the  $\gamma$  rays from each isotope were examined by gating on the RI in the PID. The PID is confirmed by the mea-

<sup>1</sup>present address: Department of Physics, Tokyo University of Science

<sup>2</sup>present address: RCNP, Osaka University

surement of the  $\gamma$  rays from nuclides with known isomeric states. In order to reduce the background from beam irradiation, the  $\gamma$  events close to the timing of the beam implantation were excluded.

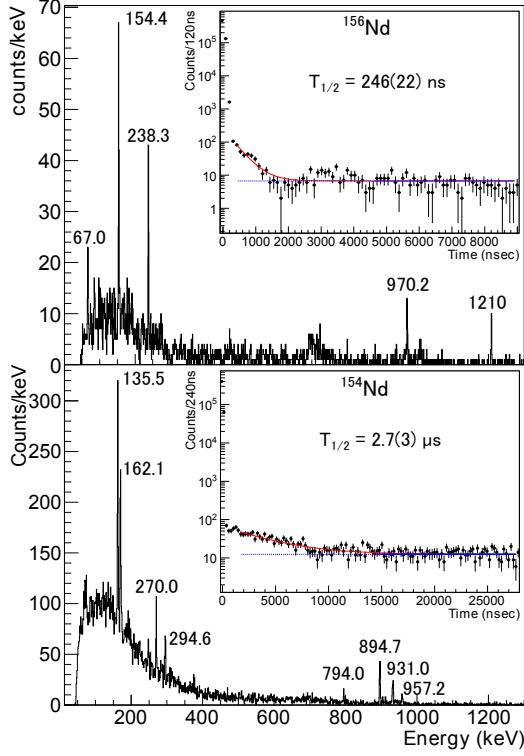


Figure 2.  $\gamma$ -ray energy spectra for  $^{154}\text{Nd}$  and  $^{156}\text{Nd}$ . The solid line shows the fitting function. The dashed line shows the component of the constant background. The region  $< 500\text{ns}$  in the timing spectra is dominated by beam irradiation, therefore, it was excluded from the fitting to enhance signal to noise ratio.

Relative intensities of the  $\gamma$  rays were also obtained for the isotopes which have two or more isomeric  $\gamma$  rays observed. The detection efficiency of  $\gamma$  rays was estimated by Monte Carlo simulation using Geant4. The total detection efficiency for a  $\gamma$  ray emitted from the center of the detector array was estimated to be 2.5% in 1333keV. Since the properties of the beams at F12 are different in each isotope, the simulation was performed for each of them. Experimental data of the position of beam implantation were used as the source point of the  $\gamma$ -ray emission in the simulation. The position was obtained from the information of the Si detectors in the TKE detector and PPAC tracker at F12.

Figure 2 shows the preliminary energy spectra and the decay curves of the delayed  $\gamma$  rays for  $^{154}\text{Nd}$  and  $^{156}\text{Nd}$ . The  $\gamma$ -ray energies are obtained by chi-square fitting of the peaks with Gaussian plus linear background. The half-lives are obtained by fitting the decay curves by the likelihood method with the function which consists of exponential decay and constant background. These quantities obtained in this study are consistent with those in Ref [2].

In addition, the relative intensity obtained in this study and the level scheme reported in the reference

are compared in Fig.3. The simple sum of the relative intensities of the  $\gamma$  rays above and below a state is conserved. The differences between above and below are 0.36(40) for 67keV state, 0.052(285) for 222keV state, and 0.088(209) for 460keV state. They are all zero within the range of the errors, which supports the level scheme in Ref [2]. Several candidates for new isomers have also been identified in  $Z \sim 60$ ,  $A \sim 100$  region. Further analysis of these new isomers is in progress.

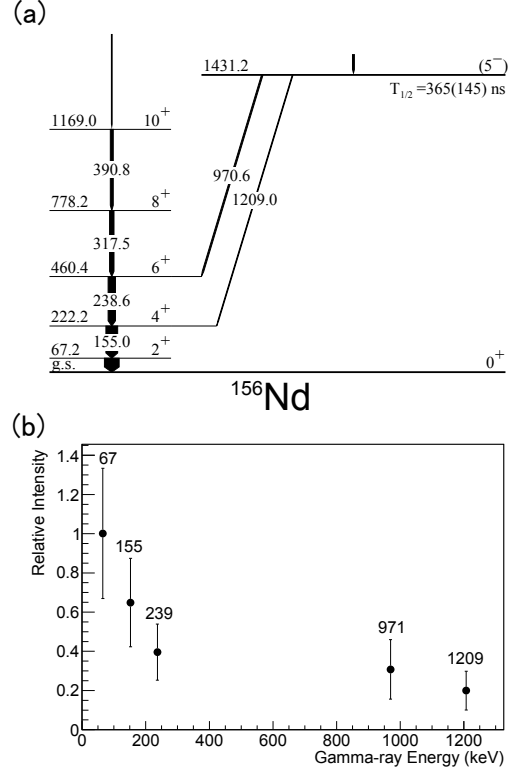


Figure 3. (a) Level scheme of  $^{156}\text{Nd}$  from Ref [2]. (b) Preliminary relative intensity of the isomeric  $\gamma$  rays obtained in this study.

## References

- [1] T. Ohnishi *et al.*: J. Phys. Soc. Japan 79, 073201 (2010).
- [2] G. S. Simpson *et al.*, Phys. Rev. C 80, 024304 (2009).



**Experiment Nuclear Physics: PHENIX  
Experiment at BNL-RHIC and ALICE  
Experiment at CERN-LHC**



# Identified particle flow measurement in Pb-Pb collisions at $\sqrt{s_{NN}}=2.76$ TeV measured by the ALICE experiment at the LHC

Y. Hori, T. Gunji, H. Hamagaki for the ALICE collaboration

Center for Nuclear Study, Graduate School of Science, University of Tokyo

## 1. Introduction

In heavy ion collisions, the azimuthal anisotropic flow is one of the most informative observables for the understanding of the collision dynamics and the collective properties of the nuclear matter created under the extreme conditions. In non-central collisions, the initial spatial anisotropy in the azimuthal direction is converted into a large anisotropy in the azimuthal direction of the particle momentum space if constituents of the matter interact strongly enough.

Anisotropic azimuthal flow is usually quantified by the coefficients  $v_n$  in the Fourier decomposition of the azimuthal distribution with respect to the reaction plane. Since the success of the ideal hydrodynamic description of the elliptic flow  $v_2$  for Au-Au collisions at RHIC [1], the hydrodynamics is considered as the most appropriate theory to describe a thermalized phase in the time evolution of the system created in a heavy-ion collision. Furthermore at the LHC energy, it is found that the non-identified charged particle  $v_2$  can be reasonably well described by the hydrodynamics [2].

Another important test of the hydrodynamic description is an interplay between the radial flow (azimuthally symmetric radial expansion, which can be indirectly measured by a slope of the  $p_T$  spectra) and anisotropic flow. It is expected that this interplay results in the particle mass dependence of the identified particle elliptic flow at small transverse momenta.

## 2. Flow measurement methodology

The collision reaction plane, which is defined by the impact parameter and the colliding nuclei direction, is not known experimentally and the anisotropic flow coefficients can be only extracted from azimuthal multi-particle correlations between produced particles. A scalar product method (SP) is one of the two-particle correlation method and the differential flow in SP is defined as:

$$v_n(p_T, \eta) = \frac{\langle Q_n \cdot u_{n,i}^*(p_T, \eta) \rangle}{2\sqrt{\langle Q_n^a \cdot Q_n^{b*} \rangle}} \quad (1)$$

where  $\langle \rangle$  denotes the average over all particles in all events.  $u_{n,i} \equiv (\cos n\phi_i, \sin n\phi_i)$  is the unit vector of the  $i$ -th particle and  $Q_n \equiv (\sum \cos n\phi, \sum \sin n\phi)$  is the event flow vector [3]. In this analysis,  $u_{n,i}$  is calculated by tracks at  $|\eta| < 0.8$  reconstructed with the time projection chamber (TPC) and  $Q_n^{a,b}$  is calculated by the VZERO detector at  $-3.1 < \eta < -1.7$ ,  $2.8 < \eta < 5.1$  ( $Q_n = Q_n^a + Q_n^b$ ), which consists of plastic scintillation counters. It is empirically known that non-flow effects on the two-particle correlations can be removed by introducing  $\eta$  gaps among  $u_{n,i}$ ,  $Q_n^a$  and  $Q_n^b$  [3].

Pions, kaons and protons/antiprotons are identified using  $dE/dx$  and time information measured by the TPC and the time-of-flight detector (TOF). For  $K_s^0$ ,  $\Lambda/\bar{\Lambda}$  and  $\phi$ , an invariant mass method of the two

daughter candidates is used for identification and reconstruction.

If the reconstruction efficiency strongly depends on the local particle density at the detector, this results in the decrease (increase) of the positive (negative) elliptic flow. We conducted a study with monte carlo simulations to estimate this effect and assigned a few % systematic error for this effect.

## 3. Results of identified particle elliptic flow

Figure 1 shows the results of identified particle elliptic flow in Pb-Pb collisions at  $\sqrt{s_{NN}} = 2.76$  TeV at collision centrality 10-20% measured by the ALICE experiment. As expected by the hydrodynamics,  $v_2$  values of the heavier particles shift toward to higher  $p_T$  direction at the low  $p_T$  region. This can be regarded as a sign of hydrodynamic pressure on particles by large radial flow. The mass dependence of  $v_2$  in  $p_T < 2.5$  GeV/c, is reasonably reproduced by viscous hydrodynamic model calculations with the color glass condensate initial condition (solid curves in Fig. 1) [2]. Models considering the hadronic cascade phase can better describe the data, particularly for heavier particles.

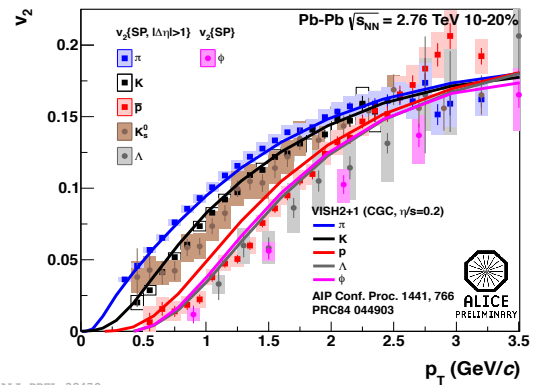


Figure 1. The  $p_T$  differential elliptic flow  $v_2$  of  $\pi$ ,  $k$ ,  $\bar{p}$ ,  $K_s^0$ ,  $\Lambda$  and  $\phi$  with theoretical predictions at centrality 10-20% [4]

## 4. Kaon elliptic flow via decay topological identification

In Fig. 1, the elliptic flow of the  $K_s^0$  is systematically lower than that of TOF-TPC Kaon although the discrepancy is within systematic errors. We also measured kaons by the kink topology method as an alternative identification method [5]. Kaons have two main decay modes,  $K \rightarrow \mu\nu$  (Branching ratio 63.55%) and  $K \rightarrow \pi\pi^0$  (Branching ratio 20.66%). These decay modes can be recognized as a kink topology in the TPC active area. Kaon can be identified at wider range of  $p_T$  with the kink topology than TOF-TPC method as shown in Fig. 2. The following kink identification cuts are

applied if kink daughters are associated to the mother track by the kink finding algorithm.

- Effective volume cuts:  $120 \text{ cm} < \text{radius from a decay point} < 220 \text{ cm}$
- Decay angle cuts:  
 $1.2 \times \text{MaxDecayAngleOfPiMu} < \text{decay angle} < 0.98 \times \text{MaxDecayAngleOfKmu}$
- Invariant mass cuts :  $0.4 < \text{invariant mass} < 0.55$
- $q_T$  cuts :  $0.12 < q_T < 0.24 \text{ GeV}/c$
- kink DCA (Distance of Closest Approach) cuts :  
 $\text{DCA} < 0.1 \text{ cm}$
- Mother track TPC  $dE/dx$  cuts :  $< 3.5\sigma$

The large fraction of kinks from pion decays and random association kinks are removed because they have a sharp peak at around decay angle  $\sim 0$  and  $q_T \sim 0$ .  $\text{MaxDecayAngleOfKmu}$  and  $\text{MaxDecayAngleOfPimu}$  are calculated by the measured momentum of mother track and the following formula.

$$(\theta^{lab})_{max} = \frac{p}{\gamma E} \frac{1}{\sqrt{\beta^2 - p^2/E^2}} \quad (2)$$

The decay angle distribution as a function of signed  $p_T$  is shown in Fig. 3. After the decay angle cuts, an invariant mass is calculated with the muon daughter assumption. Therefore, the invariant mass distribution has a peak at kaon mass for  $K \rightarrow \mu\nu$  and another peak below kaon mass for  $K \rightarrow \pi\pi^0$  as shown in Fig. 4.

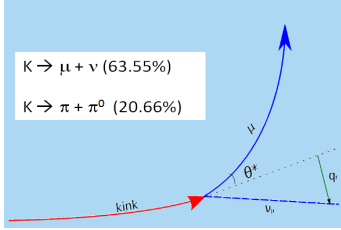


Figure 2. Kink kaon decays

Contamination is estimated by counting the entries in the side band area of the two-dimensional plots on invariant mass and  $q_T$  and by the TPC  $dE/dx$  distribution. It is confirmed to be less than 7%.

Figure 5 shows the comparison between the elliptic flow of the TOF-TPC kaon,  $K_s^0$  and kink kaon. They reasonably agree, but still the TOF-TPC kaon  $v_2$  has a bit larger values.

## 5. Summary

The elliptic flow of the identified particles was measured in Pb-Pb collisions at LHC energy and we found a larger mass splitting in  $v_2$  at the low  $p_T$  region than observed at RHIC top energy.

## References

- [1] K. H. Ackermann [STAR Collaboration], Phys. Rev. Lett. **86**, 402-407 (2001).

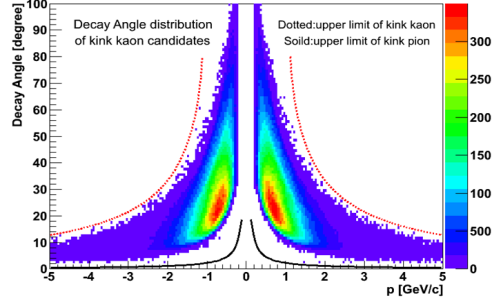


Figure 3. Decay angle distributions

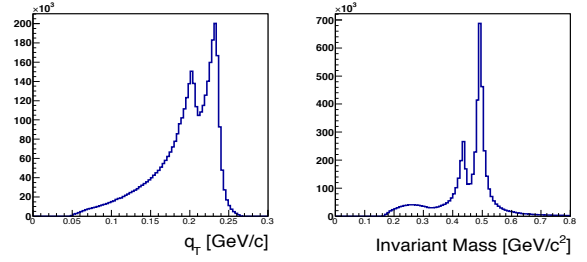


Figure 4.  $q_T$  and invariant mass distributions, two peaks correspond to the two decay mode.

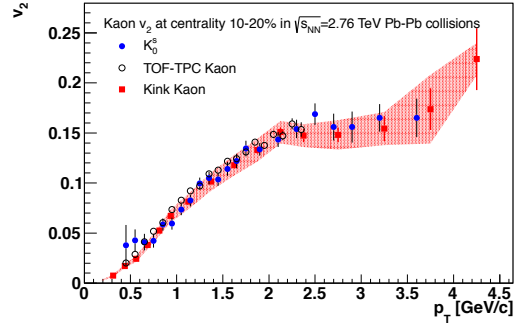


Figure 5. The  $p_T$  differential elliptic flow  $v_2$  of Kaon at centrality 10-20%

- [2] C. Shen, U. Heinz, P. Huovinen, H. Song, Phys. Rev. **C84**, 044903 (2011).
- [3] S. A. Voloshin, A. M. Poskanzer, R. Snellings, arXiv:0809.2949 [nucl-ex].
- [4] F. Noferini et al. [ALICE Collaboration], arXiv:1212.1292 [nucl-ex].
- [5] K. Aamodt et al. [ALICE Collaboration], Eur. Phys. J. C **71**(6), 1655 (2011).

# Measurements of $\pi^0$ with respect to reaction plane in $\sqrt{s_{NN}} = 2.76$ TeV Pb+Pb collisions at LHC-ALICE

T. Tsuji, H. Hamagaki, T. Gunji, H. Torii, for the ALICE collaboration

*Center for Nuclear Study, Graduate School of Science, University of Tokyo*

## 1. Introduction

It has been observed in central Pb+Pb collisions at ( $\sqrt{s_{NN}} = 2.76$  TeV at Large Hadron Collider (LHC) in CERN that the yield of charged particles at high transverse momentum ( $p_T$ ) is strongly suppressed compared to the expected yield from  $p+p$  collisions assuming the scaling with the number of binary collisions. This suppression is attributed to the energy loss of hard scattered partons within quark-gluon plasma (QGP) created in heavy ion collisions. This phenomenon is called as jet quenching. A useful way to quantify this suppression of high- $p_T$  hadrons is to introduce the nuclear modification factor ( $R_{AA}$ ) where the  $p+p$  cross section is scaled by the thickness function  $\langle T_{AA} \rangle$  of the two nuclei

$$R_{AA}(p_T) = \frac{1}{\langle T_{AA} \rangle} \frac{(1/N_{AA}^{evt})d^2N_{AA}/dp_T dy}{d^2\sigma_{pp}/dp_T dy}.$$

Experimental data can be well reproduced by multiple models with different approaches that calculate the energy lost by the hard scattered partons as they traverse the dense medium. To discriminate among these models we need to increase our experimental control of the path length  $L$ , since the energy lost by a high- $p_T$  parton increases rapidly with the distance traveled through the medium. A quadratic dependence on the path length is predicted for a static medium if the dominant energy-loss mechanism is the bremsstrahlung radiation of gluons surviving the destructive interference caused by multiple scattering [1]. For an expanding plasma the quadratic increase should be moderated to a linear dependence [2]. Thus, the measurement of the energy loss with respect to the path length is expected to enable us to obtain the detail information about the mechanism of the parton energy loss.

While dihadron correlation measurements are a successful approach to constrain  $L$  of the parton in the medium [3], the single particle observable  $R_{AA}$  typically has smaller statistical errors and higher  $p_T$  reach. In addition, if  $R_{AA}$  is measured as a function of the azimuthal angle with respect to the event plane of the collision, the average path length  $L$  can be constrained. In all but the most central ion-ion collisions, the overlap region of the nuclei is not azimuthally isotropic. The average distance the parton traverses before emerging and fragmenting varies as a function of the angle with respect to the event plane. Therefore, differential observable  $R_{AA}(\Delta\phi)$  directly probes the path length dependence of the energy loss.

The  $R_{AA}(p_T, cent, \Delta\phi)$  with respect to the azimuthal angle is factorized as,

$$R_{AA}(p_T, cent, \Delta\phi) = F(\Delta\phi, p_T) \cdot R_{AA}(p_T, cent),$$

where  $F(\Delta\phi, p_T)$  is ratio of the relative yield given as,

$$F(\Delta\phi, p_T) = \frac{N(\Delta\phi, p_T)}{\int d\phi N(\Delta\phi, p_T)},$$

where  $N(\Delta\phi, p_T)$  can be expressed in terms of a Fourier expansion with  $\Delta\phi$ .

$$N(\Delta\phi, p_T) \propto 1 + 2 \sum_{n=1}^{\infty} (v_n \cos(n\Delta\phi)),$$

where  $v_n$  is the magnitude of the harmonics of n-th order. The second harmonics,  $v_2$ , represents the strength of elliptic azimuthal anisotropy. The anisotropy  $v_2$  at low  $p_T$  is created by the collective flow, which is an origin of the background in measuring the  $R_{AA}(p_T, \Delta\phi)$  for investigating the energy loss.

## 2. Basic performance of detectors

Energy loss mechanism is studied with  $\pi^0$  for a wide momentum range using the photon spectrometer (PHOS) at the ALICE experiment. The present PHOS detector consists of three modules installed at a distance of 4.60 m from the interaction point. PHOS covers the acceptance of  $\phi = 260^\circ - 320^\circ$  in azimuthal angle and  $|\eta| < 0.12$  in pseudorapidity. Each module has 3584 detection channels in a matrix of  $64 \times 56$  cells. Each detection channel consists of a lead tungsten,  $\text{PbWO}_4$ , crystal of  $2.2 \times 2.2 \text{ cm}^2$  cross section and 18 cm length, coupled to an avalanche photo diode and a low-noise charge-sensitive preamplifier. PHOS operates at a temperature of  $-25^\circ \text{C}$  at which the light yield of the  $\text{PbWO}_4$  crystal is increased by about a factor 3 compared to room temperature. PHOS was calibrated by equalizing mean deposited energies in each channel using events with pp collisions [4].

Event plane is defined by V0C detector, which is a scintillation detector and covers from  $-3.7$  to  $-1.7$  in pseudo rapidity. The V0C is fixed at the front face of the front absorber, 90 cm from the vertex. This detector is segmented into 32 elementary counters distributed in four rings. Each ring covers 0.4 - 0.6 unit of pseudo-rapidity. The rings are divided into eight sectors of  $45^\circ$ . The elementary counter consists of scintillator material with embedded WaveLength Shifting (WLS) fibres. The light from the WLS is collected by clear fibers and transported to PhotoMultiplier (PM) installed at 3 - 5 m from the detectors, inside the L3 magnet [4].

Figure 1 (left) shows PHOS cluster multiplicity. There is expected multiplicity correlation between V0 detectors and PHOS. Figure 1 (right) shows PHOS trigger efficiency. PHOS trigger efficiency is more than 80% for photons with energies larger than 3 GeV/c in two PHOS module. On the other hand, the efficiency of 3rd of PHOS has loose curve.  $\pi^0$  can be identified at high  $p_T$  region using PHOS trigger from this figure.

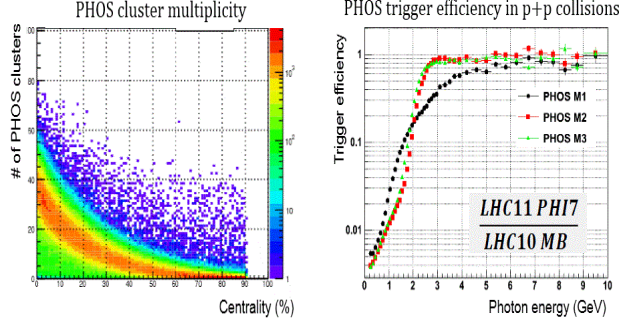


Figure 1. Left: Correlation between the number of PHOS clusters and centrality. Right: Trigger efficiency in p+p collisions as a function of  $p_T$  in each module.

If PHOS trigger is used, the number of events is 0.9M, which correspond to about 145M using minimum bias trigger. Therefore, analysis on PHOS triggered data has an advantage over that on minimum bias triggered data in identifying  $\pi^0$  in high  $p_T$  region.

### 3. Estimation of $\pi^0$ $v_2$ statistical errors

$\pi^0$   $v_2$  is extracted with  $dN/d\phi$  method. In this method,  $v_2$  is obtained by fitting the azimuthal angular distribution of  $\pi^0$  with

$$N(\Delta\phi, p_T) = N(1 + 2v_2 \cos(2\Delta\phi)).$$

$\pi^0$  are reconstructed using invariant mass with reconstructed energy by PHOS. Figure 2 shows the invariant

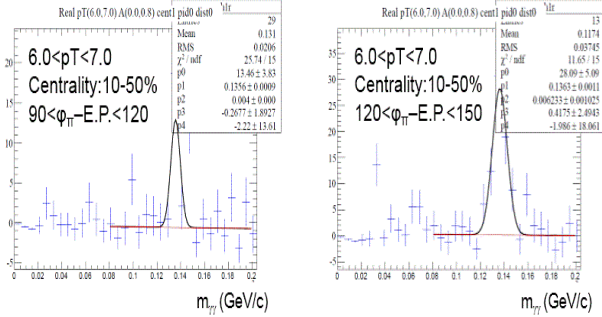


Figure 2. Invariant mass distribution with  $p_T = 6 - 7$  GeV/c and centrality = 10% - 50%. Left:  $\Delta\phi = 90^\circ - 120^\circ$ . Right:  $\Delta\phi = 120^\circ - 150^\circ$ .

mass distribution with  $p_T = 6 - 7$  GeV/c and centrality = 10% - 50%. Figure 2 (left) and Fig. 2 (right) show distribution with  $\Delta\phi = 90^\circ - 120^\circ$  and  $\Delta\phi = 120^\circ - 150^\circ$ , respectively. In these plots, the number of  $\pi^0$  is confirmed to depend on the azimuthal angle from the event plane. Calculations of  $\pi^0 v_2$  are ongoing.

Finally, the statistical errors in  $\pi^0 v_2$  was estimated. At first,  $\pi^0$  was identified up to  $p_T = 40$  GeV/c by PHOS with no division of angle. A statistical error of  $v_2$  is inversely proportional to the one-half power of twice as much as the number of events. Figure 3 shows  $v_2$  values as a function of  $p_T$ . Square points and circle points show  $v_2$  values of charged pion and charged particle, respectively. In this figure, estimated amplitude of statistical errors from half data of all PHOS triggered events in 2011 is shown as square bars. In these plots, mean values of  $\pi^0 v_2$  are conformed to those of

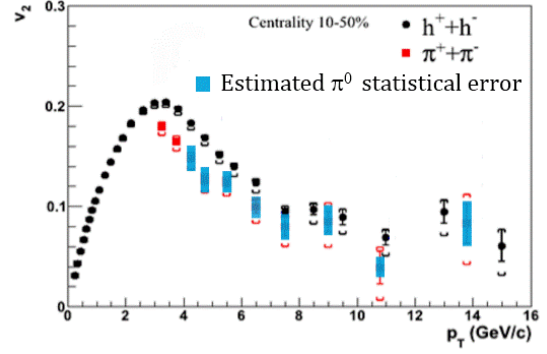


Figure 3.  $v_2$  values as a function of  $p_T$ . Square points and circle points show  $v_2$  values of charged pion and charged particle, respectively. Square bars shows estimated amplitude of statistical errors from half data of all PHOS triggered events in 2011.

charged pion  $v_2$ . Therefore, statistical errors of  $\pi^0 v_2$  are comparable in size to that of charged pion in 2010 run data.

### 4. Summary and Outlook

Jet quenching is sensitive to the density and path length of QGP. Study of dependencies of  $R_{AA}$  on path length and azimuthal angle has been started with the photon spectrometer (PHOS) at the ALICE experiment. Analysis with PHOS triggered data is advantaged relative to that with minimum bias triggered data finding  $\pi^0$  in high  $p_T$  region.  $\pi^0 v_2$  is extracted with  $dN/d\phi$  method and calculations of  $\pi^0 v_2$  are ongoing. Estimated statistical errors of  $\pi^0 v_2$  are comparable in size to that of charged pion in 2010 run data.

### References

- [1] A. Majumber, J. Phys. G: Nucl. Part. Phys. **34** (2007) S377.
- [2] M. Gyulassy, P. Levai and I. Vitev, Phys. Lett. **B538** (2002) 282.
- [3] A. Adare *et al.* (PHENIX Collaboration), Phys. Rev. **C80** (2009) 024908.
- [4] F Carminati *et al.* (ALICE Collaboration), J. Phys. G: Nucl. Part. Phys. **30** (2004) 1517.

# Measurement of $J/\psi$ photoproduction in ultra-peripheral Au+Au collisions at $\sqrt{s_{NN}}=200\text{GeV}$ using the PHENIX detector

A. Takahara, H. Hamagaki, T. Gunji, Z. Conesa del Valle<sup>a</sup>, Y. Akiba<sup>b</sup> M. Chiu<sup>e</sup>,  
J. Nystrand<sup>d</sup>, S. White<sup>e</sup>, K. Skjerdal<sup>d</sup>, E. T. Atomssa<sup>c</sup>

*Center for Nuclear Study, Graduate School of Science, University of Tokyo*  
<sup>a</sup>*CERN*

<sup>b</sup>*RIKEN BNL*

<sup>c</sup>*Stony Brook University*

<sup>d</sup>*Department of Physics, Lund University*

<sup>e</sup>*Brookhaven National Laboratory*

## 1. Introduction

We present the measurements of the photoproduction of  $J/\psi$  in ultra-peripheral Au+Au collisions at  $\sqrt{s_{NN}} = 200$  GeV at RHIC. An Ultra-Peripheral Collision (UPC) is a collision in which impact parameter is greater than the sum of nuclear radii. Measurement of  $J/\psi$  in UPC serves as a considerable role for determining gluon density in nuclei at small Bjorken  $x(\sim 0.01)$ , where the gluon density is expected to be suppressed due to gluon shadowing effect and has not been constrained by theoretical calculations [1, 2, 3]. PHENIX has measured integrated cross section of  $J/\psi$  in UPC in 2004 [4]. However, due to small statistics, it was very difficult to quantitatively discuss the gluon distribution in Au nuclei. In 2007 and 2010, PHENIX collected integrated luminosity of  $527.45 \pm 23 \mu\text{b}^{-1}$  and  $1390. \pm 37 \mu\text{b}^{-1}$  in Au+Au collisions, which corresponds to 3 and 9 times larger statistics compared to in 2004. Measurement of  $J/\psi$  photoproduction in UPC as a function of transverse momentum  $p_T$  and rapidity  $y$  has been done by using data taken in 2007 and 2010.

## 2. Data analysis

The definition of central UPC trigger is at least 1 neutron hit at one of Zero Degree Calorimeter(ZDC), no hit at both of Beam-Beam Counters, and hit at the EMCAL with energy of above 1 GeV. Here, the reason that ZDC trigger was included is to enhance the purity of the UPC trigger over the BBC and EMCAL triggers. The definition of UPC trigger at forward rapidity is 1 or more neutron detection at both sides of ZDC, no hit on BBC and muon candidate measured by the muon spectrometer. The reason of neutron tagging by both ZDCs is to calculate the collisions vertex in beam going direction. In the offline, the events, which has only two electron and muon tracks in central and forward rapidity, are selected additionally. Figure 1, 2, and 3 show invariant mass spectra of dielectrons in central rapidity and dimuons in positive and negative rapidities. The number of measured  $J/\psi$  is corrected by the detection efficiency, trigger efficiency, and integrated luminosity to extract the invariant cross section. Since BBC cannot detect 7% of most-peripheral collisions, contamination from most peripheral events in the UPC events was estimated. Figure 4 and 5 show the comparison of the number of reconstructed tracks distributions at central rapidity in UPC events and  $p-p$  collisions, where the event has dielectron and dimuon pair with the invariant mass from 2.7 to 3.5  $\text{GeV}/c^2$ . Those fig-

ures show even number of collision =1 limit, almost 2.7~3.5  $\text{GeV}/c^2$  dilepton events have 1 or more additional tracks. Most peripheral  $J/\psi$  contamination for dielectron was estimated to be 0 in UPC events for central arm analysis and 3 in UPC events for forward rapidity analysis from 0 additional tracks events per 1 or more additional tracks ratio of those distributions.

Figure 6 shows the preliminary results of the  $p_T$  distribution of  $J/\psi$  cross section in UPC, where circle, triangle and square wave correspond to the cross section at mid-rapidity with one neutron tagged by ZDC,  $-2.2 < y < -1.2$  and  $1.2 < y < 2.2$  with two neutron tagged at both sides of ZDC, respectively. From Fig.7, cross section at mid-rapidity in low  $p_T$  is very large compared to that at forward-rapidity. This is due to the dominance of coherent  $J/\psi$  production at low  $p_T$  in mid-rapidity, while incoherent production is dominated at forward rapidity. The upper limit of integrated cross section for coherent  $J/\psi$  production was extracted to be  $46.7 \pm 13 \pm 15 \mu\text{b}$  by integrating the cross-section from 0 to 0.4  $\text{GeV}/c$ . Since the cross

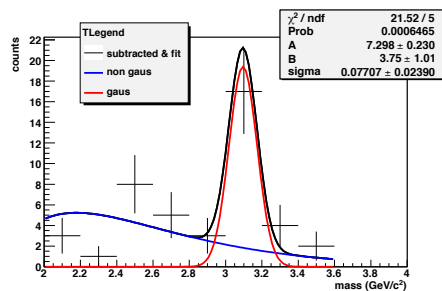


Figure 1. 2007 central arm (dielectron) invariant mass yields.

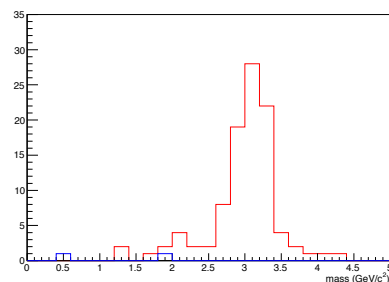


Figure 2. 2010 North arm (dimuon) invariant mass yields.  
2010 South arm (dimuon) invariant mass yields.

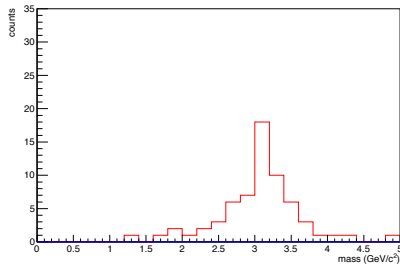


Figure 3. 2010 South arm (dimuon) invariant mass yields.

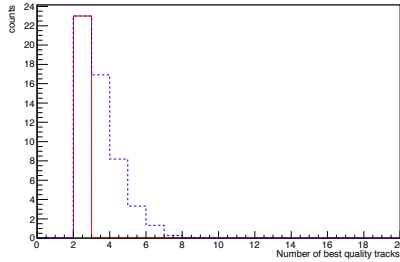


Figure 4. comparison between multiplicity distribution for central rapidity in UPC and p+p(ncoll=1,dot line) collisions with dielectron with the invariant mass between 2.7 and 3.5  $\text{GeV}/c^2$

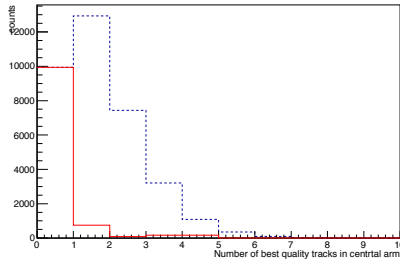


Figure 5. comparison between multiplicity distribution for central rapidity in UPC and p+p(ncoll=1,dot line) collisions with dimuon with the invariant mass between 2.7 and 3.5  $\text{GeV}/c^2$

section without any nuclear effects such as gluon shadowing is expected to be  $118\mu\text{b}$  [5]. Suppression of the gluon density at small-x ( $x=0.01$ ) is naively the order of  $\sqrt{(46.7/118)} = 0.6$ .

Figure 7 shows the cross section as a function of  $y$ , where both side neutrons are tagged. The comparison with the theoretical calculations is underway.

### 3. Summary and Outlook

Measurement of  $J/\psi$  in UPC has been performed by using 2007 and 2010 data. From the cross section as a function of  $p_T$ , the coherent production of  $J/\psi$  can be seen and integrated cross section is suppressed by a factor of 1.5 compared to the value without any nuclear effects. Further studies for both neutron tagging and theoretical understanding are on going.

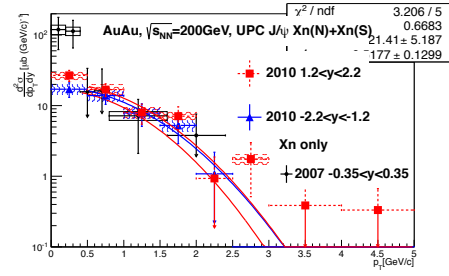


Figure 6. PHENIX 2010 dimuon (tringle and square) and 2007 dielectron(circle) UPC  $J/\psi$   $\frac{d^2\sigma}{dp_T dy}$ . Dielectron distribution has significant significant entries in low  $p_T$ , which cannot be seen at forward rapidity.

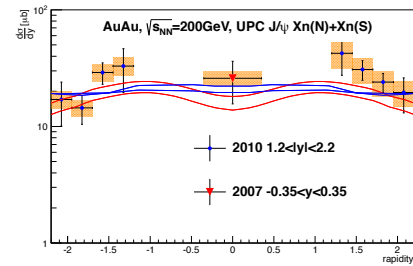


Figure 7. PHENIX 2010 RUN UPC  $J/\psi$   $\frac{d\sigma}{dy}$  distribution

### References

- [1] G. Baur, K. Hencken, D. Trautmann, S. Sadovsky, and Y. Kharlov: Phys. Rept. B, 359 (2002).
- [2] C. A. Bertulani, and S. R. Klein, J. Nystrand, Ann. Rev. Nucl. Part. Sci. B, 271 (2005).
- [3] A. Baltz et al.: Phys. Rept. B 171 (2008).
- [4] S. Afanasiev PHENIX Collaboration: Phys. Lett. B 321(2009).
- [5] A. L. Ayala Filho, V. P. Goncalves, and M. T. Griep Phys. Rev. C 78, 044904 (2008) G. Baur, K

# Neutral pion and $\eta$ meson production in proton-proton collisions at $\sqrt{s} = 0.9$ TeV and $\sqrt{s} = 7$ TeV

H. Torii for the ALICE Collaboration

Center for Nuclear Study, Graduate School of Science, University of Tokyo

Hadron production measurements in proton-proton collisions at the Large Hadron Collider (LHC) energies open a new domain in particle physics, which allows validation of the predictive power of Quantum Chromo Dynamics (QCD). A quantitative description of hard processes is provided by perturbative QCD (pQCD) supplemented with parton distribution functions (PDF)  $f(x)$  and fragmentation functions (FF)  $D(z)$ . Due to the higher collision energy at the LHC, the PDF and FF can be probed at lower values of  $x$  and  $z$ , respectively, than in previous experiments. Such measurements can provide further constraints on these functions, which are crucial for pQCD predictions for LHC energies. Furthermore, while pion production at the Relativistic Heavy Ion Collider (RHIC) is considered to be dominated by gluon fragmentation only for  $p_t < 8$  GeV/c, at LHC energies it should remain dominant for  $p_t < 100$  GeV/c [1,2]. Here, the measurement of the  $\pi^0$  and  $\eta$  at LHC energies provides constraints on the gluon to pion fragmentation in a new energy regime.

The proton-proton collision data used in this analysis were collected by the ALICE experiment in 2010 with the minimum bias trigger [3]. This trigger required the crossing of two filled bunches and a signal in at least one of the two SPD [4] pixel layers or in one of the VZERO [5] counters. An offline selection based on time and amplitude signals of them was applied to reject beam-induced and noise background. Pileup collision events were identified imposing a criterion based on multiple primary vertices reconstructed with the SPD detector, and removed from the further analysis. The cross sections for the minimum bias trigger have been calculated from other measured cross sections at the same energies with appropriate scaling factors and from a Van-der-Meer scan [6].

Neutral pions and  $\eta$  mesons are measured in ALICE via the two-photon decay channel. The photons are detected with two methods in two independent subsystems, with the Photon Spectrometer (PHOS) [7] and with the photon conversion method (PCM) in the central tracking system employing the Inner Tracking System (ITS) [4] and the Time Projection Chamber (TPC) [8]. The latter reconstructs and identifies photons converted to  $e^+e^-$  pairs in the material of the inner detectors. Neutral pions and  $\eta$  mesons are reconstructed as excess yields, visible as peaks at their respective rest mass, above the combinatorial background in the two-photon invariant mass spectrum. Invariant mass spectra demonstrating the  $\pi^0$  and  $\eta$  mesons peak in some selected  $p_t$  slices are shown in Fig.1. The background is determined by mixing photon pairs from different events and is normalized to the same event background at the right side of the meson peaks. A residual correlated background is further subtracted using a linear or second order polynomial

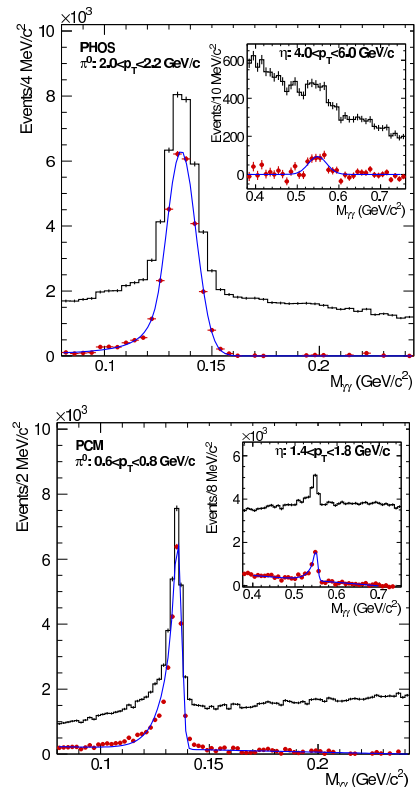


Figure 1. Invariant mass spectra in selected  $p_t$  slices in PHOS (top) and PCM (bottom) in the  $\pi^0$  and  $\eta$  meson mass regions. The histogram and the bullets show the data before and after background subtraction, respectively. The curve is a fit to the invariant mass spectrum after background subtraction.

fit. The invariant mass spectrum after background subtraction was fitted to obtain the  $\pi^0$  and  $\eta$  peak parameters. We vary the normalization and integration windows to estimate the related systematic uncertainties.

The reconstruction efficiency and acceptance are calculated in Monte Carlo simulations tuned to reproduce the detector response. In the PHOS case, the tuning included a 4.5% energy non-linearity observed in real data at  $E < 1$  GeV and was not reproduced by the GEANT simulations and an additional 6% channel-by-channel decalibration. In the PCM case, an additional smearing given by  $\sigma = \sqrt{\sigma_0^2 + \sigma_1^2 \cdot p^2}$  with  $\sigma_0 = 0.011$  GeV/c and  $\sigma_1 = 0.007$  was necessary to reproduce the measured width of the  $\pi^0$  peak. PYTHIA [9], PHOJET [10], and a single particle event generator were used as input. The small photon conversion probability of about 8.5%, compensated by the large TPC acceptance, at  $p_t > 1$  GeV/c and decreases at lower  $p_t$  due to the decrease of the efficiency of soft electron reconstruction and conversion probability. In the PHOS case, the acceptance is zero for  $p_t < 0.4$  GeV/c, increases with  $p_t$ , and saturates at about  $2.0 \times 10^{-2}$

at  $p_t > 15$  GeV/c. At high  $p_t > 25$  GeV/c the efficiency decreases due to cluster merging. The combined spectrum is calculated as a weighted average using statistical and systematic errors of the individual analyses [11]. The combined production cross sections are shown in Fig. 2 a) together with fitting results with the Tsallis function [12].

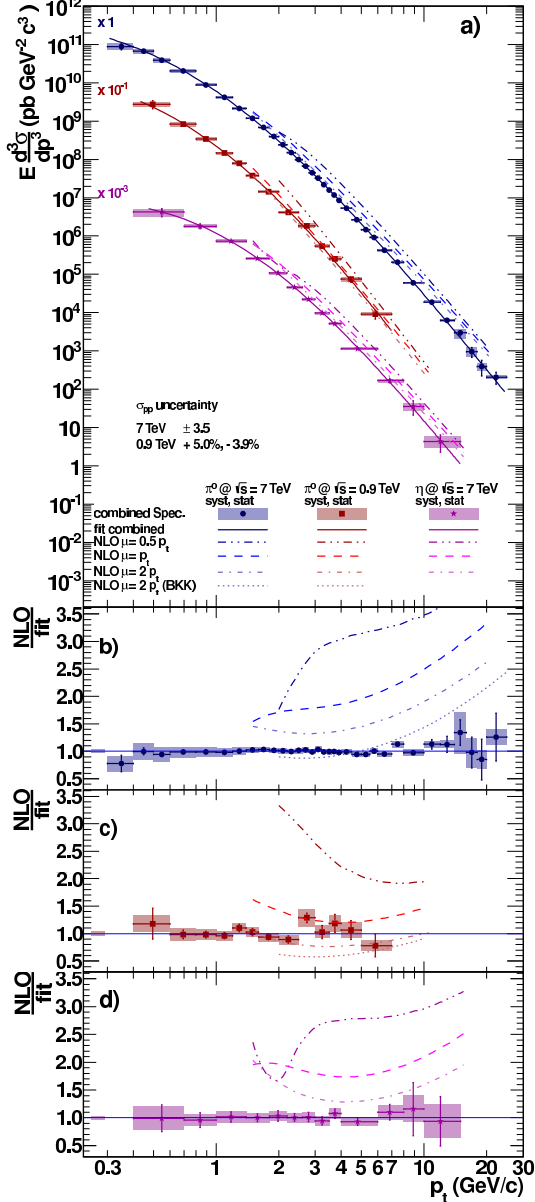


Figure 2. Differential invariant cross section of  $\pi^0$  production in pp collisions at  $\sqrt{s} = 7$  TeV (circles) and 0.9 TeV (squares) and of  $\eta$  meson production at  $\sqrt{s} = 7$  TeV (stars) and their ratios to fitting results with the Tsallis function [12]. The lines and the boxes represent the statistical and systematic error of the combined measurement, respectively. The uncertainty on the pp inelastic cross section is not included and is represented by the full boxes at unity. NLO pQCD calculations using the CTEQ6M5 PDF and the DSS (AESS for  $\eta$  mesons) FF for three scales  $\mu = 0.5p_t$ ,  $1p_t$  and  $2p_t$  are shown.

We compare our results with Next-to-Leading Order (NLO) pQCD calculations using the PDF CTEQ6M5 and DSS  $\pi^0$  [13], BKK  $\pi^0$  [14] and AESS

$\eta$  [15] NLO fragmentation functions, see Fig. 2 a). The data and NLO predictions are compared via a ratio with the fit to the measured cross section. This is shown in the bottom panels b), c) and d) in Fig. 2. In the NLO calculations the factorization, renormalization and fragmentation scales are chosen to have the same value given by  $\mu$ . At  $\sqrt{s} = 0.9$  TeV the NLO calculations at  $\mu = 1p_t$  describe the measured  $\pi^0$  data well, while at  $\sqrt{s} = 7$  TeV the higher scale ( $\mu = 2p_t$ ) and a different set of fragmentation functions are required for a description of the data. However, the latter parameter set does not provide a good description of the low energy data. In any case, the NLO pQCD calculations show a harder slope compared to the measured results. Using the INCNLO program [16], we tested different parton distribution functions (CTEQ5M, CTEQ6M, MRS99) and different fragmentation functions (BKK, KKP, DSS) and found a similar result: pQCD predicts harder slopes, and variation of PDFs and FFs does not change the shape. A similar trend is observed for the  $\eta$  meson, although the discrepancy is less significant due to the larger error bars and smaller  $p_t$  reach.

## References

- [1] R. Sassot, P. Zurita, M. Stratmann, Phys. Rev. **D82** (2010) 074011. [arXiv:1008.0540 [hep-ph]].
- [2] P. Chiappetta, et al., Nucl. Phys. B **412** (1994) 3 [arXiv:hep-ph/9301254].
- [3] K. Aamodt *et al.* [ALICE Collaboration], Eur. Phys. J. **C68** (2010) 345-354. [arXiv:1004.3514 [hep-ex]].
- [4] K. Aamodt *et al.* [ALICE Collaboration], JINST **5** (2010) P03003. [arXiv:1001.0502 [physics.ins-det]].
- [5] P. Cortese *et al.* [ALICE collaboration], CERN-LHCC-2004-025, <http://cdsweb.cern.ch/record/781854>.
- [6] K. Aamodt, *et al.* [ALICE collaboration], to be published.
- [7] G. Dellacasa *et al.* [ALICE Collaboration], CERN/LHCC 99-4, 5 March 1999.
- [8] J. Alme, et al., Nucl. Instrum. Meth. **A622** (2010) 316-367. [arXiv:1001.1950 [physics.ins-det]].
- [9] T. Sjöstrand, S. Mrenna, P. Z. Skands, JHEP **0605** (2006) 026. [hep-ph/0603175].
- [10] R. Engel, J. Ranft, S. Roesler, Phys. Rev. **D52** (1995) 1459-1468. [hep-ph/9502319].
- [11] K. Nakamura *et al.*, J. Phys. **G37** (2010) 075021.
- [12] C. Tsallis, J. Statist. Phys. **52** (1988) 479-487.
- [13] D. de Florian, R. Sassot, M. Stratmann, Phys. Rev. **D75** (2007) 114010. [hep-ph/0703242 [HEP-PH]].
- [14] J. Binnewies, B. A. Kniehl and G. Kramer, Z. Phys. **C 65** (1995) 471 [arXiv:hep-ph/9407347].
- [15] C. A. Aidala, et al., Phys. Rev. **D83** (2011) 034002. [arXiv:1009.6145 [hep-ph]].
- [16] P. Aurenche, et al., Eur. Phys. J. **C13** (2000) 347-355. [arXiv:hep-ph/9910252 [hep-ph]].

# Measurement of Di-electrons in Pb-Pb Collisions at LHC-ALICE

T. Gunji for the ALICE Collaboration

Center for Nuclear Study, Graduate School of Science, University of Tokyo, Japan

## 1. Introduction

The Large Hadron Collider (LHC) started its operation since 2010 and the ALICE experiment, which is dedicated to high energy heavy-ion collisions, has been successfully commissioned [1]. During the first two heavy-ion runs, the ALICE experiment recorded about  $10 \mu\text{b}^{-1}$  and  $100 \mu\text{b}^{-1}$  of integrated luminosity with Pb-Pb collisions at the center of mass energy per nucleon pair of 2.76 TeV in the fall of 2010 and 2011, respectively.

Di-electron production in heavy-ion collisions provide valuable information on the properties of the hot and dense QCD medium. In the low mass region (below  $1 \text{ GeV}/c^2$ ), di-electron production is expected to be sensitive to the in-medium modification of the spectral function of vector mesons ( $\rho$ ,  $\phi$ , and  $\omega$ ) [2]. Measurements of the line shape of the invariant mass and the yield of the low mass vector mesons reveal some insights of the chiral symmetry restoration. In this mass range and relatively high pair  $p_T$  region ( $p_T \geq m_{ee}$ ), di-electrons are dominated by the quasi-real virtual photons produced by a higher order QED correction to the real photon emission process. Therefore, their yield and transverse momentum distribution are related to the photon production in heavy-ion collisions (thermal photons and prompt pQCD photons).

A large enhancement of the di-electron yield in the low mass region in heavy ion collisions has been discovered by the CERES experiment at the CERN SPS, the PHENIX and the STAR experiment at the BNL RHIC [5,6]. Moreover, enhanced yield above hadronic sources is observed in low mass region and relatively high  $p_T$  region [7]. Treating the enhancement as virtual photon emission from thermalized medium, the invariant yield of direct photon is deduced and the yield is in qualitative agreement with hydrodynamical models with initial temperatures of 300-600 MeV and formation times of 0.6-0.15 fm/c. It is highly required to measure the di-electron pairs in low mass region to study the properties of the medium and chiral symmetry restoration at the LHC energy, where the collision energy is 10 times larger than that at RHIC.

## 2. The ALICE detector

The ALICE detector is composed of central barrel, muon arm, and forward detectors. The central barrel covers the pseudo-rapidity of  $|\eta| \leq 0.9$  and  $2\pi$  in the azimuthal angle and is placed inside a large solenoidal magnet with a magnetic field of 0.5 T. It comprises an Inner Tracking System (ITS) of high spatial resolution silicon detectors, a cylindrical Time-Projection Chamber (TPC), and particle identification detectors of Transition Radiation Detector (TRD) and of Time-Of-Flight (TOF) detector. There are additional central detectors, non-covering  $2\pi$  azimuth, such as High Momentum Particle Identification with ring-imaging Cherenkov device (HMPID), a high energy-

resolution PHOTon Spectrometer (PHOS) and an ElectroMagnetic Calorimeter (EMCal). Forward detectors (VZERO, TZERO, FMD, ZDC, and PMD) are used for triggering, multiplicity measurements and centrality determination

## 3. Electron Identification

Electron identification has been performed with the combination of ITS+TPC+TOF and ITS+TPC+TOF+TRD+EMCal for low  $p_T$  ( $p_T \leq 1 \text{ GeV}/c$ ) and high  $p_T$ , respectively. It is required that an associated hit is found in the first ITS layer to minimize the contribution from photon conversions. Figure 1 and Figure 2 show the measured  $dE/dx$  in TPC without any TOF cuts and with the TOF cut for electrons ( $3\sigma$  of the TOF for electrons), respectively.

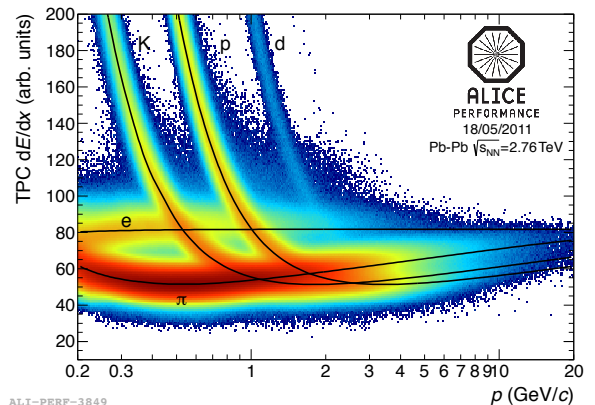


Figure 1. Specific energy loss in the TPC as a function of momentum with superimposed Bethe-Bloch lines for various particle species.

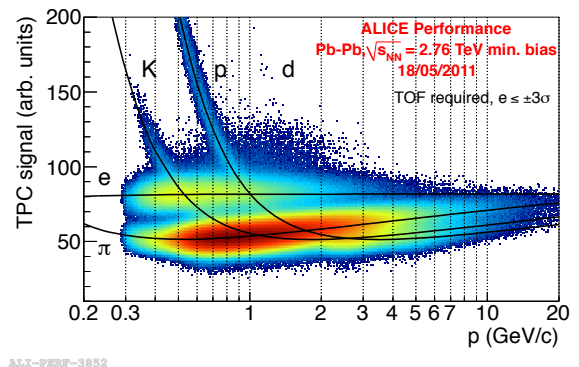
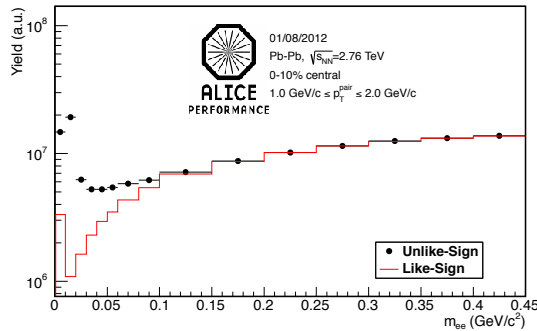


Figure 2. Specific energy loss in the TPC as a function of momentum with superimposed Bethe-Bloch lines for various particle species. This is after the  $\pm 3\sigma$  cut for electrons in the TOF, where the TOF condition is required.

It is seen that electrons with low  $p_T$  can be identified with the ITS+TPC+TOF cuts. From the  $dE/dx$  distributions, contamination of hadrons is lower than 2% below 0.5 GeV/c and 8% around 0.5 GeV/c and 1 GeV/c with  $-1.5 \leq \sigma_{dE/dx} \leq 3$  for electrons. For the electrons with higher  $p_T$ ,  $dE/dx$  and transition radiation measurement with TRD and energy-momentum matching with EMCal improve the purity of electron samples.

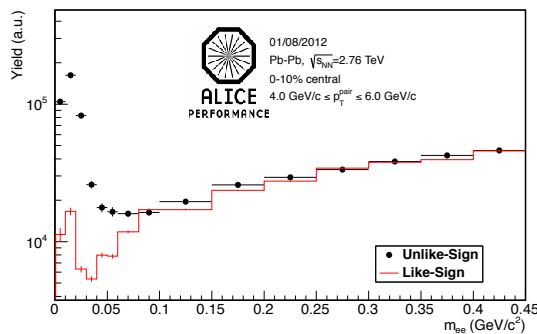
#### 4. Pair Analysis

After electron samples are selected with ITS+TPC+TOF cuts, invariant mass is calculated for each pair. For the moment, identification and rejection of the pairs from photon conversions have not been performed. Combinatorial background is estimated by like-sign pairs from same events as well as both the unlike-sign and like-sign pairs from mixed events. The difference in the acceptance between unlike-sign and like-sign pairs is estimated using the pairs from mixed events.



ALI-PERF-35225

Figure 3. Like-sign and Unlike-Sign distributions for di-electrons in central Pb+Pb event. Pair  $p_T$  is from 1 to 2 GeV/c.

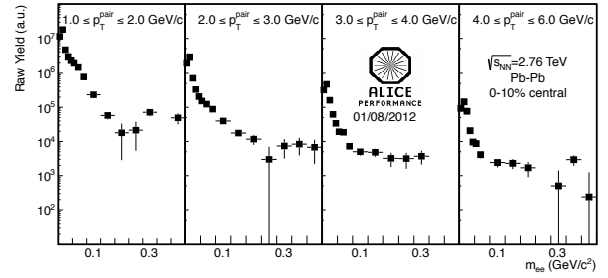


ALI-PERF-35237

Figure 4. Like-sign and Unlike-Sign distributions for di-electrons in central Pb+Pb event. Pair  $p_T$  is from 4 to 6 GeV/c.

Figure 3 and Figure 4 show the invariant mass distributions of unlike-sign pairs and like-sign pairs corrected by the different acceptance between unlike and like-sign pairs for the pair  $p_T$  of 1-2 GeV/c and 4-6 GeV/c, respectively. Strong peak in like-sign mass spectra around  $m_{ee} \sim 0$  GeV/c<sup>2</sup> is due to the correlated pairs from  $\pi^0$  double Dalitz decay and contam-

ination of very late conversions randomly associated with hits at inner detectors. The signal to noise ratio is larger than 1 for  $m_{ee} \leq 0.05$  GeV/c<sup>2</sup> and 0.01 for  $m_{ee} \geq 0.15$  GeV/c<sup>2</sup>. Figure 5 shows background subtracted invariant mass distributions for the pair  $p_T$  of 1-2, 2-3, 3-4, and 4-6 GeV/c, respectively. Further analysis such as background evaluation from correlated pairs, conversion rejection, and efficiency corrections are on going.



ALI-PERF-35221

Figure 5. Background subtracted signal in the low mass region in the di-electron channel.

#### 5. Summary and Outlook

The analysis of low mass di-electrons in Pb-Pb collisions at the ALICE has been started. First look at the invariant mass spectra of unlike-sign and like-sign pairs in same events and mixed events is performed. Further analysis will be done and thermodynamical properties of the medium will be discussed through the measurements of di-electrons.

#### References

- [1] ALICE Collaboration, Physics Performance Report Vol. 1 J. Phys. **G 30** (2003) 1517.
- [2] W. Liu, R. Rapp, Nucl. Phys. **A796**, (2007), 101; K. Dusling, I. Hid, Nucl. Phys. **A825**, (2009), 212; E. L. Bratkovskaya, W. Cassing, O. Lianna, Phys. Lett. **B670**, (2009), 428; G. E. Brown and M. Rho, Phys. Rev. Lett. **66**, (1991), 2720
- [3] R. Rapp, Phys. Rev. **C63**, (2001), 054907; C. M. Hung, E. V. Shuryak, Phys. Rev. **C 56**, (1997), 453; K. Gallmeister, B. Kampfer, and O. P. Pavlenko, Phys. Rev. **C 57**, (1998), 3276
- [4] T. Matsui and H. Satz, Phys. Lett. **B178**, (1986), 416
- [5] G. Agakichiev *et al.* (CERES collaboration), Phys. Rev. Lett. **75**, (1995), 1272
- [6] A. Adare *et al.*, (PHENIX collaboration), Phys. Rev. **C81**, (2010), 034911; J. Zhao *et al.*, (STAR Collaboration), arXiv:1106.6146
- [7] A. Adare *et al.*, (PHENIX collaboration), Phys. Rev. Lett. **104**, (2010), 132301

# Direct virtual photon measurement in $\sqrt{s} = 200$ GeV $p+p$ collisions at RHIC-PHENIX

Y.L. Yamaguchi, H. Hamagaki, Y. Akiba<sup>a</sup>, and T. Gunji, for the PHENIX collaboration

Center for Nuclear Study, Graduate School of Science, University of Tokyo

<sup>a</sup> RIKEN (The Institute of Physical and Chemical Research)

## 1. Introduction

Direct photons in  $p+p$ ,  $d+Au$  and  $Au+Au$  collisions have been successfully measured at RHIC with a wide  $p_T$  coverage through independent measurements of real and nearly-real virtual photons [1, 2, 3, 4]. The real photon measurement is statistically robust for  $p_T > 5$  GeV/ $c$ . At  $p_T < 5$  GeV/ $c$ , however, a finite energy resolution of an electromagnetic calorimeter precludes separation of the direct photon signal from a huge amount of background photons from hadron decays [3]. The key to measurements of the direct photon production at  $p_T < 5$  GeV/ $c$  is the use of virtual photons since the background of photons from  $\pi^0, \eta \rightarrow 2\gamma$  can be greatly reduced. For  $p_T < 2.5$  GeV/ $c$ , a clear enhanced yield of direct photons above the expectation from the  $p+p$  result with binary-collision scaling was observed in central  $Au+Au$  collisions, while the  $d+Au$  result is consistent with the binary-scaled  $p+p$  result within uncertainties [4]. This fact suggests the existence of an additional source producing direct photons other than initial state effects in  $Au+Au$  collisions [9].

A perturbative QCD (pQCD) calculation is not available due to a large ambiguity of the fragmentation function typically for  $p_T < 2 - 3$  GeV/ $c$ , where an excess of direct photons was observed for  $Au+Au$ . Therefore, only the measured  $p+p$  data can serve as a reference to the data for heavy ion collisions. The accuracy of the  $p+p$  data is crucial to discuss non-perturbative effects on direct photon production which can alter the direct photon spectrum compared to that for  $p+p$ . In this report, we present the latest result of direct photon measurement in  $\sqrt{s} = 200$  GeV  $p+p$  collisions for  $1 < p_T < 20$  GeV/ $c$ . The data taken in the Year-2006 RHIC run were combined with the previously published  $p+p$  data [1, 5].

## 2. Analysis

In this analysis,  $e^+e^-$  pairs with  $m_{ee} < 0.3$  GeV/ $c^2$  from internal photon conversions are detected by the two central arms of the PHENIX detector at midrapidity. It is quite important to separate signal  $e^+e^-$  pairs from pairs originating from hadron decays. Any process producing a real photon has an associated higher order process with a low mass  $e^+e^-$  pair via a virtual photon, and the relation between them can be expressed as [1, 6]

$$\frac{d^2 n_{ee}}{dm_{ee}} = \frac{2\alpha}{3\pi} \frac{1}{m_{ee}} \sqrt{1 - \frac{4m_e^2}{m_{ee}^2}} \left(1 + \frac{2m_e^2}{m_{ee}^2}\right) S(m_{ee}) dn_\gamma, \quad (1)$$

where  $\alpha$  is the fine structure constant and  $m_e, m_{ee}$  are the masses of the electron and the  $e^+e^-$  pair, respectively. A process dependent factor  $S$  is important because its mass dependence varies according to a production process. For internal conversions

*e.g.* gluon Compton scattering ( $q + g \rightarrow q + \gamma^*$ ),  $S$  approaches 1 as  $m_{ee} \rightarrow 0$  or  $m_{ee} \ll p_T$ . However, for Dalitz decays of hadrons [6]  $S$  is given by  $S(m_{ee}) = |F(m_{ee}^2)|^2 (1 - m_{ee}^2/m_h^2)^3$  which limits the production rate due to the finite mass of the parent hadron  $m_h$ . Here  $F(m_{ee}^2)$  denotes the form factor. Consequently, the contribution of internal conversions can be distinguished from hadron contaminations in the  $e^+e^-$  mass distribution by utilizing the difference in mass dependence of  $S$ . Practically,  $e^+e^-$  pairs are made from combinations between all electrons and positrons with  $p_T > 0.3$  GeV/ $c$  in an event, and then various background pairs arising from random combinations, material conversions, correlated background from double Dalitz decays of  $\pi^0, \eta$  and jet induced correlations are removed by analysis techniques [1]. Then, a two component function,  $f(m_{ee}) = (1 - r_\gamma) f_c(m_{ee}) + r_\gamma f_{dir}(m_{ee})$  is fitted to the  $e^+e^-$  mass distribution for  $0.10 < m_{ee} < 0.30$  GeV/ $c^2$  to determine the direct photon fraction denoted by  $r_\gamma$ . Here  $f_c(m_{ee}), f_{dir}(m_{ee})$  are the mass shapes of the hadronic cocktail and internal conversion direct photons, respectively. Figure 1 shows the  $e^+e^-$  mass distribution in

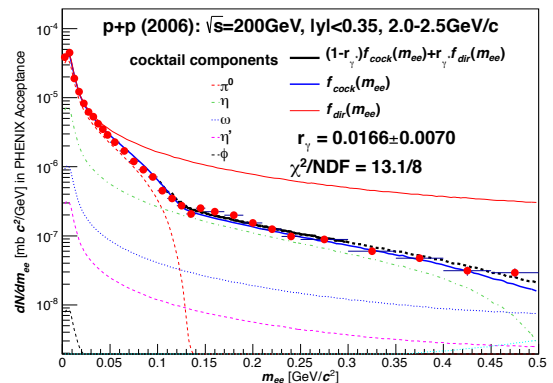


Figure 1. The  $e^+e^-$  mass distribution in  $p+p$  collisions for  $2.0 < p_T < 2.5$  GeV/ $c$  together with the two-component fit result.

$p+p$  collisions for  $2.0 < p_T < 2.5$  GeV/ $c$  together with the result of two-component fit shown with a thick solid line. The fit result extended for  $m_{ee} > 0.3$  GeV/ $c^2$ , shown as a dotted line, also well describe the data.

## 3. Results

The direct photon fraction in  $p+p$  collisions for  $1.0 < p_T < 5.0$  GeV/ $c$  is obtained, and the obtained result is combined with the published data [1]. Figure 2 shows the combined direct photon fractions as a function of  $p_T$ . The statistical and systematic uncertainties are shown by the bars and bands, respectively. Expectations from a NLO pQCD calculation [8] are also shown as curves with cutoff mass scale depen-

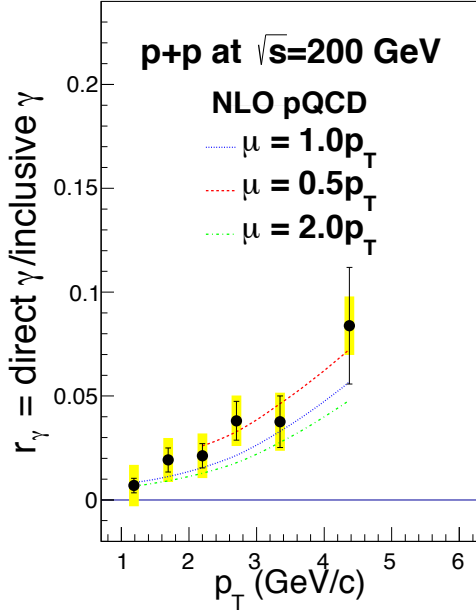


Figure 2. The combined direct photon fractions in  $p+p$  collisions for  $1.0 < p_T < 5.0$  GeV/ $c$ .

dence:  $\mu = 0.5p_T, 1.0p_T, 2.0p_T$ . The  $p+p$  data points are much improved statistically compared to the previously published data, especially above 3 GeV/ $c$  and the data are in good agreement with the NLO pQCD expectations.

The inclusive photon yield is determined from the yield of  $e^+e^-$  pairs for  $m_{ee} < 0.03$  GeV/ $c^2$  with the relation of  $\frac{d^2n_{ee}}{dm_{ee}} = \frac{2\alpha}{3\pi} \frac{1}{m_{ee}} dn_\gamma$ . Multiplying the direct photon fraction by the inclusive photon yield leads to the direct photon yield. Figure 3 shows the direct photon cross section in  $p+p$  collisions. The both results from virtual and real photon measurements are in agreement in the overlap region, and the real photon measurement extends to 20 GeV/ $c$ . The NLO pQCD calculations agree with the data for a wide  $p_T$  range, and show a preference for the choice  $\mu = 0.5p_T$  shown as a dash line. Unfortunately, the NLO pQCD calculation with a low scale is not available for  $p_T < 2.0$  GeV/ $c$ . Thus, an empirical parameterization inspired by a NLO pQCD formulation for  $p + p \rightarrow \gamma X$ ,

$$E \frac{d^3\sigma}{dp^3} = ap_T^{-(b+c \ln x_T)} (1 - x_T^2)^n, \quad (2)$$

is introduced [4]. Here  $a, b, c, n$  are free parameters and  $x_T = 2p_T/\sqrt{s}$ . The factor  $(1 - x_T^2)^n$  comes from the convolution of two parton distribution functions in colliding protons, and naturally leads to a drop of the cross section to 0 at  $x_T = 1$ . The fit is made for both virtual and real photon results simultaneously. The point-to-point uncertainty of the data is considered at the fit, and the quadratic sum of the fit uncertainty and  $p_T$ -correlated uncertainty of the data is assigned as the total fit uncertainty shown with the data over the fit. The fit describes the data very well for the entire  $p_T$  range within uncertainties as shown in the bottom panel of Fig. 3.

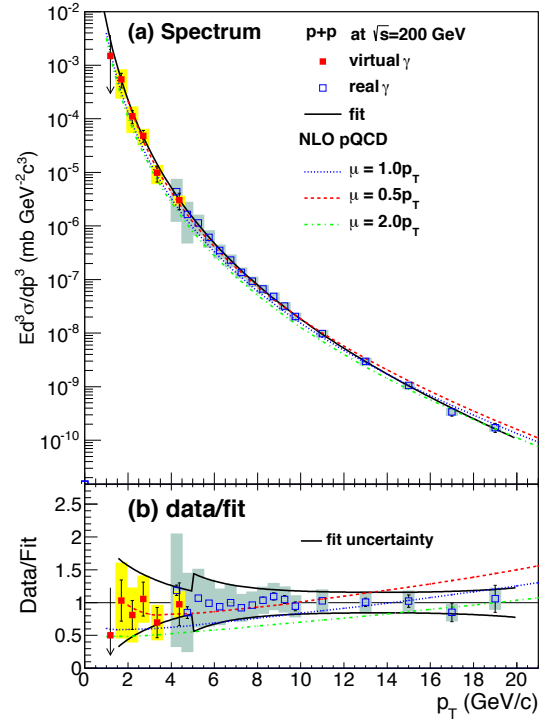


Figure 3. (a) The invariant cross section of the direct photon in  $p+p$  collisions. (b) The  $p+p$  data over the fit.

#### 4. Summary

Direct photons have been measured at  $1 < p_T < 5$  GeV/ $c$  for  $p+p$  collisions via the virtual photon analysis with the data taken in 2006 at the PHENIX experiment. The  $p+p$  spectrum has been much improved statistically by combining with the previously published data. The improved  $p+p$  data are parameterized by an empirical fit function inspired by a pQCD formulation. The fit describes the data very well for the entire  $p_T$  range. The result serves as a reference to the data for other collision systems.

#### References

- [1] A. Adare, *et al.*, Phys. Rev. Lett. **104**, 132301 (2010).
- [2] S.S. Adler, *et al.*, Phys. Rev. D**86**, 072008 (2012).
- [3] S.S. Adler, *et al.*, Phys. Rev. Lett. **109**, 152302 (2012).
- [4] A. Adare, *et al.*, arXiv:1208.1234 [nucl-ex] (2012).
- [5] S.S. Adler, *et al.*, Phys. Rev. Lett. **98**, 012002 (2007).
- [6] L.G. Landsberg, Phys. Rep. **128**, 301 (1985).
- [7] S.S. Adler, *et al.*, Phys. Rev. C**76**, 034904 (2007).
- [8] L.E. Gordon and W. Vogelsang, Phys. Rev. D**48**, 3136 (1993).
- [9] I. Vitev and B.W. Zhang, Phys. Lett. B**669**, 337 (2008).

# **Accelerator and Instrumentation**



# Development of the wide-dynamic range Front-end ASIC for the W+Si sampling Calorimeter

S. Hayashi, H. Hamagaki, T. Gunji, M. Tanaka<sup>a</sup>, and H. Ikeda<sup>b</sup>,

Center for Nuclear Study, Graduate School of Science, University of Tokyo

<sup>a</sup>KEK, Open-It

<sup>b</sup>JAXA, Open-It

## 1. Introduction

At ultra high energy hadron-hadron collisions, partonic structure inside proton and nuclei has an important role for the dynamics of collisions. Abundance of gluons inside proton is getting larger and larger with higher energy, but at some point, the abundance is expected to be saturated due to the balance of gluon fusion and gluon recombination (gluon saturation).

In order to study the gluon saturation, W+Si based sampling calorimeter (FOCAL) has been proposed as one of the upgrade plans of the LHC-ALICE experiment. FOCAL intends to measure prompt  $\gamma$ , neutral mesons and jets at forward rapidity ( $2.5 < \eta < 4.2$ ) at LHC-ALICE [2]. FOCAL is planned to be located at  $\sim 3.5$  m away from interaction point, covering  $2.5 \sim 4.2$  in  $\eta$  and  $2\pi$  in  $\phi$ .

Since the distance between  $2\gamma$  from  $\pi^0$  is quite small (2.5 mm for  $\pi_0$   $p_T \sim 50$  GeV), FOCAL needs to have a fine granularity. For this purpose, tungsten, which has small Moliere radius of 9.3mm, is used as an absorber and Si pads is used as a readout detector.

Figure 1 shows the longitudinal segmentation of FOCAL. FOCAL is composed of 3 longitudinal segments, which is composed of 7 layers of W with 3.5mm thickness each and 64 Si pads with  $1.1 \text{ cm} \times 1.1 \text{ cm}$  size of each pad. Si strip or pixel detector will be installed in the preshower stage to identify  $2\gamma$  from  $\pi_0$ .

FOCAL is assumed to measure both of MIP and  $\gamma$   $E \sim 500$  GeV, and then the front-end circuits for FOCAL are needed to cover a wide dynamic range. A good time response is also needed from the requirement of the trigger generation in LHC-ALICE. As one of the good candidates, the ASIC which consists of the preamplifiers with current conveyors is being developed. In this report, the current status of the development of front-end ASIC for FOCAL is reported.

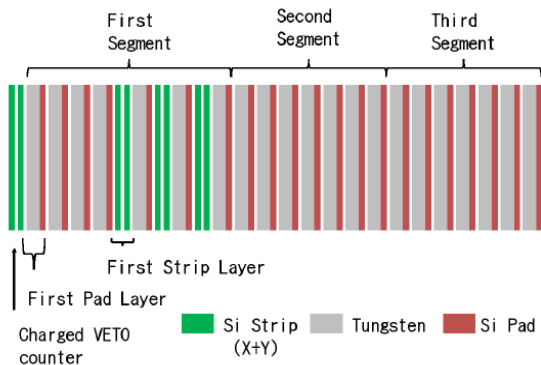


Figure 1. The longitudinal segmentation of FOCAL.

## 2. Requirement of Si pad readout

Parameter	Value
Dynamic range	50 fC - 200 pC
ENC	$< 3 \times 10^4 e^-$
Cross talk	$< 1 \%$
Trigger generation	$< 650$ ns from collisions
Number of channel	$\sim 25000$

Table 1. Requirement of front-end circuits for FOCAL

The signals from Si pads are summed up longitudinally in each segment. The capacitance of each Si pad is 25 -30 pF and the detector capacitance for each readout channel is about 200 pF. The main requirements for Si pad readout are summarized in Table 1.

In addition to the signal readout, FOCAL needs to provide a level 0 (L0) trigger. Due to the L0 requirement from the ALICE, FOCAL needs to issue the L0 trigger within 650nsec after the collisions. Therefore, the electronics should have a capability of the fast signal processing.

## 3. Design of front-end ASIC for FOCAL

Analog ASIC has been developed to cope with the requirements of the FOCAL readout. We employ current conveyor as a first stage of the amplifier since current amplifier has a good potential for the fast signal processing [4]. A wide dynamic range is achieved by implementing different gain for the mirrored current. Designing of ASICs has been done with the collaboration of OpenIT project [3].

Figure 2 shows the schematic of one readout channel of the ASIC. One chip has 6 readout channels. The ASIC contains current conveyors with 4 different gains, shapers, and analog memory cells (AMC). The shaper is a second order low pass filter with the peaking time of 250nsec. The AMC has 32 depth and is operated with 5MHz-10MHz writing rate.

Trigger signal is generated by summing up the mirrored current signal with 1/4 gain from 6 channels.

Expected performance with this ASIC has been investigated using HSPICE and TSPICE simulators. A current conveyor is constituted with input MOS and current mirror circuits. Naively, the input impedance is expressed as

$$Z_{in} = \frac{1}{\sqrt{4kI_{bias}}}, \quad (1)$$

where  $I_{bias}$  is the current of the input MOS and  $k = \frac{1}{2}\mu_0 C_{ox} W_0/L_0$ .  $C_{ox}$  is the oxide thickness of input MOS. Input impedance needs to be as small as possible, however, large bias current contributes to large

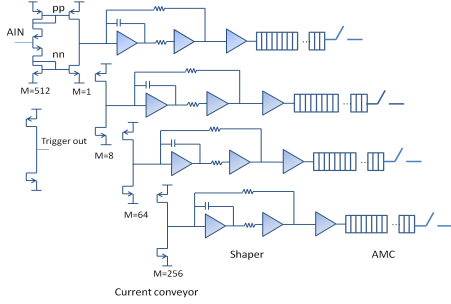


Figure 2. Schematic of one readout channel circuit

shot noise. The left panel of Fig. 3 shows the noise level as a function of frequency for different bias current.

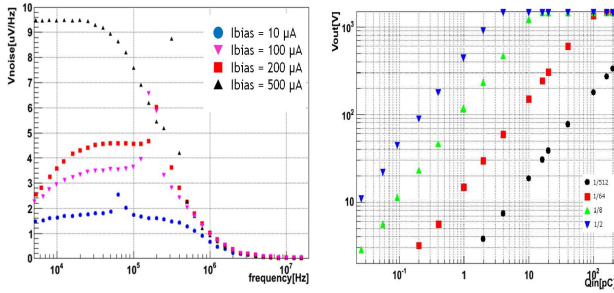


Figure 3. Left: Dependence on input bias current of the noise level of the current conveyor. Right: Linearity of shaper outputs in SPICE simulation (Blue:  $\times 1/512$ , Green:  $\times 1/64$ , Red:  $\times 1/8$ , Black:  $\times 1/2$ ).

Equivalent Noise Charge (ENC) corresponds to  $2.19 \times 10^4$ . If an input bias current is  $10 \mu\text{A}$ , S/N ratio for MIP is expected 14.2 when shaping time is 250 ns. We decide to set the input bias current of  $10\mu\text{A}$  since S/N gets worse if input bias current is larger than  $10\mu\text{A}$ . There is a peak around 60 kHz which depends on the series noise caused by the fluctuation of  $g_m$  of input MOS. The right panel of Fig. 3 shows the output voltage as a function of input charge for 4 different gains. A good linearity of 1 are expected to be achieved.

Figure 4 shows the pulse shape of trigger output. It is quite possible to trigger the signal for larger than 20 pC, which corresponds to the  $p_T$  of  $\gamma$  of 5 GeV. AMCs are operated with 10 MHz writing clock and 5

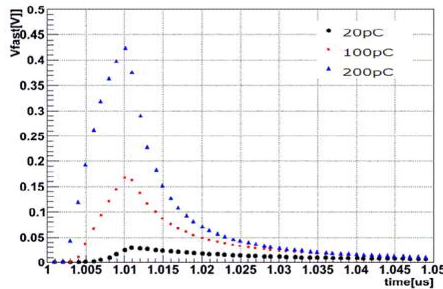


Figure 4. Pulse shape of trigger generations when output is terminated by  $50 \Omega$  resistance. Input charges are 20pC, 100pC, 200 pC, respectively.

MHz readout clock. The analog signals holded by AMC are serialized at each gain and output. Readout time is  $\sim 4(\text{sample}) \times 6(\text{readout channels}) \times 200 \text{ ns}(\text{clock}) = 4.8\mu\text{s}$

#### 4. Layout

The layout mask for the ASIC chip was done by SILICON ARTIST TECHNOLOGY [5]. Figure 5 shows the layout of overview of ASIC chip. These layouts passed a design rule check and a layout versus schematic check. This chip was fabricated by UMC

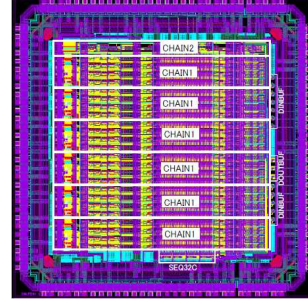


Figure 5. Layout of front-end ASIC for FOCAL

#### 5. Summary and Outlook

The front-end ASIC for FOCAL has been developed. In order to cover a wide dynamic range, the ASIC has 4 different gain ( $1/2$ ,  $1/8$ ,  $1/64$ ,  $1/512$ ) current conveyors at one readout chain. In the simulation study, wide dynamic range of  $10^4$  and good linearity has been achieved. A good noise performance is also achieved in the simulation. The S/N ratio for MIP reaches to more than 10, satisfying the requirement of the front-end circuit for FOCAL.

After the fabrication of this ASIC, some performance tests such as noise, linearity, cross talk and so on, will be executed. This ASIC will be used for the beamtest of the prototype calorimeter.

#### References

- [1] L.D. McLerran and R. Venugopalan, Phys. Rev. D 49 (1994) 2233
- [2] Y.Hori *et.al.*, 2011 J. Phys.: Conf. Ser. 293 012029
- [3] <http://openit.kek.jp/>
- [4] K. Koli *et.al.*, Helsinki University of Technology Electronic Circuit Design Laboratory Report 30, Espoo 2000
- [5] <http://www.silicon-artist.com/>

# Development of W+Si Electromagnetic Calorimeter for the LHC-ALICE Upgrade

T. Gunji, H. Hamagaki, Y. Hori, S. Hayashi, Y. Sekiguchi,  
for the ALICE-FOCAL Collaboration

Center for Nuclear Study, Graduate School of Science, University of Tokyo, Japan

## 1. Introduction

The ALICE experiment at the Large Hadron Collider (LHC) in CERN is dedicated for the study of hot and dense QCD medium created in relativistic heavy-ion collisions [1]. First two-year running of Pb+Pb collisions at the center of mass energy per nucleon ( $\sqrt{s_{NN}} = 2.76$  TeV) in ALICE reveals many experimental observations on the formation of strongly interacting medium [2, 3, 4]. Quantitative understanding of the medium properties requires detailed understanding of the initial state before collisions, dynamics of the interaction of strong color field, and space-time evolution of the system.

The W+Si electromagnetic sampling calorimeter is being proposed as one of the upgrade plans for the ALICE experiment. The role of this upgrade is to add capabilities to measure direct photons, neutral pions and jets over the full azimuth in the forward pseudo-rapidity range ( $2.5 \leq \eta \leq 4.5$ ). The physics goal with the calorimeter is to understand high density gluonic field at small Bjorken  $x$  in heavy nuclei and dynamics of the collisions shortly after the collisions.

## 2. W+Si sampling calorimeter

For the electromagnetic calorimeter, a small shower size is essential to minimize occupancy effects and to optimize the photon shower separation. In order to maintain a compact electromagnetic calorimeter with small Moliere radius and to implement a fine lateral granularity readout, tungsten is the absorber material due to its small Moliere radius (9.3 mm) and Si is chosen as a sensitive volume. Figure 1 shows the schematic view of the longitudinal structure of a W+Si sampling calorimeter. The size of this tower is  $10 \times 10 \times 15$  cm<sup>3</sup> and 132 towers will be installed to cover the rapidity of  $2.5 \leq \eta \leq 4.5$  and the full azimuth. A W+Si calorimeter consists of three or four longitudinal segments, where one segment is composed of 5-7 layers of tungsten (3.5 mm thickness/layer) followed by active silicon pad sensors ( $1 \times 1$  cm<sup>2</sup>). First segment contains 2-4 layers of high resolution Si-micro-pad ( $1 \times 1$  mm<sup>2</sup>) or Si-pixel ( $100 \times 100$   $\mu$ m<sup>2</sup>) detectors for the position measurement of electromagnetic showers and  $\pi^0$ /single  $\gamma$  separation.

## 3. Detector Prototype R&D

A prototype segment with W+Si-pad layers and a prototype of a front-end ASIC have been developed in 2011. Figure 2 shows one layer of W+Si pad module. Heavy Alloy (94W+4Ni+2Cu) with  $9.3 \times 9.3$  cm<sup>2</sup> is used in the prototype and attached by the Si sensor. The size of Si-pad sensor is  $9.3$  cm  $\times$   $9.3$  cm  $\times$   $535$   $\mu$ m (thickness) and it contains 64 readout pads with pad size of  $1.1 \times 1.1$  cm<sup>2</sup>. This Si sensor is common cathode n-doping, negative bias (-100V as full depletion

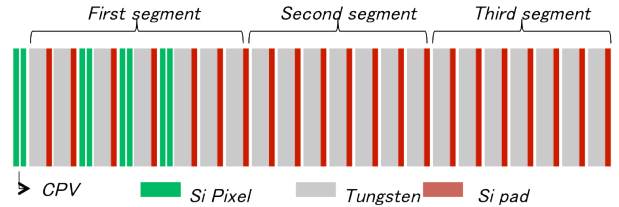


Figure 1. Schematic view of the longitudinal structure of a W+Si sampling calorimeter

voltage) is provided on each pad through 10M $\Omega$  register, and the common cathode is biased to GND. Signal from the pad is readout through the coupling capacitance of 10nF. The signals from all pads are brought off the sensor readout board via ribbon cable to the passive summing board. For each pad, the summing board performs a passive longitudinal sum of the signals from all of the individual sensor layers, to form a tower signal from the multi-layer segment. 18 layers of W+Si pad modules were produced in 2011 and 8 of them were used in the beamtest in November, 2011.

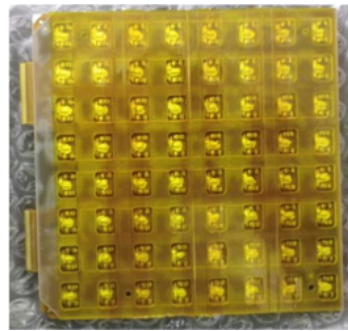


Figure 2. The view of one layer W+Si pad module (seen from the pad side).

In parallel with the prototype preparation, readout analog ASIC has been developed. Our ASIC needs to cover wide dynamic range from 10 fC to 200 pC and the noise should be less than  $3 \times 10^4$  in Equivalent Noise Charge (ENC). Cross-talk needs to be suppressed less than 1% to achieve good energy measurement. We have designed a prototype ASIC, which is composed of current conveyor with 4 different gain outputs, shaping amplifier, analog memory cell, and multiplexer. The overall performance is reported in Ref [5].

## 4. Beamtest at CERN-PS in 2011

A beam test of the prototype W+Si-pad calorimeter was conducted at the T9 beamline in the CERN-PS in November 2011. A prototype segment with 8 W+Si-pad layers was tested during this beam test. The beam

energy used in this beamtest was 3, 4, and 5 GeV with mixed pion and electrons.

Figure 3 shows the experimental setup of the beam test. In front of the prototype, three layers of single-sided silicon strip detectors with the spatial resolution of  $40\ \mu\text{m}$  were installed for the tracking of beam particles. Cherenkov counter for electron and pion separation and two scintillators for trigger were also installed in the beam line.

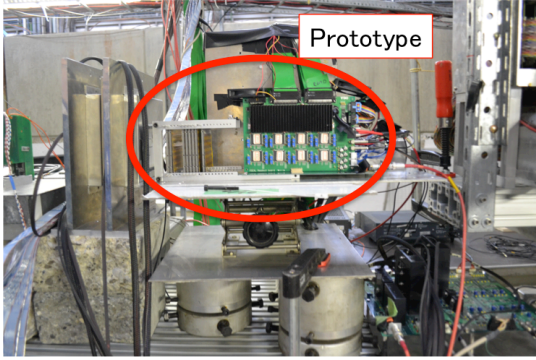


Figure 3. Experimental setup around the prototype at the beamtest in CERN-PS.

Figure 4 shows the energy distributions of the charged pion (blue) and pedestal noise (red) after removal of correlated noise. The MIP signal from charged pions is clearly separated from the noise with a S/N of around 6-10, depending on pad or electronics.

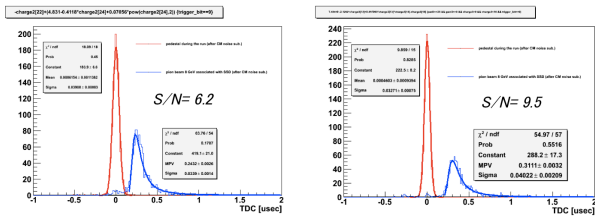


Figure 4. (color online) Energy distributions of charged pions (blue) and pedestal noise (red) for different Si-pads.

Figure 5 shows the signal distributions for electrons at beam energy of 3 (upper left), 4 (upper right), and 5 (lower left) GeV, where the energy summation was taken over  $3 \times 3$  pads. It is seen that the peak position clearly increases with the beam energy and that the relative resolution improves as the energy increases.

## 5. Summary and Outlook

We have developed W+Si-pad based electromagnetic calorimeter for the upgrade of LHC-ALICE experiment. Beamtest performed in 2011 at CERN-PS showed that our prototype successfully measured electromagnetic showers for 3, 4 and 5 GeV electrons and the energy deposition for the minimum ionizing charge particles with reasonable S/N ratio. We are planning to have another beamtest in 2013 and overall performance for higher energy electrons will be evaluated.

## References

[1] ALICE Collaboration, Physics Performance Report Vol. 1 J. Phys. **G 30** (2003) 1517.

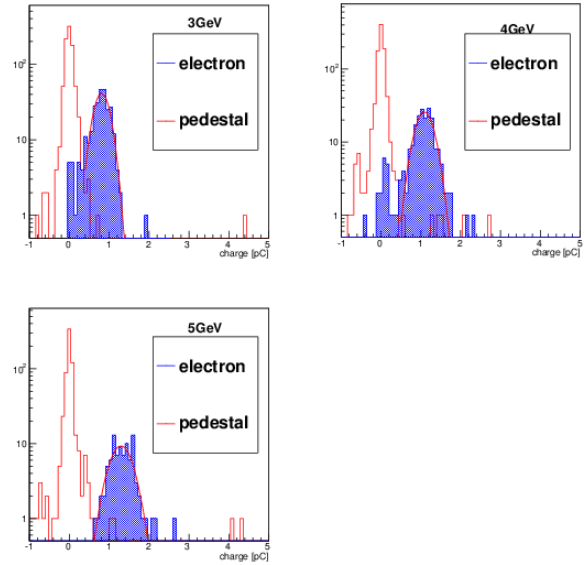


Figure 5. Measured signal distributions for electrons with 3 (upper left), 4 (upper right), and 5 GeV (lower left).

- [2] K. Aamodt *et al.*, for the ALICE Collaboration, Phys. Rev. Lett. **105**, 252301, 2010
- [3] K. Aamodt *et al.*, for the ALICE Collaboration, Phys. Rev. Lett. **105**, 252302, 2010
- [4] K. Aamodt *et al.*, for the ALICE Collaboration, Phys. Lett. **B696**, 30-39, 2011
- [5] S. Hayashi, T. Gunji, H. Hamagaki, *et al.*, In this Report

# Track Reconstruction with Silicon Vertex Tracker for the RHIC-PHENIX Experiment

R. Akimoto, Y. Akiba<sup>a,b</sup>, H. Asano<sup>c</sup>, T. Gunji, T. Hachiya<sup>a</sup>, H. Hamagaki, M. Kurosawa<sup>b</sup>,  
M. Shimomura<sup>d</sup> (for the PHENIX Collaboration)

Center for Nuclear Study, Graduate School of Science, University of Tokyo

<sup>a</sup>RIKEN (The Institute of Physical and Chemical Research)

<sup>b</sup>RIKEN BNL Research Center, USA

<sup>c</sup>Department of Physics, Kyoto University

<sup>d</sup>Iowa State University

## 1. Introduction

Heavy quark (charm and bottom) is one of the key probes to study the properties of Quark Gluon Plasma (QGP). A silicon vertex tracker (VTX) developed mainly for the measurement of heavy quarks. VTX is a barrel detector with four barrels and two arms surrounding the beam pipe, shown in Fig. 1. A silicon pixel detector [1] is used for the inner two barrels and a silicon stripixel detector [2] for the outer two barrels. Each of the VTX arms covers pseudo-rapidity of  $\pm 1.2$  and azimuthal angle of  $140^\circ$ . VTX has been successfully installed for the use in the PHENIX experiment at RHIC and  $p + p$  and Au + Au collision data were taken during RHIC-RUN11 and RHIC-RUN12 periods.

In this report, details and performances of the tracking with VTX are described.

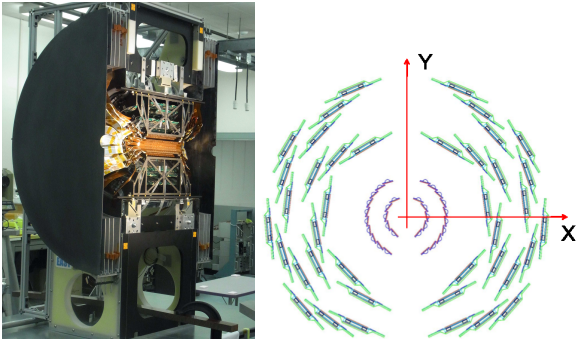


Figure 1. Left : Overall view of one arm of VTX. Right : cross-sectional view of VTX.

## 2. Flavor identification and tracking method

There are two methods to identify flavor of heavy quarks; one is a full reconstruction with all decay products of the hadronic decay and the other is a measurement of electron and positron from the semi-leptonic decay. The measurement of charmed hadrons has been made via hadronic decays [3]. However, a measurement of bottomed hadrons with the hadronic decay mode is difficult due to huge hadronic background in central Au + Au collision events and small branching ratio. The branching ratio of the hadronic decay modes of B mesons with two charged daughters is around  $10^{-5}$  and with three charged daughters is around  $10^{-4}$ . The branching ratio increases as the number of daughters increases, but background also increases exponentially. On the other hands, the background in the measurement with the semi-leptonic decay mode is smaller than

that in the measurement with the hadronic decay mode and the branching ratio of the semi-leptonic decay is around 10 %. Therefore, the semi-leptonic decay mode is appropriate for the measurement.

Charm and bottom contributions in the electrons and positrons from heavy quark decay can be separated by using the difference in their distributions of the distances of the closest approach (DCA)<sup>2</sup> for the beam collision vertex. When magnetic field does not exist, the DCA of a decay particle is represented by  $L \cdot \sin \theta$ , where  $L$  is the flight length of its mother particle and  $\theta$  is the angle between the momentum vectors of the mother and the decay particles. Therefore, the DCA distribution depends on the lifetime of the mother particle and the  $q$ -value of the decay mode.

Figure 2 shows DCA distributions of the electrons and positrons from charmed and bottomed hadrons. Charms and bottoms are created, hadronize, and decay in the calculation of PYTHIA code [5]. RMS widths of the DCA distributions for charmed and bottomed hadrons are about  $120 \mu\text{m}$  and  $300 \mu\text{m}$ , respectively. Therefore, the DCA resolution is required to be much smaller than their difference,  $180 \mu\text{m}$ , in order to distinguish charm and bottom contributions.

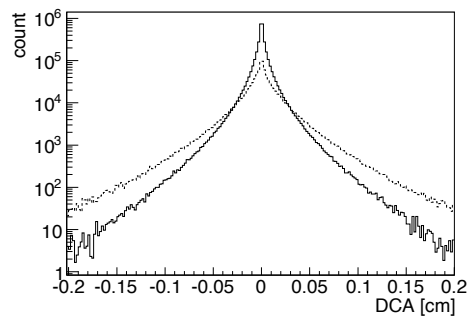


Figure 2. DCA distributions of electrons and positrons from charmed and bottomed hadrons. The solid and dashed lines show the distributions from charmed and bottomed hadrons, respectively. The transverse momentum ( $p_T$ ) range of the electron and positron is  $1 \text{ GeV}/c < p_T < 1.5 \text{ GeV}/c$ .

There are two tracking methods using VTX. One is stand-alone tracking of VTX and the other is the

<sup>2</sup>In this report, DCA in the xy-plane is called as DCA. The x and y directions are defined at Fig. 1 and the beam direction is defined as z direction.

tracking using both the PHENIX central spectrometer (CNT) [4] and VTX (CNT+VTX tracking). Both track trajectories and the beam collision vertex are necessary for the DCA measurement. The stand-alone tracking is suitable for the collision vertex measurement since the acceptance of CNT is limited,  $\pm 0.35$  in pseudo-rapidity and  $180^\circ$  in azimuthal angle, which is smaller than that of VTX.

The CNT+VTX tracking is used for the trajectory measurement. The  $p_T$  resolution of CNT is better, and thus the DCA resolution should be better than those of the stand-alone tracking.

### 3. Tracking performance

#### 3.1. Beam collision vertex resolution

The collision vertex resolution was evaluated as follows:

- the collision vertex was calculated using the reconstructed tracks for each arm;
- from the distribution of the difference between the reconstructed vertices for two arms, the collision vertex resolution was evaluated.

If the numbers of tracks reconstructed at two arms are the same, the collision vertex resolution is represented as

$$\sigma_{\text{full}} = \frac{1}{\sqrt{2}}\sigma_{\text{one}} = \frac{1}{2}\sigma_{\text{diff}},$$

where  $\sigma_{\text{full}}$ ,  $\sigma_{\text{one}}$ , and  $\sigma_{\text{diff}}$  are the resolution of the collision vertex reconstructed with tracks at both of two arms, that reconstructed with tracks at one arm, and the width of distribution of the vertex difference, respectively. The collision vertex resolution is assumed to be scaled by an inverse of a square root of the number of reconstructed tracks.

Figure 3 shows the collision vertex resolutions of x, y, and z directions as a function of the number of hits on the innermost barrel. Closed and open circles represent measured values and simulation results by HIJING code [6]. The collision vertex resolutions were better than  $180 \mu\text{m}$  but the measured resolution was worse than the simulated one. The cause for the difference is not fully understood but it is possible to be due to a misalignment or an insufficient evaluation of hot and dead areas.

#### 3.2. DCA resolution

The DCA resolution was evaluated by fitting the DCA distribution with a Gaussian. Figure 4 shows the DCA resolution as a function of  $p_T$  when the number of hits on the innermost barrel is larger than 800. When  $p_T$  was larger than  $1 \text{ GeV}/c$ , the resolution was less than  $100 \mu\text{m}$ , satisfying the requirement.

### 4. Summary and outlook

The track reconstruction with VTX was performed and the performance was evaluated with measured data. The DCA resolution is less than  $100 \mu\text{m}$  when  $p_T$  is larger than  $1 \text{ GeV}/c$  and the number of hits on the innermost barrel is larger than 800. It satisfies the requirement for the flavor identification of heavy quarks,  $180 \mu\text{m}$ . However, the resolution evaluated with measured data is worse than that with simulation, and the reason is not fully understood.

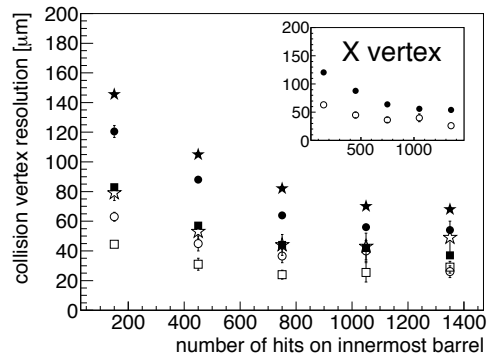


Figure 3. The circle, square, and star points show the resolution of the collision vertex in x, y, and z directions as a function of the number of hits on the innermost barrel, respectively. Closed and open circles represent measured data and simulation, respectively. The resolution in x direction is picked up and is shown at the left top panel for an example.

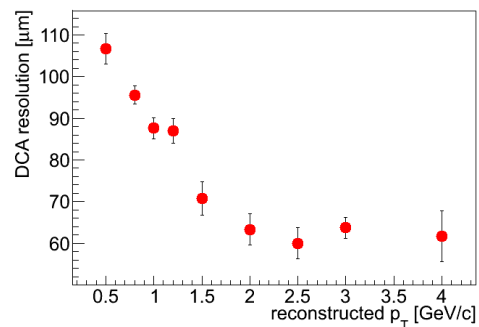


Figure 4. The DCA resolution as a function of  $p_T$  when the number of hits on the innermost barrel is larger than 800.

The outlook is that we can understand the reason by studying more detail about detector alignment and detector response.

### References

- [1] A. Taketani *et al.*, Nucl. Instr. and Meth. A **623** (2010) 374.
- [2] Z. Li *et al.*, Nucl. Instr. Meth. A **518** (2004) 300.
- [3] R. Bala *et al.*, for the ALICE Collaboration, arXiv:1208.4243.
- [4] K. Adcox *et al.*, Nucl. Instr. and Meth. A **499** (2003) 366.
- [5] <http://home.thep.lu.se/~torbjorn/Pythia.html>
- [6] <http://www-nsdth.lbl.gov/~xnwang/hijing/>

# Development of GEM with Glass Insulator

Y. Sekiguchi, H. Hamagaki, T. Gunji, and T. Tamagawa<sup>a</sup>

Center for Nuclear Study, Graduate School of Science, University of Tokyo  
<sup>a</sup>RIKEN (The Institute of Physical and Chemical Research)

## 1. Introduction

A Gas Electron Multiplier (GEM) is one of the micro-pattern gaseous detectors developed by F. Sauli in 1996 [1]. GEM has a simple structure with an insulator foil with typical thickness of  $\sim 50 \mu\text{m}$ , coated with metal foils on both sides used as electrodes. The foil has punched-through holes with typical diameter of  $\sim 70 \mu\text{m}$  aligned in close-packed hexagonal lattice with typical distance of  $\sim 140 \mu\text{m}$ . Application of different potential between upper and lower electrodes creates a high electric field inside the holes. As a result, in the holes, electrons following the electric field lines are multiplied because of the very high field.

Although most GEMs utilize Kapton, Liquid Crystal Polymer (LCP) or other organic materials as insulator materials, it has been pointed out that the hydrogen contained in the organic insulator is a significant background source because hydrogen has a relatively large elastic cross section for thermal neutrons [2]. Moreover, organic insulators are decomposed by irradiation of ions and electrons and release outgas which becomes a serious problem under the operation without gas flow. To overcome these difficulties, we have developed a new GEM with an inorganic insulator and we chose glass as an insulator. GEM with glass insulator (Glass GEM) was manufactured by SciEnergy CO. LTD. [3], using the light etching technique, with a help of HOYA Corp. [4].

## 2. Glass GEM

Figure 1 shows the view of the prototype Glass GEM (left) and its cross section view (right). The prototype Glass GEM has cross area of  $2.5 \times 2.5 \text{ cm}^2$ , thickness of  $100 \mu\text{m}$ , hole diameter of  $70 \mu\text{m}$ , and hole pitch of  $140 \mu\text{m}$ . A photosensitive glass substrate (PEG3C) produced by HOYA Corp. is employed as the insulator. The fabrication procedure is shown in Fig. 2. The glass substrate is exposed to UV light with a metal mask, and the exposed portion of glass is crystallized. The crystallized portions are removed to form holes by wet etching. The substrate is exposed to UV again, and heating process follows to harden the substrate. Finally, copper is deposited on the glass.

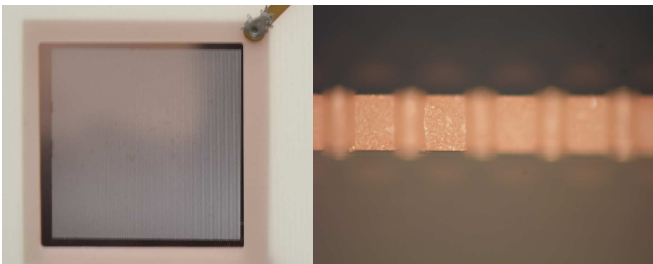


Figure 1. Photo of Glass GEM (left) and That of its cross section (right)

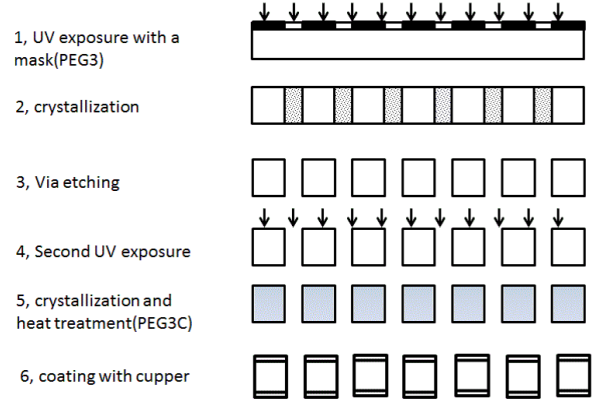


Figure 2. The fabrication procedure of Glass GEM

## 3. Measurement of Basic Properties

Measurements of gain and short-term gain stability for one single Glass GEM were carried out. Figure 3 shows the experimental setup for the measurements. A cathode mesh is mounted 7 mm above the upper electrode of GEM and readout pads ( $2.5 \times 2.5 \text{ cm}^2$ ) are placed 2.5 mm below from the lower electrode of GEM. The electric field for the drift region and the induction region were  $E_D \sim 130 \text{ V/cm}$  and  $E_I \sim 2 \text{ kV/cm}$ , respectively. Different high voltage sources were used to supply the voltage difference between the upper and the lower electrodes of the GEM. Ar 90% + CH<sub>4</sub>10% was used at atmospheric pressure and room temperature. 5.9 keV X-ray from <sup>55</sup>Fe was used in the measurements. Then, the signal was read with the preamplifier which has 1pF feedback capacitor and 100 M $\Omega$  feedback resistor.

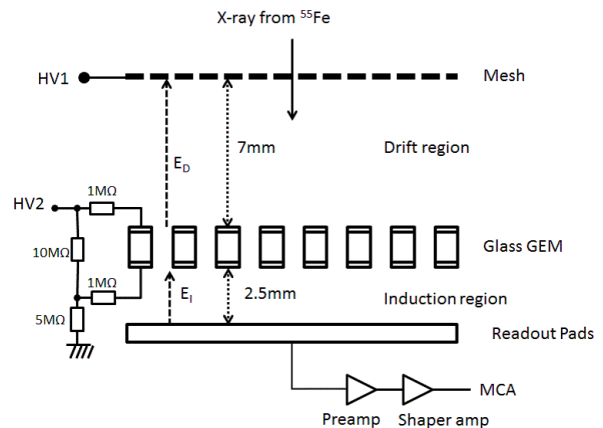


Figure 3. A scheme view of the test setup

Figure 4 shows the charge distribution with  $V_{\text{GEM}} = 550 \text{ V}$ . A full absorption peak corresponding

to 5.9 keV and an escape peak are clearly seen. The energy resolution is obtained to be approximately 10% by fitting with Double-Gaussian.

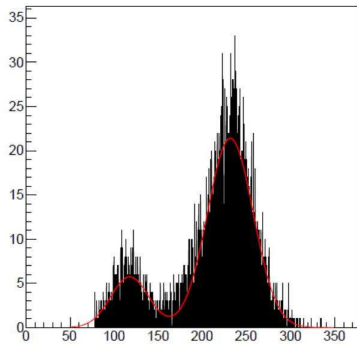


Figure 4. charge distribution at  $V_{GEM} = 550 V$

Gain as a function of  $V_{GEM}$  is shown in Fig. 5 for P10 gas. The measured gain exponentially increases with increase of  $V_{GEM}$ . Figure 6 shows the gain stability using P10 without correction by  $P/T$  dependence of the gain, where  $P$  and  $T$  are the pressure and the temperature in the chamber. The rate of signal is a few Hz.  $V_{GEM}$  is kept 560 V during the measurement. Discharge happens often during the measurement, more studies are needed to understand the reason.

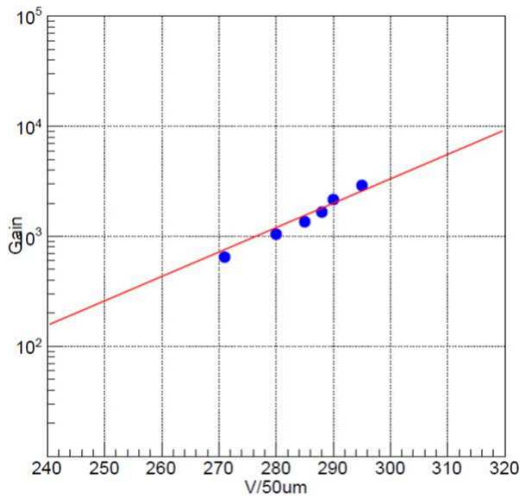


Figure 5.  $V_{GEM}$  dependence of gain for P10.

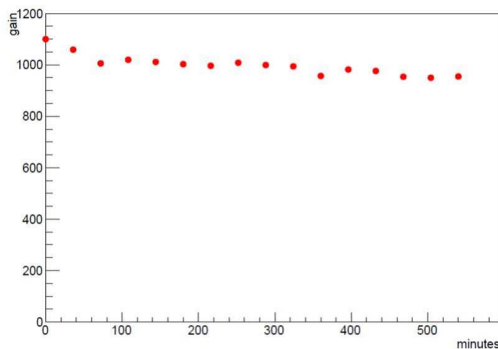


Figure 6. Gain stability with  $V_{GEM}=560V$  for P10.

#### 4. Summary and outlook

We have successfully developed a new type of GEM with glass for insulator, called Glass GEM. The basic properties of the Glass GEM such as  $V_{GEM}$  dependence of the gain and the gain stability have been investigated with P10. But there is the problem with discharge. More studies are on-going with Ne based gases which has large  $w$  value. The Ne gases are expected to have less incident of discharge.

#### References

- [1] F. Sauli, *et al.*, Nucl. Instr. and Meth. A 386 (1997) 531.
- [2] M. Klein, *et al.*, Nucl. Instr. and Meth. A 628 (2011) 9.
- [3] SciEnergy Co. Ltd., <http://www.scienergy.jp/>
- [4] HOYA Corp., <http://www.hoya.co.jp>

# SHARAQ Project — Progress in FY2011 —

S. Michimasa, S. Ota, S. Shimoura, T. Uesaka<sup>a</sup>, Y. Sasamoto, K. Miki<sup>b</sup>, S. Noji, H. Matsubara, M. Dozono<sup>a</sup>, H. Miya, H. Tokieda, S. Kasase, S. Sasano<sup>c</sup>, K. Kisamori, M. Takaki, R. Yokoyama, T. Fujii, Y. Kubota, C.S. Lee, H. Kurei, T. Kawabata<sup>d</sup>, K. Yako<sup>e</sup>, N. Yamazaki, A. Yoshino, H. Sakai<sup>a</sup>, T. Kubo<sup>a</sup>, N. Inabe<sup>a</sup>, Y. Yanagisawa<sup>a</sup>, D. Kameda<sup>a</sup>, H. Suzuki<sup>a</sup>, H. Takeda<sup>a</sup>, T. Ichihara<sup>a</sup>, H. Baba<sup>a</sup>, G.P. Berg<sup>f</sup>, P. Roussel-Chomaz<sup>g</sup>, D. Bazin<sup>c</sup>, for the SHARAQ collaboration.

*Center for Nuclear Study, Graduate School of Science, University of Tokyo*

<sup>a</sup>*RIKEN Nishina Center*

<sup>b</sup>*RCNP, Osaka University*

<sup>c</sup>*NSCL, Michigan State University*

<sup>d</sup>*Department of Physics, Kyoto University*

<sup>e</sup>*Department of Physics, University of Tokyo*

<sup>f</sup>*Department of Physics, Notre Dame University*

<sup>g</sup>*CEA Saclay*

The progress of SHARAQ project in the fiscal year 2011 is reviewed in this article. We have performed one physics run [1] with the SHARAQ spectrometer [2] and the high-resolution beam line [3] in May 2011. We have also done detector developments and ion-optics study of an achromatic beam transport for upcoming experiments.

## 1. Achromatic optics development for experiments in SHARAQ

The ion-optics of SHARAQ beam line has been computationally studied and obtained solutions of the dispersion matching (DM) mode and the high-resolution achromatic (HA) mode. The DM mode was actually used in FY2010 for the charge-exchange experiments [4,5]. The HA transport mode was developed in May, 2011 and applied to the following physics experiment [1].

Ion-optics calculation of the achromatic transport of the high-resolution beamline and SHARAQ is illustrated in Fig. 1. The HA mode has the momentum

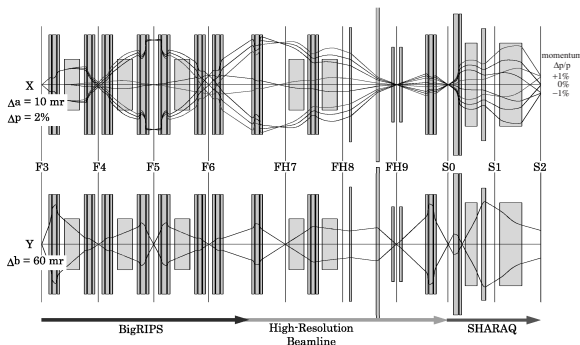


Figure 1. First-order ion-optical calculation of BigRIPS-SHARAQ beamline. The solid lines show the beam trajectories of  $\Delta p/p = +1\%$ ,  $0\%$  and  $-1\%$ . Angular spreads in  $X$  ( $Y$ ) axis are  $\pm 10$  ( $\pm 30$ ) mr.

acceptance of 2%, and has the intermediate dispersive focus at F6 with a resolution of  $\Delta p/p = 1/8500$ . The target position of SHARAQ spectrometer, S0, is designed to be an achromatic focus. Beam tracking at the F6 dispersive focus provides a beam momentum

tagging in event-by-event basis. In Fig. 1, the solid lines show beam trajectories of  $\Delta p/p = +1\%$ ,  $0\%$  and  $-1\%$ . Angular spreads in  $X$  and  $Y$  axes are  $\pm 10$  mr and  $\pm 30$  mr, respectively.

The tuning of HA transport started from the F3 of BigRIPS, where the secondary beam had momentum spread of  $\Delta p = 2\%$ , spot sizes of  $X$ : 3.2 mm,  $Y$ : 2.9 mm, and angular spreads of  $X$ : 10.1 mr,  $Y$ : 14.2 mr.

Figure 2 shows the beam spots and angular spreads measured at S0.

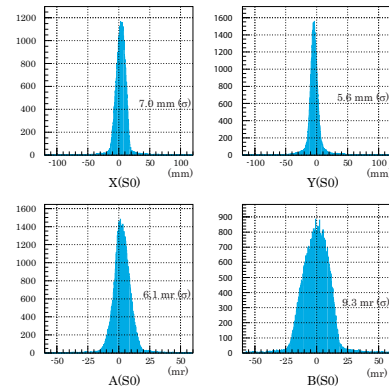


Figure 2. Distributions of horizontal position ( $X$ ), vertical position ( $Y$ ), horizontal angle ( $A$ ), and vertical angle ( $B$ ) at S0.

By the first-order optics calculation between F3 and S0, the beam profile at S0 is estimated to be  $X$ : 4.8 mm,  $Y$ : 4.1 mm,  $A$ : 6.7 mr and  $B$ : 9.9 mr, respectively. The observed beam profile was roughly consistent with the estimate, but the spot sizes ( $X$ ,  $Y$ ) were slightly larger while the angular spreads ( $A$ ,  $B$ ) were smaller than the estimate. The analysis about these difference between observation and evaluation is now in progress.

## 2. Physics run: Charge-exchange excitations in unstable $^{12}\text{Be}$ nucleus

Physics experiment on isovector type responses in unstable nucleus  $^{12}\text{Be}$  with the SHARAQ spectrometer was performed after the development of the HA ion op-

tics. The experiment is characterized by inverse kinematics measurement of the  $(p,n)$  reaction from  $^{12}\text{Be}$ . In the experiment, we adopted new detector array for low-energy neutrons (WINDS) [6] in combination with the SHARAQ spectrometer for the first time. Details on the experiment will be described in Ref. [1].

### 3. Development of two-particle detection at the final focal plane

The pulse processing system of tracking detectors [7] of SHARAQ spectrometer, which are installed at the final dispersive focal plane, was developed to achieve capability of two-particle detection. The capability is necessary for a approved experiment for investigating the stability of four neutron system via the exothermic double charge-exchange  $^4\text{He}(^8\text{He}, ^8\text{Be})4n$  reaction, because two  $\alpha$  particles produced by an immediate decay of an outgoing  $^8\text{Be}$  particle travel to the SHARAQ final focal plane. To identify two-particle detection events, flash ADC and multi-hit TDC modules were adopted for data acquisition of the charge and timing of anode signals, respectively. The identification algorithm was checked by using the data of  $(^{12}\text{Be}, ^8\text{Be})$  channel additionally obtained in the  $(^{12}\text{Be}, ^{10}\text{B})$  measurement [1]. Details on the development will be described in Ref. [8].

### References

- [1] K. Yako *et al.*, CNS Ann. Rep. 2011 (2012).
- [2] T. Uesaka *et al.*, J. Phys.: Conf. Ser. **312** (2011) 052028.
- [3] T. Kawabata *et al.*, Nucl. Instrum. Methods B **266** (2008) 4201.
- [4] Y. Sasamoto *et al.*, CNS Ann. Rep. 2011 (2012).
- [5] S. Noji *et al.*, CNS Ann. Rep. 2011 (2012).
- [6] K. Yako *et al.*, CNS Ann. Rep. 2011 (2012).
- [7] S. Michimasa *et al.*, CNS Ann. Rep. 2009 (2011) 43, and references therein.
- [8] K. Kisamori *et al.*, CNS Ann. Rep. 2011 (2012).

# $\mu$ Hodoscope using 1-mm square plastic scintillators for the experiments with high-intensity beam

Y. Kikuchi, S. Ota<sup>1</sup>, H. Matsubara, Y. Kubota, C.S. Lee, S. Kawase, and T. Uesaka<sup>a</sup>

*Center for Nuclear Study, Graduate School of Science, the University of Tokyo*

<sup>a</sup> *RIKEN Nishina Center Accelerator-Based Science*

Event-by-event tracking with high-intensity beam such as  $10^6$  Hz/cm<sup>2</sup> is required for the experimental studies of exotic nuclei, especially for high energy resolution experiments. Position information at object point of ion optics or at dispersive focus is required for a high-resolution measurement of momentum. At dispersive focus, the beam size becomes larger and the intensity per unit becomes smaller. Then, we can use MWDCs there as described in Ref. [1]. At the object point of ion optics, the beam size is as small as 1 cm (FWHM), and it is difficult to use MWDCs. We usually use MWDCs because of their high resolution of  $300 \mu\text{m}$  and small amount of materials along the beam path. However, at the object point, the resolution of 1 mm is enough and relatively large amount of materials can be used since the angular information can be measured elsewhere before the target.

The requirements for tracking detector are

1. Position resolution better than 1 mm (FWHM),
2. Withstand high beam intensity above 1 MHz,
3. Efficiency close to 100%.

We are developing a plastic scintillator hodoscope consisting of  $1\text{-mm}^2 \times 30\text{-mm}$  plastic scintillator bars, which is designed to have the position resolution of 1 mm and  $\sim 100\%$  detection efficiency. We use bulk scintillator bar without any light shield instead of the scintillating fiber to minimize the dead space due to the optical cladding. The plastic scintillator bars were produced by a company, CI-Kogyo, by cutting out a 1-mm thick plastic scintillator plate.

Since there could be crosstalks among plastics and fibers, we need to extract the charge information as well as timing information.

The light emitted from scintillator bar is transmitted using optical fiber (CLEAR-PS) produced by a company, kuraray. The shape of the cross section is rectangular shape and the width is 1 mm, which is same as the plastic scintillator bar. The transmission loss is around 0.5 dB/m, which is small enough since the maximum length of optical fiber is 2 m.

We used a 64-ch multi-anode photo-multiplier H7546B (Hamamatsu) for the conversion and amplification of signals. In a traditional system, the charge information is obtained using charge-sensitive ADCs. But in such a system, there are large dead time due to the conversion time and no multi-hit capabilities which is important for the operation with high-intensity beam. If we measure the time over threshold instead of the charge, we overcome these difficulties. A combination of preamplifier discriminator card RPA-132 (REPIC) and multi-hit TDC V1190 (CAEN) is one of the solutions. The leading edge and width of

output logic signal of the RPA-132 correspond to the timing and charge information of signals, respectively. The time constant of RPA-132 is 16 ns and the input dynamic range is from  $-1\text{pC}$  to  $+1\text{pC}$ . To adjust the charge of output signal from the PMT, we supply a HV of 700 V to the PMT, which much smaller than the rated voltage, 850 V. The V1190 can detect the leading and trailing edge of input logic signal and can record some hits in a search window. The least significant bit is 100 ps, which is smaller than the expected time resolution.

A test experiment was performed at EN course in RCNP. The aim was to evaluate the intensity dependence of the efficiency. Primary beam of  $^{12}\text{C}$  at 250 MeV bombarded two PPACs for the beam tracking and  $\mu$ Hodoscope. Two PPACs were located 482-mm apart from each other and the  $\mu$ Hodoscope was located at 78-mm downstream of the downstream PPAC. Timing signal of the upstream PPAC was used for the trigger of DAQ system. Each anode signal was amplified and discriminated by the RPA-132 and the leading- and trailing-edge timings were recorded by using the V1190. The signal from last dynode of the H7546B was input to a QDC module V792 and the V1190 as a reference to anode signal.

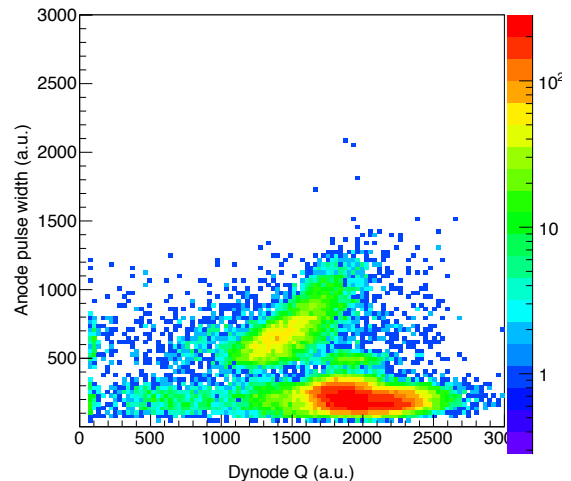


Figure 1. Correlation between charge and width information. Horizontal and vertical axis show the charge of dynode signal measured with V792 QDC and the width of anode signal measure with V1190 TDC.

Figure 1 shows the correlation between the charge of dynode signal and the width of anode signal. The width is found to be good measure to the charge since there are positive correlation between them. There are

<sup>1</sup>Corresponding author

many hits which have a small pulse width. These hits seem to be crosstalk )and can be discriminated clearly from the true signal by setting certain threshold to the pulse width. After this discrimination, we can determine the position which corresponds to the geometrical position of plastic scintillator bar where the pulse width is largest among the hits.

We measured the detection efficiency which is defined as the ratio of the number of event tracked by the hodoscope to the number of event tracked by PPAC. The efficiency for the 10-kHz, 100-kHz and 500-kHz beam are  $95.1\pm 0.5\%$ ,  $94.5\pm 0.8\%$  and  $96.7\pm 3.0\%$ , respectively.

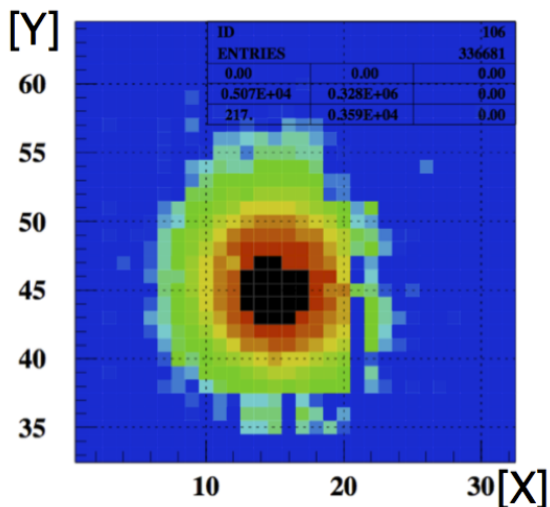


Figure 2. Two-dimensional position measured with  $\mu$ Hodoscope. Horizontal and vertical axes show the sequential number of 1-mm scintillator bars which corresponds to the position with 1-mm accuracy.

Figure 2 shows the online spectrum of two-dimensional position measured with  $\mu$ Hodoscope for  $^{56}\text{Fe}$  at HIMAC although the result is preliminary. In this analysis the maximum signal width does not always give the correct position since gain difference among the scintillator bars and the existence of crosstalks make strong correlation of signal widths between certain pairs of horizontal and vertical scintillator bars. To reject such a fake signal of maximum width, the second maximum is chosen for some combinations of fired scintillator bars. The analysis is in progress.

## References

- [1] Miya et al., CNS Ann. Rep. 2010 (2012) 43–44

# Development of LP-MWDCs for high resolution spectroscopies with high intensity RI beam

H. Miya<sup>a</sup>, S. Ota, H. Matsubara, S. Kawase, Y. Kikuchi, C. S. Lee, T. Fujii, Y. Kubota, and S. Shimoura

Center for Nuclear Study, Graduate School of Science, University of Tokyo

<sup>a</sup>Nishina Center for Accelerator-Based Science, RIKEN

We have developed Low-Pressure Multiwire Drift Chamber (LP-MWDCs) to measure tracks of the high intensity RI beam ( $Z:\text{He-N}$ ; beam energy: 100–300 MeV/nucleon; intensity: 1–2 MHz) [1]. The LP-MWDCs are used in BigRIPS and High Resolution Beam Line (HRBL). At SHARAQ spectrometer [2], high resolution missing mass spectroscopies are performed. The tracks information are needed to correct the angular and the momentum spread of the RI beams. The LP-MWDCs are required to be operational under the high intensity circumstances.

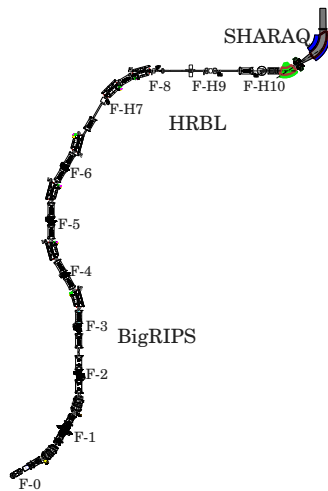


Figure 1. Layout of BigRIPS, high resolution beam line, and SHARAQ spectrometer.

In the Spring of 2012, measurement of exothermic charge exchange reactions of ( $^8\text{He}$ ,  $^8\text{Li}\gamma$ ) and ( $^8\text{He}$ ,  $^8\text{Be}$ ) are planned, which uses the BigRIPS, the High Resolution Beam Line (HRBL), and the SHARAQ spectrometer shown in Fig. 1. The  $^8\text{He}$  beam at the energy of 190 MeV/nucleon are transported in the high-resolution achromatic mode. The intensity of the  $^8\text{He}$  is  $2 \times 10^6$  cps at the secondary target.

The experiment is performed with the missing mass method. The momentum of in-coming and out-going particles at the targets need to be measured. In the beam line, the momentum of the  $^8\text{He}$  beam is measured at the F-6, which is a momentum dispersive focal plane: Designed dispersion value is 76.7 mm/%. The expected momentum resolving power is  $p/\Delta p = 7000$  in full width at half maximum (FWHM) at the F-6. The momentum resolution corresponds to the energy resolution of 0.5 MeV. The tracking detector is required to have a position resolution less than 500  $\mu\text{m}$  (FWHM). The momentum of the produced particles at the targets is analyzed by the SHARAQ spectrometer and detected by cathode readout drift chambers [3].

The beam tracks on the targets have to be determined with angular and position resolutions of 1 mrad (FWHM) and 0.5 mm (FWHM). Tracking detectors are required to have a position resolution less than 350  $\mu\text{m}$  (FWHM) when the three detectors are installed at a distance of 500 mm from each other.

For the experiment, we developed the new LP-MWDCs using at the F-6 and the F-H10. We report here on the developments of the LP-MWDCs.

In the beam line of the BigRIPS and the HRBL, LP-MWDCs are installed at F-3, F-6, F-H7, F-H9, and F-H10. A list of the LP-MWDCs is shown in table 1. The counter gas is pure isobutane at the pressure of 10 kPa. With this low pressure operation, the effect of multiple scattering in the gas can be made diminishingly small. The all LP-MWDCs are used for tuning beam ion optics. At the Physcis run of ( $^8\text{He}$ ,  $^8\text{Li}\gamma$ ) and ( $^8\text{He}$ ,  $^8\text{Be}$ ), the tracks of high intensity RI beams are measured with the LP-MWDCs at F-6 and F-H10.

The LP-MWDC using at the F-6 consists of four anode planes with wire operations ( $V:30^\circ$ ,  $U:-30^\circ$ ). By using the inclined wire planes, the counting rate per cell can be reduced for the high intensity beam. The effective area and the cell size are  $216 \times 144 \text{ mm}^2$  and  $9 \times 9 \text{ mm}^2$ , respectively. The effective area corresponds to the momentum spread of  $\pm 1\%$  at the F-6.

At the F-H10, the three LP-MWDCs are placed to measure the tracks to the target. The spot size on the target is 30  $\text{mm}^\phi$ . For nearest detector from the target, the cell size have to be smaller than two upstream detectors. The LP-MWDC consists of four anode planes with wire operation ( $X:0^\circ$ ,  $Y:90^\circ$ ). The effective area and the cell size are  $96 \times 96 \text{ mm}^2$  and  $6 \times 6 \text{ mm}^2$ , respectively.

In summary, We have developed the LP-MWDC which are used as the beam tracking detector in the high resolution experiments using high intensity RI beams at the SHARAQ spectrometer. These LP-

Table 1. List of LP-MWDCs in BigRIPS and HRBL.

Focal plane	Active area ( $\text{mm}^2$ )	Cell size ( $\text{mm}^2$ )	Config-uration	Physics runs
F-3	80×80	5×4.8	(X-X'-Y-Y') <sup>2</sup>	
	80×80	5×4.8	X-X'-Y-Y'	
F-6	216×144	9×9	V-U-U'-V'	○
F-H7	216×144	9×9	X-U-Y	
	216×144	9×9	V-U-Y	
F-H9	216×144	9×9	X-U-Y	
F-H10	216×144	9×9	X-U-V'	○
	216×144	9×9	X-U-V	○
	96×96	6×6	X-X'-Y'-Y'	○

MWDCs are installed in the BigRIPS and the HRBL for the experiment of the exothermic charge exchange reactions in April 2012.

#### **References**

- [1] H. Miya et al.: CNS Ann. Rep. 2010 (2012) 43.
- [2] S. Michimas et al.: CNS Ann. Rep. 2011 (2013).
- [3] Y. Kisamori et al.: CNS Ann. Rep. 2011 (2013).

# Development of WINDS: wide-angle inverse-kinematics neutron detectors for SHARAQ

K. Yako, H. Sakai<sup>a</sup>, M. Dozono<sup>a</sup>, T. Fujii, S. Kawase, Y. Kikuchi, K. Kisamori, Y. Kubota, H. Matsubara<sup>a</sup>, S. Michimasa, K. Miki<sup>b</sup>, H. Miya, S. Noji<sup>c</sup>, C.S. Lee, T. Ohnishi, S. Ota, Y. Sasamoto, M. Sasano<sup>a</sup>, S. Shimoura, M. Takaki, H. Tokieda, T. Uesaka<sup>a</sup>, Z.Y. Xu<sup>d</sup> and R. Yokoyama

*Center for Nuclear Study, Graduate School of Science, University of Tokyo*

<sup>a</sup>*RIKEN Nishina Center*

<sup>b</sup>*RCNP, Osaka University*

<sup>c</sup>*NSCL, Michigan State University*

<sup>d</sup>*Department of Physics, University of Tokyo*

The spin-isospin excitations in nuclei is a unique tool for studying a nuclear structure. Although charge-exchange reactions, such as  $(p, n)$  and  $(^3\text{He}, t)$  reactions at intermediate energies, are established probes used to study these excitations in stable nuclei, the charge-exchange study of unstable nuclei is currently only in its early stage. Experiments in inverse kinematics are challenging mainly because the recoils on the probe particle are small. Generally, the detection of recoil particles with kinetic energies below  $\sim 3$  MeV is required for the study of Gamow-Teller excitations (See Fig. 1 in Ref. 1 for a specific case of a  $^{12}\text{Be}(p, n)$  measurement).

We constructed a facility at SHARAQ where the  $(p, n)$  reactions on unstable nuclei can be studied. It consists of a liquid-H<sub>2</sub> (LH<sub>2</sub>) target in a scattering chamber made of 1.6 mm-thick aluminum, the magnetic spectrometer SHARAQ, and the wide-angle inverse-kinematics neutron detectors for SHARAQ (WINDS). A schematic view of the facility is shown in Fig. 1. The missing mass spectra of the  $(p, n)$  reaction are obtained from the scattering angle of the neutron ( $\theta_{\text{lab}}$ ) and its kinetic energy. The kinetic energy is measured by the time-of-flight (TOF) method using WINDS. The timing information of the start of the TOF is obtained from the plastic counter (1 mm<sup>t</sup>) at F-H10, located 2 m upstream of the target position.

WINDS is a set of neutron counters placed at both (left and right) sides of the target, covering the angular region  $60^\circ < \theta_{\text{lab}} < 120^\circ$ . The distance between the target and the counter wall is 180 cm. The left (right) counter wall consists of 30 (29) plastic scintillators (BC408) of  $60 \times 10 \times 3$  cm<sup>3</sup>. These scintillators are placed such that the 3-cm-wide planes face the target. H7195 PMTs are attached to the both ends of each scintillator through the light guides. The charge information from each PMT is digitized by a CAEN V792 QDC. The timing information is processed by a leading-edge discriminator (LeCroy 4413) and digitized by CAEN V767 TDC.

The efficiency of the neutron counter depends on the energy of neutrons as well as the threshold on light output. The typical efficiency with a counter threshold of 200 keV<sub>ee</sub> is estimated by using the code NEFF7 [2], and it is calculated as 0.36 for 2-MeV neutrons. The efficiency calibration was performed with a neutron source of  $^{252}\text{Cf}$  at the target position with a “standard” NE213 liquid scintillator at a distance of 80 cm from

the source. This allowed us to determine the efficiency of the BC408 counters relative to that of the NE213 counter, whose absolute efficiency as well as energy-/threshold-dependence were well known [2]. The detailed data analysis is currently in progress.

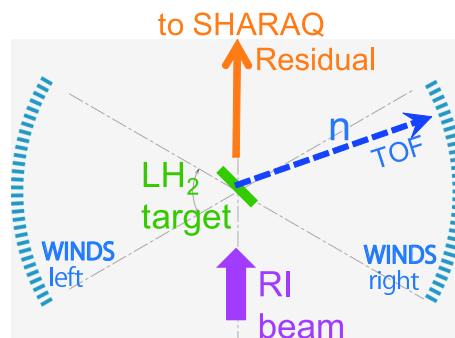


Figure 1. Schematic view of the setup of the  $(p, n)$  measurement in inverse kinematics.



Figure 2. A Photo of WINDS.

## References

- [1] K. Yako *et al.*, “Measurement of  $^{12}\text{Be}(p, n)^{12}\text{B}$  reaction at 200A MeV in inverse kinematics”, elsewhere in this Report.
- [2] G. Dietze and H. Klein, Program NEFF7 (unpublished).

# Development of the detection system for tetra-neutron experiment via ${}^4\text{He}({}^8\text{He}, {}^8\text{Be})4n$ reaction

K. Kisamori, S. Shimoura, S. Michimasa, S. Ota, S. Noji, A. Tokieda, R. Yokoyama and  
H. Baba<sup>a</sup>

*Center for Nuclear Study, Graduate School of Science, University of Tokyo*  
*<sup>a</sup>RIKEN (The Institute of Physical and Chemical Research)*

## 1. Introduction

Multi-neutron systems in nuclei have attracted much attention on both the experimental and theoretical fronts ever since candidates of bound tetra-neutron( $4n$ ) system were reported [1] [2]. However, later theoretical papers using ab-initio calculations [3] suggest that bound tetra-neutron cannot exist.

We plan to perform missing-mass spectroscopy of the  $4n$  system via the exothermic double-charge exchange reaction  ${}^4\text{He}({}^8\text{He}, {}^8\text{Be})4n$ . The experiment will be carried out at the RI Beam Factory (RIBF) at RIKEN using the SHARAQ spectrometer and a liquid He target system. To obtain the missing-mass spectrum, we measured momentum of the  ${}^8\text{Be}$  beam with the High-Resolution Beamline and momenta of two alpha particles which were the decay products of the  ${}^8\text{Be}$  projectile with the SHARAQ spectrometer.

For this experiment, we develop ion optics of the SHARAQ spectrometer in order to achieve a large solid angle, and develop a readout system of focal plane and test detection system.

## 2. SHARAQ spectrometer as a detection system of $({}^8\text{He}, {}^8\text{Be} \rightarrow 2\alpha)$ reaction

The momentum distributions of two alphas are within  $\pm 0.73\%$  and angular distributions are within  $\pm 0.2$  degree of that of the ground state of  ${}^8\text{Be}$  projectile, if we choose an incident beam energy of 200 A MeV. This kinematics enables us to detect two alpha particle at the same time in the SHARAQ spectrometer. Otherwise, events in excited states, which have energies of more than 30 MeV in addition to two-alpha events derived from background will be distributed uniformly at the focal plane.

The SHARAQ spectrometer is required to have a momentum acceptance about  $\pm 2.5\%$  to obtain  $4n$  events with an excitation energy of 40 MeV, including momentum distribution of the two-alpha ( $\pm 0.74\%$ ) and the beam ( $\pm 1\%$ ). Another requirement is that the momentum resolution achieve the  $1/10000$  which gives about 1 MeV missing-mass resolution. We calculated an ion transfer matrix using the COSY infinity [7] so that the maximum solid angle satisfy those requirements. As in Fig. 1, we obtained 4.2 msr of effective solid angle which covers required momentum area.

The maximum size of the decay-cone was estimated to be 60 mm in horizontal direction ( $x$  direction) and 14 mm in vertical direction ( $y$  direction) by a Monte Carlo simulation using the transfer matrix and angular acceptance.

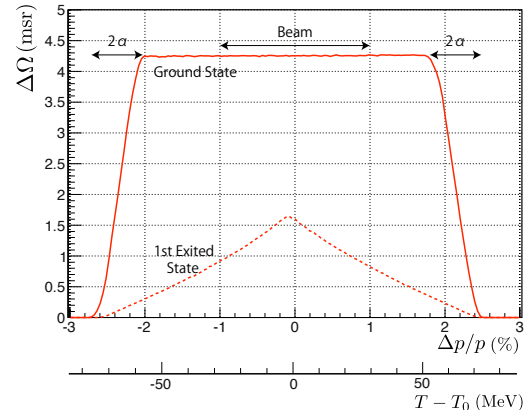


Figure 1. Effective solid angle of  ${}^8\text{Be}$ . The solid line represents ground state of  ${}^8\text{Be}$  and the dotted line for the 1st excited state (3.0 MeV).

## 3. Development of readout system at focal plane

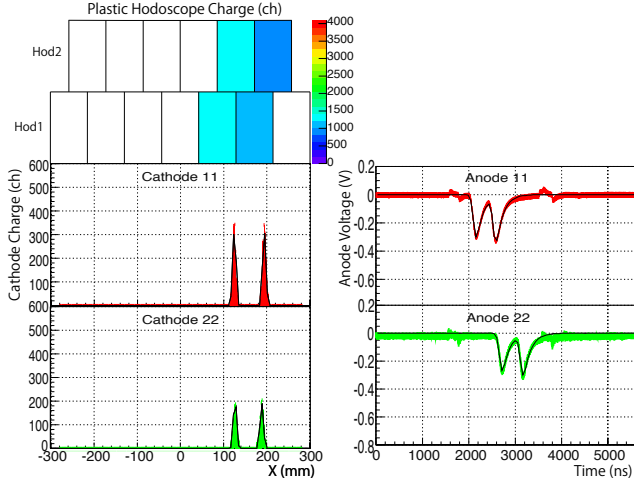
To cover the maximum size of the decay-cone sufficiently, we used the present Cathode Readout Drift Chamber (CRDC) [4] [5] which has a large effective area ( $x$ : 550 mm,  $y$ : 300 mm) and no dead-space. Two CRDCs and plastics hodoscopes and three plastic scintillator for trigger are used. The vertical and horizontal positions of charged particles are determined by measuring the drift time of electrons in the drift plane and by the center of the distribution of induced charges on the cathode pads, respectively. We introduced flash-ADC (SIS3301) for anode signal and FPGA-based logic circuit [6] for the trigger signal of cathode multiplexer. The detail of the logic circuit was described in Refs. [6]. Plastic hodoscope is constituted of 13 plastics scintillators (85 mm width  $\times$  200 mm height  $\times$  5 mm thickness).

We performed an experiment for the test of detection system at the RIBF at RIKEN using RI beam. The experiment was carried out simultaneously with a measurement of a  ${}^{12}\text{Be}(p,n)$  reaction in inverse kinematics at 200 A MeV. The purpose of this experiment is to test if the system correctly works and to evaluate a tracking efficiency of the two-alpha.

Figure 2 shows the cathode charge distribution and the anode pulse shape acquired by flash-ADC of a typical two-alpha event. The cathode charge distribution is fitted by the Secant Hyperbolic Squared (SECHS) function [8],

$$f(x|a, \mu, \sigma) = \frac{a}{\cosh^2[\pi(x - \mu)/\sigma]}. \quad (1)$$

The anode pulse shape is fitted by the ex-gaussian func-



- [8] K. Lau and J. Pyrlik, Nucl. Instrum. Methods Phys. Res. **A 366**, 298 (1995)  
 [9] Y. Lacouture and D. Cousineau, Tutorials in Quantitative Methods for Psychology 2008, Vol. 4 (1), p. 35–45.

Figure 2. The sample of an event snapshot. The upper left represents the charge of the each plastics of the hodoscope. The upper and lower rows represent CRDC1 and CRDC2 respectively. The cathode charge distribution (right side) is fitted by  $F(x) = f(x|a_1, \mu_1, \sigma_1) + f(x|a_2, \mu_2, \sigma_2)$ . The anode pulse shape (left side) is fitted by  $G(t) = g(t|a_1, \mu_1, \sigma_1, \tau_1) + g(t|a_2, \mu_2, \sigma_2, \tau_2)$ .

tion [9],

$$g(x|a, \mu, \sigma, \tau) = \frac{a}{\tau\sqrt{2\pi}} \exp\left(\frac{\sigma^2}{2\tau^2} - \frac{x-\mu}{\tau}\right) \times \Phi\left(\frac{x-\mu}{\sigma} - \frac{\sigma}{\tau}\right) \quad (2)$$

$$\Phi(y) = \int_y^\infty \exp\left(-\frac{y^2}{2}\right) dy \quad (3)$$

$$(4)$$

where  $\Phi(y)$  is the Cumulate Distribution Function.

In the fit result, if the distance between two particles is greater than the uncertainty of each particle, we are able to identify the two particles. Using this method, two particles can be identified separately for events with a distance in  $x$  direction more than 10 mm and in  $y$  direction more than 5 mm. These results indicated that this detection system can identify 95% of two alpha which are decayed from the ground state of  $^8\text{Be}$ , considering decay cone of the two-alpha particles. This result satisfies the requirement of the experiment.

## References

- [1] J. E. Ungar et al., Phys. Lett. **B 144**, 333 (1984)  
 [2] F.M.Marques *et al.*, Phys. Rev. **C 65**, 044006 (2002)  
 [3] S.C.Pieper, Phys. Rev. Lett. **90**, 252501 (2003)  
 [4] S. Michimasa *et al.*, CNS Ann. Rep. 2009 (2011)  
 [5] H. Tokieda *et al.*, CNS Ann. Rep. 2009 (2011)  
 [6] K. Kisamori *et al.*, CNS Ann. Rep. 2010 (2012)  
 [7] M. Berz and K. Makino, COSY Infinity version 9 - user's guide and reference manual

# Modification of Active Target for the forward angle scattering and measurement of deuteron induced reaction on $^{56}\text{Fe}$

S. Ota, H. Tokieda, C.S. Lee, M. Dozono<sup>a</sup>, H. Matsubara, S. Kawase, Y. Kubota, S. Michimasa, H. Yamaguchi, M. Sako<sup>b</sup>, T. Gunji, Y. Kikuchi, T. Hashimoto<sup>c</sup>, H. Hamagaki, T. Uesaka<sup>a</sup>, S. Kubono, H. Otsu<sup>a</sup>, Y. Maeda<sup>d</sup>, E. Takada<sup>e</sup>

*Center for Nuclear Study, Graduate School of Science, University of Tokyo*

<sup>a</sup> *Nishina Center for Accelerator-based science, RIKEN*

<sup>b</sup> *Department of Physics, Kyoto University*

<sup>c</sup> *Research Center for Nuclear Physics, Osaka University*

<sup>d</sup> *Department of Applied Physics, Faculty of Engineering, University of Miyazaki*

<sup>e</sup> *National Institute of Radiological Sciences*

## 1. Introduction

The supernova nucleosynthesis is one of the attractive subject. In the supernova nucleosynthesis various nuclei from the iron-group to the uranium are produced in the very short period. In this process the electron capture rates are important parameter. To extract the electron capture rates, we need the Gamow-Teller transition strength (B(GT)) distribution, especially of the iron-group nuclei. The nuclear reactions of (n,p)-type charge exchange can provide us the distribution up to highly excited region where  $\beta$ -decay can not access, while the measurement of  $\beta$ -decay gives the absolute value of B(GT) to the low-lying states below the electron capture threshold. As a (n,p)-type reaction we try to utilize (d, $^2\text{He}$ ) reaction because of its selectivity.

Another attractive subject is the equation-of-state (EoS) of nuclear matter. The EoS there are some parameters such as incompressibility and symmetry energy. The incompressibility of 230 MeV was deduced for symmetric nuclear matter from the systematics of excitation energy of Isoscalar Giant Monopole Resonance (GMR). On the other hand, there is little information on the symmetry energy. The measurements of GMR and/or dipole resonances in the neutron-rich nuclei are desired.

In these studies, we need to deduce spectra up to highly excited states and to measure the forward-angle scattering in center-of-mass frame. The highly excited states populated via charge-exchange reactions or inelastic scattering decay mainly by particle emission sometimes followed by gamma-ray emission. In the invariant-mass spectroscopy we need to measure all the particles and also gamma rays. On the other hand, in the missing-mass spectroscopy we need to measure only one or two recoiled particles. However, particles recoiled to the angle corresponding to the forward angle in center-of-mass frame have very small kinematic energy below 1 MeV/u. In order to measure such low-energy recoiled particles in the reaction, we are developing an gaseous active target.

Active target has two roles simultaneously as the target and the detector. The active target we are developing is a time-projection chamber (TPC) which has the position sensitivity in three dimensional direction. Our aim is to develop the active target to measure the reactions, especially forward-angle-scattering, of (d,d') and (d, $^2\text{He}$ ), with high intensity ( $\sim 10^6$  Hz) beam of 100–300-MeV/u kinematic energy.

The structure of active target was described in the previous report. Although the previous structure is suitable for the high-intensity such as  $10^7$  Hz, the lower-limit of the energy of the recoiled particles was about 1 MeV, which is not small enough to measure the forward angle scattering. We report, here, the modification to measure the low energy particles of 0.3 MeV/u under the operation with 1-atm gas.



Figure 1. Schematic view of modified active target. One field cage is located along the beam line and two arrays of NaI are located at the both sides of the field cage.

## 2. Modification of Active Target

To measure the low-energy recoiled particles, the beam is directly irradiated the active area of TPC, and the shape and size of the read out pad are optimized. According to the optimization of the readout pad, the total number of channels become 400 and then the manner of the signal transfer from the chamber to the outside is changed. The array of NaI, where the relatively high-energy particles are detected, is located much closer to the active area in order to enlarge the dynamic range. The DAQ system is also rearranged to effectively readout the data and to make a self-triggering system. The following subsections describe (1) the optimization of readout pad, (2) new signal transfer and (3) the modified DAQ system.

### Optimization of readout pad

The regular triangle shape is chosen to be more symmetric. The size of the pad is 5 mm along the beam path and is 10 mm at the side of beam path. The total number of the pads is 400. The position of beam particle in the pad plane is deduced by using charge division assuming the energy loss is constant and the position in the direction perpendicular to the pad plane is calculated from the drift time. However, the manner of charge division cannot be applied for the low-energy recoiled particle which stops in the active area since the change of energy loss cannot be ignored. In order to extract the trajectory of such particles, the calculated energy deposition in each pad is fitted to the measured one with the parameters of angle and position where particle stops.

The angular and position resolutions are estimated to be 30 mrad and 0.4 mm, respectively, by using a GEANT4 simulation for isotropically emitting protons of 0.3 MeV.

### Signal Transfer

The newly developed signal transfer system enables us to extract the huge number of signals from the inside of the vacuum chamber to the outside. The number of signals was limited by the size of the D-sub feed through connectors and the maximum was 25 signals in about  $35 \times 95\text{-mm}^2$  area. The signal transfer system is expected to be air tight and to transfer more signals. We decided to use Flexible Printed Circuits (FPC). The FPC consists of thin film and foil and can transfer 50 signals. For the air tightness new feedthrough connector has been developed, which can covers some FPCs. The 75 signals from the readout pad is transferred in  $60 \times 80\text{-mm}^2$  area. The density becomes twice. More signals can be transferred if we put more FPCs in the feedthrough connectors. The crosstalk among cables is 0.5% after the preamplifier, where the transient signal disappear with the integration.

### DAQ System

The DAQ system has been upgraded to realize high-throughput and self-triggering capability for TPC signals. The pulse shape should be recorded to discriminate the true signals from noises such as  $\delta$  rays and discharge and also to distinguish the tracks of two or more particles. We decided to use V1740 modules from CAEN, which has the pre-trigger sampling capability. The V1740 is 64-ch 65-MHz sampling flash ADC and can be readout through optical link, which provide the high throughput of 80-MB/sec. With this throughput and utilizing the spill structure of synchrotron, the dead-time-less data acquisition has been achieved for 300-Hz trigger rate.

## 3. Measurement of deuteron induced reaction on $^{56}\text{Fe}$

A test experiment was performed at HIMAC.  $^{56}\text{Fe}$  beam bombarded the active target operated with 1 atm. deuterium gas. The beam and recoiled particles were measured by TPC and NaI array. The supplied high voltage to the field cage was 20 kV and the resultant electric field was 0.8 kV/cm. Three GEMs were mounted so as to amplify the electrons and total gain was set to 2000 (designed value). The collected charge at the readout pad was transferred using FPC to

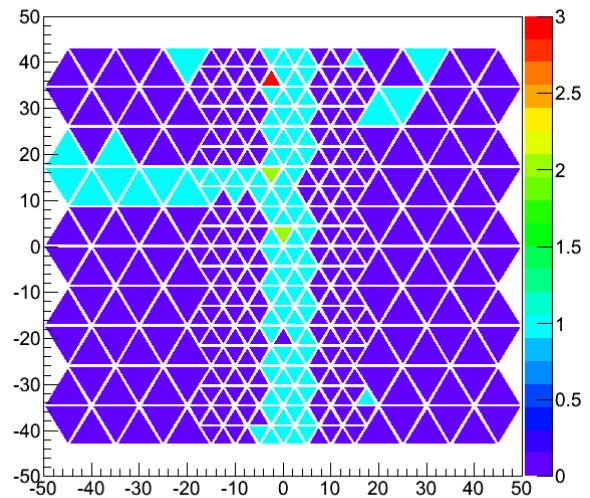


Figure 2. Typical event display with a recoiled particle. The color code corresponds to the number of hit in each pad within a certain time range. Beam particle goes from the bottom to the top. The trajectory of recoiled particle is clearly seen in the top-left region.

charge-sensitive RPA211 (REPIC) preamplifier where the charge was integrated with the time constant of 80 ns and the conversion gain of 0.2 V/pc. The voltage signal was digitized by the V1740 flash ADC and used to generate the trigger. The threshold in V1740 was around 50 mV. The scattered particles were measured by  $\mu$ Hodoscope consisted of two layers of 30 thin plastic scintillator array, which provides the time reference to the TPC and scattered position.

Typical hit pattern of the event is shown in Fig. 2. The beam particle goes from the bottom to the top. The trajectory of recoiled particle is clearly observed around top-left side. The analysis is in progress.

### References

- [1]

# The Performance Evaluation of NaI Detectors for CNS Active Target

C. S. Lee<sup>3</sup>, S. Ota, H. Tokieda, M. Dozono<sup>a</sup>, H. Matsubara, S. Kawase, Y. Kubota, S. Michimasa, H. Yamaguchi, H. Hamagaki, M. Sako<sup>b</sup>, Y. Maeda<sup>c</sup>, T. Uesaka<sup>a</sup>, H. Otsu<sup>a</sup> and S. Kubono

*Center for Nuclear Study, Graduate School of Science, University of Tokyo*

<sup>a</sup>*RIKEN Nishina Center for Accelerator Based Science*

<sup>b</sup>*Department of Physics, Kyoto University*

<sup>c</sup>*Department of Applied Physics, Faculty of Engineering, Miyazaki University*

## 1. Introduction

To extract the incompressibility of the nuclear matter experimentally, one needs to measure the energy of Isoscalar Giant Monopole Resonance (ISGMR) of the nuclei (Ref. [1], [2]). In order to determine the energy of the ISGMR, the Multipole Decomposition Analysis (MDA) is definitely required. For this analysis method, MDA, it is necessary to have the angular distribution of the differential cross section in a wide range of scattering angles with a good resolution.

When we use an active target, the detections of recoiled particles which scattered into the forward angles in the center-of-mass (CM) frame are performed well at a Time Projection Chamber (TPC) which often used in active targets (Ref. [3]). However, the backward (CM) scattering particles could not be tracked at TPC because they have larger kinetic energies than forward scatterings and the energy depositions are not sufficient to be detected in the gas target. This means that the total kinetic energy of the recoiled particles which have a relatively high energy could not be measured at TPC. Therefore, some kinds of solid detectors to measure the total kinetic energy of the backward scattering particles are required for the active target. For this reason, CNS Active Target has adopted an array of one hundred and twenty NaI(Tl) scintillators to detect the particles scattered into the backward direction. Figure 1 shows the schematic view of CNS Active Target (CAT).

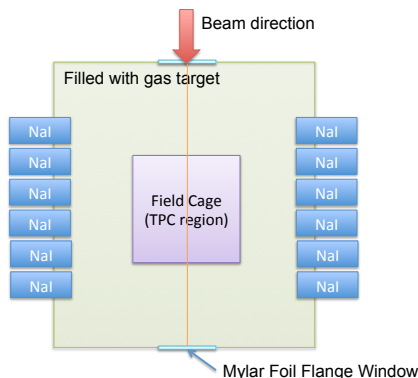


Figure 1. The schematic view of CNS Active Target. The large rectangle shows the Active Target chamber.

The total kinetic energy of the recoiled particle is related to its scattering angle. This implies that the energy resolution is also related to the angular resolution. Since the angular resolution is an important factor for

MDA method, we have to estimate the energy resolution of NaI scintillators. However, we cannot obtain an enough energy resolutions at low energy region (down to  $\sim 4$  MeV) because of less energy deposition into the NaI crystals. On the other hand, we can also use the timing information to obtain the energy resolution. If we have a good time resolution enough to determine the energy, instead of using the kinetic energy directly, energy calculated from the time could be more useful. Here we report the performance of NaI detectors for CAT.

## 2. Resolution Measurements for a Single Crystal

We measured the resolution for each single crystal which had a size of  $31 \times 31 \times 57 \text{ mm}^3$ . At the present time, double gamma rays induced from the electron-positron pairs produced by a  $^{22}\text{Na}$  source were measured by two crystals facing each other. We used the standard NIM electronics. For each PMT, the anode signal was fed to the Timing Filter Amplifier (TFA) and then to a Constant Fraction Discriminator (CFD) and a Time-to-Amplitude Converter (TAC) for the time resolution measurement. A Multichannel Analyzer (MCA) was used as a signal counter.

We had a time resolution of about 4 ns with simple circuit. Typically, NaI scintillator has an energy resolution of about 7% at 662 keV (Ref. [6]) and time resolution of about 1 ns for a  $^{60}\text{Co}$  source. Comparing those general performances, the time resolution we obtained was not so reasonable. This might be caused by a lack of gain at PMT in that the resolutions were improved when we supplied a higher voltage (See next paragraph).

After that, the measurements with the DAQ system had been performed. The circuit of the DAQ system is shown in Figure 3. This time, we used both NIM and VME electronics. In order to obtain both timing and energy, the anode outputs from PMT were divided into TFA and spectroscopic amplifier N568B. The outputs from the TFA were connected to the CFD and the multi-hit TDC (V1190) for time resolution measurements. Outputs from spectroscopic amplifiers were connected to ADC (V785) for energy measurements. The event trigger was created by taking coincidence of two time signals. About 2 ns of resolution (FWHM) was obtained for each single crystal at 511 keV. If this time resolution is used for calculation of kinetic energy  $E$ ,  $\delta E/E$  would be about 50% at 511 keV. The energy resolution  $\delta E/E \sim 9\%$  at 1274 keV and  $\sim 16\%$  at 511 keV were measured.

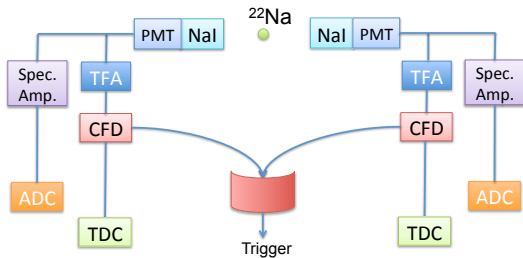


Figure 2. A part of the DAQ circuit for NaI Wall. In this measurement, the trigger was created by coincidence of two crystals. For the whole NaI Wall system, a trigger was created by one single signal among all.

The resolving power (RP) of kinetic energy from that of time for this work is very low so that we cannot use the values even in the low energy region. If there is a detector which has few hundreds pico second of time resolution, the energy RP defined as  $E/\delta E$  at low energy region (down to  $\sim 4$  MeV) will be largely improved (See Figure 5). One example is so called "Phoswich" type in which a time sensitive detector is attached in front of the other. We are considering the development to obtain a better time resolution.

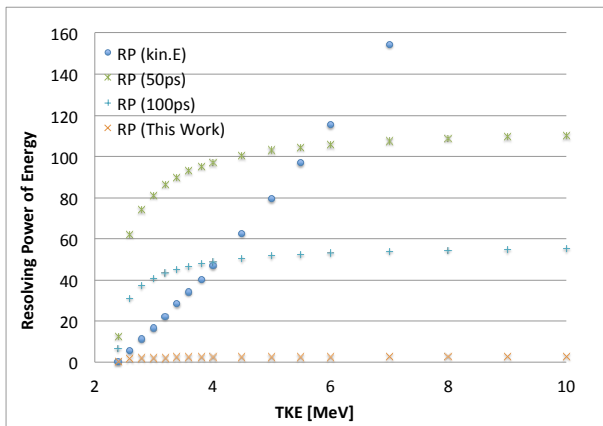


Figure 3. The resolving power estimations for deuteron with various time resolutions. If a detecting system which has a time resolution of about 100 ps is added to NaI scintillator, the energy RP by using time RP will be twiced at 3 MeV. Moreover, four time would be accomplished if a time resolution of 50 ps at 3 MeV is achieved. Note that the energy resolution was 9% in 1274 keV from this work.

### 3. Measurement of Recoiled Particles

NaI Wall which consists of 120 NaI scintillator was built for P275 and  $^{56}\text{Fe}(d, d')$  experiment was performed at HIMAC in January, 2012. Two arrays of NaI detectors were located at both sides of CAT chamber as shown in Figure 1. The dynamic range of the kinetic

energy for each detector was set to 10MeV. We measured the recoiled particles from scattering angles of 84-87 degree and lots of  $\gamma$ -ray events without recoiled particles were also observed. The correlation of TOF -  $E$  which was obtained for one crystal is shown on Figure 4. Taking events with a track measured at the active area of TPC, the  $\gamma$ -ray events might be excluded from the analysis, and then we can see the kinematical curve of recoiled particles obviously. The analysis is now in progress.

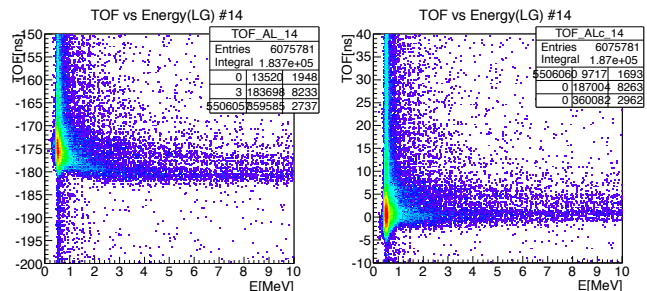


Figure 4. The correlation between time-of-flight and kinetic energy obtained at the 14th NaI crystal. The left side shows the correlation before threw correction with  $\gamma$ -ray events. The right side shows the correlation after through correction and time offset added.

### References

- [1] J. P. Blaizot *et al.*, Nucl. Phys. A **591** (1995) 435.
- [2] Dao T. Khoa *et al.*, Phys. Rev. C **56** (1997) 954.
- [3] T. Hashimoto *et al.*, Nucl. Instr. and Meth. A **556** (2006) 339.
- [4] C. Monrozeau *et al.*, Phys. Rev. Lett. **100** (2008) 042501.
- [5] D. H. Youngblood, C. M. Rozsa *et al.*, Phys. Rev. Lett. **39** (1977) 1188.
- [6] E. Sakai, IEEE Trans. on Nucl. Sci. **34** (1987) 418-422.

# Development of neutron detector for the study of neutron single particle state

Y. Kubota, T. Uesaka<sup>a</sup>, S. Ota, M. Dozono<sup>a</sup>, and Y. Kikuchi

Center for Nuclear Study, Graduate School of Science, University of Tokyo

<sup>a</sup>RIKEN (The Institute of Physical and Chemical Research)

## 1. Introduction

The single particle state gives us the basic information of nuclear structure. Recent study strongly suggests evolution of single particle properties such as the magnitude of the spin-orbit splitting in unstable nuclei [1], which is a clue to understanding some of the effective interaction used to describe the nuclei.

Intermediate-energy ( $\vec{p}, pn$ ) reaction is a powerful spectroscopic tool to study neutron single hole state directly, but no experiments by means of this reaction have been performed for unstable nuclei because of the difficulty of neutron precise measurement. Position resolution and detection efficiency of a typical neutron detector are not good compared to a detector for charged particles, which utilizes electromagnetic interaction.

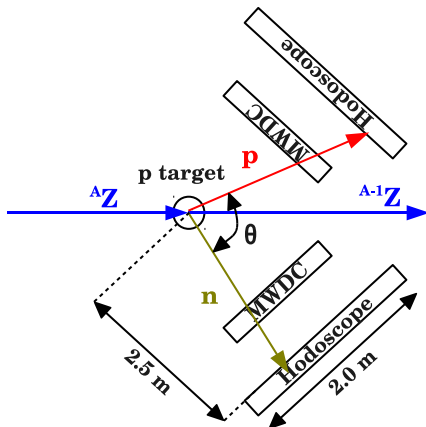


Figure 1. A schematic view of ( $p, pn$ ) experimental setup.

Two multi-wire drift chambers (MWDCs) and plastic scintillator hodoscopes located at left and right sides cover the angular range of  $25^\circ < \theta_{\text{lab}} < 65^\circ$ . Energies of scattered proton and neutron are measured by a TOF method by using hodoscopes. Scattering angles of proton and neutron are determined by MWDC and hodoscope, respectively.

Figure 1 shows an example setup of ( $\vec{p}, pn$ ) experiment. The separation energy resolution  $\Delta E_s$  needs to be less than 1 MeV to study the spin-orbit splitting of neutron single particle state.  $\Delta E_s$  is represented as  $\Delta E_s \sim \sqrt{(10 \times \Delta E/E)^2 + (0.3 \times \Delta \theta \text{ mrad})^2}$  MeV where  $E$  is energy of scattered nucleons and  $\theta$  is opening angle between scattered nucleons. Table 1 shows the requirements in order to achieve  $\Delta E_s \sim 1$  MeV in this setup. Time-of-flight (TOF) resolution  $\Delta t_{\text{TOF}}$  and position resolution  $\Delta x$  determine  $\Delta E$  and  $\Delta \theta$ , respectively.

Double-ended hodoscope, used for an orthodox neutron detector, has enough TOF resolution ( $\Delta t_{\text{TOF}} \sim$  a few hundred ps), but its typical position resolution

Position resolution $\Delta x$	5 mm FWHM
TOF resolution $\Delta t_{\text{TOF}}$	700 ps FWHM

Table 1. Requirements of a new detector. These values are needed to achieve  $\Delta E_s \sim 1$  MeV in the experimental setup showed in Figure 1.

( $\Delta x \sim$  a few cm) doesn't satisfy the requirement for angular resolution of opening angle between scattered nucleons. We have to develop a new detector to perform the ( $\vec{p}, pn$ ) experiment.

## 2. Design of a new detector

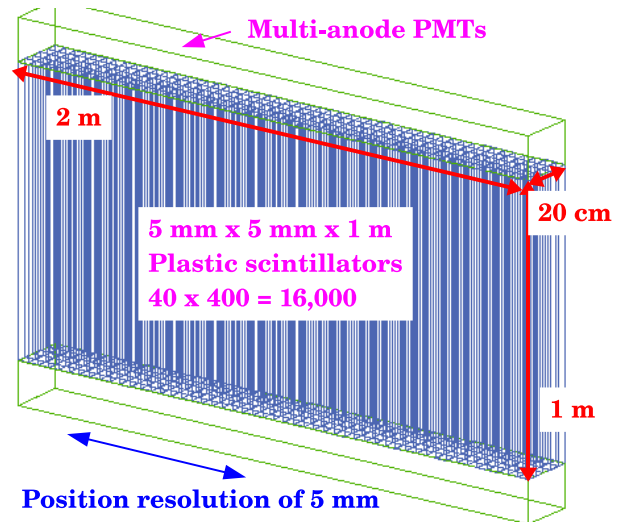


Figure 2. Concept of the detector. Plastic scintillator is finely segmented with a size of  $5 \times 5 \times 1000 \text{ mm}^3$  that the neutron hit position is determined only by using the hit pattern.

Figure 2 shows a concept of a new neutron detector. It consists of multi-anode photomultiplier tubes (MA PMTs) and finely segmented plastic scintillators with a size of  $5 \times 5 \times 1000 \text{ mm}^3$ . These scintillators are so finely segmented that needed position resolution is obtained from the hit information of neutrons.

There are concerns about the performance of the new detector. One is detection efficiency, and the other is time resolution. Small energy loss in each segment makes light output smaller. It makes the detection efficiency and the time resolution worse. In addition, long and thin shape of scintillators reduce the number of scintillation photons which reach PMTs directly without reflections. Almost all of the scintillation photons reflect many times before they reach the PMTs because the solid angle of direct path to PMT in segmented scintillator is only  $d\Omega/4\pi = 0.0008\%$ . It may spoil the time resolution. We investigated the feasibility of the

detector by means of Monte-Carlo simulation.

### 3. Simulation

The simulation was performed with Geant4 framework [2] with two free parameters, namely the segment size and the surface condition. Table 2 shows the parameters we assumed in this simulation.

Incident neutron energy	100 MeV
Scintillator thickness	20 cm
Scintillator length	1 m
Discriminator threshold	-30 mV
Software threshold	-300 mV
PMT quantum efficiency	20%
PMT gain	$10^7$

Table 2. Assumed parameters in the simulation. Signal timing is determined when the pulse height overcomes the discriminator threshold. Software threshold is set high conservatively to reduce gamma background. It limits the detection efficiency.

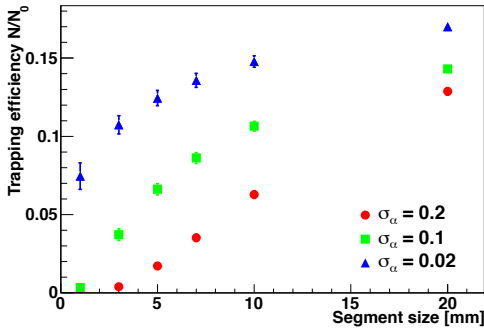


Figure 3. Trapping efficiency of scintillation photons. Result is normalized by the number of total photons generated in the segment. Three types of symbols indicate the difference of surface conditions. The triangles, squares, and circles correspond to highly polished, middle polished and ground surface, respectively.

Figure 3 shows the trapping efficiency  $N/N_0$ , where  $N_0$  is the number of total photons generated in the segment and  $N$  is that of photons which could reach to the PMT. Three types of symbols indicate the difference in the surface condition, which is characterized by standard deviation of the reflection angle in units of milliradian. Although both the segment size and the surface condition affect the trapping efficiency, we can conclude that the latter is more dominant factor.

Figure 4 shows the neutron detection efficiency. The detection efficiency of 17% will be achieved with polished surface and  $5 \times 5 \text{ mm}^2$  segment size. The result is satisfactory, since the detection efficiency decreases by only 15% from the expected value of 20% according to the rule of thumb, that is, the detection efficiency of plastic scintillator for 100 MeV neutron is typically 1%/cm.

Figure 5 shows the time resolution. In general, time resolution of a scintillator seems to be determined by spreads of arrival time of scintillation photons. We define the intrinsic time resolution of segmented scintillators as a standard deviation of rise time  $T_{100} = t_{100} - t_1$ ,

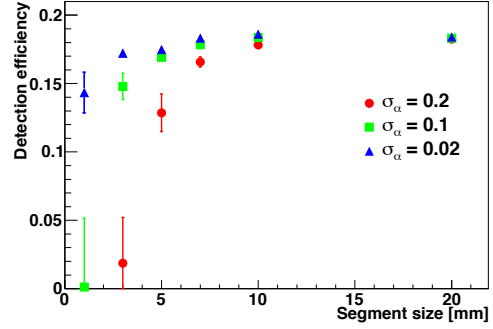


Figure 4. Neutron detection efficiency. It is determined by the software threshold  $V_{th} = -300 \text{ mV}$ .

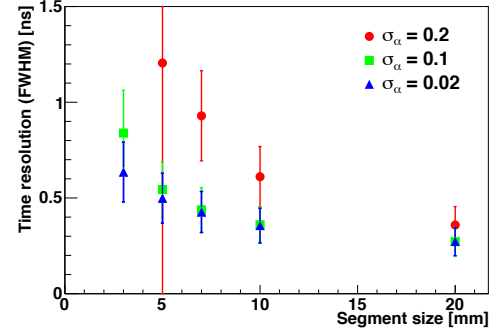


Figure 5. Time resolution  $\Delta t = \sqrt{2}\Delta t_{TOF}$ . It is defined as a standard deviation of rise time  $T_{100}$ , and represented by full-width-at-half-maximum (FWHM).

where  $t_N$  is the time when  $N$ th scintillation photon reaches the PMT. We assume  $T_{100}$  as the rise time because the pulse height overcomes the threshold of a discriminator with this amount of scintillation photons. The result is good enough as compared to the requirement  $\Delta t_{TOF} < 700 \text{ ps}$ .

### 4. Summary and outlook

We proposed the detector based on a new idea for intermediate-energy neutrons. It consists of finely segmented scintillators and MA PMTs. The simulation was performed to evaluate the feasibility of the detector, and it became apparent that both the detection efficiency and the time resolution of the detector will satisfy the requirements, but the performance strongly depends on the surface condition of the segment.

We are now in development of the prototype detector. It is made of fiber scintillators which guarantee the trapping efficiency of 4.4%, instead of segmented plastic scintillators. We are planning to evaluate its performance by using a neutron beam next year.

### References

- [1] J.P. Schiffer, et al., Phys. Rev. Lett. **92** (2004) 162501.
- [2] S. Agostinelli et al., Nucl. Instr. and Meth. A **506** (2003) 250.

# Simulation Study of the Ionization Cooling

C. S. Lee, T. Uesaka<sup>a</sup>, M. Sasano<sup>a</sup> and S. Ota

Center for Nuclear Study, Graduate School of Science, University of Tokyo  
<sup>a</sup>RIKEN Nishina Center for Accelerator Based Science

## 1. Introduction

Many nuclear physicists are eager to study the nuclei very faraway from the stability valley. In order to get the information about those nuclei experimentally, suitable facilities which can provide high intensity rare RI beam are definitely required. However, such an accelerator apparatus which satisfies every requirement of physicists does not exist yet, and also there are lots of obstacles in construction of those facilities. In order to perform a reaction experiment with those experimental conditions, for instance, with a low beam intensity about 1 pps of very rare RI beam, something new experimental technique is needed.

In the case of the typical RI reaction experiment with a solid reaction target on the straight beam line, most of the beam particles are going through the target without reaction and would be stopped at beam dump. This is a waste of most of precious rare isotopes. To improve this situation, A possible scheme was considered of recycling beam particles. Assume that a reaction occurs with 1/s of event rate within measurement time of  $T_0$  (to get enough events) when  $10^6$  pps of beam intensity is provided. If the beam intensity is decreased to 1 pps in this reaction, event rate is dropped down to  $10^{-6}$ /s, and time needed to accumulate enough statistics increases to  $T_0 \times 10^6$ . However, If the beam particles could be reused  $N$  times with the same low beam intensity of 1 pps, the efficiency of the experiment would be positively changed with a factor of  $N$  (See Table 1).

Method	Beam Intensity	Event Rate	Time Taken
Straight BL	$10^6$ pps	1/s	$T_0$
Straight BL	1 pps	$10^{-6}$ /s	$10^6 \times T_0$
Storage Ring	1 pps ( $N$ )	$N \times 10^{-6}$ /s	$10^6 \times T_0 / N$

Table 1. A comparison table between normal straight beam line (BL) and storage ring with several beam intensities.  $N$  is the number of recycle at storage ring.

In order to accomplish this plan, a storage ring contains the reaction target and RF cavity is the most appropriate apparatus. Figure 1 shows the conceptual model of the storage ring.

The emittance growth of the stored beam and the reaction rate should be carefully evaluated in this beam optics system. In this report, the emittance growth of the beam and the cooling process is mainly discussed.

## 2. Ionization Cooling

In a storage ring with a RF cavity to compensate the energy losses by re-acceleration continuously, a beam cooling effect so called "ionization cooling" will appear. This "ionization cooling" method closely resembles the synchrotron damping of relativistic electrons' with the energy loss in the thin gas target [ [1]]. The most remarkable feature of this method is that it may provide

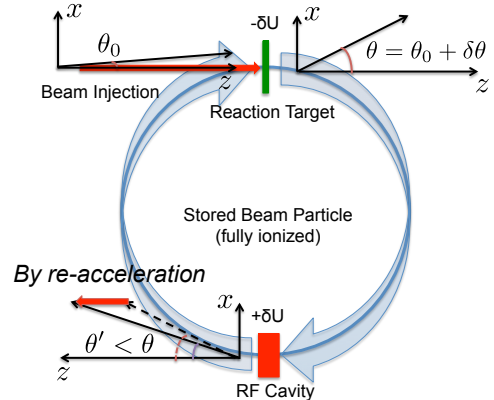


Figure 1. The conceptual model of the storage ring with reaction target and RF cavity. On the reaction target, energy loss, straggling, multiple scatterings are involved. On the other hand, RF cavity will compensate the energy losses by re-accelerations. This re-acceleration will prevent the divergence of the transverse emittance. The stored beam particle will revolve continuously until reaction occurs.

an extremely fast cooling process, compared to other traditional methods such as electron cooling or stochastic cooling.

The energy loss per single turn  $\delta U$  in the reaction target is compensated by the RF cavity, which adds only the longitudinal momentum. This will make reduction of the transverse angle of the particle (See Figure 1). Reduction of emittance  $\langle \delta A \rangle / A$  is represented

$$\frac{\langle \delta A \rangle}{A} = -\frac{\langle \delta p \rangle}{p} = -\frac{\langle \delta U \rangle}{\beta_0 p c} = -\frac{\langle \delta U \rangle}{2T} \quad (1)$$

where  $p$  is the momentum,  $\beta_0 c$  is the velocity and  $T$  is the kinetic energy of particle (Ref. [1]). In case of the storage ring, emittance after  $N$  times of circulation is written as :

$$A(N) = A_0 \exp\left(-\frac{N}{N_0}\right) \quad (2)$$

with  $N_0 \equiv \frac{2T}{\delta U}$ . This relation means that the transverse emittance decrease exponentially by repetitive re-acceleration.

On the other hand, the transverse emittance from the multiple scattering in the reaction target will grow to  $\delta \theta \times \sqrt{N}$  after  $N$  cycles. As a result, the final emittance after  $N$  cycles will be determined by competing two factors, i.e. square root term to increase the emittance and exponential term to decrease. We tried to calculate the final emittance of the beam particle using the simulations, details of which will be treated in the next section.

### 3. Simulations and Results

The simulations for rare nuclei  $^{24}\text{O}$ ,  $^{78}\text{Ni}$  and  $^{132}\text{Sn}$  were performed with a program coded with C++. The input parameters are shown in the Table 2. The input parameters are calculated by using LISE++. The maximum voltage for RF cavity is assumed as 100kV and the solid proton as reaction target. The target thickness is determined by the maximum energy compensated in the RF cavity. For instance, the ion with  $Q^+$  of the charge state will be accelerated with 100kV of voltage, therefore, compensated energy per single turn is calculated as  $\delta U = Q \times 1.60 \times 10^{-19} \text{C} \times 100 \text{kV}$ . Hence, the energy loss in the reaction target should not exceed the maximum compensation energy at RF cavity. Target thickness is decided by this restriction.

Ion	T [A MeV]	Target Thickness [mg/cm <sup>2</sup> ]	$\delta U$ [MeV]	$\sigma_{ang}$ [mrad]
$^{24}\text{O}^{8+}$	200	1.13	0.67	0.0553
$^{78}\text{Ni}^{28+}$	200	0.34	2.50	0.0327
$^{132}\text{Sn}^{50+}$	200	0.19	4.43	0.0258

Table 2. Input parameters for simulations. The physical values are calculated by using LISE++.  $\sigma_{ang}$  is the sigma of the angular deviation from multiple scattering per single turn. It is treated as the mean  $\delta\theta$ .

The result for  $^{78}\text{Ni}$  is described here. Figure 3 shows correlation between the emittance growth and the number of turns. The filled circles which include repetitive re-accelerations by RF cavity, show that the emittance is going to equilibrium without divergence. This means that the ionization cooling worked effectively. The equilibrium started from 14000 turns and this result is quite in accord with the simple estimate, as described below. The mean energy loss of  $^{78}\text{Ni}$  in the reaction target  $\delta U$  is 2.5MeV and the total kinetic energy T is 15600MeV. In this case,  $2T/\delta U$  which is the number of turns for the  $1/e$  reduction in emittance, is equal to 12480 and we can expect that the cooling effect will appear at  $\sim 13000$  turns. After 60000 turns, the difference between two lines, i.e. including RF cavity or not, is about  $5.5 \text{mrad}(\sigma_{ang})$ . This difference looks not so significant but, if the number of turns are  $10^6$ , it will increase to  $30 \text{mrad}(\sigma_{ang})$ .

If the storage ring with acceptance of  $\sim 3 \text{mrad}$  is prepared,  $^{78}\text{Ni}$  nucleus can be kept stored until it make a nuclear reaction with a target proton.

### 4. Summary

A simulation study of Ionization cooling is discussed, based on input parameters from LISE++. The ionization energy losses due to many traversals through a reaction target is compensated at each turn by an appropriate RF cavity. We checked that both multiple Coulomb scattering and straggling are "cooled" in two dimension phase space. Particles circulate in the storage ring until they undergo a nuclear process in the reaction target. Hence, the nuclear reaction probability is significantly enhanced with respect to a normal beam line experiment. In this report, we only considered the two dimensional transverse emittance in the storage ring. Further calculations should be done

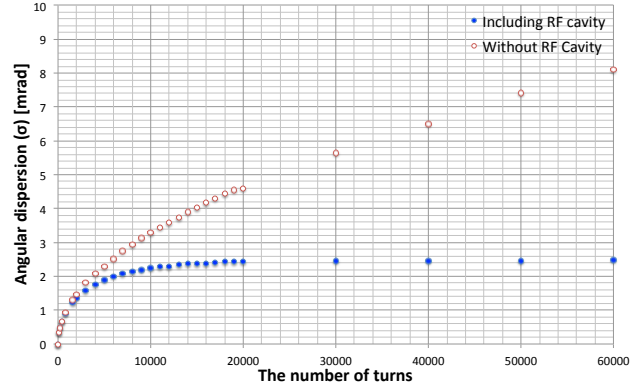


Figure 2. The correlation between the angular dispersion and the number of turns. The transverse angle will diverge (blank circles) with the number of cycles N if there are no re-acceleration at RF cavity. The filled circles, on the other hand, shows that the emittance is going to equilibrium with the number of turns i.e. the cooling effect.

with Monte Carlo method for the longitudinal emittance and the ion optical conditions.

### References

- [1] C. Rubbia *et al.*, Nuclear Instruments and Methods in Physics Research A **568** (2006) 475-487.

# Dynamic nuclear polarization on para-terphenyl at room temperature

T.L. Tang, A. Shiubusawa<sup>a</sup>, T. Kawahara<sup>a</sup>, T. Wakui<sup>b</sup>, T. Uesaka<sup>c</sup>

Center for Nuclear Study, Graduate School of Science, University of Tokyo

<sup>a</sup>Department of Physics, Toho University

<sup>b</sup>Cyclotron and Radioisotope Center, Tohoku University

<sup>c</sup>RIKEN (The Institute of Physical and Chemical Research)

The optimum condition for polarization pulses structure was studied by changing the turn-on timing of microwave irradiation and the laser pulse width. We also studied the time development of polarization. We suggested a model based on the experiment data, to describe the polarization dependence for pulse structure parameters.

Para-terphenyl (C<sub>18</sub>H<sub>14</sub>) doped with 0.05mol% pentacene (C<sub>22</sub>H<sub>14</sub>) was used for polarization. It has high melting point (389°C). Its crystal structure similar to pentacene makes it possible for doping. These factors provide a way for room temperature polarization. In a magnetic field with laser irradiation, the electrons in pentacene are polarized [1]. A microwave at the ESR (electron spin resonance) frequency perpendicular to the direction of the static magnetic field makes the polarization of electrons transferring to protons under the Hartmann-Hahn condition [2] and the degree of proton polarization can be beyond the Boltzmann distribution. The polarization in pentacene is diffused to para-terphenyl's protons through hyperfine interaction.

The experimental system is identical to the previous development [3]. It consists of a magnet, a microwave resonator with a magnetic field sweep coil, a laser feed-in optics and a NMR system for measuring proton polarization. By use of magnetic field sweep, ESR frequency broadening can be compensated. The polarization was evaluated by the area of FID (free induction decay) signal. We assumed the Hartmann-Hahn condition had been fulfilled and unchanged in this study.

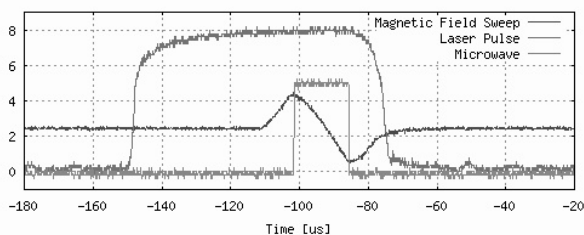


Figure 1. Timing scheme of polarization cycle around the laser pulse. The Magnetic field sweep was shifted up that the horizontal line is zero.

A typical timing scheme of polarization cycle is shown in Fig.1. It can be divided into 3 stages. First, the electrons are polarized during the laser pulse, then a microwave is applied to transfer the electron polarization to the nuclear polarization. The decay of electron excited state polarizations occurred during laser-off time. The reasons for using a pulsed laser are 2-fold: 1) the electron magnetization reaches a maximum at

certain time and 2) Exceed laser irradiation should be avoided due to the proton-electron relaxation. There is a "residual" electron polarization at the end of each cycle when the "laser-off" time is same order with the electron relaxation time (Fig. 2). This residual polarization will reduce the starting polarization at the next cycle. However, the population will reach a dynamic equilibrium after many cycles.

Table 1. Experiment Conditions

Magnetic field	0.3T
Laser	Argon 514.5nm, Multi-line
Crystal Size	6mmX2mmX2mm
Doping	0.05mol%
s ESR level	$ m = 0\rangle \leftrightarrow  m = -1\rangle$
Microwave	
Frequency	9.17 GHz
Power	0.5W
Pulse width	16 us
Magnetic Field Sweep	
pulse frequency	30kHz
field strength	$\pm 4$ mT
NMR	
frequency	12.67MHz
pulse width	2.2 $\mu$ s
power	Level=300

We measured microwave turn-on timing  $t_\mu$  for different laser output power  $P$  (Fig.2). The proton polarization indicated the electron polarization at that particular time. If we assume a simple model that:

$$\frac{dP_p}{dt} = -BP_p + \frac{AN}{2}(P_e - P_p) = \frac{AN}{2}P_e - \left(\frac{AN}{2} + B\right)P_p$$

where,  $A$  is the polarization transfer rate.  $B$  is the nuclear spin relaxation rate and  $N = N_0 + N_{-1}$  is the total population of the electron triplet state  $|m = 0\rangle$  and  $|m = -1\rangle$ . The electron population and polarization is assumed to be constant during the polarization transfer. Converting this rate equation into difference equation by discretization. We solved it and assuming the number of cycle is large, we get

$$P_p(n) \propto N_0 - N_{-1} = \Delta N_e$$

It tells us that the proton polarization is proportional to the difference between state  $|m = 0\rangle$  and  $|m = -1\rangle$ .

The electron polarization (or triplet state populations) was building up during the laser pulse. It de-

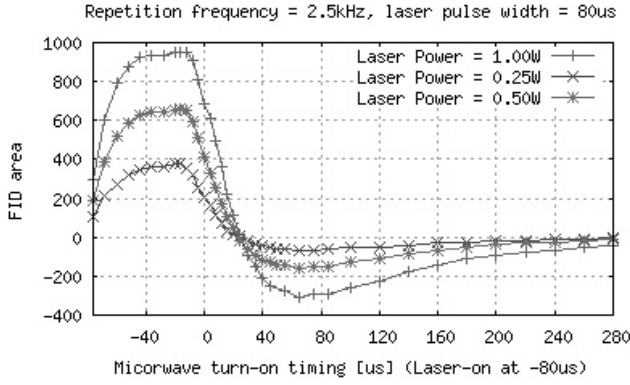


Figure 2. Polarization vs microwave timing for different laser output powers. The time zero is laser pulse end.

creased after the laser pulse had been over. It then reverted at around  $20\mu s$ . It is because the decay of  $|m = 0\rangle$  state is much faster than  $|m = -1\rangle$  state. By fitting the curves, we obtained the decay time constants are  $25\mu s$  ( $|m = 0\rangle$ ) and  $85\mu s$  ( $|m = -1\rangle$ ) consistently for all 3 curves in Fig. 2. The microwave pulse width is  $16\mu s$ . When the microwave applied at  $t = -8\mu s$ , half of the time is "laser-on", another half is "laser-off", resulting an averaging of the polarization.

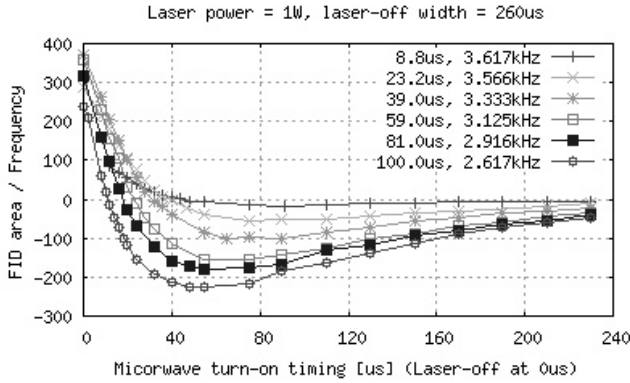


Figure 3. Laser pulse width with fixed "laser-off" width =  $260\mu s$ . See text for explanation.

If the laser-off width had been fixed and the laser pulse width was varied, the  $\Delta N_e$  can be revealed. Fig. 3 shows the results for laser-off width is  $260\mu s$ . The microwave pulse width is  $16\mu s$ , we have to stop before  $240\mu s$ . The laser pulse width about  $39\mu s$  to  $59\mu s$  gives maximum polarization. This indicated that the maximum of  $\Delta N_e$  is around  $45\mu s$ . The residual polarization is almost zero at the end of a cycle, thus, the residual effect can be neglected. The amplitudes of the FID area were divided by frequency to get the polarization of 1 cycle.

The amount of polarization transfer in one cycle should depend on the microwave pulse width setting (the turn-on timing and pulse width) and the Hartmann-Hahn condition. Therefore, the polarization transfer rate  $A$  should be equal to  $A = \gamma f$ , where  $\gamma$  is the probability of polarization transfer in 1 cycle and  $f$  is the laser repetition frequency. Thus, it is more

natural to talk about number of cycles than total polarization time in the buildup curve. In Fig.4, all curves for different repetition frequency are the same, except at the tail. That may be due to the laser pulse width difference or the spin relaxation.

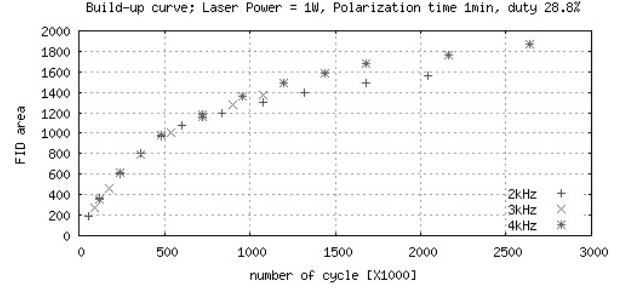


Figure 4. Buildup time in term of number of cycles.

After the above study, we propose a phenomenological model for proton polarization

$$P_p(t) = K(n) \int_{t_\mu}^{t_\mu + T_\mu} \Delta N_e(t; t_p, t_d, P) dt$$

where, the  $K(n) \propto (1 - \exp(-n/n_0))$  relates with the buildup curve.  $n$  is the number of cycle.  $n_0$  is the buildup constant.  $t_p, t_d$  are the laser on-off time.  $P$  is laser power.  $t_\mu, T_\mu$  are microwave turn-on timing and pulse width. The electron polarization can be modeled as a rate equation

$$\frac{d\vec{N}}{dt} = R \cdot \vec{N}, \quad \vec{N} = (N_{S_1}, N_1, N_0, N_{-1}, N_{S_0})$$

where  $N_{S_1}, N_1, N_0, N_{-1}$  and  $N_{S_0}$  are population of the electron first excited, triplet states and ground state, respectively.  $R$  is the transition rate matrix. The calculation and simulation is on another report.

In conclusion, the laser pulse width and repetition frequency can greatly affect the proton polarization due to the electron triplet state population and the number of cycles in given polarization time. Since the proton polarization is bounded by the electron polarization, the ideal microwave wave turn-on timing is  $40$  to  $50\mu s$  from the beginning of laser pulse. We have no clear data on the residual effect, but we expect a long relaxation time ( $\gg 85\mu s$ ) will be able to minimized the drawback. Thus, the optimum setting is that, repetition frequency is around  $8kHz$ , duty is  $30\%$  and the microwave pulse overlap and end with the laser pulse.

## References

- [1] M. Iinuma *et al.*, Phys. Rev. Lett. **84**, 171 (2000).
- [2] S.R. Hartmann and E.L. Hahn, Phys. Rev. **128**, 2042 (1962).
- [3] T. Wakui *et al.*, Nucl. Instrum. Methods A **550** 521 (2005)

# Laser pulse structure dependency on proton polarization of para-terphenyl at room temperature

T.L. Tang, T. Uesaka<sup>a</sup>

Center for Nuclear Study, Graduate School of Science, University of Tokyo  
<sup>a</sup>RIKEN (The Institute of Physical and Chemical Research)

The time development of proton polarization of para-terphenyl at room temperature depends on the structure of polarization cycle, the electron triplet state population, the inter-system crossing rate, the polarization transfer rate, the relaxation of electrons and protons spin, etc. Therefore, the optimum condition for polarization depends on many parameters. By comparing the experimental results, it is possible to deduce those parameters and understand the polarization mechanism. This report focuses on the theoretical aspect and a mathematical model from first principle.

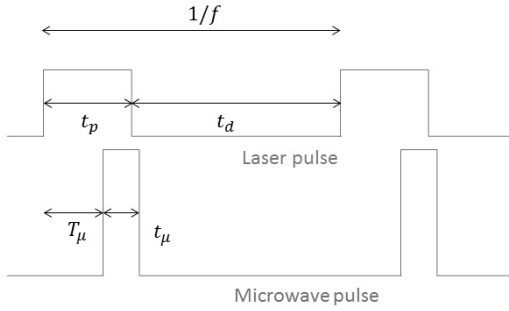


Figure 1. Simplified polarization cycle.

Pulsed laser dynamic nuclear polarization can be divided in 3 phases. A simplified polarization cycle is shown in Fig. 1. First, the electrons are excited and polarized by laser irradiation [1](Fig. 2). Then, the polarization of electron is transferred to nucleus by microwave irradiation at the ESR (electron spin resonance) frequency [2] [3]. The last phase is the relaxation of triplet states electrons to the ground state [1] and polarization diffusion among the polarized proton and its neighbor protons. Calculation of proton polarization will be separated into 3 parts: 1) time development of electron population, 2) residual effect of polarization cycle and 3) the rate equation of proton polarization.

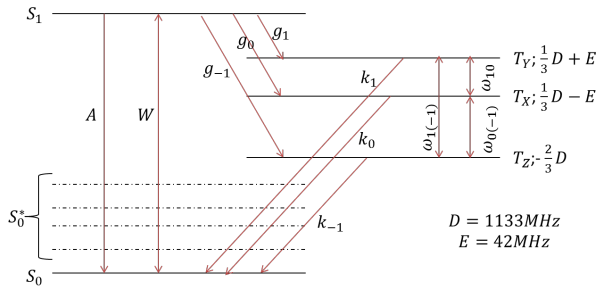


Figure 2. Simplified excited state of pentacene.  $S_0^*$  are vibration states.  $T_X$ ,  $T_Y$  and  $T_Z$  are the energy level of triplet states in pentacene's frame.

The excited energy levels of pentacene, which is the polarization agent, is shown in Fig. 2. The electron population among the first excited singlet state  $S_1$ , the ground state  $S_0$ , and the first triplet state  $N_1, N_0, N_{-1}$  in  $T_1$ , can be calculated by a rate equation:

$$\frac{d\vec{N}}{dt} = R \cdot \vec{N}, \quad \vec{N} = (N_{S_1}, N_1, N_0, N_{-1}, N_{S_0}) \quad (1)$$

where  $R = [R_{ij}]$  is the transition rate matrix between state  $j$  to state  $i$ . For example,  $R_{21} = g_1$  is the transition rate from  $S_1$  to  $N_1$ . We compared the numerical values of the transition rate from ref. [4] [5] [6]. We found that only the order of magnitude of the values are consistent. Therefore, we reproduced the parameters in order to produce similar result with the experiment. The solution of the rate equation is simple due to the time-independent rate matrix  $R$ , which is:

$$\vec{N}(t) = e^{Rt} \cdot \vec{N}(0) \quad (2)$$

Similarly, the solution of the population for laser-off is:

$$\vec{N}(t) = e^{R_0 t} \cdot \vec{N}(0) \quad (3)$$

where  $R_0$  is the transition rate matrix when laser-off, i.e. The term  $W$  in Fig. 2 becomes zero. The parameters are listed on Table 1. The parameter  $k_0$  and  $k_{-1}$  are deduced from our experiment that the decay time constant for  $|m = 0\rangle$  is  $25 \mu s$  and  $|m = -1\rangle$  is  $85 \mu s$  (see another report). The simulated evolution of the populations of the triplet state are shown in Fig. 3.

Table 1. Simulation Parameters [ $\times 10^6 s^{-1}$ ]

$A$	50 #
$W$	$0.2^* \times \text{Laser power [W]}$
Laser power	1W
$g_1$	0.100*
$g_0$	1.000*
$g_{-1}$	0.100*
$k_1$	0.0118*
$k_0$	0.040†
$k_{-1}$	0.0118†
$\omega_{10}$	0.005*
$\omega_{0-1}$	0.005*
$\omega_{1-1}$	0

# from [6]

\* guess value

† experimental value

The relaxation of electron polarization occurs during "laser-off" (Fig. 1). If some electrons left on the excited state at the beginning of next laser pulse, the populations in the next cycle will be affected. If we

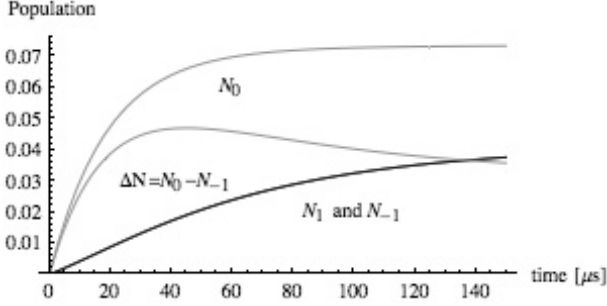


Figure 3. Triplet state population.

denote the population during the  $n$ -th laser pulse be  $\vec{N}_n(t)$ , the laser pulse width be  $t_p$  and laser-off width be  $t_d$ , we have

$$\vec{N}_n(t) = e^{Rt} \cdot \Omega^{n-1} \cdot \vec{N}_0(0), \quad \Omega = e^{Rt_d} \cdot e^{Rt_p} \quad (4)$$

The simulations are shown in Fig. 4 and 5. The simulated laser pulse width is  $80 \mu\text{s}$  and frequency  $6.25 \text{ kHz}$ . The population reaches equilibrium after 30 cycles. The residual population increases  $N_{-1}$  and reduces the magnetization ( $= \Delta N = N_0 - N_{-1}$ ). Comparing with the number of cycle in a polarization process (at least 60,000 cycles), the populations are unchanged. We can compare the result with with experiment data (in other report), such that the proton polarization is proportional to the electron magnetization (equation (9)). There are some similar features in Fig. 4 and experiment results. The magnetization has a maximum around  $50 \mu\text{s}$ . The magnetization inverted around  $20 \mu\text{s}$  after the laser pulse.

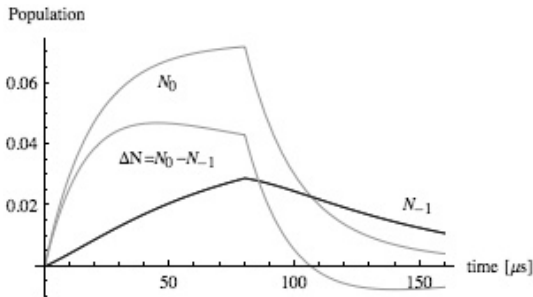


Figure 4. Triplet state population on 1st cycle. See main text.

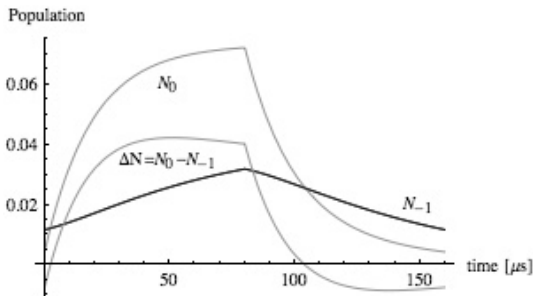


Figure 5. Triplet state population on 15th cycle. The curves are periodically continuous.

A detail calculation of polarization transfer rate on Solid Effect (SE) and Integrated Solid Effect (ISE) can be found in ref. [3]. Instead of following the calculation, we use a phenomenological approach that the proton

polarization rate equation are:

$$\frac{d\rho_{\uparrow}}{dt} = \frac{B}{2}(+\rho_{\downarrow} - \rho_{\uparrow}) + \frac{A}{2}(+N_0\rho_{\downarrow} - N_{-1}\rho_{\uparrow}) \quad (5)$$

$$\frac{d\rho_{\downarrow}}{dt} = \frac{B}{2}(-\rho_{\downarrow} + \rho_{\uparrow}) + \frac{A}{2}(-N_0\rho_{\downarrow} + N_{-1}\rho_{\uparrow}) \quad (6)$$

where,  $\rho_{\uparrow}$ ,  $\rho_{\downarrow}$  are proton spin-up or spin down population.  $A$  is the polarization transfer rate, which depends on the microwave timing and the Hartmann-Hahn condition.  $B$  is the nuclear spin relaxation rate and  $N = N_0 + N_{-1}$  is the total population of electron triplet state  $|m = 0\rangle$  and  $|m = -1\rangle$ . The electron population is assumed to be constant during the polarization transfer. The polarization is:

$$P_p = \frac{\rho_{\uparrow} - \rho_{\downarrow}}{(\rho_{\uparrow} + \rho_{\downarrow} = 1)}, P_e = \frac{N_0 - N_{-1}}{(N_0 + N_{-1} = N)}$$

$$\frac{dP_p}{dt} = \frac{AN}{2}P_e - \left(\frac{AN}{2} + B\right)P_p \quad (7)$$

Converting this differential equation into a difference equation by discretization. The polarization in the  $n$ -th laser pulse is  $P(n)$ ,

$$P_p(n) - P_p(n-1) = \frac{AN}{2f}P_e - \left(\frac{AN}{2f} + \frac{B}{f}\right)P_p(n-1) \quad (8)$$

the electron polarization and population does not change with  $n$  due to the equilibrium for large  $n$  shown in Fig. 5. Solving for the difference equation, we get:

$$P_p(n) = \frac{AN}{AN + 2B}P_e \left(1 - \left(1 - \frac{1}{f} \left(\frac{AN}{2} + B\right)\right)^n\right) \quad (9)$$

In summary, the values of the rate matrix's elements (Table 1) to produce the electron magnetization ( $\Delta N$ ). The residual effect was also studied. It turns out that the electron populations reached dynamic equilibrium after 30 cycles. The electron population was assumed that it does not change during polarization transfer and the proton polarization time development is derived in equation (9). A further study on a coupled equation on electron population and proton population should be solved to get a realistic rate equation. The quantum mechanics treatment [3] should also be applied.

## References

- [1] M. Iinuma *et al.*, Phys. Rev. Lett. **84**, 171 (2000).
- [2] S.R. Hartmann and E.L. Hahn, Phys. Rev. **128**, 2042 (1962).
- [3] Tom Wenckebach, Dynamic Nuclear Polarization using Photocited Triplet States (not published)
- [4] Sloop D *et al.*, 1981 J. Chem. Phys. **75** 3746
- [5] Labuz, M. and Kuzma, M., Phys. Status Solidi B **244** 2480. (2007)
- [6] T. Wakui *et al.*, Nucl. Instrum. Methods A **550** 521 (2005)

# Beam Scanner of The HyperECR

S. Watanabe, Y. Ohshiro, S. Yamaka, S. Kubono, H. Yamaguchi, S. Shimoura, Y. Kotaka<sup>a</sup>,  
M. Kase<sup>a</sup>, K. Hatanaka<sup>b</sup>, A. Goto<sup>c</sup>, W. Yokota<sup>d</sup>, T. Mitsumoto<sup>e</sup>

*Center for Nuclear Study, Graduate School of Science, University of Tokyo*

<sup>a</sup>*Nishina Center for Accelerator-Based Sciences, RIKEN*

<sup>b</sup>*Reserch Center for Nuclear Physics (RCNP), Osaka University*

<sup>c</sup>*National Institute of Radiological Sciences (NIRS)*

<sup>d</sup>*Japan Atomic Energy Research Institute (JAERI)*

<sup>e</sup>*Sumitomo Heavy Industry (SHI)*

## 1. Introduction

The HyperECR [1] [2] [3] is capable of producing gaseous and metallic ion species, but many other kinds are extracted together, which include the ions with different charge states, those from different isotopes, from assist gas, and from residual gas. A mass analyzing system is used to select a particular ion injected to the AVF cyclotron. However, it is often very difficult to select a specific ion out of ions with similar  $q/M$ . Recently, we introduced a new beam diagnostic system to improve the mass analyzing problem. In this report, performance of a beam scanner is described. A beam viewer to observe the beam structure of injection beam is also described.

## 2. Principle of the beam scanner

Figure 1 shows a schematic view of the beam scanner located at beam focusing position of the analyzer magnet of the HyperECR. Ion beam of  $^{29}\text{Si}^{8+}$  is observed, for example, by the beam scanner while  $^{28}\text{Si}^{8+}$  is injected into the AVF cyclotron. Since relative abundance between  $^{29}\text{Si}$  and  $^{28}\text{Si}$  is known,  $^{28}\text{Si}^{8+}$  intensity can be monitored nondestructively by measuring the  $^{29}\text{Si}^{8+}$  intensity with the beam scanner.

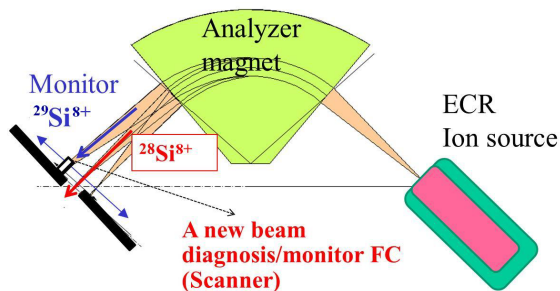


Figure 1. Schematics of the beam scanner.

The beam scanner is located at image point of the mass analyzer magnet in a low energy beam transport line (LEBT) of the AVF cyclotron. Figure 2 shows horizontal and vertical beam envelopes of the LEBT calculated with WinAGILE. Transverse beam emittances of 138(H), 91(V)  $\pi\text{mm}^*\text{mrad}$  are estimated in this calculation. The beam scanner is indicated by "Scanner" in Fig.2. The beam probe is moved horizontally to scan the beam, and records the beam intensity at each position.

The beam scanner observes the ion beam of  $M^{(q-1)+}$  or  $M^{(q+1)+}$ , while providing the beam of  $M^{q+}$ . If both the ion beam profiles are observed by using the beam

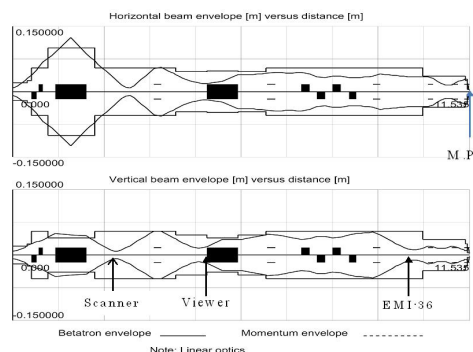


Figure 2. Calculated beam envelopes of the LEBT.

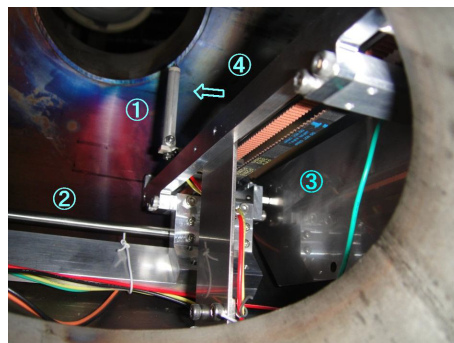


Figure 3. Photograph of the beam scanner.

scanner, distance of each is calculated as follows: A magnetic rigidity  $B\rho$  of the analyzed beam is given by  $(B\rho)^2 = 2Vm_pM/qe$ , where  $V$  is an extraction voltage of the HyperECR. Distance between both the ion beams is given by  $\eta dp/p$ . The  $\eta$  and  $dp/p$  denote a horizontal dispersion and a mean relative momentum deviation at the image point, respectively.

## 3. Mechanical structure and performance of the beam scanner

Figure 3 shows the beam scanner located at the image point of LEBT, which is indicated by "Scanner" and arrow in Figure 2. Numbers in the figure are; 1 a new beam diagnosis/monitor FC (probe), 2 a metal shaft, 3 a timing belt, 4 a direction of the ion beam coming from the HyperECR. The probe is hold on the timing belt. The timing belt is driven by the external pulse motor through the metal shaft with a gear box. A scanning accuracy of the probe is designed at 0.14 mm/pulse. A new beam diagnostic system composed of the beam scanner, a N-DIM and a computer system take the scanned beam data. Figure 4 shows the beam

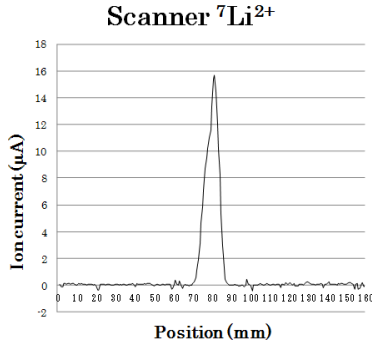


Figure 4. Beam profile of  ${}^7\text{Li}^{2+}$  measured by the beam scanner.



Figure 5. Photograph of irradiated KBr phosphor plate.

profile of  ${}^7\text{Li}^{2+}$  acquired by the one. X-axis represents a probe position. Y-axis represents an intensity of the ion beam. Floor noise is appeared however averaging is carried out. Shape of the beam is not Gaussian because of the ion beam structure.

The horizontal dispersion  $\eta$  was measured by using the beam scanner. Measured ion beam position and the magnetic field of the mass analyzer gave the  $\eta$  of 2.351m, however WinAGILE gives 2.201m.

#### 4. Beam Viewer

Study of the ion beam structure of the HyperECR is very important to improve the performance of the AVF cyclotron. A beam viewer is located at an entrance of a vertical bending magnet in the LEBT, which is indicated by "Viewer" in Figure 2. The viewer is composed of KBr phosphor plate placed with a tilting angle of 45 degrees with respect to the beam direction. For reference purpose, through-holes are provided on the KBr phosphor plate. A beam image will be taken by a CCD-camera, when the one intercepts the ion beam flux.

Figure 5 shows the beam image of  ${}^7\text{Li}^{2+}$  beam. An image data is converted to a surface plot data as shown in Figure 6. Computer simulation shows that the surface plot data and the ion beam profile measured by the beam scanner have a correlative structure and intensities. If the beam image is taken with the viewer at the beam scanner position, transverse projection of the beam image should be identical to the beam profile shown in Fig. 4.

#### 5. Summary

The beam scanner was installed in the image point of the mass analyzer of the HyperECR. When the  $M^{q+}$  ion is selected as an extracted beam, peaks correspond-

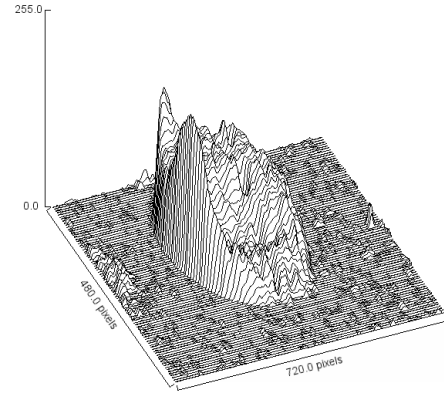


Figure 6. Surface plot data of  ${}^7\text{Li}^{2+}$  beam.

ing to  $M^{(q-1)+}$  or  $M^{(q+1)+}$  have been observed in the beam scanner. The beam viewer using the KBr is installed in the HyperECR beam line. Specifications of the beam scanner is tableted in Table 1.

Table 1. Specifications of the beam scanner

No	Name	Parameter
1	Beam Scanner	
	Probe Diameter	4 mm
	Probe E. Length	32 mm
	Probe Material	Tungsten
	Shield with 4 mm slit	SUS, 6 mm $\phi$
2	Analyzer Magnet	
	Bending Angle	90°
	Focusing Length	1.085 m

#### References

- [1] Y. Ohshiro et al. RRIKEN Accel. Prog. Rep. 35 (2002) 256
- [2] Y. Ohshiro et al. RRIKEN Accel. Prog. Rep. 38 (2005) 253
- [3] Y. Ohshiro et al. RRIKEN Accel. Prog. Rep. 39 (2006) 231

# Test operation of new extraction system

Y. Ohshiro, S. Yamaka, S. Watanabe, H. Muto<sup>a</sup>, H. Yamaguchi, and S. Shimoura

Center for Nuclear Study, Graduate School of Science, University of Tokyo

<sup>a</sup>Center of General Education, Tokyo University of Science, Suwa

## 1. Introduction

A plan to increase the beam intensity of a multi-charged heavy ion has been promoted by CNS and RIKEN group for upgrading the AVF Cyclotron at the RIBF facilities. The Maximum efficiency from a Hyper ECR ion source [1] to the Cyclotron is now approximately 30% when operating with a  $^{22}\text{Ne}^{7+}$  ion beam. Our aim is to get the best efficiency for all of ion species. Recently, a new extraction system called “virtual object type” was installed in the Hyper ECR ion source. This system can achieve high transmission efficiency by means of a small spot aperture of an extraction electrode. In this paper, we report the development of this virtual object type and some results of test operation.

## 2. Beam extraction system

Fig. 1 shows a schematic drawing of the Hyper ECR ion source. A beam extraction system of conventional type is set underneath the plasma chamber [2]. This system consists of a plasma electrode and a ground one. The shape of two electrodes is a concave to the beam direction. Ions are accelerated by a concave equipotential surface generated between the two electrodes. So, a virtual starting point of the beam in this system becomes either large or fuzzy because ions pass through a beam waist formed near a ground electrode.

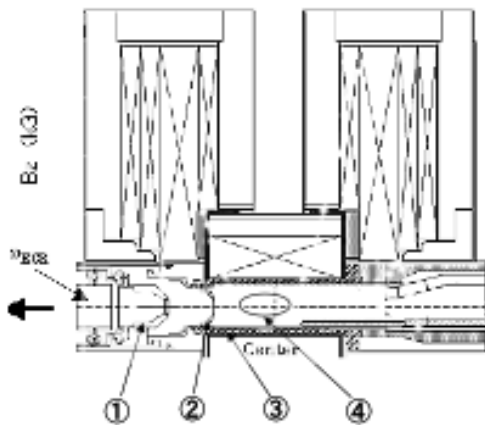


Figure 1. Schematic drawing of the Hyper ECR ion source.

① Ground electrode ② Plasma electrode ③ Plasma chamber ④ ECR zone

The new extraction system is shown in Fig. 2. The plasma electrode and the ground one are convex shape in the beam direction. Then, the virtual starting point of the beam is one point in a plasma chamber since the trajectories of the ions are divergent. The inner diameter of the plasma chamber is 5 cm. The hole of plasma electrodes and ground one is 1.2 cm and 1.6 cm in diameter, respectively. The gap between two

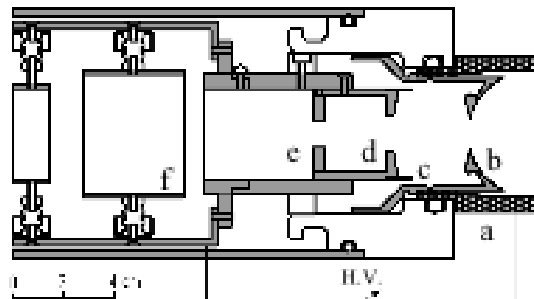


Figure 2. Cross section of the new extraction system of the Hyper ECR ion source. a. Plasma chamber b. Plasma electrode c. potential correction ring d. ground electrode e. collimator f. Einzel lens

electrodes is 3.5 cm.

## 3. Ion beam trajectory

In the ECR ion source, ions are emitted in the plasma meniscus near the plasma electrode. In many cases this meniscus can be considered as a sphere that has its axis inside the plasma chamber. If all ions emitted by the sphere have radial trajectories they seem to originate from a virtual line that can be used as an object in an optical system of convex lens. Ion beam trajectories of the new extraction system calculated by the IGUN code are shown in Fig. 3. A  $^{22}\text{Ne}^{7+}$  ion beam was simulated with an extraction voltage of 10 kV. The calculation results are as follows. 1) Spherical potential field is generated between the two electrodes. Therefore, the extraction system is designed so that ions may start from one point in the plasma chamber. 2) The trajectories are well separated from one another and the distribution is homogeneous (See Fig. 3). So, the high quality beam to have the flat top can be extracted from this system.

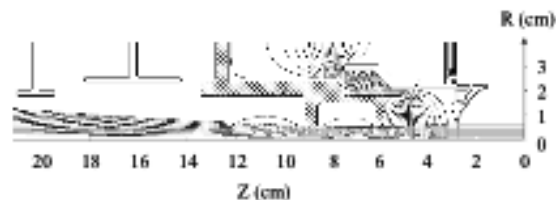


Figure 3. Beam trajectory of the virtual object extraction system calculated by IGUN code.

## 4. Results and discussions

The new extraction system has been installed in the Hyper ECR ion source and operated for 10 days beam time of the AVF Cyclotron without any troubles. The

beam was obtained by two times as high intensity as this compared with the conventional extraction system because the new system succeeded in reducing beam loss at the beam analyser of the ECR source. We operated Ar11+, Ne7+, O6+ ion beams and their intensities were 80, 88 and 150 eμA, respectively. We are going to introduce an accel-decel extraction method into the present system, to improve the beam emittance and to enhance the beam intensity at the cyclotron exit.

As mentioned above, beam loss at the beam analyzer of the ECR source was reduced. The reason of this improvement is considered that the beam emittance is smaller than the conventional system. So, test of the new extraction system has been done with a good result. On the other hand, new problems are arising such as a breakdown of the insulator of the high voltage system. Since the surface of the insulator near the potential correction ring is exposed to the plasma, improvements in the vacuum condition or a surface treatment will be considered. This problem will be solved in the near future.

Second problem is to find the optimum operation parameter for many kinds of ion species. In order to achieve a high intensity ion beam for many kinds of ion species, good performance of either ion source or LEBT has to be studied using the conventional extraction system. Similarly the trial error will be carried out by using the new extraction system.

Finally, beam transmission efficiency at the AVF cyclotron will be evaluated.

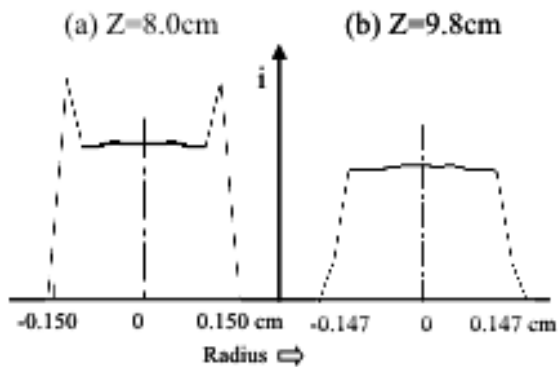


Figure 4. Typical cross section of the ion beam trajectory calculated by IGUN code. (a) at 8 cm from origin (b) at 9.8 cm from origin

## 5. Summary

We developed and installed an extraction system of virtual object type at the Hyper ECR ion source. The system has worked without any troubles. Reducing the divergence of the beam at the extraction point is expected to produce beams of better quality at the AVF Cyclotron.

## References

1. Y. Ohshiro et al., CNS. Annual Report 2000 (2001) 5.
2. Y. Ohshiro et al., CNS. Annual Report 2003 (2004) 71.



# Theoretical Nuclear Physics



# $\beta$ -Decays of Waiting-point Nuclei at $N=126$ and R-Process Nucleosynthesis

T. Suzuki, T. Yoshida<sup>a</sup>, T. Kajino<sup>b,a</sup> and T. Otsuka<sup>c,d</sup>

*Department of Physics, College of Humanities and Sciences, Nihon University*

<sup>a</sup>*Department of Astronomy, Graduate School of Science, University of Tokyo*

<sup>b</sup>*National Astronomical Observatory of Japan*

<sup>c</sup>*Center for Nuclear Study, Graduate School of Science, University of Tokyo*

<sup>d</sup>*National Superconducting Cyclotron Laboratory, Michigan State University, East Lansing, Michigan, 48824, USA*

The r-process is the most promising process for the synthesis of about a half of heavy elements beyond iron [1]. Study of the r-process element synthesis has been done by considering neutrino-driven winds in supernova explosions [2] as well as ONeMg supernovae [3] and neutron-star mergers [4].

The evaluation of  $\beta$ -decay rates, particularly at the waiting point nuclei, is one of the important issues of the nucleosynthesis through the r-process. Investigations on the  $\beta$ -decays of isotones with neutron magic number of  $N=82$  have been done by various methods including shell model [5], QRPA/FRDM [6] as well as CQRPA ones [7] etc., which lead to results consistent to one another.

For the  $\beta$ -decays at  $N=126$  isotones, however, half-lives obtained by various calculations differ to one another [8]. First-forbidden (FF) transitions become important for these nuclei in addition to the Gamow-Teller (GT) transitions in contrast to the case of  $N=82$ . Beta decays of the isotones with  $N=126$  are studied by shell model calculations taking into account both the Gamow-Teller (GT) and first-forbidden (FF) transitions. The FF transitions are found to be important to reduce the half-lives, by nearly twice to several times, from those by the GT contributions only as shown in Fig. 1 [9].

The present half-lives of the shell model calculations are shorter than those of the standard values of ref. [6] by 2.3~8.3 for even  $Z$  and by 1.4~2.0 for odd  $Z$  (except for  $Z=71$ ), respectively. They increase monotonically as  $Z$  increases showing no odd-even staggering found in FRDM's. The present half-lives are longer than those of Ref. [7] by about 1.1~1.3 (1.5) for  $Z=64\sim 67$  (68) and by twice for  $Z=69$  and 70, respectively.

Possible implications of the short half-lives of the waiting point nuclei on the r-process nucleosynthesis during the supernova explosions are investigated. We use an analytic model for neutrino-driven winds [10] for the time evolution of thermal profiles. The third peak of the abundance of the elements in the r-process has been found to be shifted toward higher mass region as shown in Fig. 2. Although the magnitude of the shift is rather modest, it is found to be a robust effect independent of the present astrophysical conditions for the r-process as well as the quenching factors of  $g_A$  and  $g_V$  adopted in the shell model calculations [9].

Recently,  $\beta$ -decay half-lives of nuclei in the region  $A=100-120$  were measured at RIKEN, and they are found to be shorter compared to those of FRDM in most of the nuclei [11]. It would be important to obtain more data of half-lives in drip-line nuclei in future.

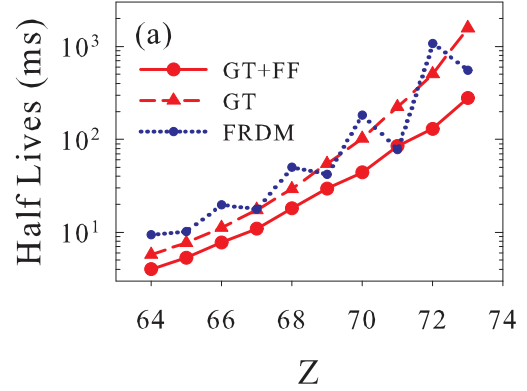


Figure 1. Calculated half-lives for the  $N=126$  isotones. Results of the present shell model calculations with GT and with GT+FF transitions are denoted by dashed and solid curves, respectively. The quenching factor of  $g_A/g_A^{\text{free}}=0.7$  is used for both the GT and FF transitions except for  $0^-$  transitions. Half-lives of Ref. [6] denoted as FRDM are shown by a dotted curve..

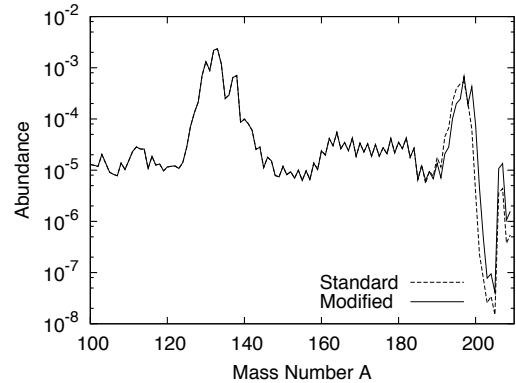


Figure 2. The abundances of elements in the r-process nucleosynthesis obtained by using the present  $\beta$ -decay half-lives for the  $N=126$  isotones (denoted as 'modified') and standard half-lives of ref. [6] (denoted as 'standard'). The quenching factor of  $g_A/g_A^{\text{free}}=0.7$  ( $g_V/g_V^{\text{free}}=1.0$ ) is used both for the GT and FF ( $1^-$  and  $2^-$ ) transitions.

## References

- [1] E. M. Burbidge et al., *Rev. Mod. Phys.* **29** (1957) 547; J. J. Cowan et al., *Phys. Rep.* **208** (1991) 267;

- K.-L. Kratz et al., *Astrophys. J.* **216** (1993) 216.
- [2] B. S. Meyer et al., 1992, *Astrophys. J.* **393** (1992) 656; S. E. Woosley et al., *ibid.* **433** (1994) 229.
- [3] S. Wanajo et al., *Nucl. Phys.* **A777**(2006) 676.
- [4] C. Freiburghaus et al., 1999, *Astrophys. J.* **525** (1999) L121.
- [5] G. Martinez-Pinedo et al., *Phys. Rev. Lett.* **75** (2003) 818.
- [6] P. Moller et al., *At. Data Nucl. Data Tables* **66** (1997) 131; *Phys. Rev. C* **67** (2003) 055802.
- [7] I. N. Borzov et al., *Phys. Rev. C* **67** (2003) 025802.
- [8] K. Langanke et al., *Rev. Mod. Phys.* **75** (2003) 818; H. Grawe et al., *Rep. Prog. Phys* **70** (2007) 1525.
- [9] T. Suzuki et al., *Phys. Rev. C* **85** (2012) 015802.
- [10] K. Takahashi et al., *Origin of Matter and Evolution of Galaxies*, eds. T. Kajino, S. Kubono, and Y. Yoshii (Singapore: World Scientific, 1997) 213.
- [11] S. Nishimura et al. *Phys. Rev. Lett.* **106** (2011) 052501.

# Systematic study of low-lying $E1$ modes using a time-dependent mean field theory

S. Ebata, T. Nakatsukasa<sup>a</sup> and T. Inakura<sup>a</sup>

Center for Nuclear Study, Graduate School of Science, University of Tokyo  
<sup>a</sup>RIKEN Nishina Center

The low-lying electric dipole ( $E1$ ) mode is often called Pygmy dipole resonance (PDR) and known as a characteristic excited state of neutron-rich nuclei. Furthermore, the PDR is important in order to understand the nucleosynthesis on the  $r$ -process path [1]. Despite the increased capability of generating and measuring unstable nuclei with new radioisotope beam facilities, it is still difficult to study nuclei on the  $r$ -process path. Hence, we strongly need a method to predict and analyze the excited state of exotic nuclei in the very neutron-rich and heavy region, such as nuclei on the  $r$ -process path. For a systematic theoretical investigation of exotic nuclei, we need to consider the effects of deformation and pairing correlation.

We proposed the canonical-basis time-dependent Hartree-Fock-Bogoliubov (Cb-TDHFB) theory [2] in the three-dimensional coordinate-space representation for studies of nuclear dynamics, which can account for any type of deformation, treating the pairing correlation in the Bardeen-Cooper-Schrieffer (BCS)-like approximation. The Cb-TDHFB equations can be derived from the full TDHFB equation [2]. They are written as

$$i\hbar\dot{\phi}_l(\mathbf{r}, t) = (\hat{h}[\rho(t)] - \eta_l(t))\phi_l(\mathbf{r}, t), \quad (1)$$

$$i\hbar\dot{\rho}_l(t) = \Delta_l^*(t)\kappa_l(t) - \Delta_l(t)\kappa_l^*(t), \quad (2)$$

$$i\hbar\dot{\kappa}_l(t) = (\eta_l(t) + \eta_{\bar{l}}(t))\kappa_l(t) + \Delta_l(t)(2\rho_l(t) - 1), \quad (3)$$

where  $\phi_l(\mathbf{r}, t)$  respects the canonical basis and  $\bar{l}$  denotes a canonical partner of  $l$ -state but does not necessarily related to the time reversal.  $\rho_l(t) = |v_l^2(t)|$  and  $\kappa_l(t) = u_l(t)v_l(t)$  are occupation- and pair-probability.  $u_l(t)$  and  $v_l(t)$  correspond to the time-dependent BCS factors for the canonical pair of states  $\phi_l(\mathbf{r}, t)$  and  $\phi_{\bar{l}}(\mathbf{r}, t)$ .  $\Delta_l(t) \equiv -\sum_{k>0} \kappa_k(t)\bar{V}_{l\bar{k}, l\bar{k}}$  indicates the pair potential, where  $\bar{V}_{l\bar{k}, l\bar{k}}$  are the antisymmetric two-body matrix elements that are time dependent because canonical-basis  $\{l, \bar{l}\}$  and  $\{k, \bar{k}\}$  are time dependent. We have gauge freedom which is fixed by choosing the time-dependent function,  $\eta_l(t) \equiv \langle \phi_l(t) | \hat{h} | \phi_l(t) \rangle + i\hbar \langle \frac{\partial \phi_l}{\partial t} | \phi_l(t) \rangle$ . Equations (1) - (3) conserve the orthonormality of the canonical basis, the average of particle number and the total energy in real time. Details of the Cb-TDHFB equations and the adopted energy functionals are given in Ref. [2].

We carried out a systematic investigation of the low-lying  $E1$  strength from light to heavy isotopes with a Skyrme energy functional (SkM\* parameter set) for the particle-hole channel. We solved the Cb-TDHFB equations in real time and computed the linear response of the nucleus. For the linear-response calculation, we added an external field  $\hat{V}_{\text{ext}}(\mathbf{r}, t) \equiv -k\hat{F}\delta(t)$  to the HF+BCS or HF ground state with finite or zero gap energy  $\Delta_l$ , respectively, where  $\hat{F}$  is a one-body operator and  $k$  is an arbitrary small param-

eter. In this study, we selected the  $E1$  operator,  $\hat{F}_{E1} = (N/A)\sum_p \hat{r}_p - (Z/A)\sum_n \hat{r}_n$ , here  $r = (x, y, z)$ . We obtained the strength function  $S(\hat{F}_{E1}; E)$  through the Fourier transformation of the time-dependent expectation value of  $\hat{F}_{E1}$ . To quantify the low-lying  $E1$  strength, we used the following ratio:

$$\frac{m_1(E_c)}{m_1} \equiv \frac{\int^{E_c} E \times S(E1; E)dE}{\int E \times S(E1; E)dE}, \quad (4)$$

where  $E_c$  is a cut-off energy. We presumed  $E_c = 10$  MeV in the present work. An example is shown in Fig.1 for  $^{26}\text{Ne}$ .

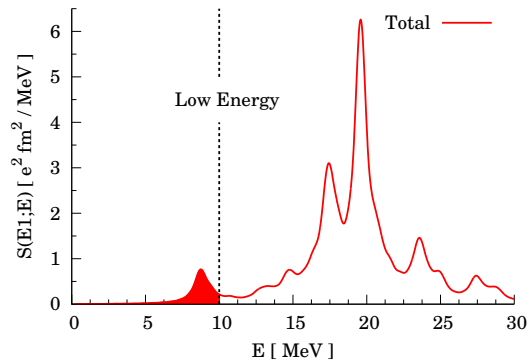


Figure 1.  $E1$  strength function for  $^{26}\text{Ne}$ . Filled part is low-lying  $E1$  strength in our definition. Dashed line denotes 10 MeV.

Figure 2 shows the low-lying  $E1$  ratio defined by Eq.(4) for light even-even isotopes with  $Z = 8 - 12$  and  $N = 8 - 28$ , as a function of neutron number. We can

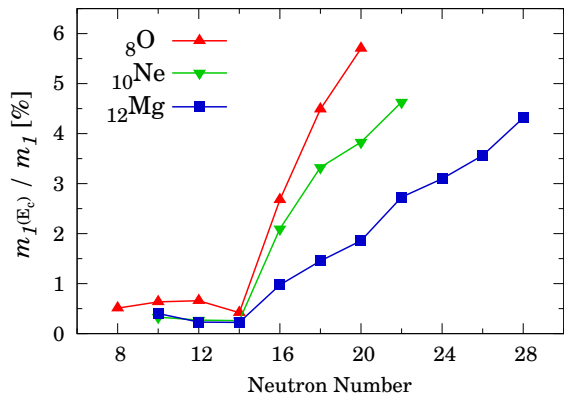


Figure 2. Neutron-number dependence of the low-lying  $E1$  ratio defined by Eq.(4) for O, Ne and Mg isotopes.

see that the nuclei with  $N = 8 - 14$  have the fractions of low-lying  $E1$  strength less than 1.0 [%], and a sud-

den jump of the ratio at  $N = 14 \rightarrow 16$  in each isotopic chain. The neutron number  $N = 16$  corresponds to the occupation of  $s_{1/2}$  orbit. Then, we can also see small jump of the ratio  $N = 20 \rightarrow 22$  which corresponds to shape transition in mean field models. In fact, the shape of HF+BCS ground state changes from spherical to prolate, in Ne and Mg isotopic chain. Figure 2 shows the neutron shell effect on low-lying  $E1$  strength, and suggests that the single-particle orbits near the Fermi level and deformation effects have important roles to increase the low-lying  $E1$  strength [2,3].

Figure 3 shows neutron-number dependence of the ratio for Ni, Zr and Sn isotopes same as Fig.2. We can also see a characteristic kink behavior at  $N = 50$  and  $N = 82$  in each isotopic chain. There are the sudden jumps of the ratio which are similar to the results in Fig.2. They indicate that neutron shell effects are still important for low-lying  $E1$  modes in heavy and unstable neutron-rich region. The deformation effects on the low-lying  $E1$  mode are seen clearly at  $N = 60$  and  $72$ . The shape change takes place at  $N = 58 \rightarrow 60$  (spherical  $\rightarrow$  prolate) and at  $N = 72 \rightarrow 76$  (prolate  $\rightarrow$  spherical) for Zr isotopes. From  $N = 60$  to  $72$ , the shape of Zr isotopes stays at prolate, which corresponds to experimental data [4]. When the shape transitions occur, the low-lying  $E1$  ratios decrease at  $N = 60$  and  $72$ . A similar effect of the shape transition appears at  $N = 20 \rightarrow 22$ , however, its behavior is different from that at  $N = 58 \rightarrow 60$ . We suppose that the deformation effects on the low-lying  $E1$  mode are sensitive to properties of the single-particle orbits in each mass region.

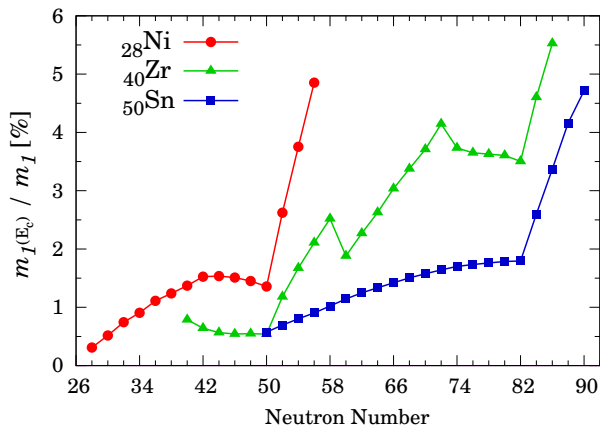


Figure 3. Same as Fig.2, but for Ni, Zr and Sn isotopes.

Figure 4 shows neutron-number dependence of the ratio for heavy neutron-rich even-even isotopes with  $Z = 38 - 54$  and  $N = 78 - 86$ . We can see a sudden jump in the ratio at  $N = 82 \rightarrow 84$  for each isotopic chain. These results also indicate a neutron shell effect on the low-lying  $E1$  strength. However in contrast to light nuclei in Fig.2, we can see sizable values of  $m_1(E_c)/m_1$  for  $N = 78 - 82$ . In light stable nuclei, the calculated low-lying  $E1$  strength is usually very small [2, 3] like results in Fig.2. However,  $^{132-136}\text{Xe}$  which are stable nuclei, have 1.5% of the low-lying  $E1$  ratio. The ratio even increases as the proton number decreases. These features suggest that the PDR in heavy nuclei has different properties from that in light nuclei.

In summary, we carried out the systematic investi-

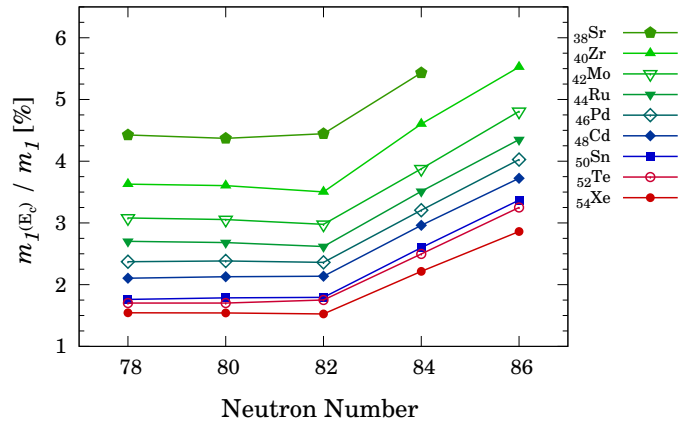


Figure 4. The low-lying  $E1$  ratio for  $Z = 38 - 54$  (Sr to Xe) around  $N = 82$  with respect to neutron number.

gation of the  $E1$  strength function using Cb-TDHF in three-dimensional coordinate space representation which can describe nuclear dynamics with any deformation effects treating pairing correlation in a BCS-like approximation. We showed the neutron number dependence of the low-lying  $E1$  strength which is often called PDR in several isotope chain. In light mass region ( $Z = 8, 10, 12$  with  $N = 8 - 28$ ), the PDR emerges when the isotope has  $N = 16$  which corresponds to occupied  $s_{1/2}$  orbit. In heavy mass region ( $Z = 28, 40, 50$  with  $N = 28 - 90$ ), the low-lying  $E1$  strength grows up from  $N = 52, 84$  dramatically. These special numbers on the low-lying  $E1$  strength are explained as neutron-shell effects in each mass region. In Zr isotopic chain, we showed the characteristic behavior of the low-lying  $E1$  strength at  $N = 58 \rightarrow 60$  and at  $72 \rightarrow 74$  which correspond to shape transition region. We found that heavy nuclei around  $N = 82$  have the low-lying  $E1$  mode whose structure is different from that of neutron-rich light nuclei.

Currently, we are investigating the origin of these differences between heavy stable nuclei and neutron-rich light nuclei. We also plan to use this method to investigate other excitation modes (monopole, quadrupole, scissors, etc.) and heavy ion-collision dynamics.

## References

- [1] S. Goriely, Phys. Lett. B **436**, 10 (1998).
- [2] S. Ebata *et al.*, Phys. Rev. C **82** (2010) 034306.
- [3] T. Inakura, T. Nakatsukasa and K. Yabana, Phys. Rev. C **84** (2011) 021302.
- [4] T. Sumikama *et al.*, Phys. Rev. Lett. **106** (2011) 202501.



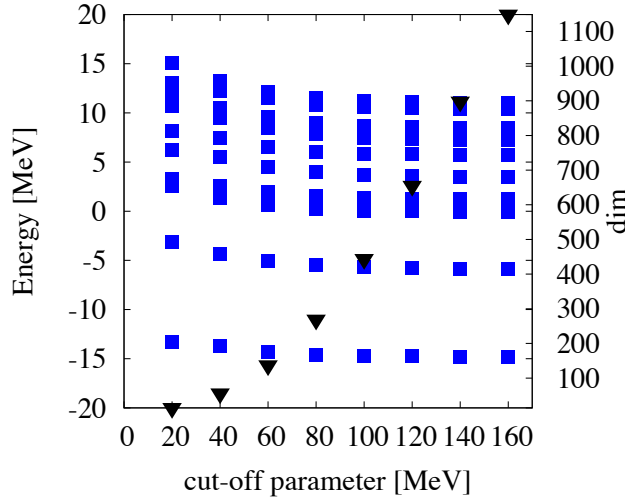


Figure 2. Energy convergence ( $^{16}\text{O}$ ). Here, the triangle dots indicate the demintion of the wavefunction and the squares dots are the  $0^+$  energies.

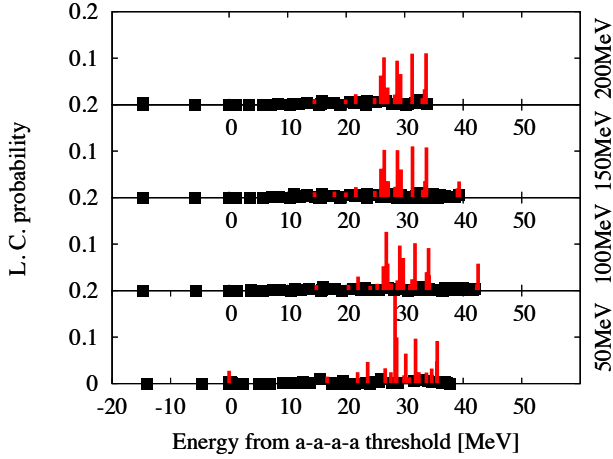


Figure 3. Linear chain region ( $^{16}\text{O}$ ). The black dots show the  $0^+$  energies and the red bars are the probabilities of the L. C. configuration of each eigen state.

To investigate  $^{16}\text{O}$  in a four- $\alpha$  model, we use the  $\mu$ -truncation method. The Pauli allowed basis state is obtained similarly to the three- $\alpha$  case.

$$U_i(\vec{r}, \vec{R}, \vec{\mathcal{R}}) = \sum_{\lambda_{12}, \mu_{12}} A_{(\lambda_{12}, \mu_{12}), N_3}^{(\lambda, \mu) \rho} V_{(\lambda_{12}, \mu_{12}), N_3}^{N(\lambda, \mu) J, \kappa}(\vec{r}, \vec{R}, \vec{\mathcal{R}}),$$

where  $(\vec{r}, \vec{R}, \vec{\mathcal{R}})$  are Jacobi-coordinates to describe four- $\alpha$  clusters. In the  $\mu$ -truncation procedure, the eigen state  $w_k(\vec{r})$  calculated within sub-space which has specific  $\mu$  quanta whose eigen energies are smaller than an appropriate cut-off parameter. This eigen states are expressed by using projection from the original basis to the truncated model space as follows,

$$u_k(\vec{r}, \vec{R}, \vec{\mathcal{R}}) = \sum_i D_i^k U_i(\vec{r}, \vec{R}, \vec{\mathcal{R}}),$$

The calculated result by the four- $\alpha$  cluster model are

mentioned below. In Fig.2, the energy convergence ( $0^+$  states) with respect to the  $\mu$ -truncation cut-off parameter are shown. Here, the model space is prepared within H. O. quanta  $N \leq 32$ . The rapid energy convergence indicates that the effect of  $\mu$ -truncation works well. In Fig. 3, the linear-chain (L. C.) state region is also estimated. Here, the L. C. state is specified by the condition  $\mu = 0$  and  $N = \lambda$ , which is the same as the case of three- $\alpha$  model. The horizontal axes show the  $0^+$  energy from the four- $\alpha$  threshold. The vertical axes show the probabilities of L. C. configuration. The cut-off parameter changes from 50 MeV (lower panel) to 200 MeV (upper panel). With the red bars, the large L. C. strength is emphasized for convenience. The strength is estimated by the overlap between the wave function obtained by the  $\mu$ -truncation including  $\mu \leq 16$  quanta. The results show that the L. C. strength is about 10 % for each cut-off parameter. The strength is smaller than the L. C. states in  $^{12}\text{C}$  which have about 50 % pure L. C. configuration. More large  $N$  quanta and angular momentum are needed to confirm the existence of L. C. as the same level as in the case of three- $\alpha$  cluster mode in future works.

## References

- [1] T. Kawabata *et al.*, Phys. Lett. B, **646**, 6 (2007).
- [2] B. F. Bayman and A. Bohr, Nucl. Phys. **9**, 596 (1959).
- [3] A. Tohsaki, H. Horiuchi, P. Schuck and G. Röpke, Phys. Rev. Lett. **87**, 192501 (2001).
- [4] T. Yamada, Y. Funaki, H. Horiuchi, K. Ikeda and A. Tohsaki, Prog. Theor. Phys. **120**, 6 (2008).
- [5] T. Yoshida, N. Itagaki and K. Katō, Phys. Rev. C **83**, 024301 (2011).
- [6] F. Arickx, Nucl. Phys. A **268**, 347 (1976).
- [7] Y. Suzuki, K. Arai, Y. Ogawa and K. Varga, Phys. Rev. C **54**, 2073 (1996).
- [8] K. Katō and H. Tanaka, Prog. Theor. Phys. **81**, 841 (1989).
- [9] S. Saitō, Prog. Theor. Phys. **41**, 705 (1969).
- [10] H. Horiuchi, Prog. Theor. Phys. **58**, 204 (1977).
- [11] E. W. Schmidt and K. Wildermuth, Nucl. Phys. A **26**, 463 (1961), C. Kurokawa and K. Katō, Nucl. Phys. A **792**, 87 (2007).

# Development of the Monte Carlo Shell Model for K computer

N. Shimizu<sup>a</sup>, Y. Utsuno<sup>b</sup>, T. Abe<sup>c</sup>, Y. Tsunoda<sup>c</sup> and T. Otsuka<sup>a,c</sup>

<sup>a</sup> Center for Nuclear Study, Graduate School of Science, University of Tokyo

<sup>b</sup> Advanced Science Research Center, Japan Atomic Energy Agency

<sup>c</sup> Department of Physics, University of Tokyo

## 1. Introduction

The nuclear theory group at CNS has been promoting the RIKEN-CNS collaboration project on large-scale nuclear structure calculations since 2001 and maintaining its parallel computing cluster [1]. Based on this experience and its achievements, we participated in activities of HPCI Strategic Programs for Innovative Research (SPIRE) Field 5 “The origin of matter and the universe” in 2011. The SPIRE project aims at an integral understanding of the origin and structure of matter and the Universe utilizing the K computer, which is the world’s fastest supercomputer in 2011 [2].

In the SPIRE project, we are in charge of the elucidation of nuclear properties using ultra large-scale simulations of quantum many-body systems. We mainly plan to utilize the Monte Carlo Shell Model (MCSM) method [3], which is a tool to overcome the limitation of the conventional shell-model calculations with the Lanczos diagonalization method. In order to perform large-scale MCSM calculations, we have developed an efficient computer program of the MCSM for massive parallel computation [4] and performed benchmark calculations at the K computer.

## 2. Recent Developments of the MCSM

In the framework of the MCSM, the shell-model wave function is approximated as a linear combination of angular-momentum- and parity-projected Slater determinants,

$$|\Psi_{N_b}\rangle = \sum_{n=1}^{N_b} \sum_{K=-I}^I f_{n,K}^{(N_b)} P_{MK}^{I\pi} |\phi_n\rangle, \quad (1)$$

where  $N_b$  is the number of the Slater-determinant basis states, and  $P_{MK}^{I\pi}$  is an angular-momentum, parity projector. Each  $|\phi_n\rangle$  is a deformed Slater determinant. The coefficients  $f_{n,K}^{(N_b)}$  are determined by the diagonalization of the Hamiltonian matrix in the subspace spanned by the projected Slater determinants,  $P_{MK}^{I\pi} |\phi_n\rangle$  with  $-I \leq K \leq I$  and  $1 \leq n \leq N_b$ . This diagonalization also determines the energy,  $E_{N_b} \equiv \langle \Psi_{N_b} | H | \Psi_{N_b} \rangle$ , as a function of  $N_b$ .

The recent developments and applications of the MCSM are:

- Implementation of the Conjugate Gradient (CG) method.
- Performance tuning of the MCSM code [5].
- Reordering technique to suppress uncertainties of the energy-variance extrapolation [6].
- Applications to no-core shell-model calculations in light nuclei [7, 8].

- Nuclear structure study of neutron-rich Cr and Ni isotopes [9].

These recent activities were reviewed in Ref. [9].

## 3. Parallel Efficiency of the MCSM Code

In this report, we briefly discuss the performance improvement of the developed MCSM code for utilizing state-of-the-art massive parallel computer. The most time-consuming part of the MCSM framework is the variational calculation to obtain the optimized Slater determinant basis states,  $|\phi_n\rangle$  in Eq.(1), one by one sequentially utilizing the CG method. This process is called Sequential Conjugate Gradient (SCG) method [6]. Another time-consuming process of the MCSM framework is to calculate the energy variance of the approximated wave function provided by the SCG method. Here, we show the parallel efficiencies of these two time-consuming processes. We take <sup>72</sup>Ge in *f5pg9* space with JUN45 effective interaction [10] for the benchmark calculation. This benchmark was performed using the Intel Fortran compiler ver.11.0 on the T2K open Supercomputer at the University of Tokyo [11].

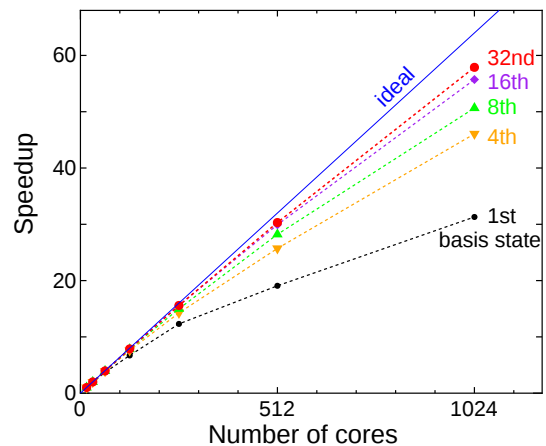


Figure 1. Speedup of the parallel computation of the SCG process in unit of the computation time using 16 CPU cores. The small circles, inverted triangles, triangles, squares, and large circles represent the inverses of computation times of the variational process to obtain 1st, 4th, 8th, 16th, and 32nd basis states respectively. The solid line shows ideal scaling to guide the eyes.

Figure 1 shows the performance gain of the parallel computation of the SCG process to determine the 1st, 4th, 8th, 16th, and 32nd basis states respectively. Although the parallel efficiency for computing the first basis state is not good because of the small amount of computation, the efficiency for the 32nd basis state with 1024 CPU cores reaches 90% of that with 16 cores.

Note that the total computation time of the first basis is roughly 1/32 of that of the 32nd basis state.

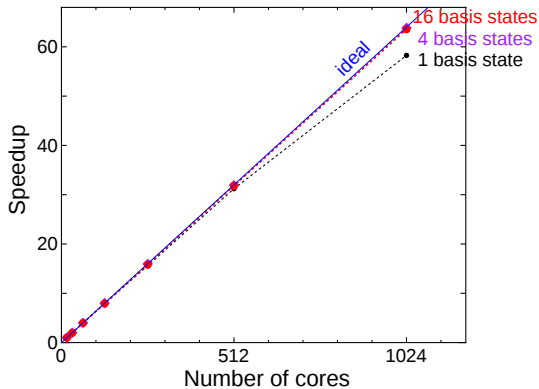


Figure 2. Speedup of the parallel computation of the energy variance in unit of the computation time using 16 CPU cores. The small circles, squares, and large circles represent the inverses of computation times of 1, 4, and 16 basis states, respectively. The solid line shows ideal scaling to guide the eyes.

Figure 2 show the parallel efficiency of the calculation of the energy variance using the formula shown in Ref. [12]. The energy variance is needed for the energy-variance extrapolation to estimate the exact shell-model energy precisely. The performance scaling of the parallel computation seems perfect at  $N_b \geq 4$ .

We have performed the benchmark test via early access to the K computer and obtained good scalability for parallel computation [9]. We plan to perform production runs at the K computer in 2012 and later. In parallel, we are promoting the study of the effective interaction, which is essential for the large-scale shell-model calculations.

## References

- [1] N. Shimizu, T. Otsuka, and Y. Utsuno, CNS Annual Rep. 2009 (2011) 73.
- [2] K computer, <http://www.aics.riken.jp/en/>
- [3] T. Otsuka, M. Honma, T. Mizusaki, N. Shimizu, and Y. Utsuno, Prog. Part. Nucl. Phys. **47** (2001) 319.
- [4] N. Shimizu, Y. Utsuno, T. Abe, and T. Otsuka, RIKEN Accel. Prog. Rep. **43** (2010) 46.
- [5] Y. Utsuno, N. Shimizu, T. Otsuka and T. Abe, arXiv:1202.2957 [nucl-th] (2012).
- [6] N. Shimizu, Y. Utsuno, T. Mizusaki, M. Honma, Y. Tsunoda, and T. Otsuka, Phys. Rev. C. **85** (2012) 054301.
- [7] T. Abe, P. Maris, T. Otsuka, N. Shimizu, Y. Utsuno, and J. P. Vary, arXiv/nucl-th:1204.1755 (2012).
- [8] L. Liu, T. Otsuka, N. Shimizu, Y. Utsuno, and R. Roth, Phys. Rev. C **86** (2012) 014302.
- [9] N. Shimizu, T. Abe, Y. Tsunoda, Y. Utsuno, T. Yoshida, T. Mizusaki, M. Honma, and T. Otsuka, Prog. Theor. Exp. Phys. **2012** (2012) 01A205.
- [10] M. Honma, T. Otsuka, T. Mizusaki, and M. Hjorth-Jensen, Phys. Rev. C **80** (2009) 064323.

- [11] T2K Open Supercomputer, <http://www.cc.u-tokyo.ac.jp/system/ha8000/>
- [12] N. Shimizu, Y. Utsuno, T. Mizusaki, T. Otsuka, T. Abe, and M. Honma, Phys. Rev. C **82** (2010) 061305(R).

# Benchmarks of the no-core MCSM method in light nuclei

T. Abe<sup>a, 1</sup>, P. Maris<sup>b</sup>, T. Otsuka<sup>a,c,d</sup>, N. Shimizu<sup>a</sup>, Y. Utsuno<sup>e</sup> and J. P. Vary<sup>b</sup>

<sup>a</sup>Center for Nuclear Study, Graduate School of Science, University of Tokyo

<sup>b</sup>Department of Physics and Astronomy, Iowa State University

<sup>c</sup>Department of Physics, University of Tokyo

<sup>d</sup>National Superconducting Cyclotron Laboratory, Michigan State University

<sup>e</sup>Advanced Science Research Center, Japan Atomic Energy Agency

## 1. Introduction

One of the major challenges in nuclear theory is to understand nuclear structure and reactions from *ab initio* methods. *Ab initio* calculations for nuclear many-body systems beyond  $A = 4$  have recently become feasible due to the rapid evolution of computational technologies these days. Among them, the No-Core Shell Model (NCSM) has been emerging for about a decade and is now available for the study of nuclear structure and reactions in the  $p$ -shell nuclei [1]. Unlike the conventional shell model with a core, the NCSM does not assume an inert core and treats all the nucleons composing the nucleus on an equal footing. The NCSM is thus said to be one of the *ab initio* approaches along with the Green's Function Monte Carlo [2] and Coupled Cluster theory [3].

As the NCSM treats all the nucleons democratically, computational demands for the calculations explode exponentially as the number of nucleons and/or the model spaces increase. Current limitation of the direct diagonalization of the Hamiltonian matrix by the Lanczos iteration is around the order of  $10^{10}$  shown in Fig. 1. In order to access heavier nuclei beyond the upper  $p$ -shell region with larger model spaces by *ab initio* shell-model methods, many efforts have been devoted for several years. One of these approaches is the Importance-Truncated NCSM [4] where the model spaces are extended by using the importance measure evaluated by the perturbation theory. Another approach is the Symmetry-Adapted NCSM [5] where the model spaces are truncated by the selected symmetry groups. Similar to these attempts, the no-core Monte Carlo shell model (MCSM) is one of the promising candidates to go beyond the Full Configuration Interaction (FCI) method [6, 7].

## 2. Benchmarks of the no-core MCSM

As an exploratory work, the original MCSM has been applied to the no-core calculations for the structure and spectroscopy of the beryllium isotopes [8]. This work motivates a further extension of the MCSM application to the *ab initio* FCI calculations [6, 7] augmented by the recent development of the MCSM algorithm [9, 10].

The main outcome of the initial benchmark project is summarized in Figure 2. In Fig. 2, we illustrate the comparisons of the energies for each state and model space between the MCSM and FCI methods. The FCI gives the exact energies in the fixed size of the mode space, while the MCSM gives approximated ones. Thus the comparisons between them show how well the MCSM works in no-core calculations. For this benchmark comparison, the JISP16 two-nucleon

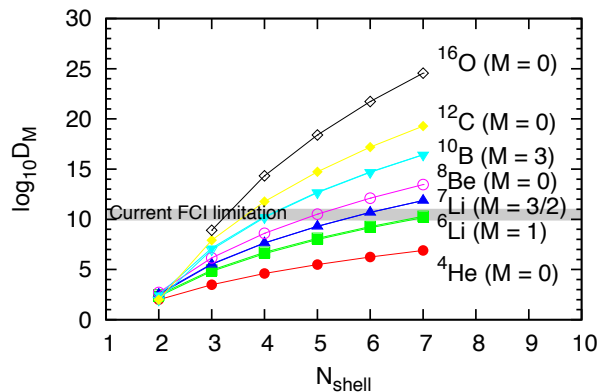


Figure 1.  $M$ -scheme dimensions as functions of basis-space size.

interaction [11] is adopted and the Coulomb force is turned off. Isospin symmetry is assumed. The energies are evaluated for the optimal harmonic oscillator frequencies where the calculated energies are minimized for each state and model space. Here the contributions from the spurious center-of-mass motion are ignored for simplicity. The comparisons are made for the states;  ${}^4\text{He}$  ( $0^+$ ),  ${}^6\text{He}$  ( $0^+$ ),  ${}^6\text{Li}$  ( $1^+$ ),  ${}^7\text{Li}$  ( $1/2^-$ ,  $3/2^-$ ),  ${}^8\text{Be}$  ( $0^+$ ),  ${}^{10}\text{B}$  ( $1^+$ ,  $3^+$ ) and  ${}^{12}\text{C}$  ( $0^+$ ). The model space ranges from  $N_{shell} = 2$  to 5 for  $A \leq 6$  ( $4$  for  $A \geq 7$ ). Note that the energies of  ${}^{10}\text{B}$  ( $1^+$ ,  $3^+$ ) and  ${}^{12}\text{C}$  ( $0^+$ ) in  $N_{shell} = 4$  are available only from the MCSM results. The  $M$ -scheme dimensions for these states ( $1.82 \times 10^{10}$  for  $M = 1$  and  $1.52 \times 10^{10}$  for  $M = 3$  in  ${}^{10}\text{B}$  and  $5.87 \times 10^{11}$  for  $M = 0$  in  ${}^{12}\text{C}$ ) are already marginal or exceed the current limitation in the FCI approach. The number of basis states are taken up to 100 in  $N_{shell} = 2 - 4$  and 50 in  $N_{shell} = 5$ . The solid (dashed) lines indicate the MCSM (FCI) results. The shaded regions express the extrapolations in the MCSM, and the lower bound of the shaded region corresponds to the extrapolated energy. Furthermore, we also plot the No-Core Full Configuration (NCFC) results for the states of  $4 \leq A \leq 8$  as the fully converged energies in the infinite model space. Although it would be hard to recognize in Fig. 2, the energies are consistent with each other where the FCI results are available to within  $\sim 100$  keV ( $\sim 500$  keV) at most of the MCSM results with(out) the energy-variance extrapolation in the MCSM. The other observables besides the energies; the point-particle root-mean-square matter radii and electromagnetic moments also give reasonable agreements between the MCSM and FCI results. The detailed comparisons among the MCSM, FCI and NCFC methods are discussed in Ref. [6].

<sup>1</sup>Present address: Department of Physics, University of Tokyo

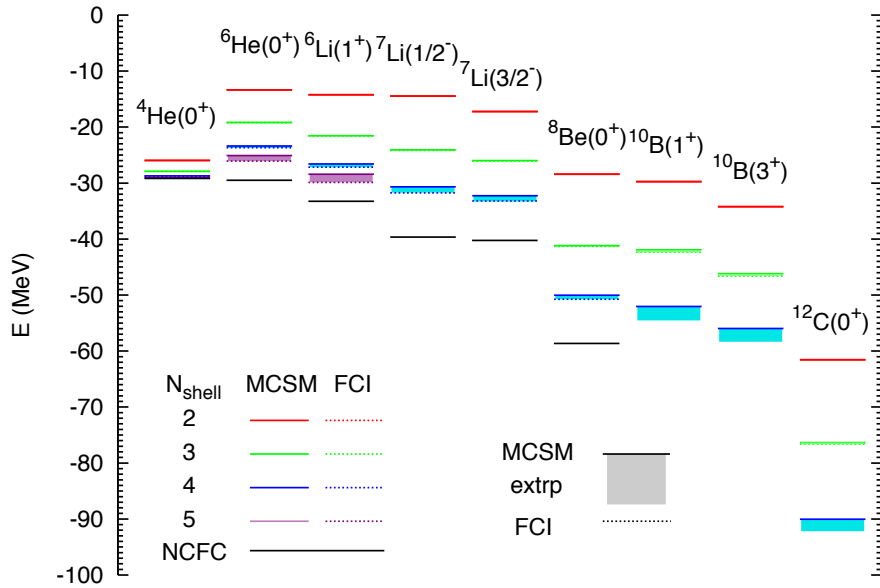


Figure 2. Comparisons of the energies between the MCSM and FCI along with the fully converged NCFC results where available [6]. The MCSM (FCI) results are shown as the solid (dashed) lines that nearly coincide where both are available. The extrapolated MCSM results are illustrated by bands. From top to bottom, the truncation of the model space is  $N_{shell} = 2$  (red), 3 (green), 4 (blue) and 5 (purple). Note that the MCSM results are extrapolated by the energy variance with the second-order polynomials [9].

### 3. Summary

By exploiting the recent development in the technique of energy-variance extrapolation [9] and the computation of the Hamiltonian matrix elements between non-orthogonal Slater determinants [10], the observables give good agreement between the MCSM and FCI results in the  $p$ -shell nuclei. From the benchmark comparison, the no-core MCSM is now verified in the application to the *ab initio* no-core calculations for light nuclei. The application to heavier nuclei is expected in the near future.

### References

- [1] P. Navrátil, J. P. Vary and B. R. Barrett, Phys. Rev. Lett. **84** (2000) 5728; Phys. Rev. C **62** (2000) 054311; S. Quaglioni and P. Navrátil, Phys. Rev. Lett. **101** (2008) 092501; Phys. Rev. C **79** (2009) 044606.
- [2] S. C. Pieper, R. B. Wiringa, and J. Carlson, Phys. Rev. C **70** (2004) 054325; K. M. Nollett, S. C. Pieper, R. B. Wiringa, J. Carlson and G. M. Hale Phys. Rev. Lett. **99** (2007) 022502.
- [3] G. Hagen, T. Papenbrock and M. Hjorth-Jensen, Phys. Rev. Lett. **108** (2012) 242501; Phys. Rev. Lett. **109** (2012) 032502 and references therein.
- [4] R. Roth, Phys. Rev. C **79** (2009) 064324; R. Roth, S. Binder, K. Vobig, A. Calci, J. Langhammer and P. Navrátil, Phys. Rev. Lett. **109** (2012) 052501.
- [5] T. Dytrych, K. D. Sviratcheva, C. Bahri, J. P. Draayer and J. P. Vary, Phys. Rev. Lett. **98** (2007) 162503; T. Dytrych, K. D. Sviratcheva, C. Bahri, J. P. Draayer and J. P. Vary, J. Phys. G. **35** (2008) 095101; T. Dytrych, K. D. Sviratcheva, J. P. Draayer, C. Bahri and J. P. Vary, J. Phys. G. **35** (2008) 123101.
- [6] T. Abe, P. Maris, T. Otsuka, N. Shimizu, Y. Utsuno and J. P. Vary, AIP Conf. Proc. **1355** (2011) 173; Phys. Rev. C **86** (2012) 054301.
- [7] N. Shimizu, T. Abe, Y. Tsunoda, Y. Utsuno, T. Yoshida, T. Mizusaki, M. Honma and T. Otsuka, Prog. Theor. Exp. Phys. (2012) 01A205.
- [8] L. Liu, T. Otsuka, N. Shimizu, Y. Utsuno and R. Roth, Phys. Rev. C **86** (2012) 014304.
- [9] N. Shimizu, Y. Utsuno, T. Mizusaki, T. Otsuka, T. Abe and M. Honma, Phys. Rev. C **82** (2010) 061305(R); N. Shimizu, Y. Utsuno, T. Mizusaki, M. Honma, Y. Tsunoda and T. Otsuka, Phys. Rev. C **85** (2012) 054301.
- [10] Y. Utsuno, N. Shimizu, T. Otsuka and T. Abe, Comput. Phys. Commun. **184** (2013) 102.
- [11] A. M. Shirokov, J. P. Vary, A. I. Mazur and T. A. Weber, Phys. Letts. B **644** (2007) 33; A. M. Shirokov, J. P. Vary, A. I. Mazur, S. A. Zaytsev and T. A. Weber, Phys. Lett. B **621** (2005) 96.

# Exploring Three-Nucleon Forces on the Lattice

T. Doi (for HAL QCD Collaboration)

*Center for Nuclear Study, Graduate School of Science, University of Tokyo*

The determination of the properties of three-nucleon forces (3NF) is one of the hottest topics in nuclear physics and astrophysics these days. There are various phenomena where 3NF may play an important role, e.g., the binding energies of light nuclei, the deuteron-nucleon elastic scattering, the properties of neutron-rich nuclei and the supernova nucleosynthesis and the nuclear equation of state (EoS) at high density relevant to the physics of neutron stars.

Despite of its phenomenological importance, microscopic understanding of 3NF is still limited. Pioneered by Fujita and Miyazawa [1], 3NF have been commonly studied from two-pion exchange ( $2\pi$ E) models with the  $\Delta$ -excitation. However, since 3NF is originated by the fact that a nucleon is not a fundamental particle, it is most desirable to determine 3NF from the fundamental degrees of freedom (DoF), i.e., quarks and gluons, on the basis of quantum chromodynamics (QCD). In this report, we perform the calculation of 3NF from first-principle lattice QCD.

As for the two-nucleon forces (2NF) from lattice QCD, an approach based on the Nambu-Bethe-Salpeter (NBS) wave function has been proposed [2, 3]. Resultant (parity-even) 2NF are found to have attractive wells at long and medium distances and central repulsive cores at short distance. The method has been extended to the hyperon-nucleon (YN) and hyperon-hyperon (YY) interactions [4]. In this report, we extend the method to the 3N system, and perform the lattice QCD simulations of 3NF in the triton channel,  $(I, J^P) = (1/2, 1/2^+)$  [5, 6, 7].

The detailed formulation for the 2NF is given in Ref. [3], and we here discuss the extension to the 3N system. We consider the NBS wave function  $\psi_{3N}(\vec{r}, \vec{\rho})$  extracted from the six-point correlator as

$$G_{3N}(\vec{r}, \vec{\rho}, t - t_0) \equiv \frac{1}{L^3} \sum_{\vec{R}} \langle 0 | (N(\vec{x}_1) N(\vec{x}_2) N(\vec{x}_3))(t) \overline{(N' N' N')}(t_0) | 0 \rangle \xrightarrow{t \gg t_0} A_{3N} \psi_{3N}(\vec{r}, \vec{\rho}) e^{-E_{3N}(t-t_0)}, \quad (1)$$

$$\psi_{3N}(\vec{r}, \vec{\rho}) \equiv \langle 0 | N(\vec{x}_1) N(\vec{x}_2) N(\vec{x}_3) | E_{3N} \rangle, \quad (2)$$

$$A_{3N} \equiv \langle E_{3N} | \overline{(N' N' N')} | 0 \rangle, \quad (3)$$

where  $E_{3N}$  and  $|E_{3N}\rangle$  denote the energy and the state vector of the 3N ground state, respectively,  $N$  ( $N'$ ) the nucleon operator in the sink (source), and  $\vec{R} \equiv (\vec{x}_1 + \vec{x}_2 + \vec{x}_3)/3$ ,  $\vec{r} \equiv \vec{x}_1 - \vec{x}_2$ ,  $\vec{\rho} \equiv \vec{x}_3 - (\vec{x}_1 + \vec{x}_2)/2$  the Jacobi coordinates.

With the derivative expansion of the potentials, the NBS wave function can be converted to the potentials through the following Schrödinger equation,

$$\left[ -\frac{1}{2\mu_r} \nabla_r^2 - \frac{1}{2\mu_\rho} \nabla_\rho^2 + \sum_{i < j} V_{2N}(\vec{r}_{ij}) + V_{3NF}(\vec{r}, \vec{\rho}) \right] \psi_{3N}(\vec{r}, \vec{\rho}) = E_{3N} \psi_{3N}(\vec{r}, \vec{\rho}), \quad (4)$$

where  $V_{2N}(\vec{r}_{ij})$  with  $\vec{r}_{ij} \equiv \vec{x}_i - \vec{x}_j$  denotes the 2NF between  $(i, j)$ -pair,  $V_{3NF}(\vec{r}, \vec{\rho})$  the 3NF,  $\mu_r = m_N/2$ ,  $\mu_\rho = 2m_N/3$  the reduced masses. If we calculate  $\psi_{3N}(\vec{r}, \vec{\rho})$  for all  $\vec{r}$  and  $\vec{\rho}$ , and if all  $V_{2N}(\vec{r}_{ij})$  are obtained by (separate) lattice calculations for genuine 2N systems, we can extract  $V_{3NF}(\vec{r}, \vec{\rho})$  through Eq. (4).

In practice, however, the computational cost is enormous, because of enlarged DoF by the 3N (i.e., 9 quarks) and factorial number of Wick contractions. In order to reduce the cost, we develop several techniques, e.g., taking advantage of symmetries, and employing the non-relativistic limit for the nucleon operator in the source. We further restrict the geometry of the 3N. More specifically, we consider the “linear setup” with  $\vec{\rho} = \vec{0}$ , with which 3N are aligned linearly with equal spacings of  $r_2 \equiv |\vec{r}|/2$ . In this setup, the third nucleon is attached to  $(1, 2)$ -nucleon pair with only S-wave. Considering the total 3N quantum numbers of  $(I, J^P) = (1/2, 1/2^+)$ , the triton channel, the wave function can be completely spanned by only three bases, which can be labeled by the quantum numbers of  $(1, 2)$ -pair as  $^1S_0$ ,  $^3S_1$ ,  $^3D_1$ . Therefore, the Schrödinger equation leads to the  $3 \times 3$  coupled channel equations with the bases of  $\psi_{^1S_0}$ ,  $\psi_{^3S_1}$ ,  $\psi_{^3D_1}$ . The reduction of the dimension of bases is expected to improve the signal-to-noise ratio as well.

We then consider the identification of genuine 3NF. It is a nontrivial work: Although both of parity-even and parity-odd 2NF are required to subtract 2NF part in Eq. (4), parity-odd 2NF have not been obtained yet in lattice QCD. In order to resolve this issue, we consider the following channel,

$$\psi_S \equiv \frac{1}{\sqrt{6}} \left[ -p_\uparrow n_\uparrow n_\downarrow + p_\uparrow n_\downarrow n_\uparrow - n_\uparrow n_\downarrow p_\uparrow + n_\downarrow n_\uparrow p_\uparrow + n_\uparrow p_\uparrow n_\downarrow - n_\downarrow p_\uparrow n_\uparrow \right], \quad (5)$$

which is anti-symmetric in spin/isospin spaces for any 2N-pair. Combined with the Pauli-principle, it is automatically guaranteed that any 2N-pair couples with even parity only. Therefore, we can extract 3NF unambiguously using only parity-even 2NF. Note that no assumption on the choice of 3D-configuration of  $\vec{r}$ ,  $\vec{\rho}$  is imposed in this argument, and we can take advantage of this feature for future 3NF calculations with various 3D-configuration setup.

We employ  $N_f = 2$  dynamical configurations with mean field improved clover fermion and RG-improved gauge action generated by CP-PACS Collaboration [8]. We use 598 configurations at  $\beta = 1.95$  and the lattice spacing of  $a^{-1} = 1.269(14)$  GeV, and the lattice size of  $V = L^3 \times T = 16^3 \times 32$  corresponds to  $(2.5 \text{ fm})^3$  box in physical spacial size. For  $u, d$  quark masses, we take the hopping parameter at the unitary point as  $\kappa_{ud} = 0.13750$ , which corresponds to  $m_\pi = 1.13$  GeV,  $m_N = 2.15$  GeV and  $m_\Delta = 2.31$  GeV. We use the wall quark source with Coulomb gauge fixing. In order to

enhance the statistics, we perform the measurement at 32 source time slices for each configuration, and the forward and backward propagations are averaged. The results from both of total angular momentum  $J_z = \pm 1/2$  are averaged as well. We perform the simulation at eleven physical points of the distance  $r_2$  with the linear setup.

In Fig. 1 (upper), we plot the radial part of each wave function of  $\psi_S = (-\psi_{1S_0} + \psi_{3S_1})/\sqrt{2}$ ,  $\psi_M \equiv (\psi_{1S_0} + \psi_{3S_1})/\sqrt{2}$  and  $\psi_{3D_1}$  obtained at  $(t-t_0)/a = 8$ . Here, we normalize the wave functions by the center value of  $\psi_S(r_2 = 0)$ . What is noteworthy is that the wave functions are obtained with good precision, which is quite nontrivial for the 3N system. We observe that  $\psi_S$  overwhelms the wave function, indicating that higher partial waves are strongly suppressed, and thus the effect of the next leading order in the derivative expansion, spin-orbit forces, is suppressed in this lattice setup.

We determine 3NF by subtracting 2NF from total potentials in the 3N system. Since we have only one channel (Eq. (5)) which is free from parity-odd 2NF, we can determine one type of 3NF. In this report, 3NF are effectively represented in a scalar-isoscalar functional form, which is often employed for the short-range 3NF in phenomenology.

In Fig. 1 (lower), we plot the results for the effective scalar-isoscalar 3NF at  $(t-t_0)/a = 8$ . Here, we include  $r_2$ -independent shift by energies,  $\delta_E \simeq 5$  MeV, which is determined by long-range behavior of potentials (2NF and effective 2NF in the 3N system) [5]. While  $\delta_E$  suffers from  $\lesssim 10$  MeV systematic error, it does not affect the following discussions much, since  $\delta_E$  merely serves as an overall offset. In order to check the dependence on the sink time slice, we calculate 3NF at  $(t-t_0)/a = 9$  as well, and confirm that the results are consistent with each other [5].

Fig. 1 (lower) shows that 3NF is small at the long distance region of  $r_2$ . This is in accordance with the suppression of  $2\pi E$ -3NF by the heavy pion. At the short distance region, on the other hand, an indication of repulsive 3NF is observed. Note that a repulsive short-range 3NF is phenomenologically required to explain the properties of high density matter. Since multi-meson exchanges are strongly suppressed by the large quark mass, the origin of this short-range 3NF may be attributed to the quark and gluon dynamics directly. In fact, we recall that the short-range repulsive (or attractive) cores in the generalized two-baryon potentials are calculated in lattice QCD in the flavor SU(3) limit, and the results are found to be well explained from the viewpoint of the Pauli exclusion principle in the quark level [9]. In this context, it is intuitive to expect that the 3N system is subject to extra Pauli repulsion effect, which could be an origin of the observed short-range repulsive 3NF. Further investigation along this line is certainly an interesting subject in future.

Since the lattice simulations in this report are carried out only at single large quark mass, quark mass dependence of 3NF is certainly an important issue to be investigated in future. In the case of 2NF, short-range cores have the enhanced strength and broaden range by decreasing the mass [3]. We, therefore, would expect a significant quark mass dependence exist in

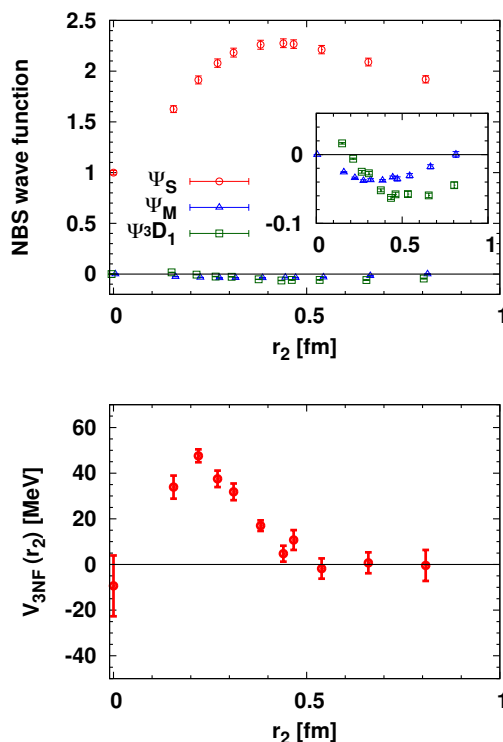


Figure 1. (Upper) 3N wave functions at  $(t-t_0)/a = 8$ . Circle (red), triangle (blue), square (green) points denote  $\psi_S$ ,  $\psi_M$ ,  $\psi_{3D_1}$ , respectively. (Lower) The effective scalar-isoscalar 3NF in the triton channel with the linear setup.

short-range 3NF as well. Quantitative investigation through lattice simulations with lighter quark masses are currently underway.

## References

- [1] J. Fujita and H. Miyazawa, Prog. Theor. Phys. **17**, 360 (1957).
- [2] N. Ishii, S. Aoki and T. Hatsuda, Phys. Rev. Lett. **99**, 022001 (2007) [nucl-th/0611096].
- [3] S. Aoki, T. Hatsuda and N. Ishii, Prog. Theor. Phys. **123**, 89 (2010) [arXiv:0909.5585 [hep-lat]].
- [4] Reviewed in S. Aoki *et al.* [HAL QCD Collaboration], arXiv:1206.5088 [hep-lat] (PTEP in press.)
- [5] T. Doi *et al.* [HAL QCD Collaboration], Prog. Theor. Phys. **127**, 723 (2012) [arXiv:1106.2276 [hep-lat]].
- [6] T. Doi [for HAL QCD Collaboration], AIP Conf. Proc. **1441**, 399 (2012) [arXiv:1109.4748 [hep-lat]].
- [7] T. Doi [HAL QCD Collaboration], PoS LATTICE **2011**, 151 (2011) [arXiv:1112.4103 [hep-lat]].
- [8] A. Ali Khan *et al.* [CP-PACS Collab.], Phys. Rev. D **65**, 054505 (2002) [E: D **67**, 059901 (2003)].
- [9] T. Inoue *et al.* [HAL QCD Collab.], Prog. Theor. Phys. **124**, 591 (2010) [arXiv:1007.3559 [hep-lat]].

## **Other Activities**



# Analysis of Gamma-ray Activities in Soils Sampled from Surrounding Area of Fukushima Daiichi Nuclear Power Plant

Susumu Shimoura, Eiji Ideguchi, Shinsuke Ota, Daisuke Nakajima, Masahiko Tanaka, Ryo Yoshino, Shintaro Go, Rin Yokoyama, and Takaharu Otsuka<sup>a</sup>

*Center for Nuclear Study, Graduate School of Science, University of Tokyo*

<sup>a</sup>*Department of Physics, University of Tokyo*

In order to prepare maps of radioactive substances deposited on the ground surface, soil samples from the 5-cm surface layer were collected for about 2,200 locations in Fukushima and nearby prefectures within approximately 100 km from the Fukushima Daiichi Nuclear Power Plant (NPP) from June 6 to 14 and from June 27 to July 8, 2011. The sampling points were on  $2 \times 2$  km<sup>2</sup> meshes for the 80-km region from the NPP and  $10 \times 10$  km<sup>2</sup> meshes for the outer region.

Some 10,000 samples in total, corresponding to five or three different points for each location, were analyzed by a collaboration (60%) among universities and institutes, including Center for Nuclear Study (CNS), RIKEN Nishina Center (RNC), Research Center for Nuclear Physics (RCNP), and other academic organizations as well as by the Japan Chemical Analysis Center (JCAC) (40%) and . CNS acted as a hub of the collaboration, where tasks such as receiving and checking about 6000 samples from Fukushima; sending them to 22 analysis groups depending on their capacities; and collecting, checking, and summarizing the results were performed. About 120 samples, collected from within 20 km of NPP, were analyzed by CNS and RNC.

Preceding to the large-scale measurements, a pilot study for sampling and measurement was performed in May, where five or more samples were collected at  $10 \times 10$  km<sup>2</sup> meshes (57 points) in the 80-km region. The activities of Cs-134, Cs-137, and I-131 were analyzed by measuring  $\gamma$ -rays emitted by all the samples using the germanium detector(s) by analysis groups (TMU, JAEA, RCNP, Osaka Univ., CNS). Activities of other substances such as Te-129m, Ag-110m were also analyzed. Inhomogeneous distribution of activities in a sample was found by the measurements of a Ge detector viewing a sample from different directions (top/bottom), which shows that a stirring procedure is important for sampling. Substantial amount of variation in total activities of the five samples from a same point is also found, which indicates that the average of the samples is to be the typical magnitude of a certain point. Based on the pilot study, protocols for samplings and for measurements were determined.

In the measurements of the large-scale investigation, each analysis group calibrated the absolute magnitudes of the activities by using the IAEA-444 standard samples [1] filled in the same U8 type containers ( $5 \text{ cm}^{\phi} \times 5 \text{ cm}^H$ ) as the soil samples that were circulated among the collaboration. Since Cs-134 and Cs-137 are involved in the IAEA-444 standard, their absolute activities were determined by the relative yields from the IAEA-444 sample and each soil sample.

Measurement time for a sample was basically one hour, whereas long runs with around 10 hours were also performed for some samples to measure the radia-

tion from I-131. However, large portion of the samples have no significant value for I-131 because of decay out through more than 10 half lives and of a large Compton backgrounds from the radiation of Cs-134 and Cs-137.

The same  $\sim 300$  samples were analyzed by multiple groups, one of which is either CNS or JCAC, for the purpose of a cross checking. Results from these different groups were consistent within 30% for each sample and within 15% for an average of five samples for each location. The deviation is considered to be due to the inhomogeneity of the activities in soil samples, since it was found that for some samples, counting rates depended on the direction of the sample relative to the detector.

The maps based on the resultant activities (Cs-137, Cs-134, I-131, Te-129m, and Ag-110m) are found from the Web pages of MEXT [2], JAEA [3], and RCNP. [4] Database of all the measured activities is also able to access from the Web page [5].

The present results are expected to be used as a basis for assessing the radiation dose in the concerned areas, further investigations in the environmental research works, and other such purposes.

The present work was in the course of the project under the 2011 Strategic Funds for the Promotion of Science and Technology, entitled “Establishment of the Base for Taking Measures for Environmental Impact of Radioactive Substances – Study on Distribution of Radioactive Substances” of MEXT.

## References

- [1] [http://nucleus.iaea.org/rpst/Documents/rs\\_iaea\\_444.pdf](http://nucleus.iaea.org/rpst/Documents/rs_iaea_444.pdf)
- [2] <http://radioactivity.mext.go.jp/>
- [3] <http://ramap.jaea.go.jp/map/>
- [4] <http://www.rcnp.osaka-u.ac.jp/dojo/>
- [5] <http://radb.jaea.go.jp/>

# The 10th CNS International Summer School (CNSSS11)

S. Michimasa, T. Gunji, H. Hamagaki, S. Kubono, T. Nakatsukasa<sup>a</sup>, T. Otsuka<sup>b</sup>, H. Sakai<sup>a</sup>,  
S. Shimoura, T. Suzuki and T. Uesaka<sup>a</sup>

*Center for Nuclear Study, Graduate School of Science, University of Tokyo*

<sup>a</sup>*RIKEN Nishina Center*

<sup>b</sup>*Department of Physics, Graduate School of Science, University of Tokyo*

The 10th CNS International Summer School (CNSSS11) was organized jointly by the Center for Nuclear Study (CNS), the University of Tokyo in the period of September 26–October 1, 2011. The summer school was held at the Nishina hall in the Wako campus of RIKEN and at the Koshiba hall in the Hongo campus, the University of Tokyo.

This summer school was the tenth one in the series which aimed at providing graduate students and post docs with basic knowledge and perspectives of nuclear physics. It consisted of lectures by leading scientists in the fields of both experimental and theoretical nuclear physics. Each lecture started with an introductory talk from the fundamental point of view and ended with up-to-date topics in the relevant field.

The list of lecturers and the title of lectures are shown below.

**R. Johnson (Surrey University),**

“Theory of nuclear reactions with loosely bound targets and projectiles”

“Exploring nuclear haloes by the ratio method”

**A.O. Macchiavelli (Lawrence Berkley National Laboratory),**

“Selected Topics in Nuclear Structure”

**S. Wanajo (Technische Universität München, Max-Planck-Institute für Astrophysik),**

“Nucleosynthesis beyond iron”

**I. Tanihata (RCNP, Osaka University),**

“Neutron halo and tensor forces in nuclei”

**T. Shimoda (Osaka University),**

“Beta-delayed decay spectroscopy with spin-polarized nuclei”

**T. Kishimoto (Osaka University),**

“Double beta decay and matter dominated universe”

**Y. Aritomo (Japan Atomic Energy Agency),**

“Dynamical aspect of synthesis of superheavy elements”

**S. Nishimura (RIKEN Nishina Center),**

“Decay spectroscopy at RIBF”

This year, 8 lecturers and 90 participants attended from fourteen countries. Three lecturers and twenty participants were from foreign institutes. Attendances communicated with each other in the free discussion time between the lectures and in the welcome and farewell parties in a relaxed atmosphere.

Five lectures on September 29 were held at the Koshiba hall in the Hongo campus and were broadcasted via Internet.

The Student and Post Doc sessions were also held in the school. Twenty talks and twenty-four posters were presented by graduate students and post docs.

All the information concerning the summer school is open for access at the following URL:

<http://www.cns.s.u-tokyo.ac.jp/summerschool/cnsss11>

This summer school was supported in part by the International Exchange Program of the Graduate School of Science, the University of Tokyo. The financial support from the program was indispensable to successfully organize this summer school. The organizers deeply appreciate various accommodations provided by RIKEN Nishina center for the school. They are also grateful to administration staffs of the CNS and the Graduate School of Science for their helpful supports. They thank graduate students and postdocs in the CNS for their dedicated efforts. Finally, the organizers acknowledge all the lecturers and participants for their contributions to this summer school.

# Laboratory Exercise for Undergraduate Students

S. Ota, K. Yako<sup>a</sup>, R. Yokoyama, C.S. Lee, H. Sakurai<sup>a</sup> and S. Shimoura

*Center for Nuclear Study, Graduate School of Science, University of Tokyo*

*<sup>a</sup>Department of Physics, University of Tokyo*

Nuclear scattering experiments were performed as a laboratory exercise for undergraduate students of the University of Tokyo. This program was aiming at providing undergraduate students with an opportunity to learn how to study subatomic physics by using an ion beam from an accelerator. In 2011, 32 students attended this program.

The four beam times were scheduled in the second semester for third-year students, and 8 students participated in each beam time. The experiment was performed at the RIBF using a 26-MeV alpha beam accelerated in the AVF cyclotron. The alpha beam extracted from the AVF cyclotron was transported to the E7B beam line in the E7 experimental hall. The scattering chamber has two separate target ports which enable perform two independent experiments. A photo is shown in Fig. 1 In each beam time, the students were divided into two groups and took one of the following two subjects:

1. Measurement of elastic scattering of incident alpha particle with  $^{197}\text{Au}$ , to learn how to determine nuclear size.
2. Measurement of gamma rays emitted from the cascade decay of highly excited  $^{154}\text{Gd}$  and  $^{184}\text{Os}$ , to learn on the nuclear deformation.



Figure 1. A photo of scattering chamber located at the E7B course in E7 experimental room. There are two target positions for independent experiments of  $\alpha$ -scattering measurement and fusion reaction measurement, respectively.

Before the experiment, the students took a course on the basic handling of the semiconductor detectors and electronic circuits at the Hongo campus, and attended a radiation safety lecture at RIKEN. They also joined a tour to the RI beam factory at RIKEN.

In the  $\alpha+^{197}\text{Au}$  measurement, the Au target with a thickness of 1.42 mg/cm<sup>2</sup>, and  $\alpha$  particles scattered from the Au target were detected by a silicon PIN-diode located 11 cm away from the target. A collimator with a diameter of 6 mm was attached on the silicon

detector. The energy spectrum of the scattered  $\alpha$  particles was recorded by a multi-channel analyzer (MCA) system. The beam was stopped by a Faraday cup in the scattering chamber. The cross section for the alpha elastic scattering was measured in the angular range of  $\theta_{\text{lab}} = 25\text{--}160^\circ$ .

The measured cross section was compared with the calculated cross section for the Rutherford scattering. The cross section was also analyzed by the potential model calculation, and the radius of the gold nucleus was discussed. Some students obtained the radius of 10 fm by using a classical model where the trajectory of the  $\alpha$  particle in the nuclear potential is obtained using the Runge-Kutta method. Others tried to understand the scattering process by calculating the angular distribution using the distorted wave Born approximation method with a Coulomb wave function and a realistic nuclear potential.

In the measurement of gamma rays, excited states in  $^{154}\text{Gd}$  and  $^{184}\text{Os}$  nuclei were populated by the  $^{152}\text{Sm}(\alpha,2n)$  and  $^{182}\text{W}(\alpha,2n)$  reactions, respectively. The gamma rays emitted from the cascade decay of the rotational bands were measured by a high-purity germanium detector located 50 cm away from the target. The energies of the gamma rays were recorded by the MCA system. The gain and the efficiency of the detector system had been calibrated with standard gamma-ray sources of  $^{22}\text{Na}$ ,  $^{60}\text{Co}$ ,  $^{133}\text{Ba}$ , and  $^{137}\text{Cs}$ . The gamma rays from the 12+ 10+ and 10+ 8+ decay in  $^{154}\text{Gd}$  and  $^{184}\text{Os}$  were successfully identified. Based on the energies of the gamma rays, the moment of inertia and the deformation parameters of the excited states were discussed by using a classical rigid rotor model and a irrotational fluid model. The students found that the reality lies between the two extreme models. The initial population among the levels in the rotational band was also discussed by taking the effect of the internal conversion into account.

We believe this program was very impressive for the students. It was the first time for most of the students to use large experimental equipments. They learned basic things about the experimental nuclear physics and how to extract physics from the data. The authors would like to thank Dr. Y. Uwamino, the CNS accelerator group, and the RIBF cyclotron crew for their helpful effort in the present program.



# Appendices

Symposium, Workshop, Seminar,  
PAC and External Review  
CNS Reports  
Publication List  
Talks and Presentations  
Personnel



# Symposium, Workshop, Seminar, and PAC

## A. Symposium

1. RIBF ULIC and CNS Symposium on Frontier of gamma-ray spectroscopy (Gamma11)  
Jun. 30 – Jul. 2, 2011, RIKEN

The purpose of the symposium was to discuss recent progress and future perspectives of gamma-ray spectroscopy as well as the recent developments of advanced gamma-ray detectors. It is hoped that the symposium will encourage international cooperation and stimulate physicists in the field of nuclear structure studies. The Organizers were E. Ideguchi (CNS, co-chair), N. Aoi (RCNP/RIKEN, co-chair), S. Michimasa (CNS), H. Scheit (RIKEN), A. Odahara (Osaka), T. Koike (Tohoku), Y. Ut-suno (JAEA), T. Nakatsukasa (RIKEN), S. Shimoura (CNS), T. Motobayashi (RIKEN), and T. Otsuka (CNS/Tokyo)

2. The 11th International Symposium on Origin of Matter and Evolution of Galaxies  
Nov. 14–17, 2011, RIKEN.

The symposium was the 11th symposium of a series, started 1988, to discuss the subjects of nuclear astrophysics and related fields. Topics related to nucleosynthesis and stellar evolutions were widely covered. Specifically, this time the symposium emphasized two topics, RI beam experiments for explosive astrophysical phenomena, and first-generation stars in relation with the evolution in the early universe. The symposium was hosted by CNS, and co-hosted by RIKEN Nishina Center, National Astronomical Observatory of Japan (NAOJ), KEK, RCNP, Osaka University (RCNP) and Konan University. 130 (81 domestic and 49 abroad) researchers participated in the symposium. In the symposium the successful research life of Prof. Kubono, who took the chair of the symposium and retired afterwards in March 2012, was reviewed and celebrated.

## B. Workshop

1. The 7th Workshop on Particle Correlations and Femtoscopy (WPCF2011)

Sep. 20–24, 2011, Koshiba Hall, the University of Tokyo

The workshop continued the tradition of bringing together experts in experimental and theoretical aspects of measuring source characteristics in high energy hadron/nuclear collisions through particle correlations and fluctuations. Number of participants was 89 (51 were from foreign countries). The proceedings were published in the PoS (<http://pos.sissa.it/cgi-bin/reader/conf.cgi?confid=154>). The WPCF2011 is co-sponsored by Center for Nuclear Study, the University of Tokyo and MEXT Scientific Research on Innovative Areas “Nuclei from Quarks”. The Local Organizing Committee members were; ShinIchi Esumi (Tsukuba Univ.), Hirotsugu Fujii (Univ. of Tokyo, Komaba), Taku Gunji (Univ. of Tokyo, CNS), Hideki Hamagaki (Univ. of Tokyo, CNS) (Co-chair), Tetsuo Hatsuda (Univ. of Tokyo, Hongo), Tetsufumi Hirano (Sophia/Univ. of Tokyo, Hongo) (Co-chair), Tetsuo Matsui (Univ. of Tokyo, Komaba), Chiho Nonaka (Nagoya Univ.), Kyoichiro Ozawa (KEK/Univ. of Tokyo, Hongo).

2. Review Meeting on CRIB Activities.

Jun 21–22, 2011, CNS Wako Campus.

The review meeting was held for summarizing the work at the low-energy RI beam separator CRIB since its construction in 2000. 16 persons, who have used CRIB for their experiments, presented their achievements, current status of the project, and future plans. 2 reviewers discussed on a worldwide status of RI beam facilities and nuclear astrophysics studies.

## C. Program Advisory Committee for Nuclear-Physics Experiments at RI Beam Factory

1. The 9th NP-PAC meeting

Date: June 24–25, 2011

Place: Conference room, 2F RIBF building

2. The 10th NP-PAC meeting

Date: December 9–10, 2011

Place: Conference room, 2F RIBF building

## CNS Reports

#87 “Alpha resonance structure in  $^{11}\text{B}$  studied via resonant scattering of  $^7\text{Li}+\alpha$ ”,  
H. Yamaguchi, T. Hashimoto, S. Hayakawa, D.N. Binh, D. Kahl, S. Kubono, Y. Wakabayashi, T. Kawabata, and T. Teranishi, Feb. 2011

#88 “CNS Annual Report 2010”,  
Edited by T. Gunji, March, 2012

# Publication List

## A. Original Papers

1. Ozawa A., Hashizume Y., Aoki Y., Tanaka K., Aiba T., Aoi N., Baba H., A. Brown B., Fukuda M., Inafuku K., Iwasa N., Izumikawa T., Kobayashi K., Komuro M., Kondo Y., Kubo T., Kurokawa M., Matsuyama T., Michimasa S., Motobayashi T., Nakabayashi T., Nakajima S., Nakamura T., Ohtsubo T., Sakurai H., Shinoda R., Shinohara M., Suzuki H., Suzuki T., Takechi M., Takeshita E., Takeuchi S., Togano Y., Yamada K., Yamaguchi T., Yasuno T., Yoshitake M., “One- and two-neutron removal reactions from  $^{19,20}\text{C}$  with a proton target”, *Phys. Rev. C* **84**, (2011) 064315,\*
2. Y. Togano, Y. Yamada, N. Iwasa, K. Yamaga, T. Modobayashi, N. Aoi, H. Baba, S. Bishop, X. Cai, P. Doornenbal, D. Fang, T. Furukawa, K. Ieki, T. Kawabata, S. Kanno, N. Kobayashi, Y. Kondo, T. Kuboki, N. Kume, K. Kurita, M. Kurokawa, Y.G. Ma, Y. Matsuo, H. Murakami, M. Matsushita, T. Nakamura, K. Okada, S. Ota, Y. Satou, S. Shimoura, R. Shinoda, K.N. Tanaka, S. Takeuchi, W. Tian, H. Wang, J. Wang, K. Yoneda, “Hindered Proton Collectivity in  $\text{S-28(16)12}$ : Possible Magic Number at  $Z=16$ ”, *Phys. Rev. Lett.* **21** (2012) 22501\*
3. H. Watanabe, K. Yamaguchi, A. Odahara, T. Sumikama, S. Nishimura, K. Yoshinaga, Z. Li, Y. Miyashita, K. Sato, L. Prochniak, H. Baba, J.S. Berryman, N. Blasi, A. Bracco, F. Camera, J. Chiba, P. Doornenbal, S. Go, T. Hashimoto, S. Hayakawa, C. Hinke, N. Hinohara, E. Ideguchi, T. Isobe, Y. Ito, D.G. Jenkins, Y. Kawada, N. Kobayashi, Y. Kondo, R. Krucken, S. Kubono, G. Lorusso, T. Nakao, T. Nakatsukasa, M. Kurata-Nishimura, H.J. Ong, S. Ota, Z. Podolyak, H. Sakurai, H. Sheit, K. Steiger, D. Steppenbeck, K. Sugimoto, K. Tajiri, S. Takano, A. Takashima, T. Teranishi, Y. Wakabayashi, P.M. Walker, O. Wieland, H. Yamaguchi “Development of axial asymmetry in the neutron-rich nucleus  $\text{Mo-110}$ ” *Phys. Lett. B* **704** (2011) 270–275\*
4. H. Watanabe, T. Sumikama, S. Nishimura, K. Yoshinaga, Z. Li, Y. Miyashita, K. Yamaguchi, H. Baba, J.S. Berryman, N. Blasi, A. Bracco, F. Camera, J. Chiba, P. Doornenbal, S. Go, T. Hashimoto, S. Hayakawa, C. Hinke, E. Ideguchi, T. Isobe, Y. Ito, D.G. Jenkins, Y. Kawada, N. Kobayashi, Y. Kondo, R. Krucken, S. Kubono, G. Lorusso, T. Nakao, M. Kurata-Nishimura, A. Odahara, H.J. Ong, S. Ota, Z. Podolyak, H. Sakurai, H. Sheit, Y. Shi, K. Steiger, D. Steppenbeck, K. Sugimoto, K. Tajiri, S. Takano, A. Takashima, T. Teranishi, Y. Wakabayashi, P.M. Walker, O. Wieland, F.R. Xu, H. Yamaguchi “Low-lying level structure of the neutron-rich nucleus  $\text{Nb-109}$ : A possible oblate-shape isomer” *Phys. Lett. B* **696** (2011) 186-190\*
5. T. Sumikama, K. Yoshinaga, H. Watanabe, S. Nishimura, Y. Miyashita, K. Yamaguchi, K. Sugimoto, J. Chiba, H. Baba, J.S. Berryman, N. Blasi, A. Bracco, F. Camera, P. Doornenbal, S. Go, T. Hashimoto, S. Hayakawa, C. Hinke, E. Ideguchi, T. Isobe, Y. Ito, D.G. Jenkins, Y. Kawada, N. Kobayashi, Y. Kondo, R. Krucken, S. Kubono, G. Lorusso, T. Nakao, M. Kurata-Nishimura, A. Odahara, H.J. Ong, S. Ota, Z. Podolyak, H. Sakurai, H. Sheit, K. Steiger, D. Steppenbeck, S. Takano, A. Takashima, K. Tajiri, T. Teranishi, Y. Wakabayashi, P.M. Walker, O. Wieland, H. Yamaguchi “Structural Evolution in the Neutron-Rich Nuclei  $\text{Zr-106}$  and  $\text{Zr-108}$ ” *Phys. Rev. Lett.* **106** (2011) 202501\*
6. S. Nishimura, Z. Li, H. Watanabe, K. Yoshinaga, T. Sumikama, T. Tatibana, K. Yamaguchi, M. Kurata-Nishimura, G. Lorusso, Y. Miyashita, A. Odahara, H. Baba, J.S. Berryman, N. Blasi, A. Bracco, F. Camera, J. Chiba, P. Doornenbal, S. Go, T. Hashimoto, S. Hayakawa, C. Hinke, E. Ideguchi, T. Isobe, Y. Ito, D.G. Jenkins, Y. Kawada, N. Kobayashi, Y. Kondo, R. Krucken, S. Kubono, T. Nakao, H.J. Ong, S. Ota, Z. Podolyak, H. Sakurai, H. Sheit, K. Steiger, D. Steppenbeck, K. Sugimoto, K. Tajiri, S. Takano, A. Takashima, T. Teranishi, Y. Wakabayashi, P.M. Walker, O. Wieland, H. Yamaguchi “beta-Decay Half-Lives of Very Neutron-Rich  $\text{Kr}$  to  $\text{Tc}$  Isotopes on the Boundary of the r-Process Path: An Indication of Fast r-Matter Flow” *Phys. Rev. Lett.* **106** (2011) 052502\*
7. Y. Togano, T. Gomi, T. Motobayashi, Y. Ando, N. Aoi, H. Baba, K. Demichi, Z. Elekes, N. Fukuda, Z. Fulop, U. Futakami, H. Hasegawa, Y. Higurashi, K. Ieki, N. Imai, M. Ishihara, K. Ishikawa, N. Iwasa, H. Iwasaki, S. Kanno, Y. Kondo, T. Kubo, S. Kubono, M. Kunibu, K. Kurita, Y.U. Matsuyama, S. Michimasa, T. Minemura, M. Miura, H. Murakami, T. Nakamura, M. Notani, S. Ota, A. Saito, H. Sakurai, M. Serata, S. Shimoura, T. Sugimoto, E. Takeshita, S. Takeuchi, K. Ue, K. Yamada, Y. Yanagisawa, K. Yoneda, A. Yoshida “Resonance states in  $\text{P-27}$  using Coulomb dissociation and their effect on the stellar reaction  $\text{Si-26}(p,\gamma)\text{P-27}$ ” *Phys. Rev. C* **84** (2011) 035808\*
8. H. Matsubara, A. Tamii, Y. Shimizu, K. Suda, Y. Tameshige, J. Zenihiro: “Wide-window gas target system for high resolution experiment with magnetic spectrometer”, *Nucl. Instrum. Methods A* **678** (2012) 122-129.\*

9. Yamaguchi T., Tanaka K., Suzuki T., Ozawa A., Ohtsubo T., Aiba T., Aoi N., Baba H., Fukuda M., Hashizume Y., Inafuku K., Iwasa N., Izumikawa T., Kobayashi K., Komuro M., Kondo Y., Kubo T., Kurokawa M., Matsuyama T., Michimasa S., Motobayashi T., Nakabayashi T., Nakajima S., Nakamura T., Sakurai H., Shinoda R., Shinohara M., Suzuki H., Takechi M., Takeshita E., Takeuchi S., Togano Y., Yamada K., Yasuno T., Yoshitake M., “Nuclear reactions of  $^{19,20}\text{C}$  on a liquid hydrogen target measured with the superconducting TOF spectrometer”, Nucl. Phys. **A864** (2011) 1–37.\*
10. Satou Y., Nakamura T., Kondo Y., Matsui N., Hashimoto Y., Nakabayashi T., Okumura T., Shinohara M., Fukuda N., Sugimoto T., Otsu H., Togano Y., Motobayashi T., Sakurai H., Yanagisawa Y., Aoi N., Takeuchi S., Gomi T., Ishihara M., Kawai S., Ong H.J., Onishi T.K., Shimoura S., Tamaki M., Kobayashi T., Matsuda Y., Endo N., Kitayama M., “ $^{14}\text{Be}(p,n)^{14}\text{B}$  reaction at 69 MeV in inverse kinematics”, Phys. Lett. B **697** (2011) 459-462.\*
11. Back T., Qi C., Moradi F.Ghazi, Cederwall B., Johnson A., Liotta R., Wyss R., Al-Azri H., Bloor D., Brock T., Wadsworth R., Grahn T., Greenlees P.T., Hauschild K., Herzan A., Jacobsson U., Jones P.M., Julin R., Juutinen S., Ketelhut S., Leino M., Lopez-Martens A., Nieminen P., Peura P., Rakkila P., Rinta-Antila S., Ruotsalainen P., Sandzelius M., Saren J., Scholey C., Sorri J., Uusitalo J., Go S., Ideguchi E., Cullen D.M., Procter M.G., Braunroth T., Dewald A., Fransen C., Hackstein M., Litzinger J., Rother W., “Lifetime measurement of the first excited  $2^+$  state in  $^{108}\text{Te}$ ”, Phys. Rev. C **84** (2011) 041306.\*
12. Sato N., Haba H., Ichikawa T., Kaji D., Kudou Y., Morimoto K., Morita K., Ozeki K., Sumita T., Yoneda A., Ideguchi E., Koura H., Ozawa A., Shinozuka T., Yamaguchi T., Yoshida A., “Production and Decay Properties of  $^{264}\text{Hs}$  and  $^{265}\text{Hs}$ ”, J. Phys. Soc. Jpn. **80** (2011) 094201.\*
13. S. Watanabe, S. Kubono, Y. Ohshiro, H. Yamaguchi, M. Kase, M. Wada, and R. Koyama, “Simple, High-Sensitive, and Non-Destructive Beam Monitor for RI Beam Facilities”, Nucl. Instr. Meth. A **633** 8–14 (2011).\*
14. J. Chen, A.A. Chen, G. Amadio, S. Cherubini, H. Fujikawa, S. Hayakawa, J.J. He, N. Iwasa, D. Kahl, L.H. Khiem, S. Kubono, S. Kurihara, Y.K. Kwon, M. La Cognata, J.Y. Moon, M. Niikura, S. Nishimura, J. Pearson, R.G. Pizzone, T. Teranishi, Y. Togano, Y. Wakabayashi, and H. Yamaguchi, “Strong  $25\text{Al}+p$  resonances via elastic proton scattering with a radioactive  $25\text{Al}$  beam” Phys. Rev. C **85** 015805 (2012).\*
15. N. Imai, Y. Hirayama, Y.X. Watanabe, T. Teranishi, T. Hashimoto, S. Hayakawa, Y. Ichikawa, H. Ishiyama, S.C. Jeong, D. Kahl, S. Kubono, H. Miyatake, H. Ueno, H. Yamaguchi, K. Yoneda, A. Yoshimi, “Isobaric analog resonances of the  $N = 21$  nucleus  $^{35}\text{Si}$ ”, Phys. Rev. C **85**, 034313 (2012). \*
16. H.S. Jung, C.S. Lee, Y.K. Kwon, J.Y. Moon, J.H. Lee, C.C. Yun, S. Kubono, H. Yamaguchi, T. Hashimoto, D. Kahl, S. Hayakawa, Choi Seonho, M.J. Kim, Y.H. Kim, Y.K. Kim, J.S. Park, E.J. Kim, C.B. Moon, T. Teranishi, Y. Wakabayashi, N. Iwasa, N.T. Yamada, Y. Togano, S. Kato, S. Cherubini, G.G. Rapisarda, “Experimental study of resonant states in  $^{27}\text{P}$  via elastic scattering of  $^{26}\text{Si}+p$ ”, Phys. Rev. C. **85**, 045802 (2012)\*
17. K. Admodt *et al.* for the ALICE Collaboration: “Rapidity and transverse momentum dependence of inclusive  $J/\psi$  production in pp collisions at  $\sqrt{s} = 7$  TeV”, Phys.Lett. B704 (2011) 442-455 \*
18. K. Admodt *et al.* for the ALICE Collaboration: “Higher Harmonic Anisotropic Flow Measurements of Charged Particles in Pb-Pb Collisions at  $\sqrt{s_{NN}} = 2.76$  TeV”, Phys. Rev. Lett. 107, 032301 (2011) \*
19. K. Admodt *et al.* for the ALICE Collaboration: “Production of pions, kaons and protons in pp collisions at  $\sqrt{s} = 900$  GeV with ALICE at the LHC”, Eur.Phys.J.C 71(6): 1655, 2011\*
20. B. Abelev *et al.* for the ALICE Collaboration: “Heavy flavour decay muon production at forward rapidity in proton-proton collisions at  $\sqrt{s} = 7$  TeV”, Phys. Lett. B 708 (2012) 265\*
21. B. Abelev *et al.* for the ALICE Collaboration: “Measurement of Event Background Fluctuations for Charged Particle Jet Reconstruction in Pb-Pb collisions at  $\sqrt{s_{NN}} = 2.76$  TeV”, JHEP 03 (2012) 053\*
22. K. Admodt *et al.* for the ALICE Collaboration: “Femtoscopy of pp collisions at  $\sqrt{s}=0.9$  and 7 TeV at the LHC with two-pion Bose-Einstein correlations”, Phys. Rev. D 84, 112004 (2011)\*
23. B.Abelev *et al.* for the ALICE Collaboration: “Measurement of charm production at central rapidity in proton-proton collisions at  $\sqrt{s} = 7$  TeV”, JHEP 01 (2012) 128\*
24. B.Abelev *et al.* for the ALICE Collaboration: “ $J/\psi$  polarization in pp collisions at  $\sqrt{s}=7$  TeV”, Phys.Rev.Lett. 108 (2012) 082001\*

25. K. Admodt *et al.* for the ALICE Collaboration: “Particle-Yield Modification in Jetlike Azimuthal Di-hadron Correlations in Pb-Pb Collisions at  $\sqrt{s_{NN}}=2.76$  TeV”, Phys. Rev. Lett. 108, 092301 (2012)\*
26. K. Admodt *et al.* for the ALICE Collaboration: “Harmonic decomposition of two particle angular correlations in Pb-Pb collisions at  $\sqrt{s_{NN}} = 2.76$  TeV”, Phys.Lett. B708 (2012) 249-264\*
27. A. Adare *et al.* for the PHENIX Collaboration: “Azimuthal correlations of electrons from heavy-flavor decay with hadrons in p+p and Au+Au collisions at  $\sqrt{s} = 200$  GeV”, Phys. Rev. C 83, 044912 (2011)\*
28. A. Adare *et al.* for the PHENIX Collaboration: “Identified charged hadron production in  $p + p$  collisions at  $\sqrt{s} = 200$  and 62.4 GeV”, Phys. Rev. C 83, 064903 (2011)\*
29. A. Adare *et al.* for the PHENIX Collaboration: “Event structure and double helicity asymmetry in jet production from polarized  $p + p$  collisions at  $\sqrt{s} = 200$  GeV”, Phys. Rev. D 84, 012006 (2011)\*
30. A. Adare *et al.* for the PHENIX Collaboration: “Suppression of away-side jet fragments with respect to the reaction plane in Au + Au collisions at  $\sqrt{s_{NN}} = 200$  GeV”, Phys. Rev. C 84, 024904 (2011)\*
31. A. Adare *et al.* for the PHENIX Collaboration: “Cold Nuclear Matter Effects on  $J/\psi$  Yields as a Function of Rapidity and Nuclear Geometry in  $d + A$  Collisions at  $\sqrt{s_{NN}} = 200$  GeV”, Phys. Rev. Lett. 107, 142301 (2011)\*
32. A. Adare *et al.* for the PHENIX Collaboration: “Production of  $\omega$  mesons in  $p + p$ ,  $d + Au$ ,  $Cu + Cu$ , and  $Au + Au$  collisions at  $\sqrt{s_{NN}} = 200$  GeV”, Phys. Rev. C 84, 044902 (2011)\*
33. A. Adare *et al.* for the PHENIX Collaboration: “Heavy-quark production in  $p + p$  and energy loss and flow of heavy quarks in  $Au + Au$  collisions at  $\sqrt{s_{NN}} = 200$  GeV”, Phys. Rev. C 84, 044905 (2011)\*
34. A. Adare *et al.* for the PHENIX Collaboration: “Suppression of Back-to-Back Hadron Pairs at Forward Rapidity in  $d + Au$  Collisions at  $\sqrt{s_{NN}} = 200$  GeV”, Phys. Rev. Lett. 107, 172301 (2011)\*
35. A. Adare *et al.* for the PHENIX Collaboration: “ $J/\psi$  suppression at forward rapidity in  $Au + Au$  collisions at  $\sqrt{s_{NN}} = 200$  GeV”, Phys. Rev. C 84, 054912 (2011)\*
36. A. Adare *et al.* for the PHENIX Collaboration: “Measurements of Higher Order Flow Harmonics in  $Au + Au$  Collisions at  $\sqrt{s_{NN}} = 200$  GeV”, Phys. Rev. Lett. 107, 252301 (2011)\*
37. Koshiroh Tsukiyama, Scott Bogner and Achim Schwenk “In-Medium Similarity Renormalization Group for Nuclei” Phys. Rev. Lett., 106.222502 (2011)
38. Naofumi Tsunoda, Takaharu Otsuka, Koshiroh Tsukiyama and Morten Hjorth-Jensen “Renormalization persistency of the tensor force in nuclei” Physical Review C 84, 044322 (2011)
39. Kosuke Nomura, Takaharu Otsuka, Noritaka Shimizu, and Lu Guo “Microscopic formulation of the interacting boson model for rotational nuclei” Phys. Rev. C 83, (2011) 041302(R)
40. K. Nomura, N. Shimizu, D. Vretenar, T. Niksic, and T. Otsuka “Robust regularity in gamma-soft nuclei and its microscopic realization” Phys. Rev. Lett. 108 (2012) 132501
41. K. Nomura, T. Niksic, T. Otsuka, N. Shimizu, and D. Vretenar “Quadrupole collective dynamics from energy density functionals: Collective Hamiltonian and the interacting boson model” Phys. Rev. C 84, 014302 (2011)
42. N. Parr, T. Suzuki, M. Honma, T. Marketin, D. Vretenar “Uncertainties in modeling low-energy neutrino-induced reactions on iron-group nuclei”, Physical Review C 84 (2011) 047305.
43. T. Suzuki, M. Honma, H. Mao, T. Otsuka, T. Kajino “Evaluation of electron capture reactions rates in Ni isotopes in stellar environments”, Physical Review C 83 (2011) 044619.
44. A. Gade, D. Bazin, B. A. Brown, C. M. Campbell, J. M. Cook, S. Effenauer, T. Glasmacher, K. W. Kemper, S. McDaniel, A. Obertelli, T. Otsuka, A. Ratkiewicz, J. R. Terry, Y. Utsuno, and D. Weisshaar “In-beam  $\gamma$ -ray spectroscopy of  $^{35}\text{Mg}$  and  $^{33}\text{Na}$ ” Phys. Rev. C 83, (2011) 044305
45. T. Suzuki, T. Yoshida, T. Kajino, T. Otsuka, “ $\beta$ -decays of isotones with neutron magic number of  $N=126$  and r-process nucleosynthesis”, Physical Review C 85 (2012) 015802.
46. K. Nomura, T. Otsuka, R. Rodriguez-Guzman, L. M. Robledo, and P. Sarriguren “Collective structural evolution in neutron-rich Yb, Hf, W, Os, and Pt isotopes” Phys. Rev. C 84, 054316 (2011)

47. K. Nomura, T. Otsuka, R. Rodriguez-Guzman, L. M. Robledo, P. Sarriguren, P. H. Regan, P. D. Stevenson, and Zs. Podolyak “Spectroscopic calculations of the low-lying structure in exotic Os and W isotopes” *Phys. Rev. C* **83**, 054303 (2011)

## B. Proceedings

1. H. Yamaguchi, T. Hashimoto, S. Hayakawa, D.N. Binh, D. Kahl, S. Kubono, “Alpha-induced astrophysical reactions studied at CRIB”, Proceedings of the International Symposium on Nuclear Astrophysics “Nuclei in the Cosmos - XI”, Heidelberg, Germany, July 19–23 2010, Proceedings of Science, PoS(NIC-XI)214, (2011).\*
2. Y. Akamatsu, H. Hamagaki, T. Hatsuda, T. Hirano “Can transport peak explain the low-mass enhancement of dileptons at RHIC?”, Proceedings of the 22nd INTERNATIONAL CONFERENCE ON ULTRA RELATIVISTIC NUCLEUS-NUCLEUS COLLISIONS, 23-28 May 2011. Annecy, France; *J. Phys. G* **38** (2011) 124184.
3. Hideki Hamagaki, “First results from the ALICE experiment at LHC” Proceedings of the 25th Nishinomiya-Yukawa Memorial International Workshop on High Energy Strong Interactions 2010: Parton Distributions and Dense QCD Matter (HESI10); *Prog. Theor. Phys. Suppl.* **187** (2011) 237-249.
4. Y. Hori, H. Hamagaki, T. Gunji, “Simulation study for forward calorimeter in LHC-ALICE experiment” Proceedings of the 14th International Conference on Calorimetry in High Energy Physics (CALOR 2010), 10-14 May 2010. Beijing, China; *J. Phys. Conf. Ser.* **293** (2011) 012029.
5. K. Aoki, H. Enyo, T. Gunji, H. Hamagaki, J. Kanaya, Y. Komatsu, S. Masumoto, K. Ozawa, T. Sato, M. Sekimoto, T. Tsuji, K. Utsunomiya, Y. Watanabe, S. Yokkaichi “A development of HBD for the J-PARC E16 experiment.” Proceedings of the 12th Vienna Conference on Instrumentation, 15-20 Feb, 2010, Vienna, Austria; *Nucl. Instrum. Meth. A* **628** (2011) 300-303.
6. Itahashi K., Berg G.P.A., Fujioka H., Geissel H., Hayano R.S., Hirenzaki S., Ikeno N., Inabe N., Itoh S., Kameda D., Kubo T., Matsubara H., Michimasa S., Miki K., Miya H., Nakamura M., Nishi T., Noji S., Ota S., Suzuki K., Takeda H., Todoroki K., Tsukada K., Uesaka T., Weick H., Yoshida K., “ Measurement of Pionic  $^{121}\text{Sn}$  atoms at the RI beam factory”, *Hyperfine Interact.* **209** (2012) 51–56.
7. T. Abe and R. Seki “Lattice EFT calculation of thermal properties of low-density neutron matter” *J. Phys.: Conf. Ser.* **321**, 012037 (2011)
8. T. Abe, P. Maris, T. Otsuka, N. Shimizu, Y. Utsuno, and J. P. Vary “Benchmark calculation of no-core Monte Carlo shell model in light nuclei” *AIP Conf. Proc.* **1355**, 173 (2011)
9. Yutaka Utsuno, Takaharu Otsuka, B. Alex Brown, Michio Honma, and Takahiro Mizusaki “Structure of unstable nuclei around  $N=28$  described by a shell model with the monopole-based universal interaction” *AIP Conf. Proc.* **1355**, 161 (2011).
10. Noritaka Shimizu, Yutaka Utsuno, Takahiro Mizusaki, Takaharu Otsuka, Takashi Abe, and Michio Honma “Extrapolation method in the Monte Carlo Shell Model and its applications “ *AIP Conf. Proc.* **1355**, pp. 138-144
11. Naoki Tajima and Takaharu Otsuka “Meaning of antiparallel proton and neutron angular momenta at low spins” *Phys. Rev. C* **84**, 064316 (2011)
12. Shuichiro Ebata, Takashi Nakatsukasa and Tsunenori Inakura “Systematic study of low-lying E1 strength using the time-dependent mean field theory” Proceedings of “Origin of Matter and Evolution of Galaxies 2011”, *AIP Conf. Proc.* **1484** (2011) 427
13. Tooru Yoshida, Naoyuki Itagaki and Kiyoshi Kato “Symplectic structure and transition properties of  $^{12}\text{C}$ ” Proceedings of “Origin of Matter and Evolution of Galaxies 2011”, *AIP Conf. Proc.* **1484** (2011) 424
14. T. Suzuki, T. Yoshida, M. Honma, H. Mao, T. Otsuka, T. Kajino, “Gamow-Teller and First-Forbidden Transition Strengths in Astrophysical Processes”, *Journal of Physics: Conference Series* **312** (2011) 042023.
15. T. Suzuki, “Spin Modes in Nuclei and Astrophysical Processes based on New Shell-Model Hamiltonians”, *Journal of Physics: Conference Series* **321** (2011) 012041.

16. T. Suzuki, T. Otsuka, "Spin modes in nuclei and nuclear forces", AIP Conference Proceedings **1355** (2011) 45-52.
17. T. Suzuki, "Neutrino-nucleus reactions at MEV region based on new shell-model Hamiltonians", AIP Conference Proceedings **1405** (2011) 271-276.
18. "Extraction of Hadron Interactions above Inelastic Threshold in Lattice QCD" S. Aoki, N. Ishii, T. Doi, T. Hatsuda, Y. Ikeda, T. Inoue, K. Murano, H. Nemura and K. Sasaki (HAL QCD Collaboration) Proc. Jpn. Acad. Ser. B **87**, 509-517 (2011), arXiv:1106.2281 [hep-lat].
19. "Three-Nucleon Forces explored by Lattice QCD Simulations" T. Doi, for HAL QCD Collaboration, PoS LAT2011, 151 (2011), arXiv:1112.4103 [hep-lat].
20. "Quark and Glue Momenta and Angular Momenta in the Proton — a Lattice Calculation" K.-F. Liu, M. Deka, T. Doi, Y.-B. Yang, B. Chakraborty, Y. Chen, S.-J. Dong, T. Draper, M. Gong, H.-W. Lin, D. Mankame, N. Mathur and T. Streuer PoS LAT2011, 164 (2011), arXiv:1203.6388 [hep-ph].
21. "The Lattice QCD Study of the Three-Nucleon Force" T. Doi, for HAL QCD Collaboration, AIP Conf. Proc. **1441**, 399-401 (2012), arXiv:1109.4748 [hep-lat].
22. "Exploring Three Nucleon Forces in Lattice QCD" T. Doi, for HAL QCD Collaboration, AIP Conf. Proc. **1388**, 636-639 (2011), arXiv:1105.6247 [hep-lat].
23. "Nucleon strangeness form factors and moments of PDF" T. Doi, M. Deka, S.-J. Dong, T. Draper, K.-F. Liu, D. Mankame, N. Mathur and T. Streuer AIP Conf. Proc. **1374**, 598-601 (2011), arXiv:1010.2834 [hep-lat].

### C. Theses

1. K. Kisamori: "Development of two-alpha detection system for exothermic double-charge exchange reaction( $^8\text{He}, ^8\text{Be}$ )", Master Thesis, the University of Tokyo, March 2012
2. M. Takaki: "Study of  $^{12}\text{Be}$  nucleus via heavy-ion doublecharge exchange reaction", Master Thesis, the University of Tokyo, March 2012
3. S. Noji: "A new spectroscopic tool by the radioactiveisotope-beam induced exothermic chargeexchange reaction", Doctor Thesis, the University of Tokyo, March 2012
4. Y. Kikuchi: "Development of hodoscope consisting of 1-mm square plastic scintillators for the experiments with high-rate unstable-nuclei beam", Master Thesis, the University of Tokyo, March 2012
5. A. Nukariya: "Development of a Readout System for the GEM-based X-ray Imaging Detector", Master Thesis, the University of Tokyo, March 2012
6. S. Hayashi: "Development of a Readout Circuit for Forward Calorimeter in LHC-ALICE experiment", Master Thesis, the University of Tokyo, March 2012
7. S. Sano: "Multi-strange Particle Production in Proton+Proton Collisions at  $\sqrt{s}=7$  TeV", Doctor Thesis, the University of Tokyo, March 2012

### D. Other Publications

1. 阿部喬発見から100年—原子核の謎に第一原理計算を駆使して挑む月刊JICFuS (<http://www.jicfus.jp/jp/promotion/pr/mj/4/>)、2011年12月
2. 月山幸四郎物質中の繰り込み群による原子核の記述日本物理学会誌, 2012 vol.67, No.5, pp. 338 - 342 「最近の研究から」
3. T. Suzuki, M. Honma, "Toward a Better Evaluation of Neutrino-Nucleus Reaction Cross Sections", Neutrinos - Properties, Sources and Detection, (Nova Science Publishers, New York) (2011) 145-150.
4. T. Suzuki, T. Yoshida, S. Chiba, T. Kajino, "Nucleosynthesis in supernovae and neutrino oscillation", BUTSURI, **67** (2012) 49-54.

## Talks and Presentations

### A. Conferences

1. Ideguchi E., “Study of high-spin states by using energy degraded RI beams”, Nuclear Physics with Energy-degraded RI Beam at RIBF, May 25, 2011, Wako, Japan.
2. Michimasa S., “Alpha-induced transfer reactions with degraded beams”, Nuclear Physics with Energy-degraded RI Beam at RIBF, May 25, 2011, Wako, Japan.
3. Michimasa S., “Gamma-ray Spectroscopy of neutron-rich Mg isotopes by using proton inelastic scattering”, RIBF ULIC and CNS Symposium on Frontier of Gamma-ray Spectroscopy (Gamma11), June 30 – July 2, 2011, Wako, Japan.
4. Sasamoto Y., “The super-allowed Fermi type charge exchange reaction ( $^{10}\text{C}, ^{10}\text{B}\gamma$ ) for studies of isovector non-spin-flip monopole resonance”, RIBF ULIC and CNS Symposium on Frontier of Gamma-ray Spectroscopy (Gamma11), June 30 – July 2, 2011, Wako, Japan.
5. Go S., “Digital pulse shape analysis method to extract interaction position for CNS-GRAPE”, RIBF ULIC and CNS Symposium on Frontier of Gamma-ray Spectroscopy (Gamma11), June 30 – July 2, 2011, Wako, Japan.
6. Nakajima D., “First results of the HypHI Phase 0 experiment”, RIBF ULIC and CNS Symposium on Frontier of Gamma-ray Spectroscopy (Gamma11), June 30 – July 2, 2011, Wako, Japan.
7. Ideguchi I., “Superdeformed Band in Asymmetric  $N > Z$  Nucleus,  $^{40}\text{Ar}$ , and High-Spin Level Structures in  $A \sim 40$  Nuclei”, RIBF ULIC and CNS Symposium on Frontier of Gamma-ray Spectroscopy (Gamma11), June 30 – July 2, 2011, Wako, Japan.
8. Michimasa S., “In-beam gamma-ray spectroscopy combined with transfer reactions” RCNP 研究会「リングサイクロトロン施設の将来」— 大強度超高品質ビームで切り拓く原子核科学のフロンティア —, Mar. 21–23, RCNP, Osaka University, Japan.
9. Shimoura S., “Physics by Brilliant project” RCNP 研究会「リングサイクロトロン施設の将来」— 大強度超高品質ビームで切り拓く原子核科学のフロンティア —, Mar. 21–23, RCNP, Osaka University, Japan.
10. S. Shimoura (invited): “Detectors for Nuclear Physics”, The Technology and Instrumentation in Particle Physics 2011 (TIPP 2011), June. 9–14, 2011, Chicago, USA.
11. H. Yamaguchi, “Studies related to  $^7\text{Be}$ ”, Review Meeting on CRIB Activities, Jun 21-22, 2011, Center for Nuclear Study, University of Tokyo, Wako, Japan.
12. S. Kubono, “Summary of Research Activities at CRIB and the Scope”, Review Meeting on CRIB Activities, Jun 21-22, 2011, Center for Nuclear Study, University of Tokyo, Wako, Japan.
13. S. Hayakawa, “Direct measurement of the  $^{11}\text{C}(\alpha, p)^{14}\text{N}$  reaction”, Review Meeting on CRIB Activities, Jun 21-22, 2011, Center for Nuclear Study, University of Tokyo, Wako, Japan.
14. H. Yamaguchi, “Alpha-induced reaction studies using low-energy RI beams at CRIB”, The 11th. International Symposium on Origin of Matter and Evolution of the Galaxies (OMEG11), Nov 14-18, 2011, Center for Nuclear Study, University of Tokyo, Wako, Japan.
15. S. Kubono, “Nuclear Physics Problems for Explosive Nucleosynthesis” The 11th. International Symposium on Origin of Matter and Evolution of the Galaxies (OMEG11), Nov 14-18, 2011, Center for Nuclear Study, University of Tokyo, Wako, Japan.
16. 大田 晋輔, “Nucleon correlation and pickup reaction”, RCNP 研究会「リングサイクロトロン施設の将来 – 大強度超高品質ビームで切り拓く原子核科学のフロンティア –」 Mar. 21-23, RCNP, Osaka University, Japan
17. S. Kawase, “Proton spin-orbit splitting in  $^{18}\text{O}$  studied by the (p,lp,2p) reaction at 200 MeV”, The international Conference on Advances in Radioactive Isotope Science (ARIS), May, 29– Jun. 3, Leuven, Belgium

18. Matsubara H., Takaki M., Uesaka T., Aoi N., Dozono M., Fujii T., Hashimoto T., Hatanaka K., Kikuchi Y., Kawabata T., Kawase S., Kisamori K., Lee C.S., Lee H.C., Maeda Y., Michimasa S., Miki K., Miya H., Noji S., Ota S., Sakaguchi S., Sasamoto Y., Shimoura S., Suzuki T., Takahisa K., Tamii A., Yako K., Yokota N., Yokoyama R., Zenihiro J., “Study of the neutron rich nuclei via heavy-ion double charge exchange reaction”, Direct Reactions with Exotic Beams (DREB2012), Mar. 26-29, 2012, Aula Magna, Faculty of SMFN, Pisa, Italy.
19. H. Hamagaki, “Experimental Overview of High Energy Density QCD”, Presented in the XLI International Symposium on Multiparticle Dynamics (ISMD2011) 25 - 30 Sep. 2011, Miyajima, Hiroshima, Japan.
20. T. Gunji: “Experimental studies of gluon shadowing/saturation (initial condition) in p+A/A+A collisions at RHIC and LHC” at the 20th Heavy Ion Cafe, Jan. 21, 2012, University of Tokyo, Komaba Campus, Japan
21. Hisayuki Torii for the ALICE Collaboration (Poster), “Neutral Meson Identified by ALICE-PHOS in Pb+Pb Collisions at  $\sqrt{s}_{NN}=2.76\text{TeV}$ ”, at Quark Matter 2011, May 26, 2011, Annecy, France
22. Yorito Yamaguchi for the PHENIX collaboration (Poster), “Low pT direct photon production in 200GeV d+Au collisions measured by the PHENIX detector” at the 22nd International conference on ultra-relativistic nucleus-nucleus collisions (QM2011), May 23–28, 2011, Annecy, France
23. Yorito Yamaguchi, “Photons at RHIC” at the High-pT Probes of High-Density QCD at the LHC (HPHD2011), May 30–June 1, 2011, Ecole Polytechnique, Paris, France
24. Yorito Yamaguchi, “Photon Measurements in Heavy Ion Collisions” at the XLI International Symposium of Multiparticle Dynamics (ISMD2011), Sep. 26–30, 2011, Miyajima, Hiroshima, Japan
25. Yorito Yamaguchi for the PHENIX collaboration, “Direct Photon Production in the Thermal Region from PHENIX” at the 27th Lake Louise Winter Institute, Feb. 19–25, 2012, Lake Louise, Alberta, Canada
26. TAKAHARA, Akihisae for the PHENIX Collaboration “ $J/\psi$  Photoproduction in ultra-peripheral Au+Au collisions measured by RHIC-PHENIX”, QXX International Workshop on Deep-Inelastic Scattering and Related Subjects, March, 2012, Bonn, Germany
27. Hisayuki Torii, “ハードプローブの最先端”, Heavy Ion Cafe/Pub 合同研究会 「QDC 物質の最先端」, June 8, 2011, Nagoya University, Japan
28. Yutaka Utsuno, Takaharu Otsuka, B. Alex Brown, Noritaka Shimizu, Michio Honma, Takahiro Mizusaki, and Takashi Abe “Recent development in the shell model: shell evolution and methodology” ECT\* Workshop “Nuclear structure seen through ground-state properties of exotic nuclei”, Trento, Italy, Oct. 17-21, 2011.
29. Yutaka Utsuno, Takaharu Otsuka, B. Alex Brown, Noritaka Shimizu, Michio Honma, and Takahiro Mizusaki “Shell evolution around and beyond N=28 studied with a large-scale shell-model calculation” YKIS2011 Symposium Frontier Issues in Physics of Exotic Nuclei (YKIS2011), Kyoto, Oct. 11-15, 2011.
30. Yutaka Utsuno, Takaharu Otsuka, Noritaka Shimizu, Michio Honma, and Takahiro Mizusaki “Location of the g<sub>9/2</sub> orbit in neutron-rich Ca isotopes studied with the shell model” RIBF ULIC and CNS Symposium on Frontier of gamma-ray spectroscopy (GAMMA11), Wako, June 30 - July 2, 2011.
31. Yutaka Utsuno and Satoshi Chiba “Cluster states around 16O studied with the shell model” YIPQS Long-term workshop Dynamics and Correlations in Exotic Nuclei (DCEN2011), Kyoto, Oct. 3, 2011.
32. Yutaka Utsuno, Takaharu Otsuka, B. Alex Brown, Michio Honma, and Takahiro Mizusaki “Structure of exotic nuclei in the sd-pf shell described by a shell model with the monopole-based universal interaction” The first International Conference on Advances in Radioactive Isotope Science (ARIS2011), Leuven, May 29 - June 3, 2011.
33. 角田直文、高柳和雄、Morten Hjorth-Jensen, 大塚孝治 “Effective interaction for the shell model in non-degenerate model space” ISPUN11, ハノイ、ベトナム、2011年11月26日
34. 角田直文、高柳和雄、Morten Hjorth-Jensen, 大塚孝治 “Microscopic derivation of the effective interaction for the shell model in more than one major shell” Frontier Issues in Physics of Exotic Nuclei (YKIS2011), 京都大学、京都、2011年10月14日
35. 角田直文、大塚孝治、月山幸志郎 “Tensor force in effective interaction of nuclear force” Advances in Radioactive Isotope Science - ARIS 2011, ルーベン、ベルギー、2011年5月

36. Tooru Yoshida, Naoyuki Itagaki and Kiyoshi Kato “Symplectic structure and monopole strength in  $^{12}\text{C}$ ” Frontier Issues in Physics of Exotic Nuclei (YKIS2011), Kyoto, Kyoto October 13 (11-15), 2011.
37. Tooru Yoshida, Naoyuki Itagaki and Kiyoshi Kato “Symplectic structure and transition properties of  $^{12}\text{C}$ ” The 11th International Symposium on Origin of Matter and Evolution of Galaxies (OMEG11), Wako, November 14 - 17, 2011.
38. Koshiroh Tsukiyama, Scott. K. Bogner and Achim Schwenk “In-medium similarity renormalization group for nuclear many-body systems” Dynamics and Correlations in Exotic Nuclei (DCEN2011), YITP, 10月5日
39. Koshiroh Tsukiyama, Scott K. Bogner and Achim Schwenk “In-medium similarity renormalization group for nuclear many-body systems” 大規模計算による原子核研究の展開、理化学研究所、2012年1月24日
40. Koshiroh Tsukiyama, Scott K. Bogner and Achim Schwenk “In-medium similarity renormalization group for nuclear many-body systems” 素核宇融合による計算基礎物理学の進展、合歓の郷、12月4日
41. Shuichiro Ebata, Takashi Nakatsukasa and Tsunenori Inakura “Cb-TDHF calculation for the low-lying E1 strength of heavy nuclei around the r-process path” Frontier Issues in Physics of Exotic Nuclei (YKIS2011)
42. Shuichiro Ebata, Takashi Nakatsukasa and Tsunenori Inakura “Study of pygmy dipole resonance with a new time-dependent mean field theory” Rutherford Centennial Conference on Nuclear Physics
43. Shuichiro Ebata, Takashi Nakatsukasa and Tsunenori Inakura “Pygmy dipole resonance of radio isotopes around r-process” RIBF ULIC and CNS Symposium on Frontier of gamma-ray spectroscopy (gamma11)
44. 江幡 修一郎, 中務 孝, 稲倉 恒法 “時間依存密度汎関数法を利用した E1 励起状態の系統的研究” HPCI 戦略プログラム分野5 「物質と宇宙の起源と構造」全体シンポジウム、秋葉原コンベンションホール、2012年3月7-8日
45. Shuichiro Ebata, Takashi Nakatsukasa and Tsunenori Inakura “Systematic calculation for low-lying E1 mode using the time-dependent mean field theory” 2nd AICS International Symposium -Computer and Computational Sciences for Exascale Computing-, AICS, March 1 - 2, 2012.
46. Shuichiro Ebata, Takashi Nakatsukasa and Tsunenori Inakura “Systematic study of low-lying E1 strength using the time-dependent mean field theory” The 11th International Symposium on Origin of Matter and Evolution of Galaxies (OMEG11), Wako, November 14 - 17, 2011.
47. Shuichiro Ebata, Takashi Nakatsukasa and Tsunenori Inakura “Canonical-basis TDHF calculation for E1 mode of heavy nuclei ( $A > 100$ )” The first International Conference on Advances in Radioactive Isotope Science (ARIS2011), Leuven, May 29 - June 3, 2011.
48. 清水則孝 “原子核理論における大規模殻模型計算” HPCI 戦略プログラム 分野2 × 分野5 異分野交流研究会 — 量子系の固有値問題と大規模計算 — 2011/07/26 筑波大学計算科学研究センター
49. Noritaka Shimizu “Recent developments toward large-scale shell-model calculations” YIPQS Long-term workshop Dynamics and Correlations in Exotic Nuclei (DCEN2011) 2011/10/05 Yukawa Institute
50. 大塚孝治, “60 years of nuclear shell model -paradigm”, achievement and future- NUSTAR Annual Meeting 2012、GENCO Fest talk GSI, Darmstadt, Germany March 1 (Feb 27-March 2), 2012、招待講演
51. 大塚孝治, “Problems and Ideas at the Dawn of Three-Body Force Effects in the Shell Model” ECT\* workshop “Three-Nucleon Forces in Vacuum and in the medium” Trento, Italy July 11 (11-15), 2011、招待講演
52. 大塚孝治, “先端大型殻模型計算による  $^{79}\text{Se}$  のベータ崩壊半減期” 2011年度核データ研究会 2011年11月17日 (16-17日) 原研テクノ交流館リコッティ、東海、招待講演
53. 大塚孝治, “Nuclear forces and spectroscopy” EGAN11 Padova, Italy June 27 (27-30), 2011、招待講演
54. 大塚孝治, “Exotic nuclei and new features of nuclear forces” Nordic Conference on Nuclear Physics Stockholm, Sweden June 14 (13-17), 2011、招待講演
55. 大塚孝治 “Structural evolution of exotic nuclei driven by nuclear forces” Frontier Issues in Physics of Exotic Nuclei (YKIS2011) Yukawa Institute for Theoretical Physics, Kyoto October 11 (11-15), 2011、招待講演

56. 大塚孝治, “Nuclear Forces, Exotic nuclei and Stellar Evolution”, 11th Int. Symp. on Origin of Matter and Evolution of Galaxies Wako, Japan November 14 (14-17), 2011、招待講演
57. 大塚孝治, “Evolution of structure in Exotic Nuclei and Nuclear Forces” 1st International Symposium on the Science with KoRIA Korea University Sejong Campus December 2 (1-2), 2011、招待講演
58. 大塚孝治, “Novelty of Structure of Exotic nuclei and Nuclear Forces” Rutherford Centennial Conference on Nuclear Physics Manchester, United Kingdom August 9 (8-12), 2011、招待講演
59. 大塚孝治, “Structure of exotic nuclei and nuclear forces” International Symposium on Physics of Unstable Nuclei (ISPUN11) Ha Noi, Vietnam November 24 (23-28), 2011、招待講演
60. 大塚孝治 “Neutron-rich Exotic Nuclei and Nuclear Forces” 3rd ANPhA Symposium Lanzhou 蘭州、中國 April 30, 2011、招待講演
61. 大塚孝治, “Single-particle states and the tensor force” ECT\* workshop “Recent Development in Transfer and Knockout Reactions”, Trento, Italy May 10 (9-13), 2011、招待講演
62. T. Suzuki, T. Otsuka: “Effects of Halo on the Coulomb Displacement Energy of the IAS of  $^{14}\text{Be}$  and Spin-Dependent Transitions in  $^{14}\text{Be}$ ”, International Conference on Advances in Radioactive Isotope Science (ARIS 2011), May 31, 2011, Leuven, Belgium.
63. T. Suzuki: “Nuclear Weak Processes of Astrophysical Interest”, International Symposium “Advances in Many-Body Nuclear Theory”, June 10, 2011, Primosten, Croatia.
64. T. Suzuki (invited): “Structure of Neutron-Rich Isotopes and Roles of Three-Body Forces”, Trento ECT\* workshop on Three-Nucleon Forces in Vacuum and in the Medium, July 13, 2011, Trento, Italy.
65. T. Suzuki, M. Honma: “Nuclear Weak Processes and Astrophysical Applications”, Rutherford Centennial Conference on Nuclear Physics, Aug. 11, 2011, Manchester, GB.
66. T. Suzuki, M. Honma, T. Otsuka, T. Kajino: “Gamow-Teller Strengths in Ni Isotopes and Nuclear Weak Processes”, Yukawa-Institute Symposium on Frontier Issues in Physics of Exotic Nuclei (YKIS 2011), Oct. 14, 2011, Kyoto, Japan.
67. T. Suzuki, T. Yoshida, T. Kajino, T. Otsuka, “Beta-decays of waiting-point nuclei at N=126 and r-process nucleosynthesis”, The 11th International Symposium on Origin of Matter and Evolution of Galaxies, Nov. 11, 2011, RIKEN, Tokyo
68. T. Suzuki, T. Yoshida, T. Kajino, T. Otsuka: “First-forbidden Transitions in N=126 Isotones and r-Process Nucleosynthesis”, The International Symposium on Physics of Unstable Nuclei, Nov. 24, 2011, Hanoi, Vietnam.
69. T. Suzuki, M. Honma: “Gamow-Teller and first-forbidden transitions in nuclear weak processes”, Direct reactions with exotic beams workshop, March 27, 2012, Pisa, Italy.

## B. JPS Meetings

1. Yokoyama R., Nishibata H., Hamatani N., Shimota T., Odahara A., Ito Y., Takatsu J., Tajiri K., Ideguchi E., “インビーム  $\gamma$  線核分光における蒸発粒子反跳効果の補正”, the JPS Autumn meeting, Sep. 16–19, 2011, Hirosaki University, Aomori, Japan.
2. “4 中性子系質量欠損核分光実験に向けた、検出器読み出しシステムの開発と性能評価” Kisamori K., Shimoura S., Michimasa S., Ota S., Noji S., Tokieda H., Yokoyama R., Baba H., “4 中性子系質量欠損核分光実験に向けた、検出器読み出しシステムの開発と性能評価” the JPS Autumn meeting, Sep. 16–19, 2011, Hirosaki University, Aomori, Japan.
3. Shimoura S., “高アイソスピン核における一粒子励起状態”, the JPS Autumn meeting, Sep. 16–19, 2011, Hirosaki University, Aomori, Japan.
4. Ideguchi E., Go S., Miya H., Kisamori K., Takaki M., Ota S., Michimasa S., Shimoura S., Koike T., Yamamoto T., Shirotori K., Ito Y., Takatsu J., Suzuki T., Morikawa T., Shinozuka T., Yang S., Shizuma T., Oshima M., Koizumi M., Toh Y., Hatsukawa Y., Kimura A., Furutaka K., Nakamura S., Kitadani F., Harada H., Sugawara M., Watanabe Y.X., Hirayama Y., Oi M., “質量数 30 領域の高スピン状態の研究”, the JPS Autumn meeting, Sep. 16–19, 2011, Hirosaki University, Aomori, Japan.

5. Takaki M., Matsubara H., Uesaka T., Aoi N., Ota S., Kawase S., Kawabata T., Kikuchi Y., Kisamori K., Kubota Y., Sakaguchi S., Sasamoto Y., Shimoura S., Suzuki T., Zenihiro J., Lee H.C., Takahisa K., Tamii A., Lee C.S., Dozono M., Tokieda H., Noji S., Hashimoto T., Fujii T., Maeda Y., Miki K., Michimasa S., Miya H., Yako K., Yokota K., Yokoyama R., Tang Leung Tsz, “重イオン二重荷電交換反応を用いた  $^{12}\text{Be}$  の研究”, the JPS Autumn meeting, Sep. 16–19, 2011, Hirosaki University, Aomori, Japan.
6. Michimasa S., Yanagisawa Y., Inafuku K., Aoi N., Elekes Z., Fulop Zs., Ichikawa Y., Iwasa N., Kurita K., Kurokawa M., Machida T., Motobayashi T., Nakamura T., Nakabayashi T., Notani M., Ong H.J., Onishi T.K., Otsu H., Sakurai H., Shinohara M., Sumikama T., Takauchi S., Tanaka K., Togano Y., Yamada K., Yamaguchi M., Yoneda K., “陽子非弾性散乱を用いた Island of inversion 核の低励起状態の研究”. the JPS Autumn meeting, Sep. 16–19, 2011, Hirosaki University, Aomori, Japan.
7. Fujii T., Ota S., Shimoura S., Aoi N., Takeshita E., Takeuchi S., Suzuki H., Baba H., Fukuchi T., Fukui T., Hashimoto Y., Ideguchi E., Ieki K., Iwasa N., Iwasaki H., Kanno S., Kondo Y., Kubo T., Kurita K., Minemura T., Michimasa S., Motobayashi T., Murakami T., Nakabayashi T., Nakamura T., Niikura J., Okumura T., Onishi T., Sakurai H., Shinohara M., Suzuki D., Suzuki M., Tamaki M., Tanaka K., Togano Y., Wakabayashi Y., Yamada I., “ $^{32}\text{Mg}$  近傍不安定核の  $\alpha$  非弾性散乱”, JPS Spring Meeting, March 24–27, 2012, Kwansai Gakuin University, Osaka, Japan.
8. Shimoura S., “土壌放射線マップの作成”, JPS Spring Meeting, March 24–27, 2012, Kwansai Gakuin University, Osaka, Japan.
9. Takaki M., Matsubara H., Uesaka T., Aoi N., Ota S., Kawase S., Kawabata T., Kikuchi Y., Kisamori K., Kubota Y., Sakaguchi S., Sasamoto Y., Shimoura S., Suzuki T., Zenihiro J., Lee H.C., Takahisa K., Tamii A., Lee C.S., Dozono M., Tokieda H., Noji S., Hashimoto T., Fujii T., Maeda Y., Miki K., Michimasa S., Miya H., Yako K., Yokota K., Yokoyama R., Tang Leung Tsz, “超多重項間遷移を用いた二重荷電交換反応  $^{12}\text{C}(^{18}\text{O}, ^{18}\text{Ne})$  測定による  $^{12}\text{Be}$  核の研究”, JPS Spring Meeting, March 24–27, 2012, Kwansai Gakuin University, Osaka, Japan.
10. Ideguchi E., Sarantites D.G., Reviol W., Chiara C.J., Devlin M., Baktash C., Janssens R.V.F., Rudolph D., Axelsson A., Carpenter M.P., Galindo-Uribarri A., LaFosse D.R., Lauritsen T., Lerma F., Lister C.J., Reiter P., Seweryniak D., Weiszflog M., Wilson J.N., “ $^{42}\text{Ca}$  の高スピン状態の研究”, JPS Spring Meeting, March 24–27, 2012, Kwansai Gakuin University, Osaka, Japan.
11. Lee C.S., Uesaka T., Ota S., Sasano M., “重イオン蓄積リングの核反応実験への適用可能性の検討”, JPS Spring Meeting, March 24–27, 2012, Kwansai Gakuin University, Osaka, Japan.
12. Tokieda H., Ota S., Dozono M., Michimasa S., Hashimoto T., Matsubara H., Kawase S., Kikuchi Y., Kubota Y., Lee C.S., Gunji T., Yamaguchi H., Kahl D.M., Akimoto R., Hamagaki H., Kubono S., Uesaka T., “重水素ガスを用いた GEM の応答”, JPS Spring Meeting, March 24–27, 2012, Kwansai Gakuin University, Osaka, Japan.
13. Kikuchi Y., Ota S., Matsubara H., Kubota Y., Lee C.S., Uesaka T., “大強度不安定核ビーム実験のための 1mm 角プラスチックシンチレータを用いたホドスコープの開発”, JPS Spring Meeting, March 24–27, 2012, Kwansai Gakuin University, Osaka, Japan.
14. S. Kawase, “陽子ノックアウト反応による酸素同位体のスピン軌道分離の研究”, the JPS fall meeting, Sep. 16–19, 2011, Hirosaki, Japan
15. Y. Kubota, T. Uesaka, S. Ota, M. Dozono, Y. Kikuchi, “不安定核実験のための高位置分解能中性子トラッカーの開発”, at the JPS fall meeting, 16–19 Sep. 2011, Hirosaki University, Japan
16. T. Gunji for the ALICE Collaboration, “Dielectron measurement in p+p and Pb+Pb Collisions at LHC-ALICE”, at the JPS Spring meeting, Mar. 24–27, 2012, Kansai-Gakuin University, Japan
17. T. Gunji, “日本の核物理の将来:高エネルギー重イオンレポート”, at the JPS fall meeting, symposium on “日本の核物理の将来”, Setp. 16–19, 2011, Hirosaki University, Japan
18. T. Gunji for the ALICE Collaboration, “Heavy Quarkonium Production in p+p and Pb+Pb Collisions at LHC-ALICE”, at the JPS fall meeting, Setp. 16–19, 2011, Hirosaki University, Japan
19. S. Hayashi, H.Hamagaki, T.Gunji, M.Tanaka, H.Ikeda, M.Kurokawa, Y.Katayose: “Development of a Front-end ASIC for Forward Calorimeter in LHC-ALICE experiment” at the JPS fall meeting, Setp. 16–19, 2011, Hirosaki University, Japan
20. S. Hayashi, H.Hamagaki, T.Gunji, M.Tanaka, H.Ikeda, M.Kurokawa, Y.Katayose: “Development of a Front-end ASIC for Forward Calorimeter in LHC-ALICE experiment” at the JPS Spring meeting, Mar. 24–27, 2012, Kansai Gakuin University, Japan

21. R. Akimoto for the PHENIX Collaboration, “Performance of the silicon vertex tracker for the RHIC-PHENIX experiment”, at the JPS fall meeting, Setp. 16–19, 2011, Hirosaki University, Japan
22. R. Akimoto for the PHENIX Collaboration “Current status of heavy quark measurement by using silicon vertex tracker at RHIC-PHENIX experiment”, at the JPS Spring meeting, Mar. 24–27, 2012, Kwansai Gakuin University, Japan
23. Y.Hori for the ALICE collaboration, “The measurement of strange hadron elliptic flow and higher harmonics in  $\sqrt{s_{NN}}=2.76\text{TeV}$  Pb-Pb collisions at LHC”, at the JPS fall meeting, Setp. 16–19, 2011, Hirosaki University, Japan
24. Y.Hori for the ALICE collaboration, “Charge dependent azimuthal correlation at  $\sqrt{s_{NN}}=2.76\text{TeV}$  Pb-Pb collisions at LHC-ALICE experiment”, at the JPS Spring meeting, Mar. 24–27, 2012, Kwansai Gakuin University, Japan
25. T. Tsuji for the ALICE Collaboration, “Measurements of  $\pi^0$  with respect to reaction plane in Pb+Pb collisions at  $\sqrt{s_{NN}} = 2.76 \text{ TeV}$ ”, at the JPS Spring meeting, Mar. 24–27, 2012, Kansei Gakuin University, Japan
26. Y.Sekiguchi, *et al*, “Development and measurement of basic properties of Glass GEM” at the JPS Spring meeting, Mar. 24–27, 2012, Kansei Gakuin University, Japan
27. A. Takahara for the PHENIX Collaboration, “Study of  $J/\psi$  photoproduction in ultra-peripheral Au+Au collisions at  $\sqrt{s_{NN}} = 200\text{GeV}$  using the PHENIX detector”, at the JPS fall meeting, Setp. 16–19, 2011, Hirosaki University, Japan
28. H. Torii for the ALICE Collaboration, “QGP through hard probes at LHC-ALICE”, at the JPS Autumn meeting, Sep. 17, 2011, Hirosaki University, Japan
29. H. Torii for the ALICE Collaboration, “Neutral meson production in p+p collisions at  $\sqrt{s}=0.9, 2.76,$  and  $7\text{TeV}$ ”, at the JPS Spring meeting, Mar. 26, 2012, Kansai-Gakuin University, Japan
30. Y. Yamaguchi for the PHENIX collaboration, “Nuclear effects on direct photon production in 200GeV d+Au collisions measured at the PHENIX experiment” at the JPS annual meeting, Mar. 24–27, 2012, Kwansai Gakuin University, Hyogo, Japan
31. A. Nukariya, H.Hamagaki, Y.Tanaka, T.Fusayasu, T.Kawaguchi, “GEM を用いた新型 X 線検出器のデータ処理部の開発” at the JPS fall meeting, Setp. 16–19, 2011, Hirosaki University, Japan
32. 阿部喬, P. Maris, 大塚孝治, 清水則孝, 宇都野穰, J. P. Vary 芯を仮定しないモンテカルロ殻模型による軽い核の構造の系統的研究日本物理学会 2001 年秋季大会、弘前大学、2011 年 9 月 16-19 日
33. 阿部喬有効場理論を用いた格子計算による低密度中性子物質の性質の解明日本物理学会 2011 年秋季大会、弘前大学、2011 年 9 月 16-19 日
34. 角田佑介、本間道雄、清水則孝、宇都野穰、大塚孝治大規模殻模型計算による Cr, Ni 偶偶核の研究日本物理学会 2011 年秋季大会、弘前大学、2011 年 9 月 18 日
35. 吉田亨、板垣直之、加藤幾芳 N アルファクラスターモデルにおける symplectic 構造とモノポール遷移強度日本物理学会 2011 年秋季大会 (弘前大学、2011 年 9 月 17 日)
36. 吉田亨、板垣直之、加藤幾芳 Sp 代数模型に基づく  $^{12}\text{C}$ ,  $^{16}\text{O}$  原子核の励起状態の研究日本物理学会 第 67 回年次大会、関西学院大学、2012 年 3 月 24-27 日
37. 清水則孝、水崎高浩対相関基底による変分モンテカルロ計算と射影法日本物理学会 2011 年秋季大会 2011/09/16 弘前大学
38. 清水則孝、宇都野穰、水崎高浩、大塚孝治、本間道雄、阿部喬多基底変分による大規模殻模型計算とその応用日本物理学会 2011 年秋季大会 2011/09/18 弘前大学
39. 宇都野穰 RIBF と RCNP 実験から引き出される殻構造の進化日本物理学会 2011 年秋季大会、弘前大学、2011 年 9 月 16-19 日
40. 江幡修一郎、中務孝、稲倉恒法 Cb-TDHF による重い核 ( $100 \lesssim A$ ) に対する低エネルギー双極子振動の系統的な研究日本物理学会 2011 年秋季大会
41. 江幡 修一郎重イオン反応への Cb-TDHF の応用日本物理学会 第 67 回年次大会、関西学院大学、2012 年 3 月 24-27 日

## C. Lectures

1. H. Hamagaki, “Ultra-hot QCD matter studied using high-energy heavy-ion collisions”, a series of lectures, made for the Division of Physics and Astronomy, the Graduate School of Science, Kyoto University, 28 - 30 June 2011.
2. Shimoura S., 「原子核と放射線 — 放射線って何？それはどこから、どうして、どのように？ — 」学校の先生のための放射線勉強会, May 8 and July 16, 2011, University of Tokyo, Tokyo, Japan.
3. Shimoura S., 「土壌中のガンマ線放出核種分析による福島周辺放射線マップ」理学系研究科シンポジウム「大震災復興へ向けての理学・理学者の役割」Feb. 3, 2012, University of Tokyo, Tokyo, Japan.
4. Shimoura S., 「放射能とは何か」東京大学 理工医農 4 研究科横断講義「放射線を知る」, Nov. 11, 2012, University of Tokyo, Tokyo, Japan.
5. 阿部喬素核宇宙融合レクチャー シリーズ第 4 回「原子核殻模型の基礎と応用」京都大学 基礎物理学研究所、2012 年 1 月 11,12 日

## D. Seminars

1. 松原礼明: 「sd 殻領域の M1 遷移強度分布とクエンチング」, May 20, 2011, Chiba University, Chiba, Japan.
2. T. Gunji, “Experimental Studies of Hot and Dense QCD medium at LHC-ALICE” at the 20th Hadron Seminar at JAEA, Oct. 5t 2012, JAEA, Japan
3. H. Hamagaki, “New progress in the experimental study of high-energy heavy-ion collisions”, presented in the colloquium of Research group Physics II, the Graduate School of Science, Kyoto University, 28 June 2011.
4. H. Torii, “クォークグルーオンプラズマ物性研究が開く扉”, 東大駒場核理論研究室セミナー、July 6, 2011, Tokyo University, Japan
5. 阿部喬, P. Maris, 大塚孝治, 清水則孝, 宇都野穰, J. P. Vary No-Core Monte Carlo Shell Model at the HPCI Strategic Program 研究会「素核宇融合による計算基礎物理学の進展 - ミクロとマクロのかけ橋の構築 -」、合歓の郷、2011 年 12 月 3-5 日
6. 阿部喬, P. Maris, 大塚孝治, 清水則孝, 宇都野穰, J. P. Vary 閉殻を仮定しないモンテカルロ殻模型計算の進展状況 HPCI 戦略プログラム分野 5 研究会「大規模計算による原子核研究の展開 — 核子多体系を中心に—」、理化学研究所 RIBF 棟、2012 年 1 月 24, 25 日
7. Yutaka Utsuno, Noritaka Shimizu, Takaharu Otsuka, and Takashi Abe Efficient computation of Hamiltonian matrix elements between non-orthogonal Slater determinants Computer Physics Communications
8. 宇都野穰超並列計算機に適する殻模型計算アルゴリズムの考察 HPCI 戦略プログラム分野 5 研究会大規模計算による原子核研究の展開 — 核子多体系を中心に—、理化学研究所、2012 年 1 月 24、25 日
9. 中務 孝, 江幡 修一郎正準基底表示の時間依存平均場理論と超流動原子核の線形応答日本物理学会誌、最近の研究から
10. 江幡 修一郎, 中務 孝, 稲倉 恒法光核反応に対する密度汎関数理論の応用研究会「素核宇融合による計算基礎物理学の進展 - ミクロとマクロのかけ橋の構築 -」、合歓の郷、2011 年 12 月 3-5 日
11. 江幡 修一郎, 中務 孝, 稲倉 恒法 Cb-TDHFB による低エネルギー E1 分布の系統的計算 E0,E1 励起を通じて探る原子核の低い励起エネルギーのエキゾチックな構造、基礎物理学研究所、2011 年 12 月 7-9 日
12. 吉田亨, 板垣直之, 加藤幾芳 Sp 代数模型に基づく 16O における E0 遷移強度の研究 E0,E1 励起を通じて探る原子核の低い励起エネルギーのエキゾチックな構造、基礎物理学研究所、2011 年 12 月 7-9 日

## E. Others

1. Shimoura S., Ikeuchi Y., Otsuka T., “Analysis of gamma-ray emitting nuclides in the soils of Fukushima and surrounding area” 日本原子力学会、2012 年春の年会、2012.3.19-21、福井大学.

## Personnel

### Director

OTSUKA, Takaharu *Professor, Department of Physics,  
Graduate School of Science*

### Scientific Staff

SHIMOURA, Susumu *Professor*  
KUBONO, Shigeru *Professor*  
HAMAGAKI, Hideki *Associate Professor*  
SHIMIZU, Noritaka *Associate Professor*  
IDEGUCHI, Eiji *Lecturer*  
YAMAGUCHI, Hidetoshi *Assistant Professor (~ Nov.)*  
*Lecturer (Nov. ~)*  
MICHIMASA, Shin'ichiro *Assistant Professor*  
GUNJI, Taku *Assistant Professor*  
OTA, Shinsuke *Assistant Professor*

### Guest Professors

SUZUKI, Toshio *Nihon University*  
MITSUMOTO, Toshinori *Sumitomo Heavy Industries, Ltd.*

### Technical Staff

OHSHIRO, Yukimitsu *YAMAZAKI, Norio*

### Technical Assistants

YAMAKA, Shoichi

UCHIYAMA, Kiyoshi

WATANABE, Shin'ichi (Jul.~)

YOSHINO, Rho (~ Aug.)

NINOMIYA, Hideaki

KUREI, Hiroshi

TANAKA, Masahiko (~ Aug.)

### Post Doctoral Associates

TORII, Hirayuki

TUKIYAMA, Koshiro

HASHIMOTO, Takashi

DOZONO, Masanori (~April)

SASAMOTO, Yoshiko

DOI, Takumi (Jul.~)

NAKAJIMA, Daisuke (Jun.~Jul.)

ABE Takashi

YOSHIDA, Tohru

MATSUBARA, Hiroaki

EBATA, Shuichiro

NOJI, Shunpei

HU, Jun (Nov~)

### Graduate Students

HAYAKAWA, Seiya

SANO, Satoshi

MIYA, Hiroyuki

AKIMOTO, Ryohji

TANG, Leung

KAWASE, Shoichiro

KISAMORI, Keiichi

MUKARIYA, Atsushi

KIKUCHI, Yosuke

HUJII, Toshihiko

KUBOTA, Yuki

KHAL, David

TAKAHARA, Akihisa

TOKIEDA, Hiroshi

HORI, Yasuto

GO, Shintaro

TUJI, Tomoya

TAKAKI, Motonobu

HAYASHI, Shin'ichi

YOKOYAMA, Rin

SEKIGUCHI, Yuko

LEE, CheongSoo

### Administration Staff

HIRANO, Midori

YAMAMOTO, Ikuko

ENDO, Takako

ASAKAWA, Yuko (Mar, 2012~)

KISHI, Yukino

ITAGAKI, Toshiko

SOMA, Yuko

## Committees

### Steering Committee

YAMAGATA, Toshio	<i>Department of Earth and Planetary Science, Graduate School of Science, UT</i>
AIHARA, Hiroaki	<i>Department of Physics, Graduate School of Science, UT</i>
HAYANO, Ryugo	<i>Department of Physics, Graduate School of Science, UT</i>
OTSUKA, Takaharu	<i>Department of Physics, Graduate School of Science, UT</i>
KUBONO, Shigeru	<i>Center for Nuclear Study, Graduate School of Science, UT</i>
SHIMOURA, Susumu	<i>Center for Nuclear Study, Graduate School of Science, UT</i>
GONOKAMI, Makoto	<i>Department of Physics, Graduate School of Science, UT</i>
NAGAMIYA, Shoji	<i>J-PARC Center, KEK and JAEA</i>
KOBAYASHI, Tomio	<i>International Center for Elementary Particle Physics, UT</i>
TAKAHASHI, Hiroyuki	<i>Department of Nuclear Engineering and Management, Graduate School of Engineering, UT</i>

